Platinum catalysts for the sustainable oxidation of biomass related compounds

Costanza Cucuzzella

Doctor of Philosophy in
Chemical Engineering and Applied Chemistry

ASTON UNIVERSITY
Energy and Bioproducts Research Institute

December 2019

Try to comprehend a little more every day. Have holy curiosity.

Thesis summary

The project described in this thesis is concerned with the platinum catalysed aerobic oxidation of biomass related model compounds, to explore new clean catalytic routes for the production of relevant intermediates in the field of fine chemicals and materials.

This work started with the optimisation of mesoporous and hierarchical TLCT SBA-15 structures through systematic variation of their textural properties, including pore diameter, surface area and metal loading. The successful synthesis has been validated via extensive characterisation of the materials. Pore-expanded mesoporous and macro-mesoporous Pt-TLCT SBA-15 materials have been subsequently applied to the aerobic oxidation of dodecanal. The attentive choice of the type of support architecture conferred significant advantages in terms of internal diffusion and catalytic activity, evidencing the elimination of mass-transport barriers inherent to SBA-15 materials.

Furthermore, a green and sustainable alternative for the selective synthesis of cinnamic acid from cinnamaldehyde has been investigated, as cinnamic acid is a promising compound to be developed in the medical field. The complex reaction mechanism has been studied, to identify the optimal conditions that favour the formation of cinnamic acid while minimising the production of benzaldehyde, the main by-product of this reaction. Air as oxidative agent together with a Pt-SiO_2 catalyst decreased the activity of the oxidative cleavage mechanism that promotes the formation of benzaldehyde, rendering the reaction more selective towards cinnamic acid.

Finally, the aerobic oxidation of 5-hydroxymethylfurfural has been explored with platinum nanoparticles dispersed over fumed silica, a non-porous acidic support that has not been extensively investigated in previous scientific literature, to assess the importance of the solid support in this reaction. A comprehensive study to investigate the catalytic abilities of Pt-SiO_2 has been conducted, exploring the effect of different temperatures, pressures and amount of base. The employed catalysts have been prepared with two platinum precursors, in order to examine if different precursors had a remarkable impact on the catalysis. The obtained results led to the conclusion that, between the two precursors used, hydrogen hexachloroplatinate (IV) hexahydrate represents the most suitable one for HMF aerobic oxidation, since it allowed smaller nanoparticle size, which in turn afforded higher platinum content located on the surface of the catalyst, where the reaction occurred.

Keywords: platinum, dodecyl aldehyde, cinnamaldehyde, hydroxymethylfurfural, heterogeneous catalysis.

Acknowledgements

To start, I would like to thank my supervisors, Dr Marta Granollers-Mesa and Dr Georgios Kyriakou. You have supported and guided me listening to my ideas without imposing yours, always allowing open discussions about my project. This has been priceless, and gave me the chance to conclude my PhD the way I wanted. Thanks for all your advice, help and guidance. Marta, correcting my thesis in such a short time and all your patience over the last three months are especially appreciated.

Furthermore, I am grateful to EBRI researchers and students. Every one of you has been supportive anytime I needed help or advise. Special thanks go to Drs Amin Osatiashtiani and Jinesh Manayil for the support with SEM, STEM and XPS data.

Well, it is finally time to look back at these three tortuous, yet exciting, years. All the adversities I faced over my PhD made me realise the type of person I want to be, dedicated to honesty and clear knowledge, without compromising my ethical integrity in terms of research.

Science taught me the art of patience. It taught me to never stop questioning, and that something is true until proven otherwise. It taught me that the most important thing for a researcher is having a creative mind, otherwise it is all about endless and repetitive series of data.

My journey through the PhD has been made much more tolerable by a lot of good people, from inside and outside EBRI – where real life happens. Some have crossed my path for a short time, but the time spent together has been worth it. Some others have been around for longer, and we became real friends. Some of you made me understand things that I would have never fathomed by myself. All of you guys helped me growing into a more mature person, more able to cope with whatever life puts me through, and I am so blessed for having shared this part of my life with you. A few kind and generous souls have really been there for me, you know who you are – love ya!

Mum, I want to thank you above anything else. Your enormous love and infinite support not only helped me through my lowest moments, but also reinforced the happiest ones. Achieving this step without your constant encouragement would have been impossible, thank you for always putting up with me – I know, sometimes I can be very quick-tempered! *“C’è chi ha due genitori, ma tu vali per tre. E yo mamma”.*

Finally, I truly loved writing this thesis, despite how energy consuming and sleep depriving it has been. Somebody told me to fight for my passions, to do whatever I want no matter how hard it is. I am doing it.

Table of contents

List of abbreviations

ß	Full-with half maximum of a peak
Δ	Heat
θ	Diffraction angle
λ	Wavelength of incident/reflected beam
a	Pore spacing
acac	Acetylacetonate
ATP	Ammonium tetrachloroplatinate (II)
BA	Benzaldehyde
BDE	Bond dissociation energy
BE	Binding energy specific of the element
BET	Brunauer-Emmet-Teller
BJH	Barret-Joyner-Halenda
BRIC	Brazil, Russian, India and China
C	Multilayer adsorption parameter in BET equation
CA	Cinnamic acid
CMT	Critical Micellisation Temperature
CO-OP SA	Co-operative Self-Assembly
CP	Cloud-point
CPA	Chloroplatinic acid (IV) hexahydrate
CTA^+	Cetyltrimethylammonium
d	Interplanar distance
DF	Dark field
DFF	2,5-diformylfuran
DMF	2,5-dimethylfuran
E_1	Heat of adsorption for the first layer
EDX	Energy dispersive X-rays
E_L	Heat of adsorption for the second subsequent nitrogen layers
FAME	Fatty acid methyl esters
FDCA	2,5-furandicarboxylic acid
FFA	Free fatty acids

GC-FID	Gas-Chromatography with Flame Ionisation Detector
GC-MS	Gas-Chromatography with Mass Spectrometry
GHG	Greenhouse gases
HFCA	5-hydroxymethyl-2-furancarboxylic acid
HMF	5-hydroxymethylfurfural
HPLC	High-Pressure Liquid Chromatography
HQ	Hydroquinone
HT-TLCT	Hydrothermally treated True Liquid Crystal Templating SBA-15 supports
HT/SA-TLCT	Hydrothermally and TMB (swelling agent) treated True Liquid Crystal Templating SBA-15 supports
hv	Energy of the incident radiation
ICP-MS	Inductively Coupled Plasma Mass Spectrometry
IPE	Isoelectric point
IR	Initial rate
IUPAC	International Union of Pure and Applied Chemistry
k	Particle morphology in Scherrer equation
KE	Photoelectron kinetic energy
L	Mean cross-sectional area of nitrogen molecule
L	Crystallite size
LCT	Liquid Crystal Templating
m	Mass of adsorbed sample
M-0	Pt CO-OP SA SBA-15 catalyst
M-1	Pt TLCT SBA-15 catalyst
M-2	Pt HT-TLCT SBA-15 (100 ˚C) catalyst
M-3	Pt HT-TLCT SBA-15 (120 ˚C) catalyst
MA	Maleic anhydride
MCM-41	Mobil Composition of Matter No. 41
MM-1	Pt *MM*-TLCT SBA-15 catalyst with PS size = 354 nm
MM-2	Pt HT-*MM*-TLCT SBA-15 catalyst (120 ˚C) catalyst with PS size = 229 nm
MM-3	Pt HT-*MM*-TLCT SBA-15 catalyst (120 ˚C) catalyst with PS size = 354 nm

MM-4	Pt HT-*MM*-TLCT SBA-15 catalyst (120 ˚C) catalyst with PS size = 426 nm
mmol$_0$	mmol of reactant at time zero
mmol$_r$	mmol of reactant at any time
mmol$_t$	mmol of reactant at specific time t
mmol$_{x=I}$	mmol of product i
MM-TLCT	Macro-mesoporous True Liquid Crystal Templating
N$_A$	Avogadro’s number
NP	Nanoparticle
OMSs	Ordered mesoporous silicas
P$_0$	Saturated pressure of nitrogen
P123	Surfactant agent Pluronic P123
PD	Pore diameter
PEO	Poly(ethylene oxide)
PET	Polyethylene terephthalate
PID	Proportional integral derivative
PNN	Tetraammineplatinum (II) nitrate
PPO	Poly(propylene oxide)
PS	Polystyrene
PSD	Pore size distribution
PWT	Pore wall thickness
PV	Pore volume
R	Universal gas constant
RF	Radio frequency
RID	Refractive index detector
S	Specific BET surface area
SA	Surface area
SA-TLCT	True Liquid Crystal Templating SBA-15 supports treated with swelling agents
SBA-15	Santa Barbara Amorphous-15
SEM	Scanning Electron Microscopy
Σmmol$_x$	Sum of mmol of all products produced during the reaction
STEM	Scanning Transmission Electron Microscopy

T	Analysis temperature
TAG	Triglycerides
TEOS	Tetraethoxysilane
TGA-MS	Thermogravimetric analysis with Mass spectrometry
TLCT	True Liquid Crystal Templating
TMB	1,3,5-trimethylbenzene
TMOS	Tetramethoxysilane
TSE	Tensile strength effect
v	Molar volume of adsorbate gas
V	Volume of nitrogen adsorbed
V_m	Monolayer adsorption volume of nitrogen
XPS	X-ray Photoelectron Spectroscopy
XRD	Powder X-ray Diffraction
Φ_s	Spectrometer “work function”

List of figures, tables, schemes and equations

CHAPTER 1: Introduction

CHAPTER 2: Materials and methods

CHAPTER 3: TLCT SBA-15 and *MM*-TLCT SBA-15 materials and catalysis

CHAPTER 4: Cinnamaldehyde aerobic oxidation

CHAPTER 5: Hydroxymethylfurfural aerobic oxidation

CHAPTER 1:

Introduction

1.1. The role of heterogeneous catalysis in green chemistry

The most serious threats for the environment that have been arising during the twenty-first century are energy crisis, global warming and melting of glaciers. These are principally caused by the emissions of greenhouse gases (GHG), of which carbon dioxide (CO_2) is reported to contribute 60% of the total global warming [1] and is mainly released from fossil fuel consumption in the transportation industry and power generation plants. [2]

The GHG in the Earth's atmosphere are made up primarily of water vapour, carbon dioxide, methane, nitrous oxide and ozone. The high CO_2 emissions are mainly associated with the use of fossil fuels, and their concentration has been continuously increasing over the last century [3] (**Figure 1.1**).

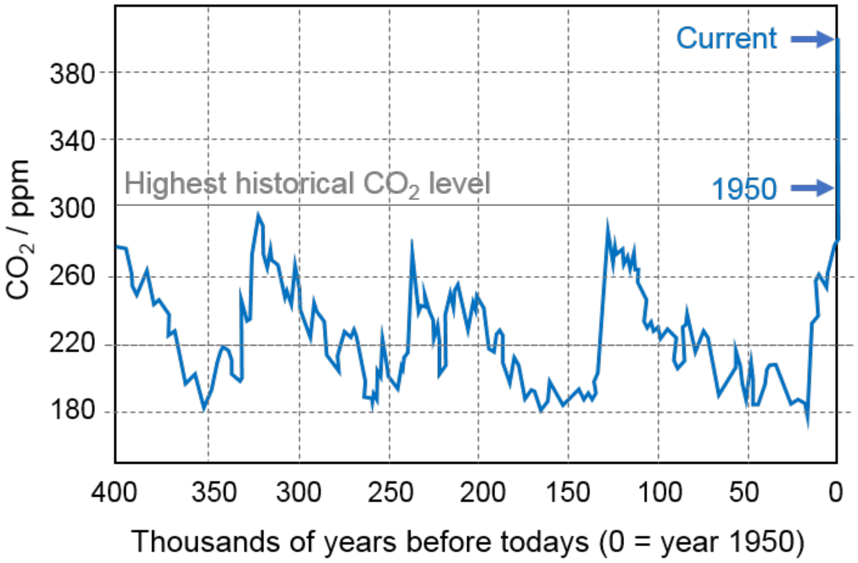

Figure 1.1: Change of CO_2 concentration over the last 400000 years (adapted from ref. [4]).

The high levels of GHG emissions led to rising concerns regarding global warming and climate change. In order to meet the needs of a future sustainable environment, it is vital to investigate and implement technologies that aim to reduce CO_2 emissions and limit its concentration in the atmosphere.

It has been estimated that the total worldwide energy consumption is approximately 515 EJ y^{-1}, most of which is currently supplied by fossil fuels, such as coal and petroleum. [5] The global energy consumption has been increasing exponentially over the last hundred years, especially from countries like Brazil, Russia, India and China (BRIC). [6] In order to tackle energy consumption, potential alternatives such as biomass, wind, water and solar radiation represent the renewable energy sources in which scientists have been recently investing the majority of their work. Of the sustainable sources above mentioned, biomass represents the only direct source of carbon for renewable fuels and chemicals production that can be inserted into existing markets. The global biomass supply potential is estimated in the range of 97-147 EJ in 2030. [7]

Lignocellulosic biomass represents the only renewable carbon source for the sustainable production of fuels, chemicals and materials. [8] Typically, it refers to plant-based biomass (such as corn stover, straw, forestry and agricultural residues) [8] and is composed of an organic fraction consisting of polymers that contain three major macromolecules: cellulose, hemicellulose and lignin, as shown in **Figure 1.2**. In addition to these primary polymers, some biomasses contain a small quantity of lipids, pectin and extractives, which do not exceed 10% w/w. [5]

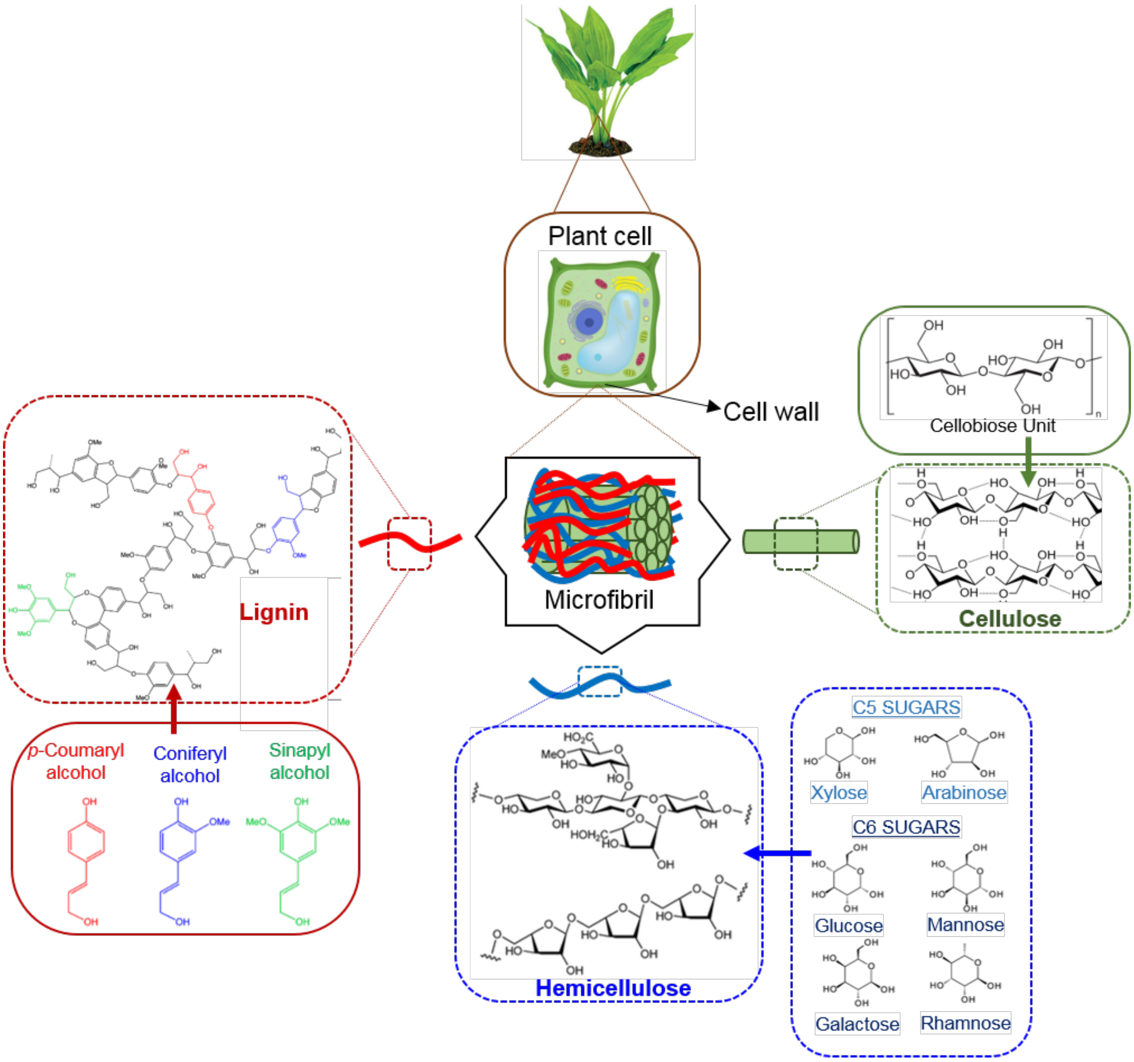

Figure 1.2: The main components and structure of lignocellulose (adapted from ref. [9]).

Owing to its abundance on Earth and bio-renewability, biomass is an alternative platform to fossil fuels. By employing different treatment methods, it is possible to obtain over 200 value-added compounds. [9]

The concept of sustainability has become considerably important both in industry and in society since mid-1900. Green chemistry, a concept that has been brought to the attention of the global community in the last two decades, consists of the design of chemical products and processes that aim to reduce, or eliminate, the use and generation of hazardous substances for the environment and health. The term "green chemistry" was coined in 1998 by Anastas and colleagues. [10] The Twelve Principles of Green Chemistry embody the main features to reach sustainability: waste prevention instead of remediation, atom efficiency, less hazardous/toxic chemicals, safer products by design, innocuous solvents and auxiliaries, preferably renewable raw materials and catalytic rather than stoichiometric reagents, are some of the ideas that make synthesis cleaner and safer. The Twelve Principles also identify catalysis as one of the most important tools for implementing green chemistry, as it offers several advantages including lower energy requirements, catalytic versus stoichiometric amounts of materials, increased selectivity and decreased use of processing and separation agents, guaranteeing the use of less toxic materials.

The environmental impact of a catalytic process is mainly measured by two features: the environmental factor (E factor), [11] namely the waste generated per kilogram of product, and the atom economy, [12] which is the conversion efficiency of a chemical process in terms of the amount of atoms incorporated into the final desired product(s). The solution to the problem of waste lies on the substitution of stoichiometric methodologies with green catalytic alternatives that are more atom economical and have fewer steps of reaction and, consequently, have lower E factors.

Homogeneous and heterogeneous catalysis are traditionally separate disciplines. Homogeneous catalysts are prepared using organic synthesis and contain well-defined and single-site active centres that can be characterised with different techniques. This not only leads to a high level of knowledge on the structure and spatial surroundings of the active centre but also the reaction mechanism can be reasonably understood, particularly for the interaction of the catalytic centre with the substrate and the structure of the transition state. [13] However, generally, homogeneous catalysts are not suitable for continuous flow reactions, and their separation from the reaction products is difficult and expensive as the catalysts are on the same phase as the reactants, thus they cannot be recovered and recycled. On the other hand, heterogeneous catalysis allows easy product separation from the reaction mixture and the material can be recycled and reused until loss of the catalytic activity. Heterogeneous catalysts can also be used in continuous flow processes, and industrially relevant materials are employed for the petrochemical and bulk chemical industries as solids. However, contrary to homogeneous catalysts, they suffer from an unsatisfactory level of understanding of the transformations at the molecular level. [13] Considering advantages and disadvantages of homogeneous and heterogeneous catalysis, the latter is more desirable since it offers low energy routes to products, eliminating the requirement for auxiliary species and facilitating catalyst recovery in order to minimise waste generation. In this context, heterogeneous catalysis adequately meets the needs of green chemistry, since it guarantees an easy separation of the catalyst from the products, having these two species different phases. For this reason, either their separation simply occurs via filtration, or there is no need for separation because the solid catalyst is allocated in a fixed bed reactor while the reactants and products flow through the different units in gas or liquid phase. This allows the elimination of steps such as distillation or extraction. [14]

Heterogeneous catalysis contributes to more than 90% of the global chemical output and several branches of industry rely upon heterogeneously catalysed processes, such as petrochemical, polymers, fine chemicals and environmental. [14] Heterogeneous catalysis is currently offering a sustainable and green solution to the rising CO_2 emissions and associated climate change since it makes use of biomass, the only non-petroleum route to organic molecules for the manufacture of bulk, fine and speciality chemicals and polymers, and the production of sustainable transportation fuels. [15] Potential biomass feedstocks include waste lignocellulosic or oil-based materials derived from plant or aquatic sources. Biomass processing is called biorefinery, defined as *the sustainable processing of biomass into a spectrum of marketable products and energy,* [16] which offers the co-production of biofuels, platform chemicals and energy. As biomass has a different chemical structure than fossil resources, it is necessary to develop new catalytic materials and routes to migrate feasibly towards biorefineries. Hence, heterogeneous catalysis is undertaking challenges to catalytic biomass processing in order to maximise biomass valorisation. As in the past decades catalytic technologies have played a crucial role in the economic development of petrochemical industry and modern society, now that a post-petroleum era is supervening, it is becoming necessary for catalysis to underpin analogous biorefinery technologies for the production of chemical intermediates, advanced functional materials and fuels from non-petroleum feedstocks. [15] This means that novel catalysts must be adapted in terms of their architecture, structure and functionality to new feedstocks and new process routes.

1.2. Mesoporous templated silicas

Over the past 30 years, chemists and engineers have focused much attention on a class of nanomaterials called ordered mesoporous silicas (OMSs). Due to their high surface areas, large volumes of ordered mesopores and different morphologies, this class of materials has major importance in the field of nanoscience. Applications of OMSs include catalysis, sorption, photonics, electronics, drug delivery, sensors and nanodevices. [17, 18] Depending on their pore size, these materials have been classified into three categories, according to the IUPAC nomenclature: microporous (< 2 nm), mesoporous (2-50 nm) and macroporous (> 50 nm), as illustrated in **Figure 1.3**. [19]

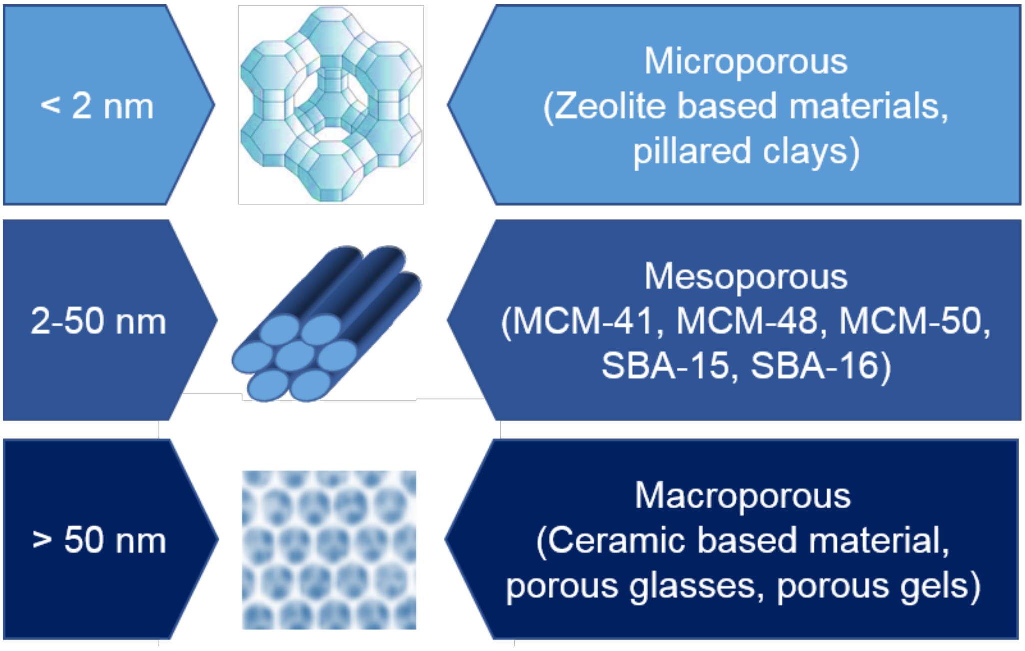

Figure 1.3: IUPAC classification of porous materials (adapted from ref. [19]).

In recent years, the potential catalytic applications of mesoporous materials have been investigated. Several reactions, such as Knoevenagel condensation, and selective oxidation reactions in the conversion of hydrocarbons and hydrodesulphurization, have been performed by using mesoporous materials as supports. [20-24]

Typically, OMS materials are prepared based on the sol-gel chemistry, which consists of silica-surfactant self-assembly of non-ionic (or amphiphilic) surfactants with the simultaneous condensation of the inorganic species, affording mesophases with different geometries and arrangements in a simple and reproducible way. [25] The most investigated pore topologies are the hexagonally packed cylindrical pores, as found in SBA-15, and the complex cubic pore system present in the KIT-6 structure, due to their large and uniform pore sizes, ordered mesochannels, large surface areas and periodic and ordered arrangements. [26]

The first discovered material belonging to OMSs is labelled as MCM-41. It has been reported by Mobil Corporation scientists in 1992. [27] It is commonly synthesised using a cationic cetyltrimethylammonium (CTA^+) surfactant and has a mono-dimensional mesoporous structure with pore spacing of about 4 nm and pore sizes of 2-3 nm.

A breakthrough in the synthesis of OMSs came at a later time with the appearance of two-dimensional hexagonal silicas, prepared by using amphiphilic block copolymers as templates, which are an important family of surfactants widely used in pharmaceutical [12] and petrochemical industries, as well as in household applications. [28] Besides possessing excellent interfacial stabilisation properties, these copolymers are low-cost, non-toxic and biodegradable. In composite material synthesis, they are used as structure-directing agents whose self-assembly features lead to ordered structures. [29] One representative example of two-dimensional mesoporous templated silica prepared with amphiphilic block copolymers is SBA-15, first synthesised by Zhao and co-workers in 1998. [29, 30] They reported the successful synthesis of a well-ordered hexagonal material possessing a *p6mm* symmetry that exhibits cylindrical pores of 4-5 nm and pore spacing of 10-12 nm, with improved thermal stability with respect to MCM-41.

A final example of mesoporous silica is represented by KIT-6, which shows a three-dimensional and cubic symmetry named *Ia3d*. Its synthesis was first reported by Kleitz and co-workers in 2003. [31] In this case, the preparation requires the use of a triblock copolymer ($PEO_{20}PPO_{70}PEO_{20}$)-butanol mixture in aqueous solution, in order to obtain a structure containing easily accessible and uniform large pores bigger than 5 nm (**Figure 1.4**).

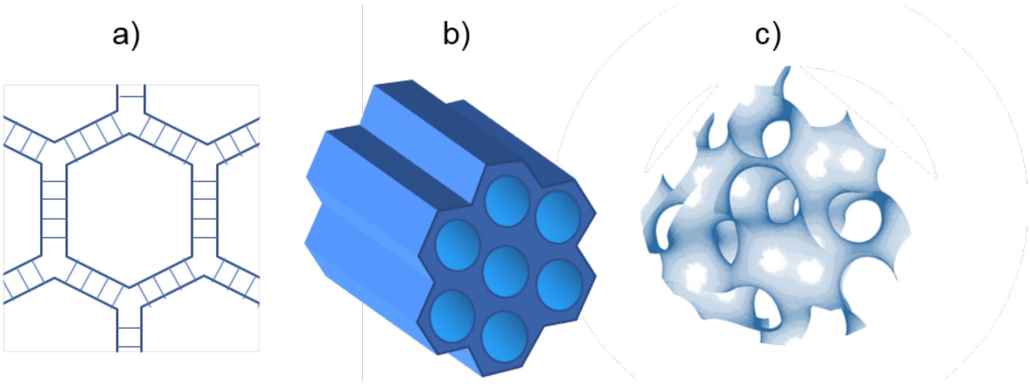

Figure 1.4: Representation of: **a)** mono-dimensional MCM-41, **b)** two-dimensional SBA-15, **c)** three-dimensional KIT-6 (Figures **a**, **b** and **c** adapted from ref. [32], [33] and [34], respectively).

1.2.1. Synthetic routes to SBA-15 materials

Since its discovery, [29, 30] SBA-15 has been receiving much attention by catalytic scientists because of its larger pores, thicker pore walls and higher hydrothermal stability [35] in comparison to its mono-dimensional analogous MCM-41. Besides, its high surface area (700 m^2 g^{-1}), tuneable pore size and ordered hexagonal structure render it an ideal support for the introduction of active sites in heterogeneous catalysis, especially for liquid-phase reactions. [36, 37]

Traditionally, SBA-15 is synthesised under acidic conditions using an amphiphilic triblock copolymer Pluronic P123 ($PEO_{20}PPO_{70}PEO_{20}$, where PEO and PPO stand for poly(ethylene oxide) and poly(propylene oxide), respectively) dissolved in an aqueous hydrochloric acid (HCl) and tetraethoxysilane (TEOS) mixture. This method is called “Cooperative Self-Assembly Liquid Crystal Templating” (CO-OP SA or LCT SBA-15) because the liquid crystal phase is not present at the beginning of the preparation, but it is held to form during the silica condensation. [26] The final material contains mesopores as well as micropores, and this is why it possesses high surface area (700-900 m^2 g^{-1}).

A different protocol for the synthesis of SBA-15 was applied later on by Wainwright and co-workers, [38] who adopted the previously developed method called “True Liquid Crystal Templating” (TLCT SBA-15) developed by Attard and co-workers in 1995. [39] This methodology allows better control of the silica morphology as the liquid crystal mesophase is pre-formed before the sol-gel condensation. As a consequence, since good control over the pore network is accomplished, the microporosity is much reduced, resulting in a decreased surface area (400 m^2 g^{-1}) and in a better location of metal nanoparticles within the silica skeleton that can be better directed inside the mesopore array. [38]

However, both synthetic routes are carried out under strongly acidic conditions by using an amphiphilic triblock copolymer P123 (**Figure 1.5**) as a template. It is well-known that $PEO_mPPO_nPEO_m$ triblock copolymers in water form micelles, in which the core and mantle are composed of hydrophobic PPO and hydrophilic PEO blocks, respectively. [40]

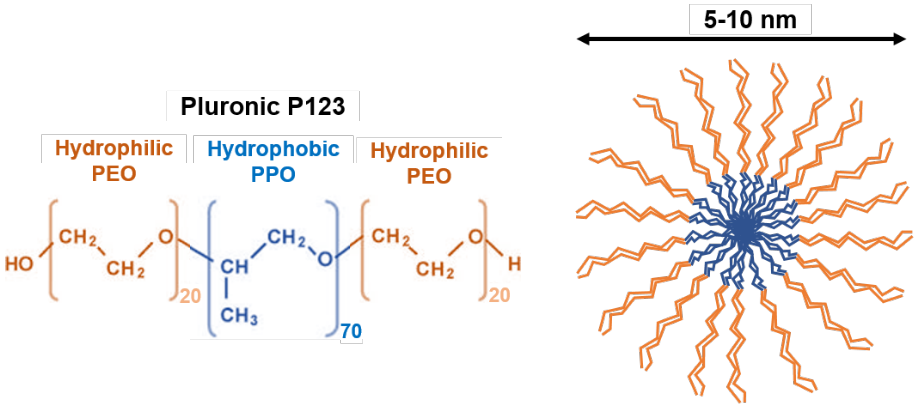

Figure 1.5: Triblock copolymer PEO$_{20}$-PPO$_{70}$-PEO$_{20}$, known as P123 (adapted from ref. [15]).

Micellisation is a spontaneous process occurring when the amphiphile self-aggregates, and is driven by the hydrophobic effect (or dehydration) of the PPO blocks, shunned by water molecules as these form hydrogen bonds with the hydrophilic PEO blocks. [41] The micelles so-formed are arranged in a hexagonal phase, a very common form of arrangement, which consists of stacks of rod-like micelles ordered into hexagonal arrays. [40]

To select the temperature of the synthesis, two factors have to be taken into consideration: the critical micellisation temperature (CMT) and the cloud-point (CP) of the surfactant. [26] When non-ionic surfactants are used as templates, the reaction temperature is typically higher than room temperature because of their higher CMT values compared to cationic surfactants. Many non-ionic surfactants may become insoluble in water at elevated temperatures, due to their CP value (85 °C in the case of Pluronic P123). [42] This phenomenon is observed when the solutions become cloudy due to phase separation, and the surfactants begin to precipitate. [26] Therefore, the synthesis temperature must be lower than the CP value of a surfactant. In the synthesis of SBA-15 templated by triblock copolymer P123, the optimal synthetic temperature is 35-40 °C, due to its solubility limit and CMT value for the formation of micelles.

The general procedure for the synthesis of SBA-15 involves several steps. First, a homogeneous solution is obtained by dissolving the surfactant in acidic water. Ordered mesoporous silicates are generally synthesised under basic or acidic conditions. Neutral and slightly basic solutions are unsuitable for this purpose because at pH between 6.0 and 8.5 the condensation rate of silicates occurs too rapidly to achieve good control of the surfactant-templating assembly. [43] At strong basic pH (ranging from 9.5 to 12.5), the polymerisation and cross-linkage of silicate species are fast and reversible. The breakthrough for the synthesis of highly ordered mesoporous silicates under strongly acidic conditions was realised in 1994 by Huo and co-workers. [44] When the synthesis is carried out under acidic conditions, the precipitation rate depends on the pH. Generally, the triblock copolymer is more hydrophilic at higher acid concentration because the PEO moieties of the surfactant are readily protonated. The silicate oligomers and the micelles show interactions at pH = 2-2.5, the isoelectric point (IEP) of silica. [25, 45, 46] For the synthesis of CO-OP SA SBA-15 it has been proven that at pH > 2.5 (above the IEP of silica) little control over the silica morphology is obtained as slow hydrolysis and fast condensation occur at the same time. Conversely, at pH < 2.5 (below the IEP) the reverse situation takes place, which is ideal for the synthesis of ordered mesoporous SBA-15. [25, 46]

When the silicate precursor is added to the solution, it undergoes acid catalysed hydrolysis, to form a solution of silicate oligomers. Siliceous oligomers and monomers are suitable precursors owing to the irreversible polymerisation of silicates under acidic conditions. The interaction between oligomers and surfactant micelles give rise to assembly and aggregation, with precipitation from a gel. During this step, a continuous condensation of silicate oligomers occurs, and precipitation affords well-ordered mesostructures. In the case of non-ionic surfactant P123 used as the template, the formation of mesostructures is slow; in fact, it lasts typically 30 minutes or even longer. [26] Scientific literature concerning the synthesis of CO-OP SA SBA-15 normally reports the use of TEOS as inorganic silicate precursor, [30] while reports on the preparation of TLCT SBA-15 make use of tetramethoxysilane (TMOS). [38] The latter results in a faster formation of mesoporous silica structures than the former, phenomenon that can be attributed to hydrolysis rates. [26] The type of interaction that is formed between non-ionic surfactant with silicate species consists of weak double-layer hydrogen bonds.

Subsequent solidification and reorganisation further proceed to form an ordered mesostructure. In the case of CO-OP SA SBA-15, hydrothermal treatment is then carried out to induce the complete condensation and solidification and to improve the organisation of the silica skeleton. The resultant product is finally cooled down to room temperature, filtered, washed and dried. The porosity is finally obtained after removal of the organic template via calcination. Different removal methods influence the characteristics of mesoporous materials. The most common method to remove templates is calcination, owing to the easy operation and complete elimination of the template. Organic surfactants can be decomposed or oxidised under oxygen or air atmosphere. The temperature programming rate should be low enough to prevent the structural collapse caused by local overheating. Upon continuous heating at high temperatures (up to 550 °C), the carbon chain fragments are eliminated, and the surface available becomes hydrophilic. The HCl from the acidic solution does not affect the quality of the products as it can be removed upon calcination. [47]

When applying the synthetic route devised by Attard and co-workers for the preparation of *true* or semi-liquid crystal mesophase, what differs from the methodology previously explained is the use of non-ionic surfactant at such high concentration that a liquid crystal forms at the beginning of the preparation. [39] The term “liquid crystal” is used to describe a matter with properties belonging to isotropic liquids (fluidity and viscosity) and crystalline solids (long-range orientational order) phases. In this way, the condensation of the inorganic precursor is improved due to the confined growth around the surfactant with formation of ceramic-like frameworks. TMOS is added in a 1:4 ratio with respect to water, in order to have complete hydrolysis of the former. After condensation, the template can be removed by calcination. The inorganic materials “cast” the mesostructures, pore sizes and symmetries from the liquid crystal scaffolds, resulting in a more rigid framework than CO-OP SA SBA-15. [26] In addition, the use of an inorganic precursor with a low polymerisation degree can improve the assembly at the organic-inorganic interface, namely P123 and silica species, respectively. This is the reason why the TLCT route makes use preferably of TMOS instead of TEOS as silica precursor.

During solvent evaporation (methanol developed from TMOS), the inorganic precursor further hydrolyses and cross-links. The highly concentrated surfactant form liquid crystal phases in the presence of inorganic oligomers during the final stage of solvent evaporation, so that organised mesostructures can form, stemming from the surfactant-templating assembly.

Materials prepared following the TLCT synthesis present a lack of microporosity, which is possibly due to either a lower extent of inclusion of PEO segments into the inorganic framework or the retraction of PEO chains under the present self-assembly conditions. [26] The fact that the TLCT preparation method assures the formation of a hexagonal mesophase before the introduction of silica precursor, avoids the PEO chains insertion into the silica framework, minimising the formation of micropores. Experiments of polarised optical microscopy of the preceding P123/H_2O gel formed in the initial step of the TLCT route revealed the presence of a hexagonal mesophase before the incorporation of the silica precursor. [38] This indicates a priori control of the silica support architecture.

Conversely, the large surface area typical of CO-OP SA SBA-15 is due to a high degree of microporosity, present as randomly distributed between interconnecting pores and/or as a corona around the mesopores. [38, 42] As a consequence of the arrangement of P123 in water, the micelles are surrounded by a corona of hydrated PEO chains that protrude by nearly 1 nm from the average micelle surface. [48] These chains repel each other, forming a distance of 3-4 nm, in such a way that they do not share their hydration shells. With the addition of the inorganic precursor, the majority of PEO chains insert into the silicate framework, generating micropores after the removal of the template.

The two pathways through which ordered mesostructured SBA-15 is synthesised are shown in **Figure 1.6**.

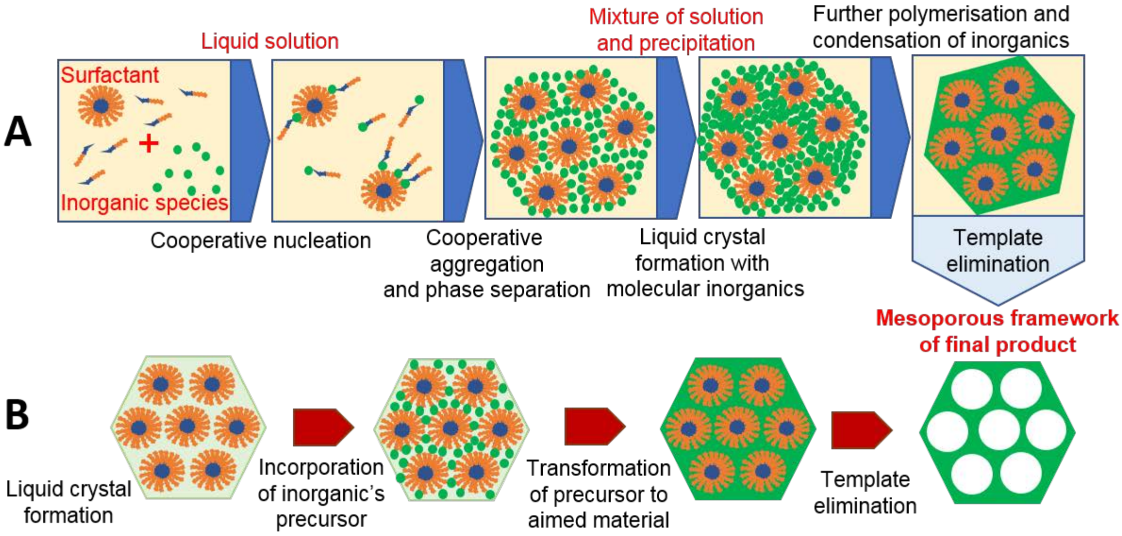

Figure 1.6: Schematic representation of CO-OP SA (**A**) and TLCT (**B**) SBA-15 synthesis (adapted from ref. [26]).

However, common to both preparation methods, the pore wall thickness of SBA-15 range from 3.1 to 4.8 nm, thicker than that of MCM-41, resulting in higher thermal and hydrothermal stability. [26]

The silica frameworks of SBA-15 are amorphous and possess a large number of hydroxyl groups (SiOH) on the surface, rendering it hydrophilic and offering excellent opportunities in further modification of the materials. [35]

1.2.2. Pore-expanded SBA-15 materials

The improvement of reactant diffusion inside the porous architecture of supports in heterogeneous catalysis has represented a significant and challenging matter for the application of these materials in the catalysis of large molecules. Several methodologies can be implemented in this regard, such as pore swelling, the introduction of macroporosity in mesostructures or utilisation of three-dimensional structures (i.e. KIT-6). However, the last case presents diffusion restrictions as the mass transfer of the reactant may undergo limited speed inside the porous network, due to the presence of a higher number of directions it can diffuse.

SBA-15 represents a valid support with regards to architecture expansion not only due to its tuneable pore size but also because additional macroporosity can be easily inserted to afford hierarchical structures. The development of ordered porous materials with pore sizes beyond 100 nm (macroporous) was reported for the first time using colloidal templates, i.e. polystyrene latex spheres in a colloidal solution, described by Velev and co-workers in 1997. [49]

From a practical point of view, pore-expansion of SBA-15 confers a striking activity enhancement toward several reactions. An emblematic example is the synthesis of fatty acid methyl esters (FAME) from triglycerides (TAG) and free fatty acids (FFA), which showed improved activity, attributed to better mass transport and active sites accessibility. [37] Introduction of porosity in an ordered fashion with interconnectivity between the pores and with hierarchical structure would be advantageous for a variety of applications, such as catalytic supports, adsorbents, electrode materials, slow drug delivery, optics and electronics. [50] As for pore expanded mesoporous silica, the insertion of an additional porosity finds advantages in catalytic applications, where reactants need to access the interior pore structure readily in a material where the internal surface area is maximised. Another important advantage of employing mesoporous architectures into which macropores have been incorporated consists of the minimisation of diffusional barriers and the potential enhancement of the distribution of the active site during catalyst preparation. [36, 51] Furthermore, these structures help to achieve enhancements in in-pore accessibility, for example by stabilising high active site dispersion, [51-53] or enhancing reagent diffusion during catalytic reactions especially in the case of bulky reagents. [51, 54]

In the last two decades, thanks to its tuneable pore size, the capability of CO-OP SA SBA-15 to swell its pore size has been widely investigated, as it has been widely proved how pore-expanded supports allow for important catalytic enhancements, such as improved mass transport and active sites accessibility, resulting in better reaction performances. [37] The main routes by which it is possible to achieve pore enlargement of SBA-15 make use of heat [47, 55, 56] and swelling agents (or porogens), such as hexane, [57-61] heptane, [59-62] cyclohexane, [57, 61] 1,3,5-triisopropylbenzene [57] and 1,3,5-trimethylbenzene. [63-65] Often, heat and micelle expanders have been combined, [30, 37, 65-67] to achieve a more significant effect on pore enlargement. All the above-mentioned pore-expansion methodologies have been exclusively applied to the conventionally synthesised CO-OP SA SBA-15 and, up to date, there are no reports concerning the application of these methods to the TLCT route.

Hydrothermal treatment is one of the most efficient methods to swell the pore diameter of mesoporous materials. According to the methodology applied to CO-OP SA SBA-15, during hydrothermal treatment the mesostructures undergo reorganisation, growth and crystallisation. The treatment temperature is relatively low, between 80 and 150 °C, in which the range of 95-100 °C has been mostly used. Higher temperature would result in the degradation of ordering and the decomposition of surfactants. In the scientific literature is suggested that the pore expansion depends on a modification of the hydrophobicity of the whole micelle domain upon high temperature.

As **Figure 1.5** represents, the PPO blocks of Pluronic P123 are strongly hydrophobic. The hydrophobicity of the PEO blocks increases with temperature, [30, 42, 47] resulting in a dramatic decrease in the degree of hydration of the PEO chains at elevated temperatures. This occurs because at low temperatures these chains are surrounded by water molecules and as the temperature is increased, the PEO chains tend to interact with fewer water molecules. As anticipated in section 1.2.1 (Synthetic routes to SBA-15), the silica framework is templated by micelles with extended PEO blocks and thus it may be penetrated by these blocks, which explains the formation of micropores. As Galarneau and co-workers reported, [42] these chains arrange in the micellar solution at a distance of 3-4 nm due to repulsion. When the temperature is increased above 80 °C, water becomes a less efficient solvent, and PEO chains become more hydrophobic. In this way, they withdraw towards the core of the micelle, and an intermicellar attraction arises from PEO-PEO interactions between adjacent micelles (**Figure 1.7**).

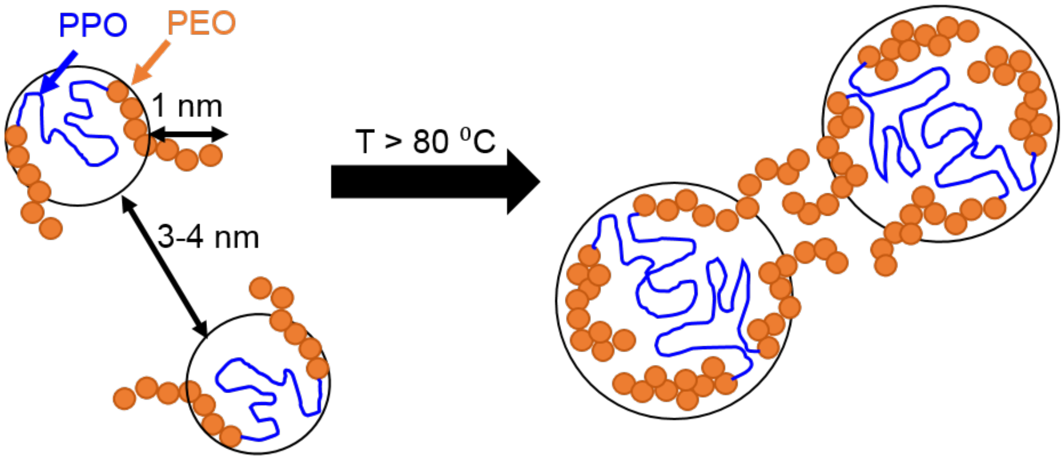

Figure 1.7: Schematic representation of micelle dehydration upon temperature (adapted from ref. [42]).

Silica-embedded micelles behave like micelles in water; therefore, the explanation above reported is valid when hydrothermal treatment is applied during the preparation of SBA-15. [42] This explains the expansion of pore diameter and consequent decrease of pore wall thickness, which corresponds to the minimum distance between the micelles in the solution. Pore wall thickness is an important parameter of OMSs' framework, as it indicates the degree of structure and order of mesoporous arrangements [68] as well as thermal and hydrothermal stability of the materials in question. [26, 69]

Adding organic swelling agents (called also porogens) represents another valid route to expand pore sizes of SBA-15. The hydrophobic organic species can be solubilised inside the hydrophobic regions of surfactant micelles, which leads to their swelling. The solubility of organic additives in the aqueous mixtures is an important parameter to be considered for swelling roles. [47] In order to appreciate pore enlargement, the porogens need to possess a moderate swelling ability that does not ruin the ordered hexagonal structure of the silica, together with a certain extent of solubilisation in the micellar solution. The effect of the porogen, which depends proportionally on its amount, is related to its capability to enter the micelles so that the micellar pore volume and total pore volume are increased. [57]

The first experimental chapter of this thesis (Chapter 3, TLCT SBA-15 and *MM*-TLCT SBA-15 materials and catalysis) is concerned with the topics described in section 1.2 (Mesoporous templated silicas). The chapter describes the synthesis and characterisation of mesoporous and hierarchical TLCT SBA-15 materials and their further application in the catalysis of a large molecule.

1.3. Platinum as a heterogeneous catalyst in oxidation reactions

Platinum-group metals (particularly platinum and palladium) and gold are active catalysts in the liquid-phase oxidation of alcohols, diols and carbohydrates with molecular oxygen under mild conditions. [70-75] A dehydrogenation mechanism of the reaction has been generally accepted over the years, and it is assumed that the role of oxygen is to oxidise the co-product hydrogen formed in the rate-determining step, shifting the equilibrium toward the carbonyl compound.

Supported noble metal catalysts have several applications in commercially important processes, including (de)-hydrogenation, naphtha reforming, oxidation and automotive exhaust catalysis. [76] Over the years, it has been established that the support influences the catalytic activity of the supported metal nanoparticles. [77-80] In particular, noble metals are strongly influenced by the acidity/alkalinity of the support. This dependence between metal and support has been generally ascribed to a modification of the electronic properties of the metal particles induced by the interaction with the support. [80]

Specifically, platinum nanoparticles supported on mesoporous silicas have attracted significant interest because of their potential application in catalysis. [81-84] A methodology widely utilised to load metal nanoparticles from their precursor is called wet-impregnation. [85, 86] Typically, a metal precursor is dissolved in an aqueous solution and brought into the pores of the support, which is then dried to remove the excess solvent. In order to remove the ligands associated with the precursor and obtain metal particles, the impregnated support has to be pre-treated before application in catalysis. Generally, pre-treatment consists of temperature-programmed steps that can take place in different gaseous environments (i.e. H_2, He or O_2), depending on the process required to remove the ligands. This process determines the particle size and particle distribution observed in the final material, as small particle sizes are crucial to obtain a high fraction of catalytic-active surface atoms, as catalysis is a process that occurs on the surface. [87]

Several platinum precursors have been employed over the years, each of them with its unique properties based on the type and number of ligands attached to the metal that define the nature of the material. The most utilised precursors in heterogeneous catalysis have been hexachloroplatinic acid (H_2PtCl_6), [53, 88-92] tetraammineplatinum nitrate ($Pt(NH_3)_4(NO_3)_2$), [87, 91] ammonium tetrachloroplatinate ($(NH_4)_2PtCl_4$), [93, 94] and platinum bis(acetylacetonate) ($Pt(acac)_2$). [92, 95] A disadvantage of hexachloroplatinic acid precursor is that, if chlorine is retained on the material after reduction under hydrogen, its presence alters the acidity of the support, poisoning the catalyst. [87, 96]

1.3.1. Dodecyl aldehyde aerobic oxidation (Chapter 3)

Dodecyl aldehyde, also known as dodecanal and lauraldehyde, together with C_8 and C_{10} aldehydes is an organic compound widely utilised in the perfume industry and for the synthesis of citrus oil. [97, 98] Dodecanoic acid is a medium-length long-chain fatty acid that makes up about half of the fatty acids within coconut oil. It possesses antimicrobial properties against skin bacterium *Propionibacterium acnes*, which promotes follicular inflammation (inflammatory acne); therefore, it can be used as an alternative treatment for antibiotic therapy of acne vulgaris. Besides, it has stronger antimicrobial properties than that of benzoyl peroxide, one of the most frequently used topical medications for acne treatment. [99]

Dodecyl aldehyde is a large molecule whose metal catalysed aerobic oxidation has not been reported in the scientific literature up to this date. Hence, the aim of the first experimental chapter of this thesis (Chapter 3, TLCT SBA-15 and *MM*-TLCT SBA-15 materials and catalysis) is the application of platinum catalysis to the oxidation of this reactant making use of pore-expanded mesoporous and macro-mesoporous silica supports, which have been prepared based on the concepts described in section 1.2.2 (Pore-expanded SBA-15). In this way, dodecyl aldehyde aerobic oxidation (**Scheme 1.1**) represents a clean, sustainable and effective transformation for the production of a compound that finds applications in the antibiotic therapy of acne vulgaris.

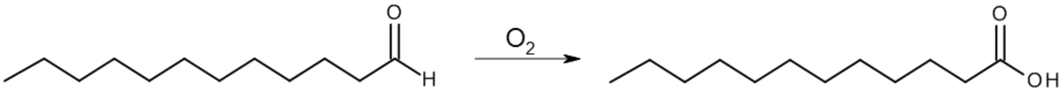

Scheme 1.1: Aerobic oxidation of dodecyl aldehyde to dodecanoic acid.

1.3.2. Cinnamaldehyde aerobic oxidation (Chapter 4)

The aerobic oxidation of cinnamaldehyde, a lignin-derived chemical [9, 100] and the main component of cassia oil [101] as well as cinnamon bark oil, [101, 102] represents a sustainable and environmentally friendly molecular transformation for the production of two main products: cinnamic acid and benzaldehyde (**Scheme 1.2**).

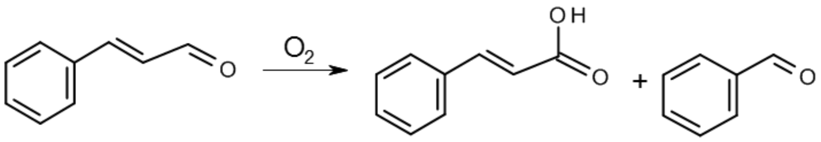

Scheme 1.2: Aerobic oxidation of cinnamaldehyde to cinnamic acid and benzaldehyde.

Cinnamic acid is an organic acid with low toxicity present naturally in all green plants, [103] and it has a broad spectrum of biological properties, such as hepatoprotective (damage prevention to the liver), [103] antimalarial [104] and antioxidant [105] activities.

Together with its derivatives, it is a promising compound to be developed in the medical field. Furthermore, cinnamic acid has antimicrobial activity, and its derivatives are antioxidants, due to their free radical scavenging properties, and also antibacterial, antiviral and antifungal. [106] Over the last decades, there has been significant attention towards cinnamic acid on its antitumor efficacy. [107] In fact, it has been proven that it causes a reduction of cell proliferation in different carcinoma cells. [108] *Trans*-cinnamic acid and its derivatives also present α-glucosidase inhibitory activity, important to cure diabetes mellitus type 2, [109] and represent potential antimalarial agents when conjugated with heterocyclic moieties. [110] Cinnamic acid is one of the significant constituents commonly found in cinnamon and chocolate, [111] and a precursor to the sweetener aspartame. [112]

On the other hand, benzaldehyde is an important intermediate for perfumes, organic synthesis and pharmaceuticals, [113] and its synthesis via oxidative cleavage of cinnamaldehyde has been widely investigated over the past decades. In order to have high conversion and selectivity, several procedures have been developed, which make use of different heterogeneous catalysts, such as metalloporphyrins, [102] β-cyclodextrin polymer [114, 115] and hydrotalcites. [116] Analysis of cinnamon oil samples [101, 117] has proven that the decomposition of cinnamaldehyde to benzaldehyde is spontaneous when heat-induced (above 60 ˚C). The formation of benzaldehyde has also been observed when cinnamyl alcohol or cinnamaldehyde have been exposed to air and heat as pure chemicals. [118, 119] Besides the formation of benzaldehyde, heat and atmospheric oxygen cause cinnamaldehyde's spontaneous partial oxidation to cinnamic acid, as some examples in literature confirm. [58, 117, 119] The first study reporting that aldehydes are converted into their corresponding acids in the presence of air dates back to early 1800, when Justus von Liebig observed this phenomenon. [120] However, the spontaneous transformation of cinnamaldehyde leads to a higher amount of benzaldehyde than cinnamic acid. As it will be explained in detail in Chapter 4, other side-products are formed in smaller amounts during cinnamaldehyde aerobic oxidation, such as benzoic acid, phenylcetaldehyde, acetophenone, benzyl benzoate and benzyl cinnamate.

Traditionally, the complete oxidation of cinnamaldehyde to cinnamic acid is carried out by using stoichiometric amounts of toxic and hazardous inorganic agents, such as chromates, [121] permanganates [122] and hydrogen peroxide, [123] which lead to the production of contaminated waste and consequently represent a danger for the environment. On the other hand, the use of heterogeneous catalysis based on supported transition metal nanoparticles in catalytic amounts offers a sustainable and green alternative, as it uses air as the oxidant, which is inexpensive and non-toxic. However, contrary to benzaldehyde, heterogeneously catalytic methods for the synthesis of cinnamic acid have not been developed to date. Therefore, there is a need to develop clean and sustainable methodologies that allow for its selective formation, since it is a beneficial model compound with three functionalities (the phenyl group, the α,β-unsaturated bond and the carboxylic acid) that can be converted to further valuable compounds.

Platinum group metals have been successfully employed as heterogeneous catalysts for the aerobic selective oxidation of various alcohols and aldehydes [74, 124-127] but, specifically, the selective oxidation of cinnamaldehyde to cinnamic acid remains mostly unexplored. However, initial attempts have been recently made in this regard. [94]

The aim of the second experimental chapter of this thesis (Chapter 4, Cinnamaldehyde aerobic oxidation) is developing a sustainable and green alternative for the selective synthesis of cinnamic acid starting from cinnamaldehyde in order to meet the principles of green chemistry, guaranteeing no production of waste or use of hazardous substances.

1.3.3. Hydroxymethylfurfural aerobic oxidation (Chapter 5)

While the aerobic oxidation of dodecyl aldehyde and cinnamaldehyde currently remains mostly unexplored, 5-hydroxymethylfurfural (HMF) oxidation has been widely investigated with different heterogeneous catalysts and reaction conditions. Therefore, the rationale of the mechanism of the reaction has been repeatedly reported over the last decade.

As anticipated in section 1.1 (The role of heterogeneous catalysis in green chemistry), lignocellulosic biomass has a complex structure and is made up of three polymers, namely cellulose, hemicellulose and lignin. While cinnamaldehyde is derived from lignin (section 1.3.2, Cinnamaldehyde aerobic oxidation), HMF and furfural are derived from the other polymers, through biological or chemical conversion. They can be efficiently produced by the acid-catalysed dehydration of pentose and hexose, respectively (**Figure 1.8**). [128, 129]

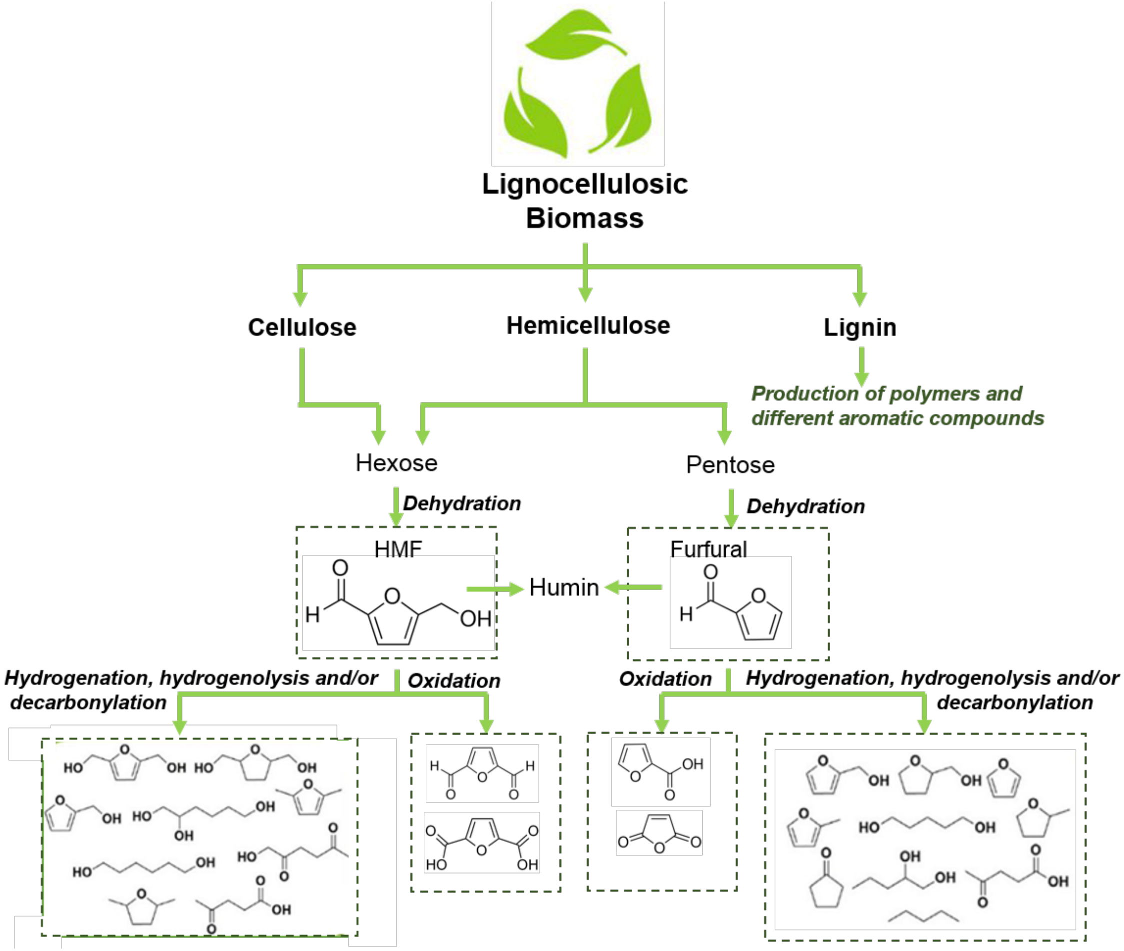

Figure 1.8: Representation of various pathways for the transformation of lignocellulosic biomass to industrially important value-added chemicals via biomass-derived furans (adapted from ref. [130]).

Furfural and HMF represent building-blocks to be utilised as platform materials in biorefinery for the efficient production of chemicals and biofuels that find applications in various industrial sectors. [130-134] In fact, both sugar-based furans possess highly reactive aldehyde and alcohol side chains. Therefore the production of different valuable chemicals, including 2,5-furandicarboxylic acid (FDCA), 2-furoic acid, levulinic acid, 2,5-dimethylfuran (DMF), adipic acid, maleic anhydride (MA), is worthy of attention due to their applications in pharmaceutical and polymer industries, as well as in the production of fuel components. [130]

In this regard, different methodologies (classical and catalytic) have been extensively explored for the production of various chemicals from furfural and HMF. [135-137] As far as the catalytic options are concerned, several monometallic and bimetallic heterogeneous and homogeneous catalysts (mainly based on Pd, Au, Ru, Ir, Re, Rh, Ni, Cu, and Co metals) have been extensively studied to achieve efficient upgrading of furans. [130]

Specifically, the selective oxidation of HMF in liquid water has been widely investigated as a green alternative to oxidation in organic solvents. Water represents a low-cost, polar and environmentally benign solvent for oxygenated molecules derived from biomass such as HMF, and catalytic oxidation in water provides a sustainable and environmentally-friendly route for conversion of biomass-derived feedstocks. However, a high pH is often required for the reaction to proceed. [138]

The third experimental chapter of this thesis (Chapter 5, Hydroxymethylfurfural aerobic oxidation) focuses on the platinum catalysed aerobic oxidation of HMF. Metal nanoparticles have been supported over silica, a slightly acidic material whose role has not been much investigated in this reaction.

One of the most important oxidised products of HMF is FDCA, which is considered to be a promising build block for the production of sustainable polymeric materials, as it is a bio-based and environmentally friendly substitute for petroleum-derived terephthalic acid, which is widely used in the plastics industry as a monomer for the manufacture of polyethylene terephthalate (PET) bottles and films. [139] Moreover, 2,5-diformylfuran (DFF), the partially oxidised form of HMF, is also an important starting material used for the production of polymers, fungicides, pharmaceuticals and so on. [140, 141]

All the possible oxidation products obtained from HMF oxidation reaction are shown in **Scheme 1.3**.

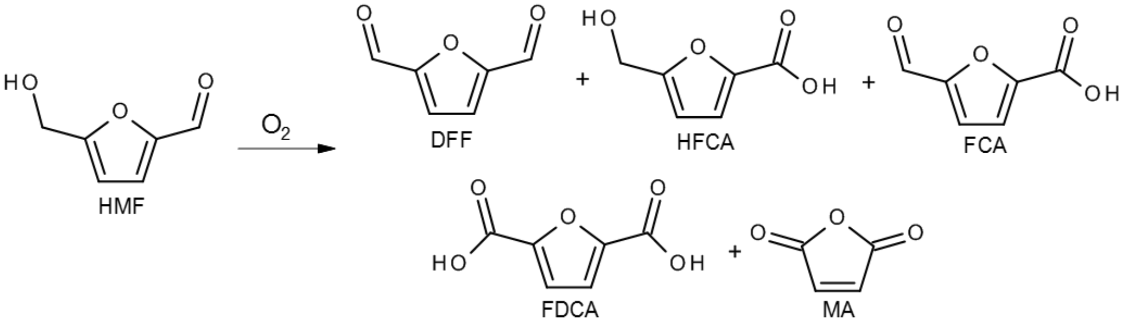

Scheme 1.3: Products obtained from HMF oxidation reaction.

The identified products are: 2,5-diformylfuran (DFF), 5-hydroxymethyl-2-furancarboxylic acid (HFCA), 5-formyl-2-furancarboxylic acid (FCA), 2,5-furandicarboxylic acid (FDCA) and maleic anhydride (MA).

1.4. References

1. Yu C.H., Huang C.H., Tan C.S., A review of CO_2 capture by absorption and adsorption. Aerosol and Air Quality Research, 2012. **12**(5): p. 745-769.
2. Lakhi K.S., Cha Wang S., Choy J.H., Al-Ejji M., Abdullah Aboubakr M., Al-Enizi Abdullah M., Vinu A., Synthesis of mesoporous carbons with controlled morphology and pore diameters from SBA-15 prepared through the microwave-assisted process and their CO_2 adsorption capacity. Microporous and Mesoporous Materials, 2016. **233**: p. 44-52.
3. Roy N., Suzuki N., Terashima C., Fujishima A., Recent improvements in the production of solar fuels: from CO_2 reduction to water splitting and artificial photosynthesis. Bulletin of the Chemical Society of Japan, 2019. **92**(1): p. 178-192.
4. NASA. Global climate change: vital signs of the planet 2019. Last updated: 12/12/2019.
5. Pecha M.B., Arbelaez J.I.M., Garcia-Perez M., Chejne F., Ciesielki P.N., Progress in understanding the four dominant intra-particle phenomena of lignocellulose pyrolysis: chemical reactions, heat transfer, mass transfer, and phase change. Green Chemistry, 2019. **21**(11): p. 2868-2898.
6. Cortés M.E., Suarez Mahecha H., Pardo Carrasco S., Biocombustibles y autosuficiencia energética. Dyna, 2009. **76**(158): p. 101-110.
7. Saygin D., Kempener R., Wagner N., Ayuso M., Gielen D., The implications for renewable energy innovation of doubling the share of renewables in the global energy mix between 2010 and 2030. Energies, 2015. **8**(6): p. 5828-5865.
8. Gómez Millán G., Hellsten S., Llorca J., Luque R., Sixta H., Balu A.M., Recent advances in the catalytic production of platform chemicals from holocellulosic biomass. ChemCatChem, 2019. **11**(8): p. 2022-2042.
9. Isikgor F.H., Becer C.R., Lignocellulosic biomass: a sustainable platform for the production of bio-based chemicals and polymers. Polymer Chemistry, 2015. **6**(25): p. 4497-4559.
10. Anastas P.T., Warner J.C., Green chemistry : theory and practice. 1998, Oxford [England]; New York: Oxford University Press.
11. Sheldon Roger A., Atom efficiency and catalysis in organic synthesis. Pure and Applied Chemistry. 2000. **72**(7): p. 1233.
12. Trost B.M., The atom economy-a se arch for synthetic efficiency. Science, 1991. **254**(5037): p. 1471-1477.
13. Corma A., Garcia H., Crossing the borders between homogeneous and heterogeneous catalysis: developing recoverable and reusable catalytic systems. Topics in Catalysis, 2008. **48**(1): p. 8-31.
14. Anastas P.T., Kirchhoff M.M., Williamson T.C., Catalysis as a foundational pillar of green chemistry. Applied Catalysis A: General, 2001. **221**(1): p. 3-13.
15. Wilson K., Lee A.F., Catalyst design for biorefining. Philosophical Transactions of the Royal Society A: Mathematical, Physical and Engineering Sciences, 2016. **374**(2061): p.1-23.
16. Sanders J.P.M., Annevelink B., van der Höven D., The development of biocommodities and the role of North West European ports in biomass chains. Biofuels, Bioproducts and Biorefining, 2009. **3**(3): p. 395-409.

17. Taguchi A., Schüth F., Ordered mesoporous materials in catalysis. Microporous and Mesoporous Materials, 2005. **77**(1): p. 1-45.
18. Davis M.E., Ordered porous materials for emerging applications. Nature, 2002. **417**(6891): p. 813-821.
19. Chaudhary V., Sharma S., An overview of ordered mesoporous material SBA-15: synthesis, functionalization and application in oxidation reactions. Journal of Porous Materials, 2017. **24**(3): p. 741-749.
20. Wach A., Drozdek M., Ddek B., Latka P., Kustrovski P., Control of availability of poly(vinylamine)-derived basic sites, catalytically active in Knoevenagel condensation, by deposition on various mesoporous silicas. Microporous and Mesoporous Materials, 2016. **226**: p. 433-443.
21. Perego C., Bosetti A., Biomass to fuels: the role of zeolite and mesoporous materials. Microporous and Mesoporous Materials, 2011. **144**(1): p. 28-39.
22. Climent M.J., Corma A., Iborra S., Conversion of biomass platform molecules into fuel additives and liquid hydrocarbon fuels. Green Chemistry, 2014. **16**(2): p. 516-547.
23. Li Y., Feng Z., van Santen R.A., Hensen E.J.M., Li C., Surface functionalization of SBA-15-ordered mesoporous silicas: oxidation of benzene to phenol by nitrous oxide. Journal of Catalysis, 2008. **255**(2): p. 190-196.
24. Paul L., Banerjee B., Ahaumik A., Ali M., Functionalized SBA-15 supported nickel (II)–oxime–imine catalysts for liquid phase oxidation of olefins under solvent-free conditions. Journal of Solid State Chemistry, 2016. **237**: p. 105-112.
25. Owens G.J., Singh R.K., Foroutana F., Alqaysi M., Han C.M., Mahapatra C., Kim H.W., Knowles J.C., Sol-gel based materials for biomedical applications. Progress in Materials Science, 2016. **77**: p. 1-79.
26. Wan Y., Zhao D., On the controllable soft-templating approach to mesoporous silicates. Chemical Reviews, 2007. **107**(7): p. 2821-2860.
27. Beck J.S., Vartuli J.C., Roth W.J., Leonowicz M.E., Kresge C.T., A new family of mesoporous molecular sieves prepared with liquid crystal templates. Journal of the American Chemical Society, 1992. **114**(27): p. 10834-10843.
28. Meziani A., Touraud D., Zradba A., Pulvin S., Pezron I., Clausse M., Kunz W., Comparison of enzymatic activity and nanostructures in water/ethanol/brij 35 and water/1-pentanol/brij 35 systems. The Journal of Physical Chemistry B, 1997. **101**(18): p. 3620-3625.
29. Zhao D., Huo Q., Feng J., Chmelka B.F., Stucky G.D., Nonionic triblock and star diblock copolymer and oligomeric surfactant syntheses of highly ordered, hydrothermally stable, mesoporous silica structures. Journal of the American Chemical Society, 1998. **120**(24): p. 6024-6036.
30. Zhao D., Huo Q., Feng J., Melosh N., Chmelka B.F., Fredrickson G.H., Stucky G.D., Triblock Copolymer Syntheses of Mesoporous Silica with Periodic 50 to 300 Angstrom Pores. Science, 1998. **279**(5350): p. 548-552.
31. Kleitz F., Hei Choi S., Ryoo R., Cubic *Ia3d* large mesoporous silica: synthesis and replication to platinum nanowires, carbon nanorods and carbon nanotubes. Chemical Communications, 2003. (17): p. 2136-2137.
32. Lehman S.E., Larsen S.C., Zeolite and mesoporous silica nanomaterials: greener syntheses, environmental applications and biological toxicity. Environmental Science: Nano, 2014. **1**(3): p. 200-213.

33. Koh K., Seo J.E., Lee J.H., Goswami A., Yoon C.W., Asefa T., Ultrasmall palladium nanoparticles supported on amine-functionalized SBA-15 efficiently catalyze hydrogen evolution from formic acid. Journal of Materials Chemistry A, 2014. **2**(48): p. 20444-20449.
34. Malgras V., Hanzie J., Takei T., Yamauchi Y., Hybrid methylammonium lead halide perovskite nanocrystals confined in gyroidal silica templates. Chemical Communications, 2017. **53**(15): p. 2359-2362.
35. Zhang F., Yan Y., Yang H., Meng Y., Yu C., Tu B., Zhao D., Understanding effect of wall structure on the hydrothermal stability of mesostructured silica SBA-15. The Journal of Physical Chemistry B, 2005. **109**(18): p. 8723-8732.
36. Dhainaut J., Dacquin J.P., Lee A.F., Wilson K., Hierarchical macroporous-mesoporous SBA-15 sulfonic acid catalysts for biodiesel synthesis. Green Chemistry, 2010. **12**(2): p. 296-303.
37. Dacquin J.P., Lee A.F., Pirez C., Wilson K., Pore-expanded SBA-15 sulfonic acid silicas for biodiesel synthesis. Chemical Communications, 2012. **48**(2): p. 212-214.
38. Wainwright S.G., Parlett C.M.A., Balckley R.A., Zhou W., Lee A.F., Wilson K., True liquid crystal templating of SBA-15 with reduced microporosity. Microporous and Mesoporous Materials, 2013. **172**: p. 112-117.
39. Attard G.S., Glyde J.C., Goltner C.G., Liquid-crystalline phases as templates for the synthesis of mesoporous silica. Nature, 1995. **378**(6555): p. 366-368.
40. Wanka G., Hoffmann H., Ulbricht W., Phase diagrams and aggregation behavior of poly(oxyethylene)-poly(oxypropylene)-poly(oxyethylene) triblock copolymers in aqueous solutions. Macromolecules, 1994. **27**(15): p. 4145-4159.
41. Alexandridis P., Hatton T.A., Poly(ethylene oxide)-poly(propylene oxide)-poly(ethylene oxide) block copolymer surfactants in aqueous solutions and at interfaces: thermodynamics, structure, dynamics, and modeling. Colloids and Surfaces A: Physicochemical and Engineering Aspects, 1995. **96**(1): p. 1-46.
42. Galarneau A., Cambon H., Di Renzo F., Ryoo R., Choi M., Fajula F., Microporosity and connections between pores in SBA-15 mesostructured silicas as a function of the temperature of synthesis. New Journal of Chemistry, 2003. **27**(1): p. 73-79.
43. Zha J., Roggendorf H., Sol-gel science, the physics and chemistry of sol-gel processing, Ed. by C. J. Brinker and G. W. Scherer, Academic Press, Boston 1990, xiv, 908 pp., ISBN 0-12-134970-5. Advanced Materials, 1991. **3**(10): p. 522-522.
44. Huo Q., Margolese D.I., Ciesla U., Feng P., Gier T.E., Stucky G.D., Generalized synthesis of periodic surfactant/inorganic composite materials. Nature, 1994. **368**(6469): p. 317-321.
45. Göltner-Spickermann C., Non-ionic templating of silica: formation mechanism and structure. Current Opinion in Colloid & Interface Science, 2002. **7**(3): p. 173-178.
46. Boissière, C., Larbot A., Bourgaux C., Prouzet E., Bunton C.A., A study of the assembly mechanism of the mesoporous MSU-X silica two-step synthesis. Chemistry of Materials, 2001. **13**(10): p. 3580-3586.
47. Kruk M., Jaroniec M., Ko C.H., Ryoo C., Characterization of the porous structure of SBA-15. Chemistry of Materials, 2000. **12**(7): p. 1961-1968.

48. Israelachvili J.N., Wennerstroem H., Entropic forces between amphiphilic surfaces in liquids. The Journal of Physical Chemistry, 1992. **96**(2): p. 520-531.
49. Velev O.D., Jede T.A., Lobo R.F., Lenhoff A.M., Porous silica via colloidal crystallization. Nature, 1997. **389**(6650): p. 447-448.
50. Sen T., Tiddy G.J.T., Casci J.L., Anderson M.W., Synthesis and characterization of hierarchically ordered porous silica materials. Chemistry of Materials, 2004. **16**(11): p. 2044-2054.
51. Parlett C.M.A., Keshwalla P., Wainwright S.G., Bruce D.W., Hondow N.S., Wilson K., Lee A.F., Hierarchically ordered nanoporous pd/sba-15 catalyst for the aerobic selective oxidation of sterically challenging allylic alcohols. ACS Catalysis, 2013. **3**(9): p. 2122-2129.
52. Parlett C.M.A., Bruce D.W., Hondow N.S., Wilson K., Lee A.F., Support-enhanced selective aerobic alcohol oxidation over pd/mesoporous silicas. ACS Catalysis, 2011. **1**(6): p. 636-640.
53. Parlett C.M.A., Isaacs M.A., Beaumont S.K., Bingham L.M., Hondow N., Wilson K., Lee A.F., Spatially orthogonal chemical functionalization of a hierarchical pore network for catalytic cascade reactions. Nat Mater, 2016. **15**(2): p. 178-182.
54. Pirez C., Caderon J.M., Dacquin J.P., Wilson K., Lee A.F., Tunable KIT-6 mesoporous sulfonic acid catalysts for fatty acid esterification. ACS Catalysis, 2012. **2**(8): p. 1607-1614.
55. Fulvio P.F., Pikus S., Jaroniec M., Tailoring properties of SBA-15 materials by controlling conditions of hydrothermal synthesis. Journal of Materials Chemistry, 2005. **15**(47): p. 5049-5053.
56. Celer E.B., Jaroniec M., Temperature-programmed microwave-assisted synthesis of SBA-15 ordered mesoporous silica. Journal of the American Chemical Society, 2006. **128**(44): p. 14408-14414.
57. Cao L., Man T., Kruk M., Synthesis of ultra-large-pore SBA-15 silica with two-dimensional hexagonal structure using triisopropylbenzene as micelle expander. Chemistry of Materials, 2009. **21**(6): p. 1144-1153.
58. Shan W., Wang W., Ru H., Siliceous mesocellular foams modified via a partitioned cooperative self-assembly process using hexane as pore swelling agent. Journal of Non-Crystalline Solids, 2015. **425**: p. 183-189.
59. Sun J., Zhang H., Ma D., Chen Y., Bao X., Klein-Hoffman A., Pfaender N., Su D.S., Alkanes-assisted low temperature formation of highly ordered SBA-15 with large cylindrical mesopores. Chemical Communications, 2005(42): p. 5343-5345.
60. Zhang H., Sun J., Ma D., Weinberg G., Su D.S., Bao X., Engineered complex emulsion system: toward modulating the pore length and morphological architecture of mesoporous silicas. The Journal of Physical Chemistry B, 2006. **110**(51): p. 25908-25915.
61. Nagarajan R., Solubilization of hydrocarbons and resulting aggregate shape transitions in aqueous solutions of Pluronic (PEO-PPO-PEO) block copolymers. Colloids and Surfaces B: Biointerfaces, 1999. **16**(1): p. 55-72.
62. Johansson E.M., Córdoba J.M., Odén M., The effects on pore size and particle morphology of heptane additions to the synthesis of mesoporous silica SBA-15. Microporous and Mesoporous Materials, 2010. **133**(1): p. 66-74.

63. Calin N., Galarneau A., Cacciaguerra T., Denoyel R., Fayula F., Epoxy-functionalized large-pore SBA-15 and KIT-6 as affinity chromatography supports. Comptes Rendus Chimie, 2010. **13**(1): p. 199-206.
64. Qiao W.J., Zhai S.R., Zhang F., Xiao Z.Y., An Q.D., Song X.W., Correlation between pore-expanding and dye adsorption of platelet C/SBA-15 prepared by carbonization and oxidation of P123-TMB/SBA-15 composites. Journal of Sol-Gel Science and Technology, 2014. **70**(3): p. 451-463.
65. Ma J., Liu Q., Chen D., Wen S., Wang T., Synthesis and characterisation of pore-expanded mesoporous silica materials. Micro & Nano Letters, 2015. **10**(2): p. 140-144.
66. Chen S.Y., Chen Y.T., Lee J.J., Cheng S., Tuning pore diameter of platelet SBA-15 materials with short mesochannels for enzyme adsorption. Journal of Materials Chemistry, 2011. **21**(15): p. 5693-5703.
67. Kruk M., Cao L., Pore size tailoring in large-pore SBA-15 silica synthesized in the presence of hexane. Langmuir, 2007. **23**(13): p. 7247-7254.
68. Santos E.C., Santosa E.C., Costa L.S., Oliveira E.S., Bessa R.A., Freitas A.D.L., Oliveira C.P., Nascimento R.F.,. Loiola A.R., Al-MCM-41 synthesized from kaolin via hydrothermal route: structural characterization and use as an efficient adsorbent of methylene blue. Journal of the Brazilian Chemical Society, 2018. **29**: p. 2378-2386.
69. Wang J., Ge H., Bao W., Synthesis and characteristics of SBA-15 with thick pore wall and high hydrothermal stability. Materials Letters, 2015. **145**: p. 312-315.
70. Vinke P., Wit D., De Goede A., van Bekkum H., Noble metal catalyzed oxidation of carbohydrates and carbohydrate derivatives. Studies in Surface Science and Catalysis, P. Ruiz and B. Delmon, Editors. 1992, Elsevier. p. 1-20.
71. Mallat T., Baiker A., Oxidation of alcohols with molecular oxygen on platinum metal catalysts in aqueous solutions. Catalysis Today, 1994. **19**(2): p. 247-283.
72. Gallezot P., Selective oxidation with air on metal catalysts. Catalysis Today, 1997. **37**(4): p. 405-418.
73. Biella S., Castiglioni G.L., Fumagalli C., Prati L., Rossi M., Application of gold catalysts to selective liquid phase oxidation. Catalysis Today, 2002. **72**(1): p. 43-49.
74. Besson M., Gallezot P., Selective oxidation of alcohols and aldehydes on metal catalysts. Catalysis Today, 2000. **57**(1): p. 127-141.
75. Kluytmans J.H.J., Markusse A.P., Kuster B., Marin G.B., Schouten J.C., Engineering aspects of the aqueous noble metal catalysed alcohol oxidation. Catalysis Today, 2000. **57**(1): p. 143-155.
76. Oil & gas journal data book. Oil & gas journal dataBook, 1985.
77. Anderson J.B.F., Burch R., Cairns J.A., The influence of metal-support interactions on the reaction of methylcyclopentane over supported Pt catalysts. Journal of Catalysis, 1987. **107**(2): p. 351-363.
78. Besoukhanova C., Guidot J., Barthomeuf D., Breysse M., Bernard J.R., Platinum-zeolite interactions in alkaline L zeolites. Correlations between catalytic activity and platinum state. Journal of the Chemical Society, Faraday Transactions 1: Physical Chemistry in Condensed Phases, 1981. **77**(7): p. 1595-1604.
79. Koningsberger D.C., de Graaf J., Mojet B.L., Ramaker D.E., Miller J.T., The metal-support interaction in Pt/Y zeolite: evidence for a shift in energy of metal

d-valence orbitals by Pt-H shape resonance and atomic XAFS spectroscopy. Applied Catalysis A: General, 2000. **191**(1): p. 205-220.

80. Mojet B.L., Miller J.T., Ramaker D.E., Koningsberger D.C., A new model describing the metal-support interaction in noble metal catalysts. Journal of Catalysis, 1999. **186**(2): p. 373-386.

81. Song H., Rioux R.M., Hoefelmeyer J., Komor R., Niesz K., Grass M., Somorjai G.A., Hydrothermal growth of mesoporous sba-15 silica in the presence of pvp-stabilized pt nanoparticles: synthesis, characterization, and catalytic properties. Journal of the American Chemical Society, 2006. **128**(9): p. 3027-3037.

82. Giovanetti L.J., Ramallo-Lopez J.M., Foxe M., Jones L.C., Kebel M.M., Requejo F., Shape changes of Pt nanoparticles induced by deposition on mesoporous silica. Small, 2012. **8**(3): p. 468-473.

83. Zhu J., Kailasam K., Xie X., Shomaecker R., Thomas A., High-surface-area sba-15 with enhanced mesopore connectivity by the addition of poly(vinyl alcohol). Chemistry of Materials, 2011. **23**(8): p. 2062-2067.

84. Pushkarev V.V., Musselwhite N., An K., Alayoglu S., Somorjai G., High structure sensitivity of vapor-phase furfural decarbonylation/hydrogenation reaction network as a function of size and shape of Pt nanoparticles. Nano Letters, 2012. **12**(10): p. 5196-5201.

85. Komiyama M., Design and preparation of impregnated catalysts. Catalysis Reviews, 1985. **27**(2): p. 341-372.

86. Schwarz J.A., Contescu C., Contescu A., Methods for preparation of catalytic materials. Chemical Reviews, 1995. **95**(3): p. 477-510.

87. Oudenhuijzen M.K., Kooyman P.J., Tappel B., van Bokhoven J.A., Understanding the influence of the pretreatment procedure on platinum particle size and particle-size distribution for SiO_2 impregnated with $[Pt^{2+}(NH_3)_4](NO^{3-})_2$: a combination of HRTEM, mass spectrometry, and quick EXAFS. Journal of Catalysis, 2002. **205**(1): p. 135-146.

88. Li N., Hu Z., Zheng M., Lu H., Formation of Pt nanoparticles in mesoporous silica channels via direct low-temperature decomposition of $H_2PtCl_6{\cdot}6H_2O$. Materials Letters, 2013. **106**: p. 193-196.

89. Ait Rass H., Essayem N., Besson M., Selective aqueous phase oxidation of 5-hydroxymethylfurfural to 2,5-furandicarboxylic acid over Pt/C catalysts: influence of the base and effect of bismuth promotion. Green Chemistry, 2013. **15**(8): p. 2240-2251.

90. Niu W., Wang D., Yang G., Jian S., Tsubaki N., Pt nanoparticles loaded on reduced graphene oxide as an effective catalyst for the direct oxidation of 5-hydroxymethylfurfural (HMF) to produce 2,5-furandicarboxylic acid (FDCA) under mild conditions. Bulletin of the Chemical Society of Japan, 2014. **87**(10): p. 1124-1129.

91. Sahu R., Dhepe P.L., Synthesis of 2,5-furandicarboxylic acid by the aerobic oxidation of 5-hydroxymethyl furfural over supported metal catalysts. Reaction Kinetics, Mechanisms and Catalysis, 2014. **112**(1): p. 173-187.

92. Reyes P., Oportus M., Pecchi G., Frety R., Moraweck B., Influence of the nature of the platinum precursor on the surface properties and catalytic activity of alumina-supported catalysts. Catalysis Letters, 1996. **37**(3): p. 193-197.

93. Durndell L.J., Parlett C.M.A., Hondow N., Wilson K., Lee A.F., Tunable Pt nanocatalysts for the aerobic selox of cinnamyl alcohol. Nanoscale, 2013. **5**(12): p. 5412-5419.
94. Durndell L.J., Cucuzzella C., Parlett C.M.A., Isaacs M., Wilson K., Lee A.F., Platinum catalysed aerobic selective oxidation of cinnamaldehyde to cinnamic acid. Catalysis Today, 2018. **333**: p.161-168.
95. Fiddy G.S., Newton M., Corker J., Turin S., Campbell T., Evan T., Evan J., Salvini G., In situ energy dispersive EXAFS (EDE) of low loaded $Pt(acac)_2$/HI SiO_2 catalyst precursors on a timescale of seconds and below. Chemical Communications, 1999(9): p. 851-852.
96. Mojet B.L., Ramarker D., Miller J., Koningsberger D.C., Observation of a hydrogen-induced shape resonance on Pt/LTL catalysts and its relation with support acidity/alkalinity. Catalysis Letters, 1999. **62**(1): p. 15-20.
97. Braddock R.J., Kesterson J.W., Quantitative analysis of aldehydes, esters, alcohols and acids from citrus oils. Journal of Food Science, 1976. **41**(5): p. 1007-1010.
98. Ranveer A.C., Ranade S.V., Mistry C.K., Selective oxidation of lauryl alcohol to lauraldehyde under liquid-liquid phase transfer catalysis (LL-PTC) with potassium chromate as the oxidizing agent. Iranian Journal of Chemistry and Chemical Engineering (IJCCE), 2018. **37**(6): p. 89-94.
99. Nakatsuji T., Kao M., Fang J., Zouboulis C., Zhang L., Gallo R., Huang C.M., Antimicrobial property of lauric acid against propionibacterium acnes: its therapeutic potential for inflammatory acne vulgaris. Journal of Investigative Dermatology, 2009. **129**(10): p. 2480-2488.
100. Garrote G., Cruz J.M., Moure A., Dominguez H., Parajo J.C., Antioxidant activity of byproducts from the hydrolytic processing of selected lignocellulosic materials. Trends in Food Science & Technology, 2004. **15**(3): p. 191-200.
101. Gholivand M.B., Ahmadi F., Simultaneous determination of *trans*-cinnamaldehyde and benzaldehyde in different real samples by differential pulse polarography and study of heat stability of *trans*-cinnamaldehyde. Analytical Letters, 2008. **41**(18): p. 3324-3341.
102. Chen H., Ji H., Zhou X., Xu J., Wang L., Aerobic oxidative cleavage of cinnamaldehyde to benzaldehyde catalyzed by metalloporphyrins under mild conditions. Catalysis Communications, 2009. **10**(6): p. 828-832.
103. Lichtenthaler H.K., Schweiger J., Cell wall bound ferulic acid, the major substance of the blue-green fluorescence emission of plants. Journal of Plant Physiology, 1998. **152**(2): p. 272-282.
104. Wiesner J., Mitsch A., Wissner P., Jomaa H., Schlitzer M., Structure-activity relationships of novel anti-malarial agents. Part 2: cinnamic acid derivatives. Bioorganic & Medicinal Chemistry Letters, 2001. **11**(3): p. 423-424.
105. Natella F., Nardini M., Di Felice M., Scaccini C., Benzoic and cinnamic acid derivatives as antioxidants: structure-activity relation. Journal of Agricultural and Food Chemistry, 1999. **47**(4): p. 1453-1459.
106. Sova M., Antioxidant and antimicrobial activities of cinnamic acid derivatives. Mini Reviews in Medicinal Chemistry, 2012. **12**(8): p. 749-767.
107. De P., Baltas M., Bedos-Belval F., Cinnamic acid derivatives as anticancer agents, a review. Current Medicinal Chemistry, 2011. **18**(11): p. 1672-1703.

108. Liu L., Hudgins R., Shack S., Yin Q., Samid D., Cinnamic acid: a natural product with potential use in cancer intervention. International Journal of Cancer, 1995. **62**(3): p. 345-350.
109. Adisakwattana S., Sookkongwaree K., Roengsumran S., Petsom A., Yibchockanun S., Structure-activity relationships of *trans*-cinnamic acid derivatives on α-glucosidase inhibition. Bioorganic & Medicinal Chemistry Letters, 2004. **14**(11): p. 2893-2896.
110. Gayam V., Ravi S., Cinnamoylated chloroquine analogues: a new structural class of antimalarial agents. European Journal of Medicinal Chemistry, 2017. **135**: p. 382-391.
111. Muhammad D.R.A., Praseptiangga D., van de Walle D., Dewettinck K., Interaction between natural antioxidants derived from cinnamon and cocoa in binary and complex mixtures. Food Chemistry, 2017. **231**: p. 356-364.
112. Evans C.T., Choma C., Peterson W., Misawa M., Bioconversion of *trans*-cinnamic acid to L-phenylalanine in an immobilized whole cell reactor. Biotechnology and Bioengineering, 1987. **30**(9): p. 1067-1072.
113. Murray W.D., Williams R.E., Katz I., Microbiological and Enzymatic Production of Flavor and Fragrance Chemicals. Critical Reviews in Biotechnology, 1989. **9**(2): p. 105-169.
114. Chen H., Ji H., β-Cyclodextrin promoted oxidation of cinnamaldehyde to natural benzaldehyde in water. Chinese Journal of Chemical Engineering, 2011. **19**(6): p. 972-977.
115. Yang Z., Zeng H., Zhou X., Ji H., Mechanism into selective oxidation of cinnamaldehyde using β-cyclodextrin polymer as phase-transfer catalyst. Tetrahedron, 2012. **68**(29): p. 5912-5919.
116. Yadav G.D., Fernandes G.P., Selective synthesis of natural benzaldehyde by hydrolysis of cinnamaldehyde using novel hydrotalcite catalyst. Catalysis Today, 2013. **207**: p. 162-169.
117. Friedman M., Kozukue N., Harden L.A., Cinnamaldehyde content in foods determined by Gas Chromatography-Mass Spectrometry. Journal of Agricultural and Food Chemistry, 2000. **48**(11): p. 5702-5709.
118. Rucinska E., Miedziak P., Pattisson S., Brett G., Sankar M., Hutchings G.J., Cinnamyl alcohol oxidation using supported bimetallic Au-Pd nanoparticles: an investigation of autoxidation and catalysis. Catalysis Science & Technology, 2018. **8**(11): p. 2987-2997.
119. Pound A.W., Pound J.R., Note on the oxidation of cinnamaldehyde. The Journal of Physical Chemistry, 1933. **38**(8): p. 1045-1049.
120. Liebig J., Justus Liebig's Annalen der Chemie. Annalen der Chemie, 1832.
121. Lee D.G., Spitzer U.A., Aqueous dichromate oxidation of primary alcohols. The Journal of Organic Chemistry, 1970. **35**(10): p. 3589-3590.
122. Prabhakaran P.V., Venkatachalam S., Ninan K.N., Permanganate ion supported over crosslinked polyvinylamine as an oxidising agent for alcohols. European Polymer Journal, 1999. **35**(9): p. 1743-1746.
123. Sato K., Hyodo M., Takagi J., Aoki M., Noyori R., Hydrogen peroxide oxidation of aldehydes to carboxylic acids: an organic solvent-, halide- and metal-free procedure. Tetrahedron Letters, 2000. **41**(9): p. 1439-1442.
124. Mallat T., Baiker A., Oxidation of alcohols with molecular oxygen on solid catalysts. Chemical Reviews, 2004. **104**(6): p. 3037-3058.

125. Muzart J., Palladium-catalysed oxidation of primary and secondary alcohols. Tetrahedron, 2003. **59**(31): p. 5789-5816.
126. Anderson R., Griffin K., Johnston P., Alsters P., Selective oxidation of alcohols to carbonyl compounds and carboxylic acids with platinum group metal catalysts. Advanced Synthesis & Catalysis, 2003. **345**(4): p. 517-523.
127. Ali M.E., Rahman M., Sarkar S., Hamid S., Heterogeneous metal catalysts for oxidation reactions. Journal of Nanomaterials, 2014. **2014**: p. 23.
128. Liu B., Zhang Z., Catalytic conversion of biomass into chemicals and fuels over magnetic catalysts. ACS Catalysis, 2016. **6**(1): p. 326-338.
129. Zhou P., Zhang Z., One-pot catalytic conversion of carbohydrates into furfural and 5-hydroxymethylfurfural. Catalysis Science & Technology, 2016. **6**(11): p. 3694-3712.
130. Gupta K., Rai R.K., Singh S.K., Metal catalysts for the efficient transformation of biomass-derived hmf and furfural to value added chemicals. ChemCatChem, 2018. **10**(11): p. 2326-2349.
131. Besson M., Gallezot P., Pinel C., Conversion of biomass into chemicals over metal catalysts. Chemical Reviews, 2014. **114**(3): p. 1827-1870.
132. Sankar M., Dimitratos N., Miedziak P., Wells P., Kiely C., Hutchings G.J., Designing bimetallic catalysts for a green and sustainable future. Chemical Society Reviews, 2012. **41**(24): p. 8099-8139.
133. Li H., Yang S., Riisager A., Pandey A., Luque R., Zeolite and zeotype-catalysed transformations of biofuranic compounds. Green Chemistry, 2016. **18**(21): p. 5701-5735.
134. Serrano-Ruiz J.C., Luque R., Sepúlveda-Escribano A., Transformations of biomass-derived platform molecules: from high added-value chemicals to fuelsvia aqueous-phase processing. Chemical Society Reviews, 2011. **40**(11): p. 5266-5281.
135. Li X., Jia P., Wang T., Furfural: a promising platform compound for sustainable production of C4 and C5 chemicals. ACS Catalysis, 2016. **6**(11): p. 7621-7640.
136. Bohre A., Dutta S., Saha B., Abu-Omar M., Upgrading furfurals to drop-in biofuels: an overview. ACS Sustainable Chemistry & Engineering, 2015. **3**(7): p. 1263-1277.
137. van Putten R.J., van der Waals J.C., de Jong E., Rasrendra C., de Vries J., Hydroxymethylfurfural, a versatile platform chemical made from renewable resources. Chemical Reviews, 2013. **113**(3): p. 1499-1597.
138. Davis S.E., Zope B.N., Davis R.J., On the mechanism of selective oxidation of 5-hydroxymethylfurfural to 2,5-furandicarboxylic acid over supported Pt and Au catalysts. Green Chemistry, 2012. **14**(1): p. 143-147.
139. Jain A., Jonnalagadda S., Ramanuijachary K., Mugweru A., Selective oxidation of 5-hydroxymethyl-2-furfural to furan-2,5-dicarboxylic acid over spinel mixed metal oxide catalyst. Catalysis Communications, 2015. **58**: p. 179-182.
140. Takagaki A., Takahashi M., Nishimura S., Ebitani K., One-pot synthesis of 2,5-diformylfuran from carbohydrate derivatives by sulfonated resin and hydrotalcite-supported ruthenium catalysts. ACS Catalysis, 2011. **1**(11): p. 1562-1565.
141. Carlini C., Patrono P., Galletti A., Sbrana G., Zima V., Selective oxidation of 5-hydroxymethyl-2-furaldehyde to furan-2,5-dicarboxaldehyde by catalytic systems based on vanadyl phosphate. Applied Catalysis A: General, 2005. **289**(2): p. 197-204.

CHAPTER 2:

Materials and methods

2.1. Chemicals

Synthesis of silica supports:

Fumed silica, Pluronic P123, tetraethoxysilane, tetramethoxysilane, 1,3,5-trimethylbenzene (mesitylene), heptane, styrene and potassium persulphate were sourced from Sigma Aldrich and Acros Organics with > 98% purity.

Synthesis of platinum catalysts:

Ammonium tetrachloroplatinate (II), tetraammineplatinum (II) nitrate and chloroplatinic acid (IV) hexahydrate platinum precursor salts were sourced from Sigma Aldrich and Alpha Aesar.

Aerobic oxidation reactions:

Toluene (solvent) was sourced from Fisher Chemical with HPLC grade (≥ 99.8%).

Mesitylene (internal standard) was sourced from Acros Organics with 99% purity.

Dodecyl aldehyde (92% purity) and standard (dodecanoic acid, 99% purity) were sourced from Sigma Aldrich.

Cinnamaldehyde (≥ 99% purity), hydroquinone (99% purity), and standards (cinnamic acid, benzaldehyde, benzoic acid, benzyl alcohol, benzyl formate, benzyl benzoate, phenylacetaldehyde, acetophenone, 1,2-dibenzoylethane, benzyl cinnamate, 2-hydroxyacetophenone, cinnamyl alcohol, ethylbenzene, cinnamyl cinnamate, 3-phenyl-1-propanol, > 98% purity) were sourced from Sigma Aldrich and Lancaster.

5-hydroxymethylfurfural (≥ 99% purity) and standards (5-hydroxy-2-furancarboxylic acid, 2,5-diformylfuran, 5-formyl-furan-2-carboxylic acid, 2,5-furandicarboxylic acid, maleic anhydride, > 98% purity) were sourced from Sigma Aldrich.

2.2. Synthesis of silica supports

2.2.1. Synthesis of CO-OP SA SBA-15 mesoporous silica

Pluronic P123 (1 g) was dissolved in water (7.5 mL) and hydrochloric acid (2 M, 29.15 mL) with stirring at 35 °C for 4 hours. Tetraethoxysilane (2.2 mL) was added and left for 20 hours with agitation. The resulting gel was aged for 24 hours at 80 °C without agitation. The solid was filtered, washed with water and dried at room temperature before calcination at 550 °C for 6 hours in air (ramp rate 1 °C min^{-1}).

2.2.2. Synthesis of TLCT SBA-15 mesoporous silica

STEP 1: Pluronic P123 (2 g) was added to deionised water (2 mL) that had been brought to pH = 1.8 with hydrochloric acid 37%, and the mixture sonicated at 40 °C for 2 hours to produce a homogeneous gel, which exhibited a hexagonal mesophase. Tetramethoxysilane (4.08 mL) was then added at 40-45 °C and stirred rapidly at 350 r.p.m. to form a homogeneous, free-flowing liquid within 5 minutes. The evolved methanol was removed under a light vacuum (100 mBar) at 40 °C for 2 hours by vacuum oven to form a white solid.

STEP 2: The solid obtained in STEP 1 was then exposed to the atmosphere at room temperature for 24 hours to complete condensation before calcination at 550 °C for 6 hours in air (ramp rate 1 °C min^{-1}).

2.2.3. Synthesis of pore-expanded TLCT SBA-15 with hydrothermal treatment

STEP 1: As STEP 1 in section 2.2.2 (Synthesis of TLCT SBA-15 mesoporous silica).

STEP 2: Immediately after methanol evaporation, the sample was finely ground and redispersed in 100 mL of water, to be aged at different temperatures (80 to 150 ˚C) and times (1 and 7 days) in the oven. After the aging step, the sample was filtered and calcined at 550 °C for 6 hours in air (ramp rate 1° C min^{-1}).

2.2.4. Synthesis of pore-expanded TLCT SBA-15 with swelling agents

STEP 1: Pluronic P123 (2 g) and required amount of swelling agent (0.25-2 g of 1,3,5-trimethylbenzene, 8.5 g of heptane) were added to water (2 mL) that had been brought to pH = 1.8 with HCl 37%, and the mixture was sonicated at 40 °C for 2 hours to produce a homogeneous gel, which exhibited a hexagonal mesophase. Tetramethoxysilane (4.08 mL) was then added at 40-45 °C and stirred rapidly at

350 r.p.m. to form a homogeneous, free-flowing liquid within 5 minutes. The evolved methanol was removed under a light vacuum (100 mBar) at 40 °C for 2 hours by vacuum oven to form a white solid.

STEP 2: As STEP 2 from section 2.2.2 (Synthesis of TLCT SBA-15 mesoporous silica).

2.2.5. Synthesis of polystyrene nanospheres

Polystyrene (PS) nanospheres were synthesised by the method of Sen and co-workers. [1] 100 mL of styrene (the monomer source) were washed five times each with 0.1 M NaOH and deionised water to remove polymerisation inhibitors and added to 1 L of deionised water previously degassed overnight in a 2 L Radleys Reactor-Ready jacketed glass reactor, under 1 bar flowing nitrogen. The styrene was stirred in the reactor for 1 hour at 80 °C. Simultaneously, 0.33 g of potassium persulphate (the initiator) was dissolved in 50 mL deionised water at room temperature for 1 hour. Then it was added dropwise to the styrene mixture to initiate polymerisation and stirred at 300 r.p.m. under flowing nitrogen for 22 hours. After this time, the liquid was recovered and centrifuged. The resultant solid was exposed to air until complete drying. A final yield of 100% of polystyrene nanospheres of size of 354 ± 12 nm was obtained. Polystyrene nanospheres of sizes of 229 ± 26 nm and 426 ± 22 nm were also synthesised, following the scheme in **Figure 2.1** (scheme based on experimental data carried out during the current thesis project).

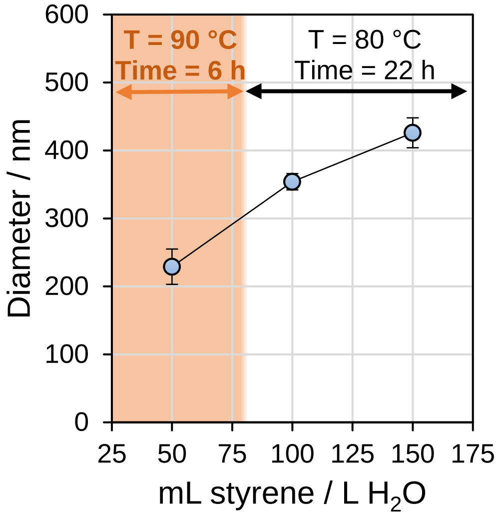

Figure 2.1: Required styrene amount for each PS beads diameter.

Polystyrene beads of 229 ± 26 nm were obtained with 70% yield, while beads of 426 ± 22 nm were obtained with 100% yield.

The centrifugation conditions for each polystyrene size are summarised in **Table 2.1**.

PS size / nm	Centrifugation conditions
229 ± 26	14000 r.p.m., 1 h
354 ± 12	8000 r.p.m., 1 h
426 ± 22	14000 r.p.m., 2 h

Table 2.1: Centrifugation conditions for PS nanospheres of different sizes.

The centrifugation conditions, namely centrifugation time and velocity, depended on polystyrene particle size and density effects.

2.2.6. Synthesis of *MM*-TLCT SBA-15 macro-mesoporous silica

STEP 1: Pluronic P123 (2 g) was added to water (2 mL) that had been brought to pH = 1.8 with HCl 37%, and the mixture sonicated at 40 °C for 2 hours to produce a homogeneous gel, which exhibited a hexagonal mesophase. Tetramethoxysilane (4.08 mL) was then added at 40-45 °C and stirred rapidly at 350 r.p.m. to form a homogeneous, free-flowing liquid within 2 minutes, and then polystyrene beads (6 g) were added to the slurry within 5 minutes, to form a homogeneous gel. The evolved methanol was removed under a light vacuum (100 mBar) at 40 °C for 2 hours by vacuum oven to form a white solid.

STEP 2: The white solid formed in STEP 1 was then exposed to the atmosphere at room temperature for 24 hours to complete condensation before calcination at 550 °C for 6 hours in air (ramp rate 1 °C min^{-1}).

Figure 2.2 shows the schematic representation of the incorporation of polystyrene nanospheres in the mesoporous silica framework, followed by its removal via calcination.

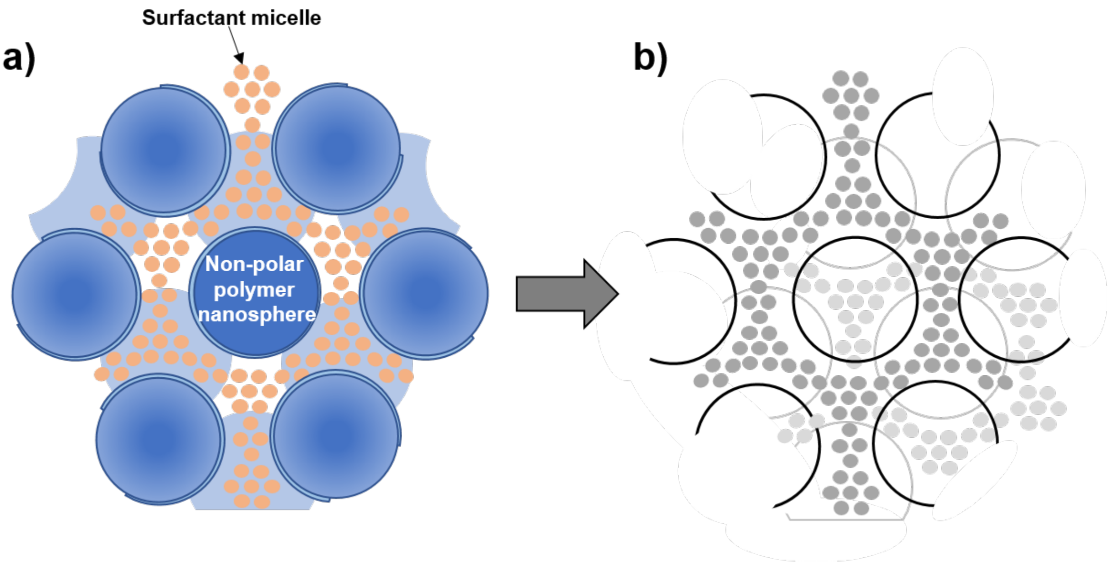

Figure 2.2: a) Representation of parent PS colloidal nanospheres encapsulated within a P123 templated SBA-15 silica network. **b)** Representation of ordered macroporous framework after selective removal of PS macropore template via calcination (adapted from ref. [2]).

2.2.7. Synthesis of pore-expanded *MM*-TLCT SBA-15 with hydrothermal treatment

STEP 1: As STEP 1 in section 2.2.6 (Synthesis of *MM*-TLCT SBA-15 macro-mesoporous silica).

STEP 2: Immediately after methanol evaporation, the sample obtained in STEP 1 was finely ground and redispersed in 100 mL of water, to be aged at different temperatures (80 to 150 ˚C) for 1 day in the oven. After the aging step, the sample was filtered and calcined at 550 °C for 6 hours in air (ramp rate 1 °C min^{-1}).

2.3. Synthesis of platinum catalysts

All the platinum catalysts used in this thesis have been prepared following the wet-impregnation method, a traditional procedure for supporting metal nanoparticles on solid materials. It consists of adding a precursor to a solid support, which is then dried to remove the excess solvent.

2.3.1. Dodecyl aldehyde aerobic oxidation (Chapter 3)

The parent supports (CO-OP SA SBA-15, TLCT SBA-15 and *MM*-TLCT SBA-15, 1 g) were stirred in aqueous ammonium tetrachloroplatinate (II) solution to impart a specific wt% by weight loading of platinum upon the support (0.5 wt%). The solutions were stirred for 18 hours at room temperature. A dry powder was obtained by gentle heating at 50 °C for 10 hours to evaporate water and by drying overnight in the oven (50 °C), followed by calcination at 500 °C for 2 hours in air (ramp rate 1 °C min^{-1}) and reduction at 400 °C under hydrogen (ramp rate 10 °C min^{-1}) for 2 hours, yielding monometallic platinum nanoparticles.

2.3.2. Cinnamaldehyde aerobic oxidation (Chapter 4)

The parent support (fumed SiO_2, 2 g) was stirred in aqueous tetraammineplatinum (II) nitrate and chloroplatinic acid (IV) hexahydrate solutions to impart a specific wt% by weight loading of platinum upon the support (0.05 and 2 wt%). The solutions were stirred for 18 hours at room temperature. A dry powder was obtained by gentle heating at 50 °C for 10 hours to evaporate water and by drying overnight in the oven (50 °C), followed by calcination at 500 °C for 2 hours in air (ramp rate 1 °C min^{-1}) and reduction at 400 °C under H_2 (ramp rate 10 °C min^{-1}) for 2 hours, yielding monometallic platinum nanoparticles.

2.3.3. Hydroxymethylfurfural aerobic oxidation (Chapter 5)

The parent support (fumed SiO_2, 2 g) was stirred in aqueous ammonium tetrachloroplatinate (II) and chloroplatinic acid (IV) hexahydrate solutions to impart a specific wt% by weight loading of platinum upon the support (0.1 and 2 wt%). The solutions were stirred for 18 hours at room temperature. A dry powder was obtained by gentle heating at 50 °C for 10 hours to evaporate water and by drying overnight in the oven (50 °C), followed by calcination at 500 °C for 2 hours in air (ramp rate 1 °C min^{-1}) and reduction at 400 °C under H_2 (ramp rate 10 °C min^{-1}) for 2 hours, yielding monometallic platinum nanoparticles.

The detailed procedure of wet-impregnation procedure is presented in **Figure 2.3**.

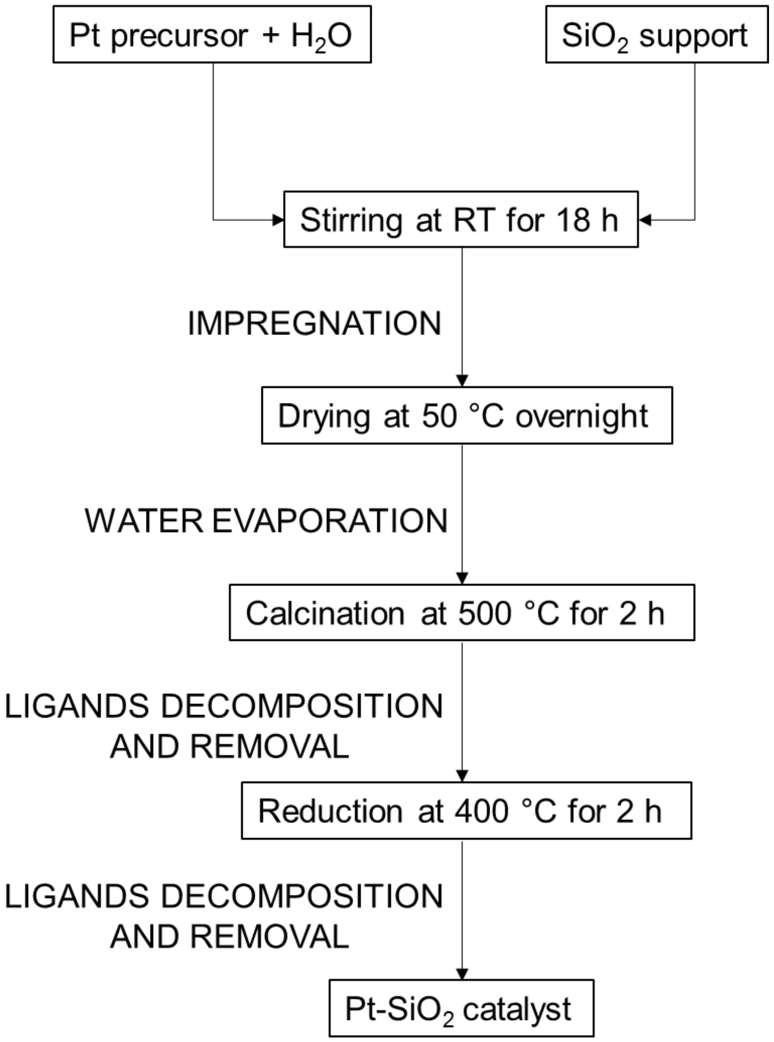

Figure 2.3: Typical procedure for the synthesis of Pt-SiO_2 catalysts using wet-impregnation methodology (adapted from ref. [3]).

2.4. Experimental techniques

2.4.1. Powder X-ray Diffraction

X-ray diffraction (XRD) patterns were collected on a Bruker D8 Advance diffractometer, using Cu Kα radiation (λ = 0.154 nm). Samples were finely ground before analysis and were homogeneously packed into poly(methyl methacrylate) sample holders.

Low-angle scans ranged between 0.45-8° (step size = 0.01°, scan rate = 0.6 s), wide-angle scans ranged between 10-80° (step size = 0.02°, scan rate = 1 s). Peak fitting for calculation of average crystallite sizes from the Scherrer equation was performed using CasaXPS software to evaluate the full-width half maximum (FWHM).

X-ray diffraction is a rapid analytical technique primarily used for phase identification of a crystalline material and can provide information on unit cell dimensions. It is a non-destructive analysis technique, as the scanned sample can be reclaimed for further characterisation or catalysis.

The measurements are based on the interaction of an incident X-ray radiation (Cu) with the lattice planes of a crystalline material. This interaction generates a vacancy in the core electron level that is filled by an electron in a higher shell; this energy change produces an X-ray. The resulting radiation is angled towards the sample through a monochromator. The analysed sample consists of a large array of crystallites with correct orientation to allow for constructive interference with the incident X-rays, giving rise to the displayed diffraction pattern of the material scanned. The process occurring when an X-ray hits a crystal is depicted in **Figure 2.4**.

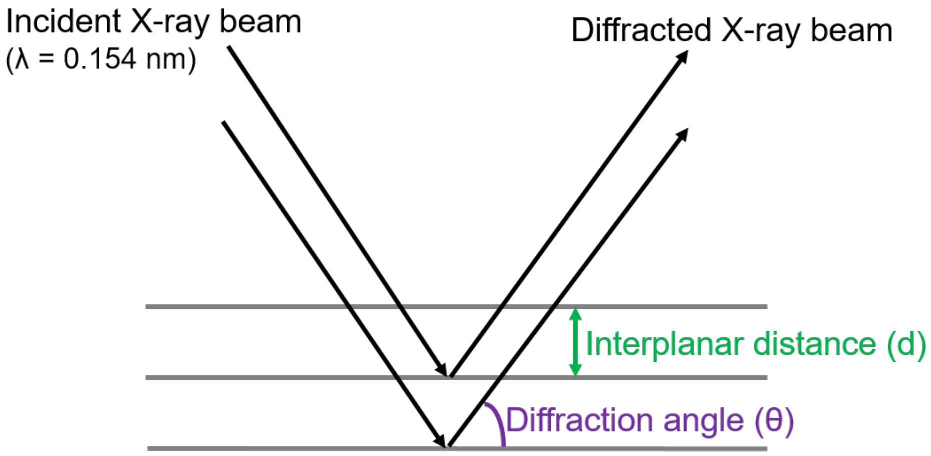

Figure 2.4: Interaction of an incident X-ray radiation with the lattice planes of a crystalline material.

The incident beam strikes the sample with a specific wavelength at a specific known angle θ, which will have the same value of the resulting X-ray that bounces off the crystal. Thus, the only unknown parameter in the figure above is the interplanar distance “d”. The rationale behind the constructive interference has been described by William and Lawrence Bragg, who elucidated the relationship between the wavelength of the X-ray beam, diffraction angle and interplanar distance in the Bragg’s law: [4]

$$n\lambda = 2d \sin\theta$$

Equation 2.1: Bragg’s law.

Where:

- **n** is an integer of λ (dimensionless)
- **λ** is the wavelength of incident/reflected beam (nm)
- **θ** is the diffraction angle (˚)
- **d** is the interplanar distance (2 θ)

Solving the Bragg’s law obtains the d-spacing between the crystal’s lattice planes of atoms that produce constructive interference, which occurs when the travel path difference between two X-ray beams is equal to an integer (n) of the wavelength (λ). A crystal contains different lattice planes. If they exhibit long-range order, the repeating layers give rise to diffraction peaks in the XRD pattern. **Figure 2.5** shows the X-ray diffractograms of a generic Pt-SBA-15 catalyst:

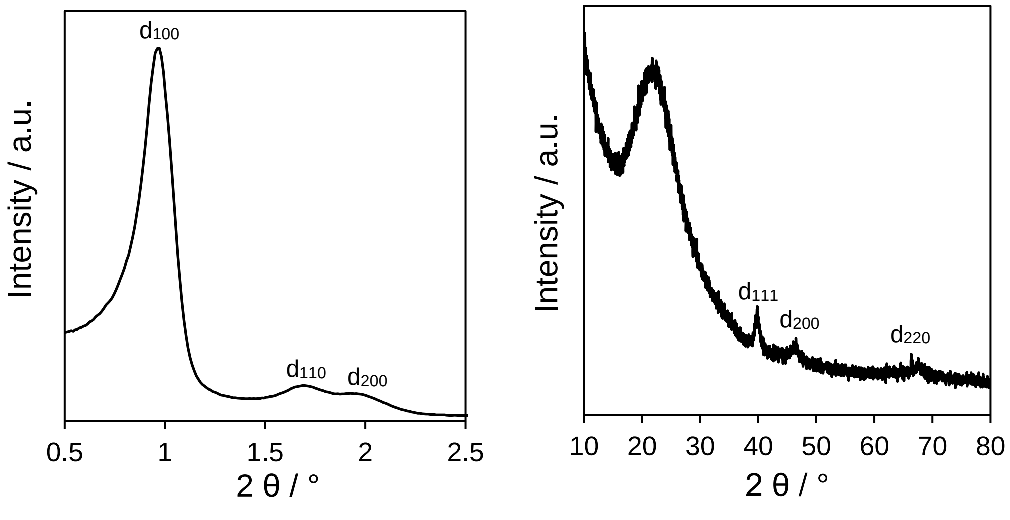

Figure 2.5: Examples of low-angle (left) and wide-angle (right) XRD patterns of a generic SBA-15 support and a Pt-SBA-15 catalyst, respectively (materials used in this thesis).

Figure 2.5 (left) represents the diffractogram of a mesoporous silica support (SBA-15), therefore the reflections correspond to the distance between the pores, while **Figure 2.5** (right) represents supported platinum nanoparticles on the support. A Miller index can be assigned to the observed peaks in **Figure 2.5**. Each plane is described by its Miller indices (*h k l*), which is useful to see in a three-dimensional cubic structure in which the planar directions are labelled as *x, y, z*. The Miller indices are then determined as the reciprocal of each planar direction (**Equation 2.2**), and those relative to metal particles are described in **Figure 2.6**:

$$(h,k,l) = (1/a,\ 1/b,\ 1/c)$$

Equation 2.2: Miller indices.

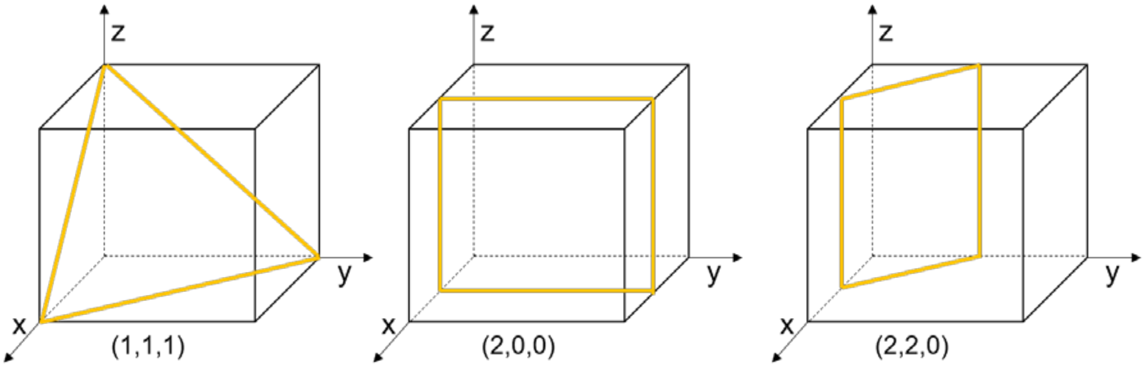

Figure 2.6: Representation of lattice planes in a cubic unit cell.

XRD can also give an estimate of the average crystallite size (L) (**Figure 2.5**, right), as calculated by the Scherrer equation [5] (**Equation 2.3**):

$$L = k\lambda / \beta \cos\theta$$

Equation 2.3: Scherrer equation.

Where:

- **k** is a dimensionless shape factor that describes the particle morphology (0.89)
- **λ** is the wavelength of the incident X-ray
- **ß** is the full-width half maximum (FWHM) of the peak
- **θ** is the diffraction angle

As the Scherrer equation shows, the crystallite size is inversely proportional to the FWHM of the peak. This is consistent with the fact that as crystallites become smaller, the peak broadens. In general, peaks belonging to larger crystallites exhibit a sharp maximum in the diffraction pattern because they possess a high number of lattice planes that allow the fully constructive interaction at the Bragg's angle. Conversely, smaller crystallites exhibit an enhanced peak broadening because the number of lattice planes is minor; hence the signal in the Bragg's angle is reduced, as there is less interference of the X-rays that give rise to the diffraction peak. Therefore, when the size of the crystallites is ≤ 3 nm, the peak is less pronounced because it will begin to broaden and lose its shape, due to destructive interference not being removed from the signal. Due to this limitation, the crystallite detection with XRD is more reliable when particles are bigger than 3 nm, while for smaller particles the destructive interference does not fully allow the calculation of the actual size. However, this technique is a useful tool that can be used as an early indication of particle size before advanced characterisation such as Scanning Transmission Electron Microscopy (explained further on in the course of this chapter).

2.4.2. Nitrogen physisorption porosimetry

Nitrogen physisorption isotherms were recorded using Nova 4000e gas sorption analysers on samples (50-100 mg) that had previously been degassed under vacuum for 2 hours ranging from 80 to 120 °C to ensure water removal, before analysis at -196 °C (77 K) with liquid nitrogen. Data were analysed utilising a Brunauer-Emmer-Teller (BET) plot, *t*-plot and Barret-Joyner-Halenda (BJH) theory using the Quantachrome Novawin 11.0 software package.

The material exposed to nitrogen physisorption adsorbs a specific volume of gas on its surface, and the instrument records the partial pressures at which this occurs, giving rise to isotherms of adsorption and desorption. The amount of nitrogen bound to the surface is then calculated to determine monolayer coverage. The interaction between the nitrogen molecules and the material in question is based upon relatively weak intermolecular forces (van der Waals). While the temperature is kept constant at 77 K, the pressure is gradually increased across the analysis, assuming equilibrium between adsorption and desorption. Due to the low analysis temperature, nitrogen interacts with other nitrogen molecules to form multilayers.

Measurement of the specific surface area is carried out using the Brunauer-Emmett-Teller [6] equation:

$$\frac{P}{V(P_0-P)} = \frac{C-1}{V_mC} \times \frac{P}{P_0} + \frac{1}{V_mC}$$

Equation 2.4: BET equation.

Where:

- **V** is the volume of nitrogen adsorbed (cm^3)
- $\mathbf{P_0}$ is the saturated pressure of nitrogen (Pa)
- **P** is the partial pressure of nitrogen at 77 K (Pa)
- $\mathbf{V_m}$ is the monolayer adsorption volume of nitrogen (cm^3)
- **C** is the multilayer adsorption parameter, derived from adsorption thermodynamics of the adsorbent gas and the surface material in question

The BET plot of **$P/V(P_0-P)$** *versus* **P/P_0** yields a straight line whose intercept is **$1/V_mC$** and whose gradient is **$C-1/V_mC$**, and this allows the determination of the monolayer adsorption volume.

The theory behind the determination of surface area stems from the original Langmuir theory, which does not consider nitrogen multilayer formation. Therefore, this theory was slightly modified, establishing the constant **C** to account for interactions between adlayers of nitrogen. The specific surface area is then calculated from the linear region of the BET plot (**Equation 2.4**), which indicates monolayer coverage assuming that the packing between nitrogen molecules is equal to 0.162 nm^2. The multilayer interaction constant is defined in **Equation 2.5**.

$$C \propto \exp\left(\frac{E_1 - E_2}{RT}\right)$$

Equation 2.5: Multilayer interaction constant.

Where:

- **C** is the multilayer adsorption parameter (dimensionless)
- **E_1** is the heat of adsorption for the first nitrogen layer (J mol^{-1})
- **E_2** is the heat of adsorption for the second subsequent layers (J mol^{-1})
- **R** is the universal gas constant (8.314 J mol^{-1} K^{-1})
- **T** is the analysis temperature (K)

Equation 2.6 defines the specific BET surface area (S) in m^2 g^{-1}, assuming equal spacing between nitrogen molecules:

$$S = \frac{V_m\ N_A\ L}{m\ v} \times 10^{-9}$$

Equation 2.6: Specific BET surface area.

Where:

- **V_m** is the monolayer volume (cm^3)
- **N_A** is the Avogadro's number (6.02×10^{23} mol^{-1})
- **L** is the mean cross-sectional area of the N_2 molecule (0.162 nm^2)
- **m** is the mass of adsorbent sample (g)
- **v** is the molar volume of adsorbate gas (cm^3 mol^{-1})

To evaluate the microporosity of a material, it is necessary to use the *t*-plot method, whose gradient corresponds to the surface area occupied by multilayer adsorption. To obtain the exact micropore area, the *t*-plot will be subtracted from the specific surface area.

The mesoporous pore size distribution (PSD) is calculated using the Barret-Joyner-Halenda (BJH) [7] method based on the Kelvin equation, which provides a relationship between pore diameter and pore condensation pressure, predicting that pore condensation shifts to a higher relative pressure with increasing pore diameter and temperature. [8]

In 2015, the International Union of Pure and Applied Chemistry (IUPAC) published an updated classification of the types of physisorption isotherms. [8] Each of them is characteristic of a specific material; hence it gives an important indication of the nature of the sample undergoing the analysis (**Figure 2.7**):

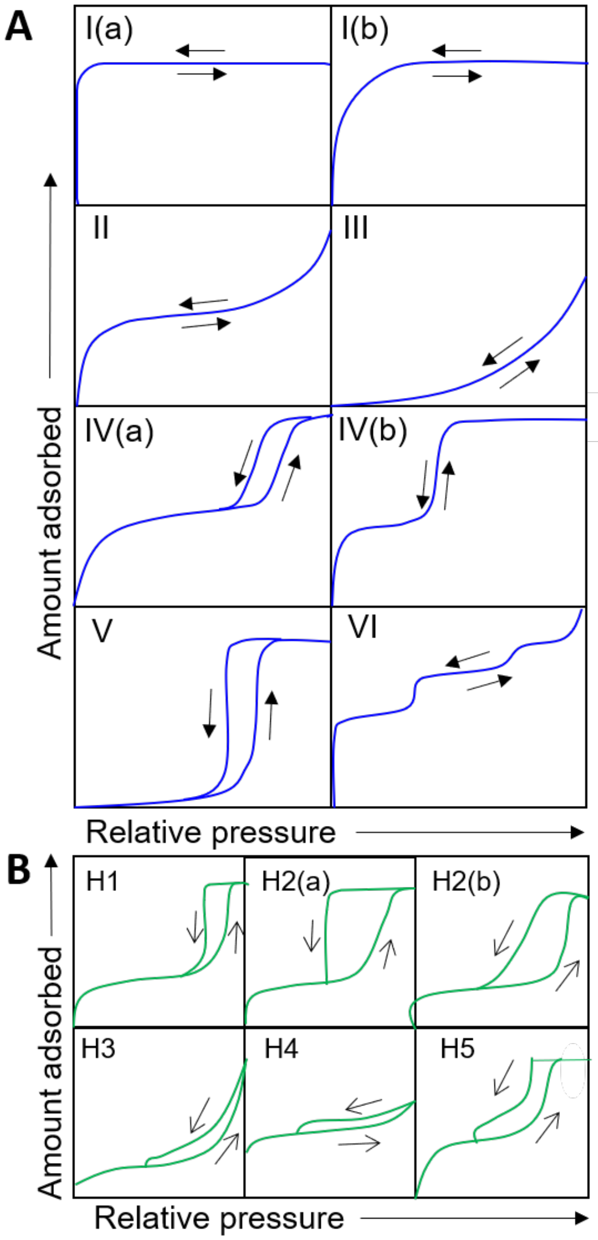

Figure 2.7: a) IUPAC classification of physisorption isotherms and **b**) hysteresis loops (adapted from ref. [8]).

Type IV(a) and IV(b) isotherms in **Figure 2.7** (a) are typical of mesoporous materials, where the difference between the two is related to the mesopore size of the adsorbent. In the former case, capillary condensation is accompanied by hysteresis (**Figure 2.7**, b). This phenomenon occurs when the pore diameter exceeds a certain width, which is dependent on the adsorption system and the temperature. In the case of cylindrical pores adsorbing nitrogen at 77 K, hysteresis starts to occur when pores are wider than ≈ 4 nm. This indicates that adsorption and desorption of the gas are occurring at different pressures. Conversely, adsorbents having mesopores of smaller width will show reversible type IV(b) isotherms. Mesopores fill via pore condensation, a phenomenon whereby the gas condenses to a liquid-like phase in pores at a pressure less than the saturation pressure of the bulk fluid. The H1-type hysteresis is dominant in ordered mesoporous materials with uniform cylindrical pores (i.e. MCM-41 and SBA-15). In order to fully characterise the pore structure of the material at issue, it is important a comprehensive understanding of the observed isotherm shape and hysteresis loop. [8]

Three well-defined stages are usually identified in the typical adsorption-desorption isotherms of SBA-15 materials: (1) a slow increase in nitrogen uptake at low relative pressures, corresponding to monolayer-multilayer adsorption on the pores walls; (2) a sharp step at intermediate relative pressures that is indicative of capillary condensation in mesopores; (3) a plateau at high relative pressures associated with multilayer adsorption on the external surface. Finally, the desorption process is associated with the equilibrium vapour-liquid transition.

Nitrogen physisorption allows assessing pore sizes from the micropore to the mesopore range and not in the macropore range, as pores having diameters greater than 50 nm cannot be filled with the adsorbate at atmospheric pressure. As the BET method does not distinguish between meso- and microporosity and the materials discussed in the present thesis contain a certain degree of microporosity, this had to be assessed using the *t*-plot method. This method is routinely employed to determine the microporous volumes in porous materials including hierarchical zeolites, [9] and it plots the volume of nitrogen adsorbed against the multilayer thickness for the adsorption of nitrogen on a non-porous reference material *t*. The extrapolation of the linear region of the plot intercepts the *y*-axis and provides the micropore volume.

Throughout the entire thesis, the BET surface area and micropore area have been reported with a 10% instrumental error. Unless otherwise specified, one measurement for each sample of surface area, micropore area, pore diameter and pore volume has been carried out.

2.4.3. Inductively Coupled Plasma – Mass Spectrometry

The analyses were undertaken using a Thermoscientific iCAP 7000 Series ICP-MS spectrometer.

Platinum catalysts were digested into a solution of HF, in order to achieve the complete solubilisation of the analytes and the complete decomposition of the matrix, while avoiding the loss or contamination of the species of interest. The acid digestion occurred by solubilising 10 mg of sample and 100 mg of ammonium fluoride in a solution of various acids (HNO_3, HCl, H_2SO_4, H_3BO_3) and water in polypropylene vessels.

Inductively Coupled Plasma-Mass Spectrometry (ICP-MS) is a highly sensitive spectroscopy technique employed for elemental determination, and it is capable of multi-elemental analysis at the sub-parts per trillion level. [10] It has been used to determine the metal contents of all catalysts described in the following chapters.

ICP-MS consists of a high temperature Inductively Coupled Plasma source and a Mass Spectrometer. The former converts the atoms of the elements in the sample to ions, which are then separated and detected by the latter. Typically, the ICP is formed in a stream of argon gas (8-20 L min^{-1}) flowing through the plasma torch, which consists of three concentric quartz tubes. [11] A copper coil surrounds the top portion of the torch and is connected to a radio frequency (RF) generator. As the RF power is applied to the coil, a high-frequency alternating current begins to oscillate (generally at a frequency of either 27 or 40 MHz) within the coil and generates a strong electromagnetic field in the top of the torch. Here, as argon flows through, a high-voltage spark is applied to the gas by the electromagnetic field, and as a consequence some argon atoms are stripped of their electrons, which are then accelerated by the magnetic field and collide with other argon atoms, stripping off their electrons in turn. This process continues, resulting in an ICP discharge consisting of argon atoms, argon ions and electrons, which is continually sustained within the torch by the influx of RF power into the load coil [12] (**Figure 2.8**).

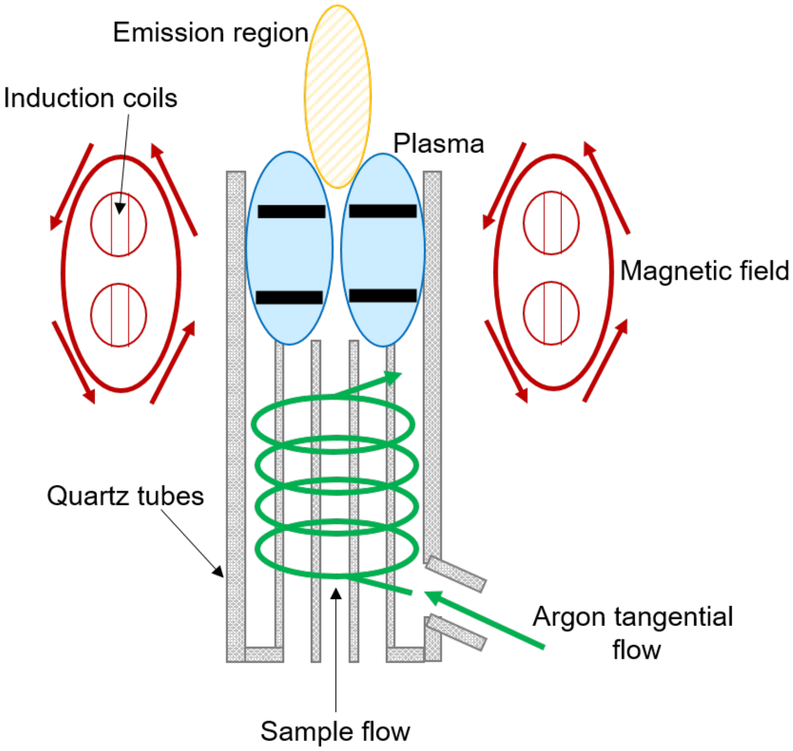

Figure 2.8: Detailed diagram of an ICP-MS torch (adapted from ref. [13]).

Finally, the ions produced from the ICP are directed towards the MS, able to separate and quantify the amount of each element in the sample according to the m/z ratios of their respective ions. The typical ICP-MS setup consists of several components, namely a nebuliser, a plasma torch, a spray chamber and a detector (**Figure 2.9**).

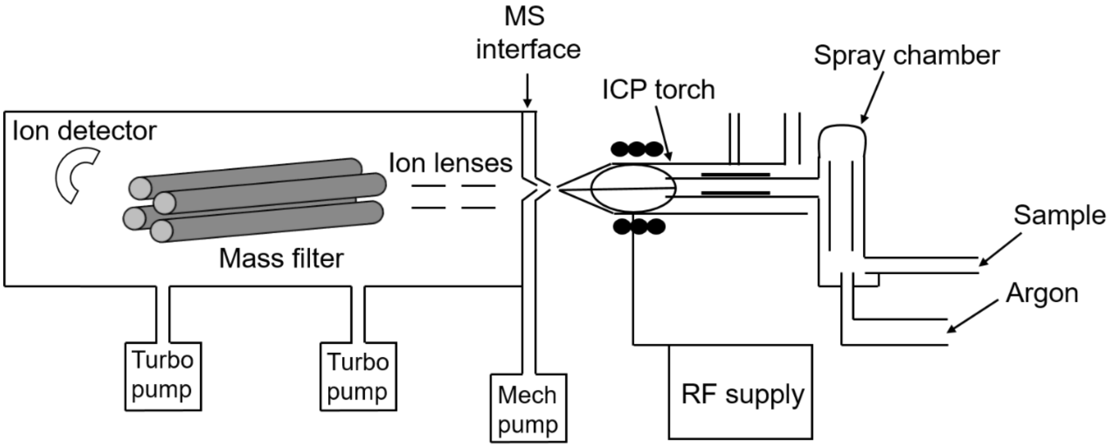

Figure 2.9: Schematic diagram of a typical ICP-MS setup (adapted from ref. [12]).

In order to be analysed, the liquid sample is pumped into a nebuliser, where it is converted into an aerosol, a suspension of liquid droplets in gas, by the presence of argon. These droplets are then separated in a spray chamber to obtain a finer aerosol, which in turn will be transported into the plasma torch using a sample injector. Here the sample is vaporised and broken down into atoms, the majority of which become ionised. Once the ions are formed, they are then directed towards a vacuum chamber. From this region the ions are allowed to pass through to the ion optics system (held at 10^{-3} Torr), a series of electrostatic lenses meant to focus the ions towards the mass spectrometer while excluding photons, solid particulate matter and neutral species. The ion beam then enters the mass spectrometer, typically a quadrupole, which is kept at 10^{-6} Torr employing a turbomolecular pump and separates the ions based on their mass to charge ratio. Finally, the ions are detected by an ion counting detector or an analogue detector, [14] where an electromagnetic signal is produced as a result of recombination of these ions. The radiation has a characteristic wavelength, which is then analysed and a ppm value is generated according to an array of calibration standards previously created. Typically, due to elemental overlap, three separate wavelengths are compared for each sample.

2.4.4. Scanning Transmission Electron Microscopy

Microscopy analysis was completed on a Scanning Transmission Electron Microscope (STEM) utilising a Cs aberration-corrected JEOL 2100F microscope at 200 kV. Images were collected using a Gatan Ultrascan 4000 digital camera operated by Digital Micrograph software. Samples were dispersed in methanol and drop cast on 200-mesh carbon-coated copper grids and dried under ambient conditions. Images were processed using ImageJ version 1.41 software.

A beam of electrons is passed through a thin layer of sample deposited on the carbon-coated grid. The resulting electron absorption leads to an image shown on a fluorescent screen; this image can then be magnified and focused like a conventional microscope. STEM microscope can focus the beam into a very narrow stream that then sweeps the sample line by line. The instrument is also fitted with dark-field (DF) imaging. This makes the resolution of nanoparticles easy to measure because DF signal is proportional to the atomic number Z of the imaged species. [15] Platinum, whose atomic number is 78, is strongly visible on the support compared to other metal nanoparticles with lower Z, as shown in **Figure 2.10**.

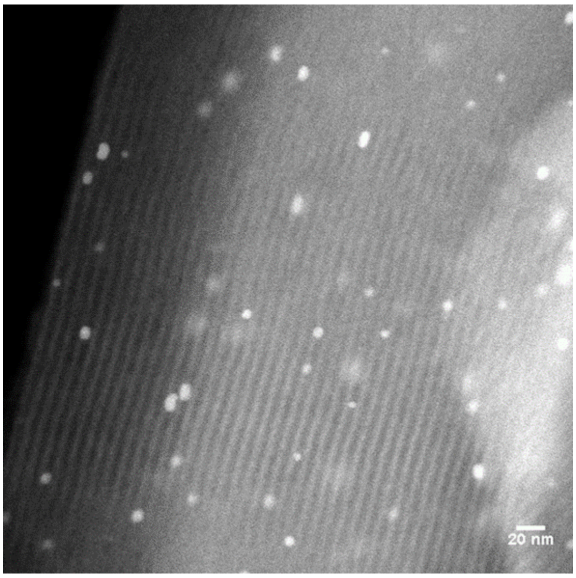

Figure 2.10: Dark-field STEM image of a generic Pt-SiO_2 catalyst (material used in this thesis).

As shown in **Figure 2.11**, electrons are emitted from an electron gun at the top of the microscope and then travel through the vacuum in the microscope. Electromagnetic lenses focus the electrons on a very thin beam so that it can go through the specimen. Depending on the density of the material, some of the electrons are scattered and disappear from the beam. At the bottom of the microscope, the unscattered electrons hit a fluorescent screen, which gives rise to a “shadow image” of the specimen.

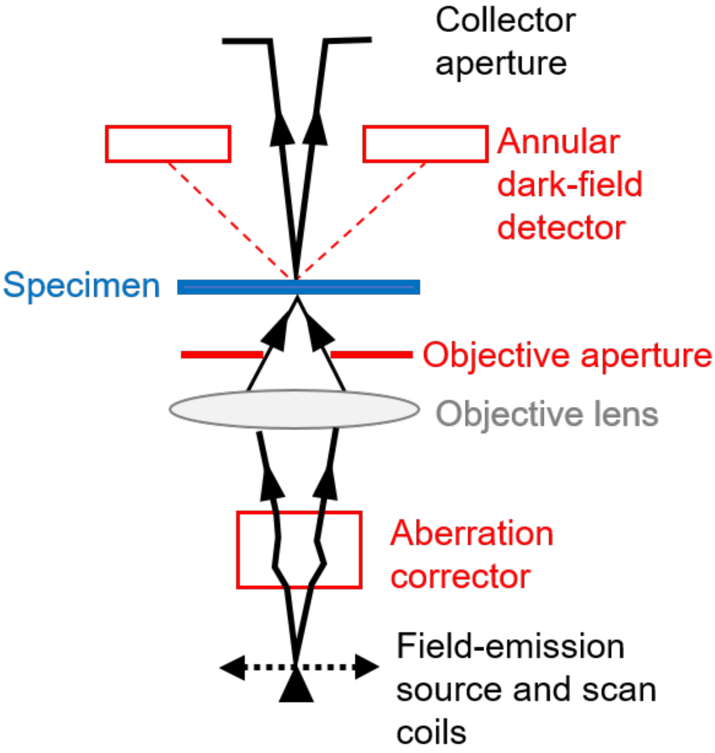

Figure 2.11: Schematic diagram of STEM (adapted from ref. [16]).

STEM provides topographical, morphological, compositional structure but also crystalline information of a small representative section of the sample, differently from XRD (2.4.1, Powder X-ray Diffraction), which gives information about the entire sample. This difference between the two techniques leads to discrepancies in the calculation of the metal particle size of the materials analysed throughout the entire thesis. Therefore, the following experimental chapters (3rd, 4th, 5th) will provide particle sizes obtained with both techniques, taking into account the following limitations:

1) XRD is not able to provide the actual particle size for crystallites ≤ 3 nm, hence the average size results to be bigger than that obtained with STEM;
2) STEM provides the representation of a portion of the sample; therefore, the remaining parts that have not been photographed by the operator might contain metal particles with different size and/or clusters of particles.

The particle dimension evaluated by STEM has been gauged over ≈ 250 particles throughout the entire thesis.

2.4.5. Scanning Electron Microscopy

Scanning Electron Microscopy (SEM) has many uses in biological and materials science; however, during this work, it has been employed to determine the macroporous structure of the silica supports.

The basic operating principles are represented in **Figure 2.12**.

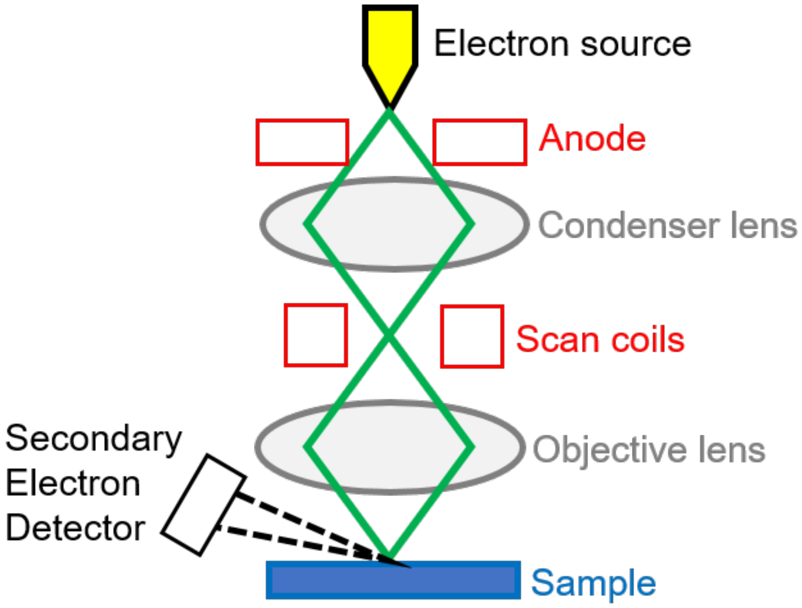

Figure 2.12: Schematic representation of the basic SEM components (adapted from ref. [17]).

This technique uses a cathode filament to produce an electron beam, which is passed through a positively charged anode, followed by lenses and scan coils to focus and direct the electron beam, respectively. The electron beam strikes the sample, expelling what is known as a secondary electron from the sample atom's inner shell. This is identified and quantified using a positively charge secondary electron detector, with the number of electrons being calculated into *n* shaded pixel on the display. In a route similar to the relaxation process in Auger electron spectroscopy, the partially vacant inner shell is filled with an outer shell electron, releasing an X-ray photon with an energy characteristic to the sample atom element which is detected in a process known as energy dispersive X-ray analysis (EDX). This second void is filled by a free electron, releasing more distinguishing photons. After the pixel has been recorded, the scan coils move the beam to the next spot and the process is repeated, resulting in an image of electron density and an elemental map of the area.

The entire device needs to be kept under vacuum. Like all the components of an electron microscope, the electron source is sealed inside a special chamber in order to preserve vacuum and protect it against contamination, vibrations or noise. Not only the vacuum protects the electron source from being contaminated but also allows the acquisition of a high-resolution image. Furthermore, high vacuum increases the collection efficiency of electrons by the detectors that are in the column.

Figure 2.13 illustrates an example of macro-mesoporous SBA-15 that has been synthesised and characterised during this project.

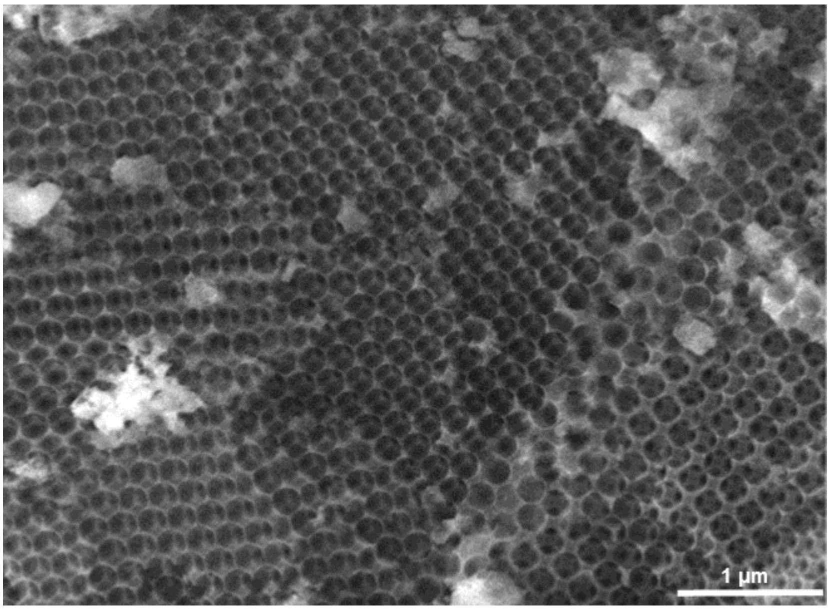

Figure 2.13: SEM image of a generic macro-mesoporous SBA-15 (material used in this thesis).

This technique is ideal for imaging macroporous materials, as it allows a spatial resolution of 50 to 100 nm. [18]

2.4.6. X-ray Photoelectron Spectroscopy

Analysis of surface regions of platinum catalysts was undertaken using a Kratos Axis HSI spectrometer with an Al Kα monochromator (1486.6 eV) and fitted with a charge neutraliser. Detection of photoelectrons was undertaken using a pass energy of 40 eV for high-resolution scans. The photoelectron peaks were fitted using CasaXPS software for carbon (1s) platinum (4f), silicon (2p) and oxygen (1s) regions, to evaluate the wt% composition of each element on the surface of the materials. In literature is reported that $Pt^{(0)}$ has a binding energy of 71.1 eV for $4f_{7/2}$, which shifts in the presence of an oxide phase such as Pt^{2+} (72.3 eV) or Pt^{4+} (73.8 eV). [19] Fits of the platinum photoelectron peaks were obtained by adjusting the position of two platinum components at an energy separation of 3.3 eV for metallic $Pt^{(0)}$, with a spin-orbit splitting ratio ($4f_{5/2}$:$4f_{7/2}$) of 0.75. [20] Literature reports that $Si^{(0)}$ has a binding energy of 99.4 eV that shifts at 103.5 eV if it is oxidised to Si^{4+}. [21] The chemical shift towards higher binding energies of elements depends on their oxidation state. Energy calibration correction was taken from the carbon 1s region, which is fixed at a binding energy of 284.6 eV. [22]

X-ray Photoelectron Spectroscopy (XPS) is a surface sensitive technique, as it measures electrons that are emitted from the top 1-10 nm of the material analysed. It provides valuable information about oxidation state, surface population and trace elemental content in materials.

During analysis, the sample is irradiated with a source that emits monochromatic X-rays (an Al Kα monochromator). The photoelectrons emitted from the sample are directed into the detector, which is an electrostatic retardation filter that decelerates the electrons so that they can travel through the analyser, and their energy measured by the detector (**Figure 2.14**).

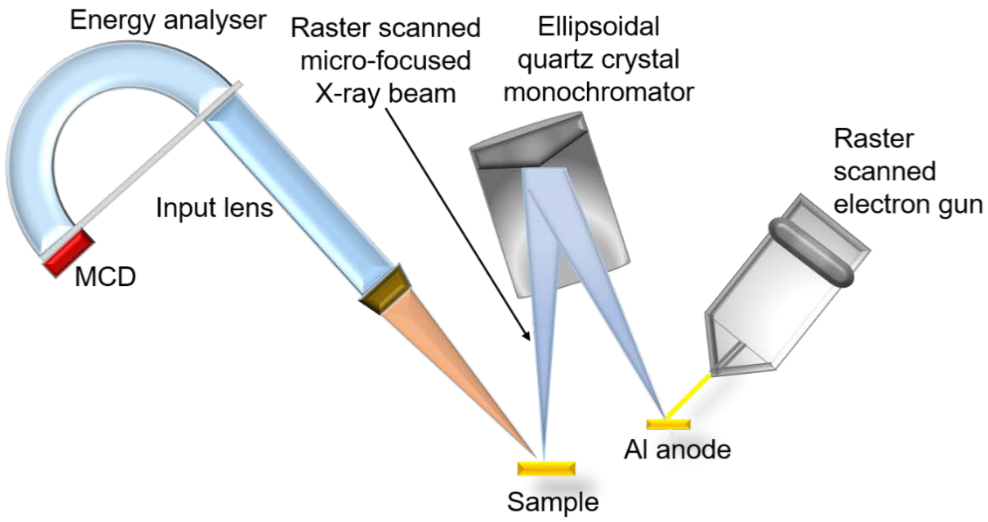

Figure 2.14: Diagram of XPS (adapted from ref. [23]).

As the energy of the electrons ranges from 50 to 1000 eV, XPS has to be measured in vacuum. Since this technique is based on the electron removal from the sample, it follows the photoelectric effect. When the material has been irradiated with X-rays with appropriate energy, there is a subsequent ejection of a core electron. Upon emission, the core hole is left in an excited state, and the overall electronic configuration is temporarily in an unstable state. As a result, outer electrons are demoted to fill the core hole, and the atom is returned to a stable state. The ejected photoelectron possesses specific kinetic energy that is detected by the instrument, and it corresponds to a specific oxidation state of an element. The energy of the incident X-ray beam is known, hence the kinetic energy of the photoelectron can be related to the binding energy (BE) of the electron residing within a specific atomic orbital, through the following equation: [24]

$$KE = hv - BE - \Phi_S$$

Equation 2.7: Photoelectron kinetic energy.

Where:

- **KE** is the photoelectron kinetic energy (J)
- **BE** is the binding energy specific of the element (J)
- **hv** is the energy of the incident radiation (J)
- **Φ_s** is the spectrometer “work function” (J)

The binding energy gives chemical information about the sample under analysis. It is sensitive to the oxidation state and electronegativity of the elements, as it increases with the former, producing a chemical shift. This happens because the binding energy depends on the oxidation state of the element and from the coulomb contributions (charge) that stem from the neighbour's elements, as first observed by Siegbhan. [25]

As anticipated in Chapter 1 (section 1.3. Platinum as a heterogeneous catalyst in oxidation reactions), a disadvantage of chloroplatinic acid precursor (which will be employed in Chapters 4 and 5) is represented by six atoms of chlorine, which may be difficult to remove during the pre-treatment step. XPS analysis did not detect the presence of chlorine in any of the catalysts used, indicating that the pre-treatment carried out under hydrogen was successful for the removal of all the ligands.

2.4.7. Thermogravimetric Analysis – Mass Spectrometry

Experiments have been performed using thermogravimetry analyser Mettler Toledo TGA/DSC 2 coupled with mass spectrometer Pfeiffer Vacuum Thermostar. 10 mg of the sample has been weighed and placed on an alumina crucible under an inert atmosphere of nitrogen. A flow rate of 40 mL min^{-1} of nitrogen gas was fed into the system. Subsequently, the sample was heated from 40 to 800 °C (heating rate of 10 °C min^{-1}) under oxygen (flow rate of 20 °C min^{-1}).

Thermogravimetric Analysis (TGA) is used to measure the mass variation of the materials upon temperature increase, whereas the Mass Spectrometer (MS) is used to measure the products.

The experimental setup of TGA-MS is illustrated in **Figure 2.15**.

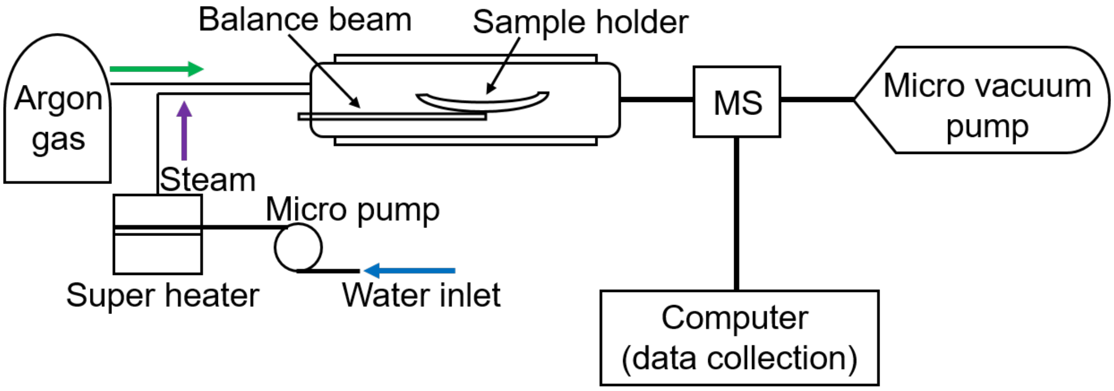

Figure 2.15: Experimental setup of TGA equipment coupled with MS (adapted from ref. [26]).

A typical thermogravimetric analyser consists of a precision balance with a sample pan located inside a furnace with a programmable control temperature. The temperature is generally increased at a constant rate (or for some applications the temperature is controlled for a constant mass loss) to incur a thermal reaction. The thermal reaction may occur under a variety of atmospheres including ambient air, vacuum, inert gas, oxidising/reducing gases, and different pressures such as high vacuum, high and constant pressure.

TGA combined with MS is a powerful technique that can be used to characterise solid and liquid samples. The mass of the sample material is monitored while it is heated so that the mass loss can be plotted as a function of temperature. TGA is widely used in the study of polymers, pharmaceuticals and petrochemicals to determine degradation temperatures, characterise thermal decomposition and monitor solvent and moisture content.

During the present thesis, this technique has been employed to identify the mass loss of the reactant as a function of temperature, in such a way to mimic the reaction conditions. In this way, TGA-MS served as an effective tool to help to identify the side-products of the oxidation reaction at issue.

2.5. Catalytic testing

2.5.1. Dodecyl aldehyde aerobic oxidation (Chapter 3)

The aerobic oxidation of dodecyl aldehyde to dodecanoic acid was carried out in a Radleys StarFish carousel reactor on a 10 mL scale under 1 bar O_2 (flow rate = 5 mL min^{-1}). The reaction mixture contained 2 mmol of dodecyl aldehyde (370 mg), 0.05 mL of mesitylene as internal standard, 10 mL of toluene solvent and 25 mg of catalyst. Reactions were periodically sampled for 24 hours. The reaction mixtures were heated to 90 °C and stirred at 700 r.p.m. The consumption of dodecyl aldehyde and the formation of the product was monitored with a Gas-Chromatogram (GC Shimadzu-2010 Plus) with AOC-20i autosampler fitted with a Zebron ZB-50 column (30 m x 0.32 mm x 0.25 µm).

The internal standard has been used to correct changes in the Gas-Chromatogram's operating conditions and effects due to the interaction between matrix and sample, which may enhance or suppress the analyte signal.

The GC was setup based on the following programme: injection temperature and volume were 250 °C and 1.5 µL, respectively. The oven temperature was programmed at 80 °C and increased up to 330 °C with a 30 °C min^{-1} ramp rate. It was maintained at 330 °C for 8 minutes. The total duration of analysis was 16.33 minutes.

Dodecyl aldehyde conversion (%) was calculated from **Equation 2.8**.

$$[(mmol_0 - mmol_t) / mmol_0] \times 100$$

Equation 2.8: Conversion.

Where **$mmol_0$** is the initial mmol of reactant and **$mmol_t$** is the number of mmol of the reactant at the specific time **t**.

The yield (%) of dodecanoic acid (major product) was calculated from **Equation 2.9**, as this was the only product of the reaction that was identified with a gas-chromatogram coupled with mass spectrometry (GC-MS Shimadzu), with AOC-20i autosampler fitted with a Shimadzu SH-Rtx-5ms column (30 m x 0.25 mm x 0.25 µm). Further minor side-products were not identified with GC-MS and remained unknown.

$$[mmol_{x=i} / (mmol_0)] \times 100$$

Equation 2.9: Yield.

Where **$mmol_{x=i}$** is the mmol of the product **i,** and **$mmol_0$** is the initial mmol of reactant.

The total mass balance (%) of the reaction was calculated from **Equation 2.10**.

$$[(\text{mmol}_r + \text{mmol}_{x=i}) / \text{mmol}_0] \times 100$$

Equation 2.10: Total mass balance.

Where **mmol_r** are the mmol of the reactant at any time, **$\text{mmol}_{x=i}$** is the mmol of the product **i** at any time**,** and **mmol_0** is the initial mmol of reactant.

Initial rate (mmol h^{-1}) was calculated over the first 30 minutes of reaction in order to obtain an $R^2 \geq 0.9$ in "time *vs* reactant mmol" straight-line equation.

Platinum normalised initial rate (mmol h^{-1} g_{Pt}^{-1}) was determined from **Equation 2.11**.

$$\text{Initial rate (mmol h}^{-1}\text{) / total mass of Pt (g)}$$

Equation 2.11: Normalised initial rate.

Where the **total mass of Pt** was calculated multiplying the amount of catalyst used in the reaction by its metal loading.

2.5.2. Cinnamaldehyde aerobic oxidation (Chapter 4)

The aerobic oxidation of cinnamaldehyde to cinnamic acid was carried out in a Radleys StarFish carousel reactor on a 10 mL scale when the experiments were run under N_2, air and 1 bar O_2 (flow rate = 5 mL min^{-1}). The reaction mixtures contained 8.4 mmol of cinnamaldehyde (1.11 g), 0.1 mL of mesitylene as internal standard and 10 mL of toluene solvent. Reactions were periodically sampled for 24 hours.

High pressure (10 bar O_2) oxidations were performed in a Parr 5513 100 mL stainless steel stirred autoclave on a 40 mL scale to ensure accurate kinetic analysis, using the same ratio of reactant to internal standard and solvent as in the previous oxidations. Reactions were periodically sampled for 6 hours (instead of 24 hours) for safety reasons, as the autoclave was not kept running overnight.

The reaction mixtures under any pressure condition were heated to 90 °C and stirred at 700 r.p.m. The consumption of cinnamaldehyde and the formation of products were monitored with a Gas-Chromatogram (GC Bruker Scion456) with 8400 autosampler fitted with a FactorFour VF-5ms column (30 m x 0.25 mm x 0.25 µm). The products were also identified with a gas-chromatogram coupled with mass spectrometry (GC-MS Shimadzu) with AOC-20i autosampler fitted with a Shimadzu SH-Rtx-5ms column (30 m x 0.25 mm x 0.25 µm).

The GC was setup based on the following programme: injection temperature and volume were 300 °C and 1.5 µL, respectively. The oven temperature was programmed at 55 °C and maintained at this temperature for 10.8 minutes. Then it was raised to 140 °C with a 70 °C min^{-1} ramp rate, to 150 °C with a 4 °C min^{-1} ramp rate and to 325 °C with a 40 °C min^{-1} ramp rate, at which temperature was maintained for 2 minutes. The total duration of analysis was 20.89 minutes.

Cinnamaldehyde conversion (%) was calculated from **Equation 2.8**.

Selectivity (%) of the products was calculated from **Equation 2.12**.

$$[mmol_{x=i} \ / \ (\Sigma mmol_x)] \times 100$$

Equation 2.12: Selectivity.

Where $\mathbf{mmol_{x=i}}$ is the mmol of the product **i,** and $\mathbf{\Sigma mmol_x}$ is the sum of all products produced during the reaction.

Initial rate (mmol h^{-1}) was calculated over the first 10 minutes of reaction in order to obtain an $R^2 \geq 0.9$ in "time *vs* reactant mmol" straight-line equation.

Platinum normalised initial rate (mmol h^{-1} g_{Pt}^{-1}) was determined from **Equation 2.11**.

2.5.3. Hydroxymethylfurfural aerobic oxidation (Chapter 5)

The aerobic oxidation of 5-hydroxymethyl furfural (HMF) to furandicarboxylic acid (FDCA) was carried out in a Radleys StarFish carousel reactor on a 10 mL scale when the experiments were run under 1 bar O_2 (flow rate = 40 mL min^{-1}). The reaction mixture contained 0.4 mmol of HMF (50.4 mg), 0, 1, 2 or 4 equivalents of Na_2CO_3 (0, 42.4, 84.8 or 169.6 mg, respectively) and 10 mL of water solvent. Reactions were periodically sampled for 24 hours.

High pressure (10 bar O_2) oxidations were performed in a Parr 5513 100 mL stainless steel stirred autoclave on a 40 mL scale to ensure accurate kinetic analysis, using the same ratio of reactant to base and solvent as in the previous oxidations. Reactions were periodically sampled for 6 hours (instead of 24 hours) for safety reasons, as the autoclave was not kept running overnight.

The reaction mixtures under any pressure condition were heated to 80 and 130 °C and stirred at 700 r.p.m. The consumption of HMF and the formation of products were monitored by High-Performance Liquid Chromatography (HPLC, Agilent technologies, 1260 Infinity) with a Hi-Plex H column (300 x 7.7 mm). The mobile phase was 5 mM H_2SO_4, with a flow rate of 0.6 mL min^{-1}. The column was kept at a constant temperature of 65 °C, and the sample was injected with a volume of 5 µL. The total duration of analysis was 60 minutes.

The products were identified by injecting the standards in the HPLC and checking their retention times.

HMF conversion (%) was calculated from **Equation 2.8**.

Yield (%) of the products was calculated from **Equation 2.9**.

Selectivity (%) of the products was calculated from **Equation 2.12**.

Initial rate (mmol h^{-1}) was calculated over the first 30 minutes of reaction in order to obtain an $R^2 \leq 0.9$ in "time *vs* reactant mmol" straight-line equation.

Platinum normalised initial rate (mmol h^{-1} g_{Pt}^{-1}) was determined from **Equation 2.11**.

2.5.4. Aerobic oxidation reactions setups

The arrangements of the oxidation reactions are illustrated below.

Figure 2.16 shows the setup of aerobic oxidations carried out in batch under 1 bar O_2 pressure. The two-neck round-bottom glass reactors had a total capacity of 25 mL, and the cooling fluid used in the condenser was water. The temperature was regulated by a stirring hot plate located under the 5-reactor metal holder (maximum temperature of 300 °C and a maximum stirring speed of 1400 r.p.m.), and the stirring was provided by the magnetic stirrer inside the reactor.

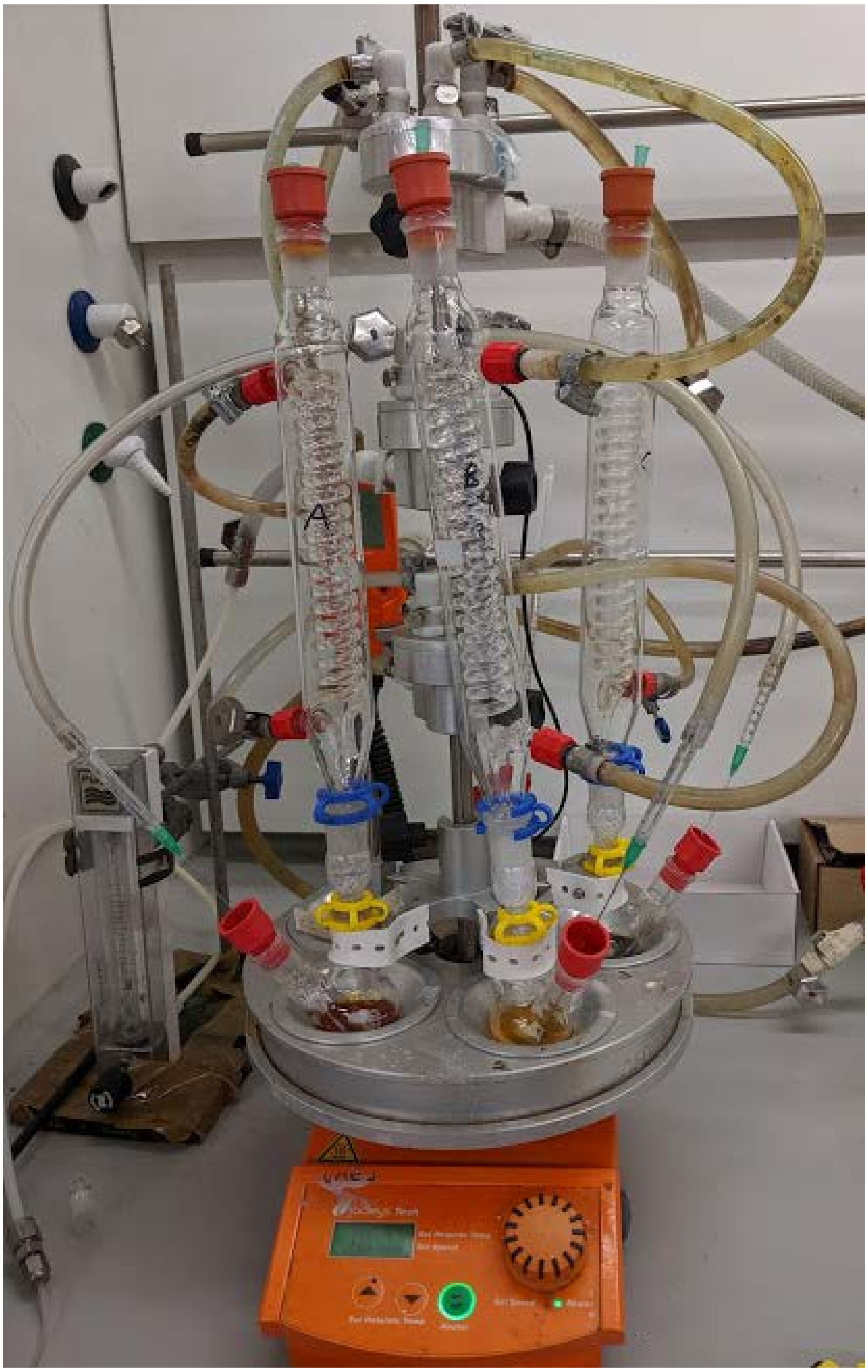

Figure 2.16: Setup of aerobic oxidations carried out under 1 bar O_2.

Figure 2.17 shows the setup of aerobic oxidations carried out in the high-pressure stainless-steel autoclave under 10 bar O_2 pressure. The total volume of the reactor vessel was 50 mL; the temperature was maintained and regulated by an electric jacket connected to a PID controller (max temperature 350 °C). The pressure was increased and reduced in the reactor via two manual valves, and the pressure was monitored by a digital manometer and a needle manometer (maximum pressure allowed

200 bar). The stirring was provided by top mechanical stirrer with a turbine agitator and regulated with a PID controller (maximum stirring speed 1700 r.p.m.)

Figure 2.17: Setup of aerobic oxidations carried out under 10 bar O_2.

2.6. References

1. Sen T., Tiddy G., Casci J., Anderson M., Synthesis and characterization of hierarchically ordered porous silica materials. Chemistry of Materials, 2004. **16**(11): p. 2044-2054.
2. Parlett C.M.A., Isaacs M.A., Beaumount S.K., Bingham L.M., Hondow N., Wilson K., Lee A.F., Spatially orthogonal chemical functionalization of a hierarchical pore network for catalytic cascade reactions. Nat Mater, 2016. **15**(2): p. 178-182.
3. Achouri I.E., Abatzoglou N., Fauteux-Lefebvre C., Braidy N., Diesel steam reforming: Comparison of two nickel aluminate catalysts prepared by wet-impregnation and co-precipitation. Catalysis Today, 2013. **207**: p. 13-20.
4. Atkins P.W., De Paula J., Atkins' physical chemistry. 2006, Oxford; New York: Oxford University Press.
5. Patterson A.L., The Scherrer formula for X-ray particle size determination. Physical Review, 1939. **56**(10): p. 978-982.
6. Brunauer S., Emmett P.H., Teller E., Adsorption of gases in multimolecular layers. Journal of the American Chemical Society, 1938. **60**(2): p. 309-319.
7. Barrett E.P., Joyner L.G., Halenda P.P., The determination of pore volume and area distributions in porous substances. I. Computations from nitrogen isotherms. Journal of the American Chemical Society, 1951. **73**(1): p. 373-380.
8. Cychosz K.A., Guillet-Nicolas R., Garcia-Martinez J., Thommes M., Recent advances in the textural characterization of hierarchically structured nanoporous materials. Chemical Society Reviews, 2017. **46**(2): p. 389-414.
9. Galarneau A., Villemont F., Rodriguez J., Fajula F., Coasne B., Validity of the *t*-plot method to assess microporosity in hierarchical micro/mesoporous materials. Langmuir, 2014. **30**(44): p. 13266-13274.
10. Agatemor C., Beauchemin D., Matrix effects in inductively coupled plasma mass spectrometry: a review. Analytica Chimica Acta, 2011. **706**(1): p. 66-83.
11. Fiddy S.G., Newton A.M., Corker J., Turin S., Savini G., In situ energy dispersive EXAFS (EDE) of low loaded Pt(acac)$_2$/HI SiO$_2$ catalyst precursors on a timescale of seconds and below. Chemical Communications, 1999(9): p. 851-852.
12. Thomas R., Practical guide to ICP-MS. 2004.
13. Tissue B.M., Inductively-Coupled Plasma (ICP) excitation source, 1996. Last update: 12/12/2019.
14. Wilschefski S.C., Baxter M.R., Inductively Coupled Plasma Mass Spectrometry: introduction to analytical aspects. the clinical biochemist. Reviews, 2019. **40**(3): p. 115-133.
15. Yamashita S., Kikkawa J., Yanagissawa K., Nagai T., Ishizuka K., Kimoto K., Atomic number dependence of Z contrast in scanning transmission electron microscopy. Scientific Reports, 2018. **8**(1): p. 12325.
16. Pennycook S.J., Varela M., Hetherington C., Kirkland A., Materials advances through aberration-corrected electron microscopy. MRS Bulletin, 2011. **31**(1): p. 36-43.
17. ATA Scientific Instruments, The applications and practical uses of scanning electron microscopes, 2019. Last update: 12/12/2019.
18. Swapp S., University of Wyoming, Scanning Electron Microscopy (SEM). Geochemical Instrumentation and Analysis, 2017. Last update: 19/05/2020.

19. Ono L.K., Yuan B., Heinrich H., Cuenya B.R., Formation and thermal stability of platinum oxides on size-selected platinum nanoparticles: support effects. The Journal of Physical Chemistry C, 2010. **114**(50): p. 22119-22133.
20. Neri G., Rizzo G., Arico A.S., Crisafulli C., One-pot synthesis of naturanol from α-pinene oxide on bifunctional Pt-Sn/SiO_2 heterogeneous catalysts: Part I: The catalytic system. Applied Catalysis A: General, 2007. **325**(1): p. 15-24.
21. ThermoScientific, XPS simplified, 2013. Last update: 16/12/2019.
22. Karhu H., Kalantar A., Väyrynen I.J., Salmi T., XPS analysis of chlorine residues in supported Pt and Pd catalysts with low metal loading. Applied Catalysis A: General, 2003. **247**(2): p. 283-294.
23. University of Virginia webpage, Scanning X-ray Photoelectron Spectrometer (XPS). 2019. Last update: 12/12/2019.
24. Watts J.F., X-ray photoelectron spectroscopy. Vacuum, 1994. **45**(6): p. 653-671.
25. Lindgren I., Chemical shifts in X-ray and photo-electron spectroscopy: a historical review. Journal of Electron Spectroscopy and Related Phenomena, 2004. **137-140**: p. 59-71.
26. Kumar A., Singh J., Baskar C., Ramakrishna S., Bioenergy: biofuels process technology. Advances in Bioprocess Technology, P. Ravindra, Editor. 2015, Springer International Publishing: Cham. p. 165-207.

CHAPTER 3:

TLCT SBA-15 and *MM*-TLCT SBA-15 materials and catalysis

Since its discovery, [1, 2] SBA-15 has been receiving much attention by catalytic scientists, because of its large pores, thick pore walls and high hydrothermal stability. [3] Besides, its high surface area, tuneable pore size and ordered hexagonal structure render it an ideal support for the introduction of active sites, especially for liquid-phase reactions. [4, 5] Traditionally, SBA-15 is synthesised under acidic conditions using an amphiphilic triblock copolymer Pluronic P123 dissolved in aqueous HCl and tetraethoxysilane mixture. This method is called “Cooperative Self-Assembly Liquid Crystal Templating” (CO-OP SA) because the liquid crystal phase is not present at the beginning of the preparation, but it is held to form during the silica condensation. [6] The final material contains both mesopores and micropores, and this is why its surface area is high. A different protocol was applied later on by Wainwright and co-workers, [7] who adopted the previously developed method called “True Liquid Crystal Templating” (TLCT). [8] This methodology allows better control of the silica morphology, as the liquid crystal mesophase is pre-formed before the sol-gel condensation. In this way, the microporosity is reduced to almost zero, resulting in a decreased surface area and a better location of metal nanoparticles within the silica skeleton. [7]

It is important to tailor the porosity of mesoporous silica materials to improve the internal diffusion of the reactant inside the pores. The more smoothly it flows inside the pores, the easier it will reach the active sites located inside them. This helps improve the catalyst performance, as a superior mass-transport of the bulky reactant is achieved, leading to significant enhancement of mass-transport rate and conversion. The main routes by which it is possible to accomplish pore enlargement of CO-OP SA SBA-15 make use of heat [9-11] and swelling agents, i.e. hexane, [12-16] heptane, [14-17] cyclohexane, [12, 16] 1,3,5-triisopropylbenzene [12] and 1,3,5-trimethylbenzene. [18-20] Often, heat and micelle expanders have been combined, [1, 5, 20-22] to achieve a more significant effect on pore enlargement. Another methodology used to achieve enhanced internal diffusion consists of the insertion of macropores inside the mesoporous SBA-15 framework.

In the current chapter of this thesis, the methodologies listed above have been applied for the first time to TLCT SBA-15, to investigate its capability to tune key structural properties, such as pore diameter, pore volume and surface area. After an extensive study of TLCT supports, the pore-expanded mesoporous and macro-mesoporous materials have been applied to the catalysis of a large molecule.

3.1. Characterisation of mesoporous silica supports

3.1.1. CO-OP SA SBA-15 and TLCT SBA-15: a comparison

CO-OP SA SBA-15 was synthesised based on the traditional synthesis employed by Zhao and co-workers, [2] while TLCT SBA-15 was synthesised following the procedure described by Wainwright and co-workers. [7]

Low-angle X-ray diffractograms (XRD) of both materials are shown in **Figure 3.1** (left).

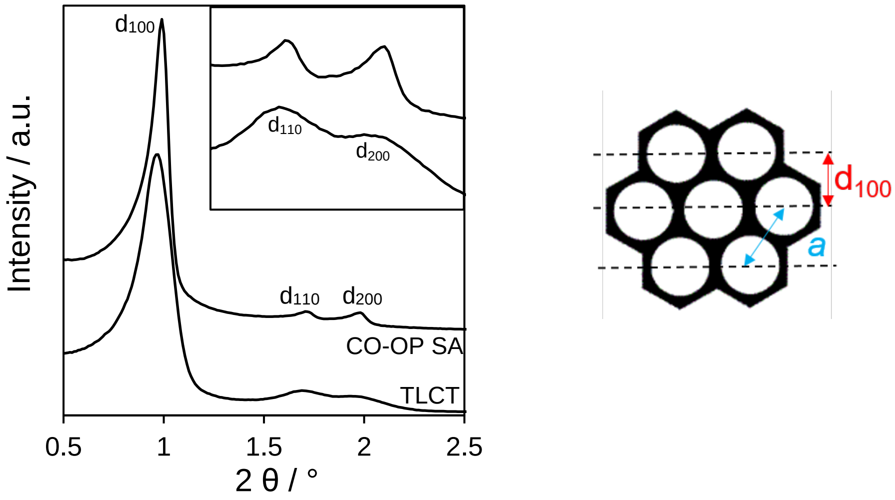

Figure 3.1: Low-angle XRD patterns of CO-OP SA and TLCT SBA-15 (left), inset: detail of d_{100} and d_{200} peaks (offset for clarity). Representation of the typical hexagonal mesostructure of SBA-15 (right).

Both low-angle XRD patterns show three reflections corresponding to (100), (110) and (200) planes of the repeating structure, as explained in detail in Chapter 2 (section 2.4.1. Powder X-ray diffraction). These three reflections are characteristic for materials belonging to *p6mm* space group with hexagonal symmetry. When porous channels exhibit long-range order, the repeating layers give rise to diffraction peaks called d_{100}, d_{110}, d_{200}, where d_{100} is identified as the layer spacing. By manipulation of the Bragg's law (**equation 2.1**, section 2.4.1, Chapter 2), it is possible to calculate the d_{100} spacing and the unit cell parameter (pore spacing – *a*), identified as the distance between the centre of the pores (**Figure 3.1**, right). To do that, the Pythagoras theorem is applied, and the d_{100} peak value is multiplied by $(2/\sqrt{3})$. Furthermore, by taking the difference of *a* and mesopore diameter (PD, calculated from nitrogen physisorption porosimetry), it is possible to evaluate the thickness of the silica walls (PWT). Both low-angle XRD patterns in **Figure 3.1** (left) are representative of a long-range ordered hexagonal structure belonging to mesoporous SBA-15.

Nitrogen physisorption porosimetry was also carried out on the two samples, and adsorption-desorption isotherms and pore size distributions (PSD) are shown in **Figure 3.2.**

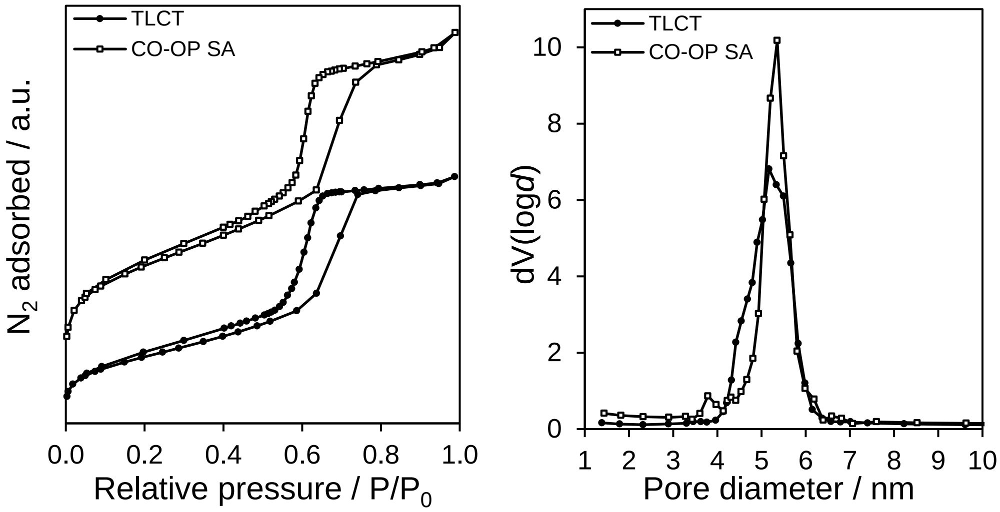

Figure 3.2: Adsorption-desorption N_2 isotherms (left) and PSD (right) of CO-OP SA and TLCT SBA-15 (offset for clarity).

The isotherms of the two silicas look very similar, both exhibiting a type IV isotherm with an H1-type hysteresis loop, characteristic of SBA-15 mesoporous materials. The steep capillary condensation step indicates a narrow pore size distribution, reflected in **Figure 3.2** (right). PSD, obtained from the desorption branches of the isotherms using the BJH algorithm, yielded a pore diameter of 5.4 and 5.2 for CO-OP SA and TLCT SBA-15, respectively. Also, the pore volume of the former is slightly bigger than that of the latter (0.9 and 0.7 cm^3 g^{-1}). Both increases observed in CO-OP SA material can be attributed to the hydrothermal treatment step (80 ˚C) during the synthesis, which is known to induce pore swelling. In addition, the TLCT approach yielded a material with a BET surface area (SA) of 466 ± 47 m^2 g^{-1} with no complementary microporosity, evaluated using the *t*-plot statistical thickness method. Conversely, the SBA-15 prepared using the conventional methodology, possessed a total BET surface area of 805 ± 81 m^2 g^{-1}, of which 229 ± 23 m^2 g^{-1} (≈ 25%) was due to complementary microporosity. This highlights that the higher surface area observed in the second case is due to its elevated microporosity, which has been completely removed when the TLCT methodology was adopted. All the parameters described up until now are summarised in **Table 3.1**.

SBA-15 type	***a* / nm**	**PD / nm**	**PWT / nm**	**SA (MA) / m^2 g^{-1}**	**PV / cm^3 g^{-1}**
CO-OP SA	10.3	5.4	4.9	805 ± 81 (229 ± 23)	0.9
TLCT	10.5	5.2	5.3	466 ± 47 (0.0 ± 0)	0.7

Table 3.1: Structural properties of CO-OP SA and TLCT SBA-15, (*a* = pore spacing, PD = pore diameter, PWT = pore wall thickness, SA = BET surface area, MA = micropore area, PV = pore volume).

In conclusion, the preparation of two different mesoporous SBA-15 has been carried out, utilising the CO-OP SA and TLCT route, the latter affording a material with no microporosity. From this point on, this chapter will focus on the characterisation and catalysis of TLCT SBA-15 materials, whose capability of pore expansion has never been explored to date, and represents a valid alternative to the conventional counterpart silica in terms of preparation and catalytic performance.

3.1.2. TLCT SBA-15: reproducibility and characterisation

After differentiating between two different synthetic routes for the preparation of mesoporous silica materials, the first stage of this project was the identification of conditions that allowed the reproducible synthesis of TLCT SBA-15, which was optimised by tailoring the pH of the solution employed for its preparation.

As low-angle XRD diffractograms in **Figure 3.3** show, seven exact samples of TLCT SBA-15 were prepared under two slightly different pH (1.8 and 2-2.2), to check which one afforded the best reproducibility. Under pH = 1.8, it was possible to obtain excellent reproducibility, whereas pH = 2-2.2 did not permit to obtain the same results.

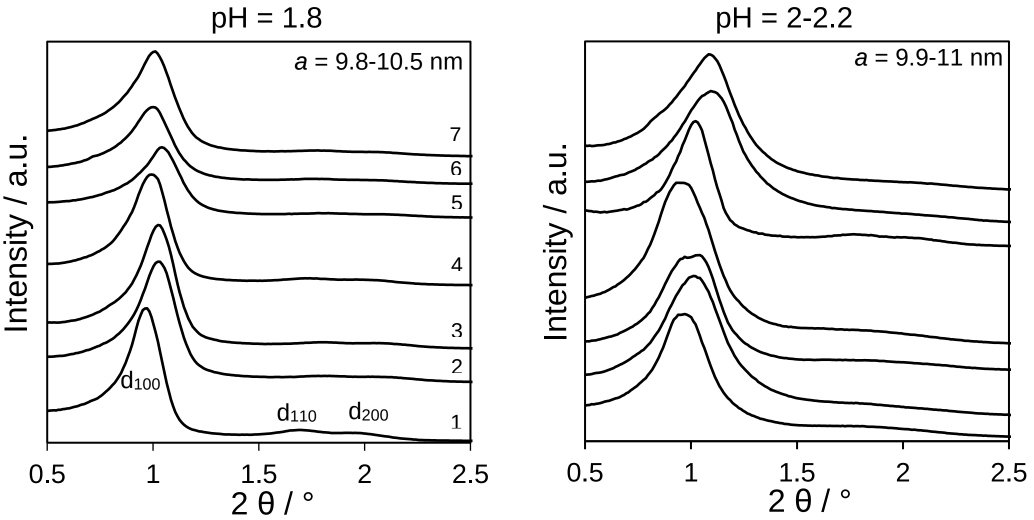

Figure 3.3: Low-angle XRD patterns of seven TLCT SBA-15 samples prepared under different pH (offset for clarity), (*a* = pore spacing).

Only at lower pH, every low-angle XRD diffractogram was very similar to each other, suggesting a good reproducibility. At higher pH, the resulting stacked diffractograms did not display the same long-range order and reproducibility (**Figure 3.3**, right), with less defined diffraction peaks. In the latter case, pore spacings showed more significant fluctuation, ranging from 9.9 to 11 nm, compared to those obtained at pH = 1.8 (9.8-10.5 nm). Nonetheless, both series of diffractograms confirmed *p6mm* symmetry, characteristic of SBA-15 materials.

Examining the low-angle XRD patterns more in-depth (**Figure 3.4**), the effect of different acidities is more appreciable.

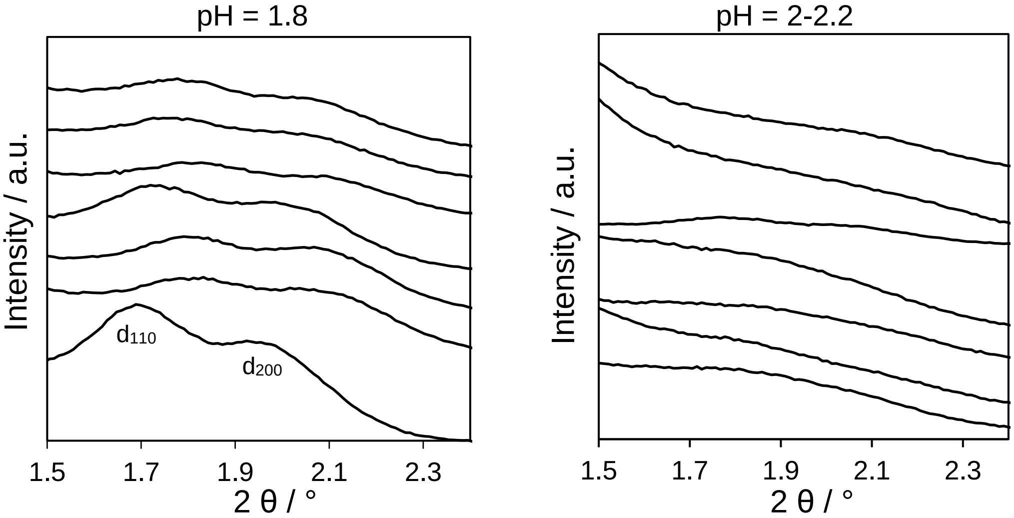

Figure 3.4: (110) and (200) reflections of low-angle XRD patterns of seven TLCT SBA-15 samples prepared under different pH (offset for clarity).

While **Figure 3.4** (left) helps to gauge the consistency of the extent of long-range order of the seven samples, the quasi-disappearance of the (110) and (200) reflections in **Figure 3.4** (right) is symptomatic of two important factors: 1) dramatic loss of long-range order of the periodic mesostructures and 2) loss of homogeneity of the pores, [23] as will be explained more in detail further on in this section.

Nitrogen physisorption porosimetry represents further proof of the fact that the two classes of materials do not possess the same structural properties (**Figure 3.5**).

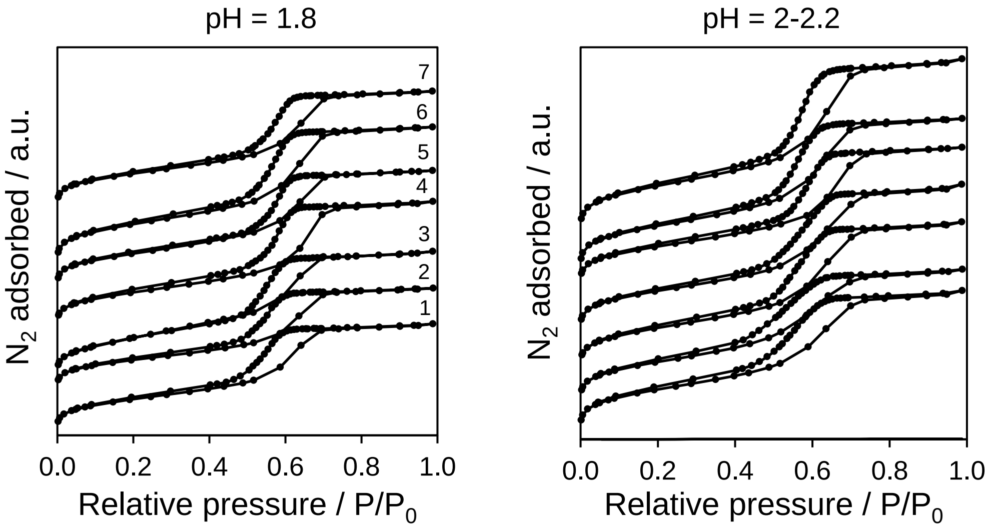

Figure 3.5: N_2 physisorption isotherms of seven TLCT SBA-15 samples prepared under different pH (offset for clarity).

At pH = 1.8, samples showed identical type IV adsorption-desorption isotherms with H1-type hysteresis loop typical of ordered mesoporous materials, while under pH = 2-2.2 the shape of the isotherm varied across the series, indicating a lower degree of reproducibility. Also, at higher pH the isotherm shapes are visibly more elongated than those obtained at pH = 1.8, indicating higher surface area (average SA at pH 1.8 = 442 ± 44 $m^2\ g^{-1}$, average SA at pH 2 to 2.2 = 546 ± 55 $m^2\ g^{-1}$) and higher micropore area (average MA at pH 1.8 = 24 ± 2 $m^2\ g^{-1}$, average MA at pH 2 to 2.2 = 27 ± 3 $m^2\ g^{-1}$). Surface areas obtained at pH = 1.8 meet the standard values for TLCT SBA-15, as Wainwright and co-workers reported (≈ 400 $m^2\ g^{-1}$). [7]

In addition, PSD of the materials prepared under different pH appeared slightly different (**Figure 3.6**).

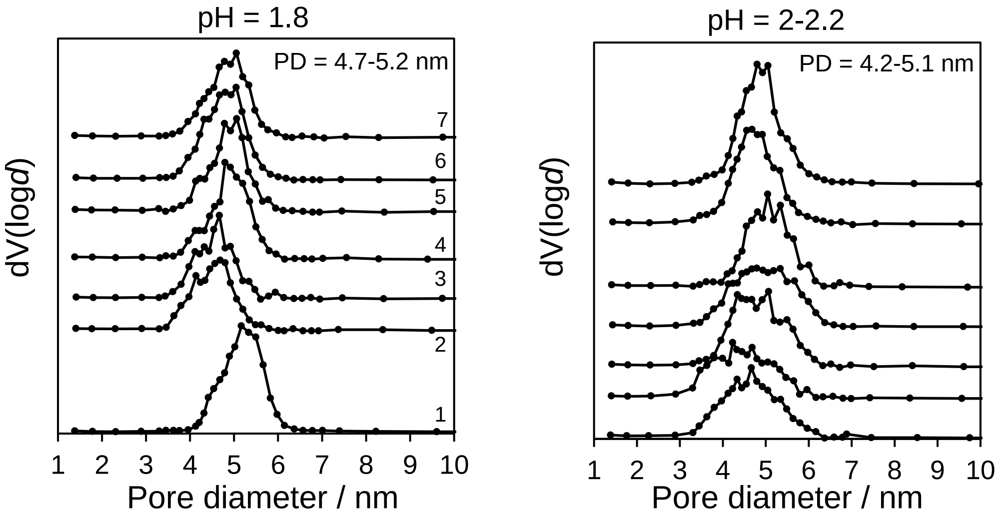

Figure 3.6: PSD of seven TLCT SBA-15 samples prepared under different pH (offset for clarity), (PD = pore diameter).

As **Figure 3.6** shows, the narrower PSD was obtained at lower pH, whereas at higher pH pore diameters PSD was broader and less consistent across the series, which corresponds to a reduced order of homogeneity of the pores. [23]

The two main parameters that identify the properties of porous materials, namely pore spacing and pore diameter, were compared for both series (**Figure 3.7**), as a further demonstration that carrying out the synthesis with a more acidic solution is preferable, in order to obtain batches with more reproducible and reliable structural properties. As during the present project, it was necessary to prepare multiple batches of supports at different times, finding the conditions that allowed the preparation of reproducible materials has been crucial for the continuation of the thesis.

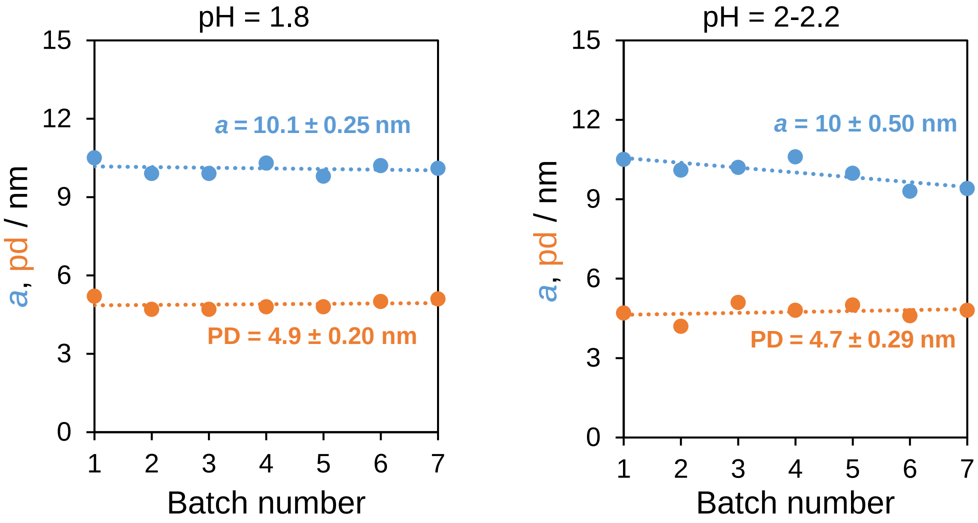

Figure 3.7: Reproducibility estimation of two TLCT SBA-15 batches prepared at different pH (*a* = pore spacing, PD = pore diameter).

Figure 3.7 underlines pore spacing and pore diameter trends for materials prepared at both pHs. Higher acidity is the condition that allowed obtaining less error for both parameters, whereas using an acidic solution at pH = 2-2.2 caused a broader fluctuation that led to lack of reproducibility.

The results explained above clarified that, in order to obtain precisely reproducible TLCT SBA-15 materials that possess long-range order, the value of acidity needs to be accurately adjusted and monitored during preparation. A slight difference of pH resulted in a massive change of key mesoporous material properties, such as pore spacing and pore diameter, critical for the overall material performance. As explained in detail in Chapter 1 (section 1.2.1. Synthetic routes to SBA-15), the difference observed between batches prepared at pH = 1.8 and 2-2.2 might be attributed to the rate of condensation of the silicate oligomers and the non-ionic surfactants micelles. A high acid concentration leads to a slower condensation of the silica species and fast hydrolysis rate, resulting in better control on the silica morphology. Conversely, when the pH is higher, the hydrolysis is slower, and the condensation of silica species is faster, causing less control of the morphology. [24, 25] Generally, when the concentration of H^+ is higher, the block copolymer is more hydrophilic because the PEO moieties are readily protonated in the strongly acidic media. [6]

Scanning Transmission Electron Microscopy (STEM) of sample **1** (from **Figure 3.3**, **Figure 3.5** and **Figure 3.6**) is displayed in **Figure 3.8**.

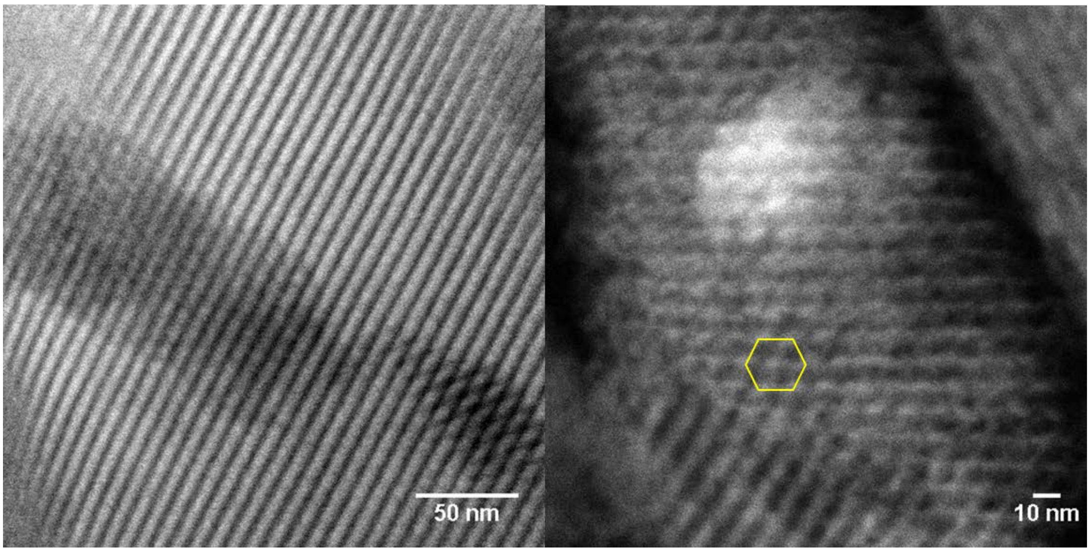

Figure 3.8: Bright field STEM images of TLCT SBA-15 (sample **1**) in two different scales. Image taken vertical to the parallel pore channels (left), and along the parallel pore channels (right).

This technique identified the parallel pore architecture (**Figure 3.8,** left) and the hexagonal arrangement of the mesopores (**Figure 3.8**, right), confirming the *p6mm* symmetry previously identified with low-angle X-ray diffraction. **Figure 3.9** describes from which angulation the STEM images have been taken.

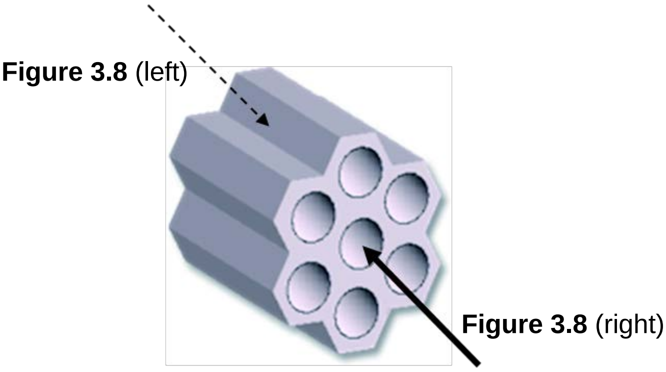

Figure 3.9: Angulations of TLCT SBA-15's STEM images.

3.1.3. Characterisation of TLCT SBA-15 with hydrothermal treatment

A key aspect of this project aims for the successful expansion of TLCT SBA-15 mesopore diameter, to enhance the internal mass diffusion of reactants inside the pores.

Pore expansion can be achieved via hydrothermal aging, but although such methodology has been adopted for CO-OP SA SBA-15 over the past years, alone [9-11] or in combination with organic swelling agents, [5, 20-22] it has never been applied to TLCT materials up to date.

Contrary to the preparation of standard TLCT SBA-15, when the materials were exposed to hydrothermal treatment, no difference in samples treated at slightly different pH was observed in the outcome; therefore, the acidity does not play a critical role for this purpose, presumably due to the hydrothermal step that involves the use of a high amount of neutral water ($H_2O/H^+:H_2O_{HT}$ = 2 g:100 g). TLCT SBA-15 was exposed to aging temperatures ranging from 80 to 150 °C for 24 hours and 7 days, in order to observe the extent of pore expansion over different temperatures and times.

Comparing the results of hydrothermally treated materials (HT-TLCT SBA-15) to the non-aged TLCT SBA-15 (sample **1**), the d_{100} diffraction peaks in the low-angle XRD patterns shift towards lower angles by increasing both temperature and time, indicating that heat is causing pore spacing increment (**Figure 3.10**).

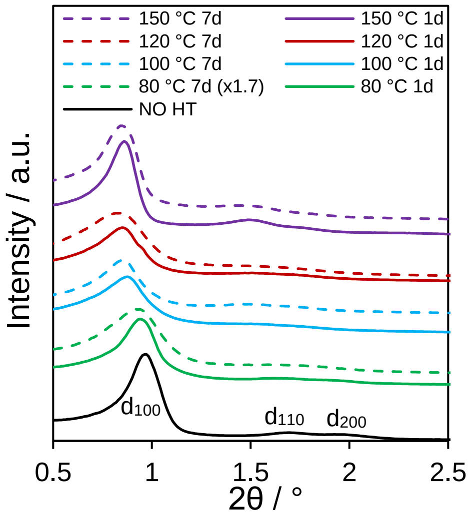

Figure 3.10: Low-angle XRD patterns of HT-TLCT SBA-15 at 80, 100, 120 and 150 °C for 1 (solid line) and 7 d (dashed line), compared to the untreated one (sample **1**), (offset for clarity).

This fact is further confirmed by nitrogen physisorption porosimetry (**Figure 3.11**).

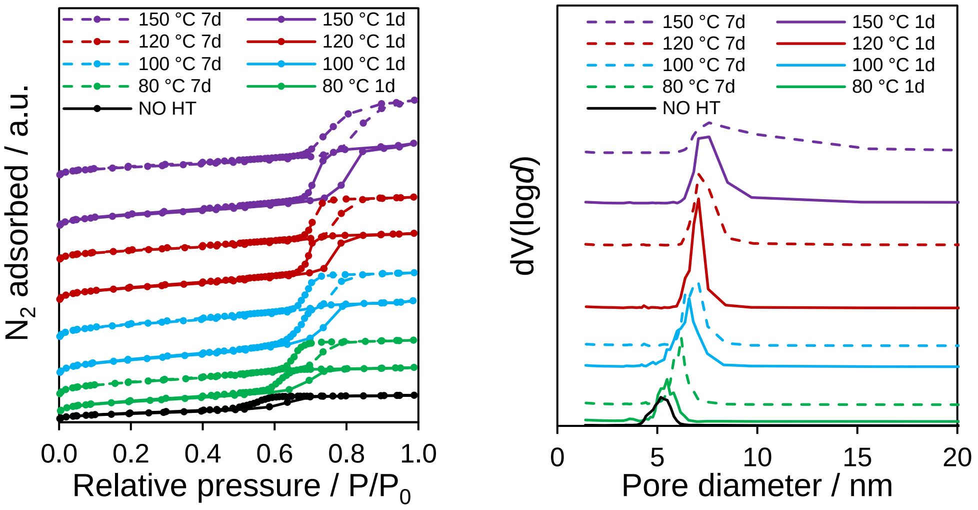

Figure 3.11: N_2 porosimetry of HT-TLCT SBA-15 at 80, 100, 120 and 150 °C for 1 (solid line) and 7 d (dashed line), compared to the untreated one (sample **1**), (left, isotherms; right, PSD), (offset for clarity).

Adsorption-desorption isotherms shifted gradually in the direction of higher relative pressures and their height increased as well, indicating an enlargement in pore width and pore volume, which has also been reported by Celer and Jaroniec [11] as an indication of successful application of hydrothermal treatment.

It is noticeable how pore size distribution curves become wider, reflecting a smaller pore size uniformity at higher temperatures and when longer times are employed (**Figure 3.11**, right). Materials treated at 150 °C showed a more extensive range of pore diameter ranging roughly from 5 to 15 nm in case of 7 days treatment, whereas when treated up to 120 °C the pore diameter was confined to narrower values. The steep step and narrow hysteresis loops in the adsorption/desorption branches evidence retention of the cylindrical and parallel pore channels.

The properties of all HT-TLCT SBA-15 materials are shown in **Table 3.2**, where pore spacing, pore diameter and pore wall thickness trends are compared.

HT-TLCT SBA-15	***a* / nm**		**PD / nm**		**PWT / nm**		**PV / cm^3 g^{-1}**	
NO HT (Sample **1**)	10.5		5.2		5.3		0.7	
T / °C	***1 d***	***7 d***	***1 d***	***7 d***	***1 d***	***7 d***	***1 d***	***7 d***
80	10.8	11.0	5.5	6.2	5.3	4.8	1.0	1.1
100	11.6	11.9	6.3	7.0	5.3	4.9	1.2	1.3
120	11.9	12.2	6.8	7.1	5.1	5.1	1.4	1.3
150	13	13.9	7.1	7.6	5.4	6.3	2.6	1.5

Table 3.2: Comparison of *a*, PD, PWT and PV of TLCT SBA-15 with and without HT, (*a* = pore spacing, PD = pore diameter, PWT = pore wall thickness, PV = pore volume).

Pore wall thickness was determined from the difference between pore spacing (calculated from low-angle XRD) and pore size (calculated from nitrogen porosimetry). Compared to the untreated material (sample **1**), pore wall thickness remained constant when the temperature was applied for one day. This means that pore spacing and pore diameter increase to the same extent so that their difference is constant. When the aging step was protracted to seven days, pore walls tended to shrink at 80 and 100 °C. At 120 °C, it remained constant compared to sample **1**, and at 150 °C grew thicker. The fact that pore wall thicknesses remained constant when the aging was applied for one day indicates that these materials possess hydrothermal stability, a highly desired feature for supports. When the treatment was extended to seven days, in contrast, the pore wall thickness changed with temperature, indicating a decreased hydrothermal stability. As Zhao stated in 1998, higher temperatures or longer reaction times result in larger pore sizes and thinner silica walls. [1] They explained that this behaviour might be a consequence of temperature-dependent hydrophobicity of the PEO block of the copolymer Pluronic P123. Temperature provokes an increase of hydrophobicity of the PEO blocks through their dehydration. [26] This leads to an increase in the total hydrophobic domain volumes that contributes to pore size enlargement. This concept has been previously examined in Chapter 1 (section 1.2.2. Pore-expanded SBA-15). As from **Table 3.2**, when the hydrothermal treatment lasts seven days, two phenomena are occurring at the same time at lower temperatures: pore diameter's increment is more significant than pore spacing's increment in relation to sample **1**, therefore pore wall thickness result thinner (**Figure 3.12**). However, at 150 ˚C the situation is reversed: pore diameter increment is smaller than pore spacing increment for 7 days treatment, consequently pore wall thickness will be thicker.

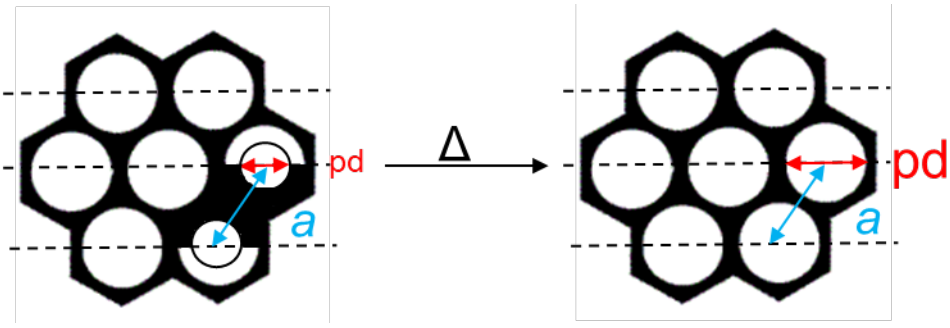

Figure 3.12: PD increment when pore spacing does not increase as much, leads to thinner PWT (black space), (*a* = pore spacing, PD = pore diameter, PWT = pore wall thickness, Δ = heat).

Rationalising how pore spacing and pore diameter change when hydrothermal treatment is applied to the material helps understand their structural properties and decide which treatment allows decent pore expansion that, at the same time, does not ruin the fundamental characteristics of the support.

Also, surface and micropore area's trends of the HT-TLCT SBA-15 materials were rationalised, and are gathered in **Table 3.3**.

HT-TLCT SBA-15	**SA / m^2 g^{-1}**		**MA / m^2 g^{-1}**		**Net SA / m^2 g^{-1} (mesopores)**	
NO HT (Sample **1**)	466 ± 47		0		466 ± 47	
T / °C	***1 d***	***7 d***	***1 d***	***7 d***	***1 d***	***7 d***
80	805 ± 80	905 ± 90	203 ± 20	284 ± 28	602 ± 60	621 ± 62
100	876 ± 88	866 ± 87	142 ± 14	173 ± 17	734 ± 73	693 ± 69
120	895 ± 89	622 ± 62	168 ± 17	104 ± 10	727 ± 73	518 ± 52
150	1200 ± 120	542 ± 54	165 ± 16	88 ± 9	1035 ± 103	454 ± 45

Table 3.3: Comparison of SA, MA and net SA of TLCT SBA-15 with and without HT, (SA = BET surface area, MA = micropore area).

It is important to notice that surface area, a key morphological feature of supports, showed opposite trends for the materials aged for 1 and 7 days. In the first case, the surface area increased while micropore area decreased, meaning an overall increment of the net surface area of mesopores. On the other hand, when the aging step was extended to one week, both surface area and micropore area decreased. Although microporosity appeared in the materials aged at 80 ˚C, then it decreased in both short and longer treatment times as the temperature was raised. This phenomenon is explained with the effect of high temperature and long treatment time that contribute to closing the micropores. [17] As previously explained, microporosity stems from the penetration of the hydrophilic PEO tails of the surfactant in the silica framework. [9] Higher temperature renders the PEO chains more hydrophobic; consequently, they tend to retract from the silica walls, and therefore the microporosity is diminished due to less penetration of PEO inside the walls. [9, 26] In both CO-OP SA and TLCT preparation routes, the hydrothermal treatment step is applied when the surfactant is still present; thus, the temperature minimises the microporosity in both cases.

In order to prepare a support with larger surface area, a highly desirable characteristic for supports employed in heterogeneous catalysis, from **Table 3.3,** it is clear that a shorter treatment is more effective. The high surface area corresponds to more available space to locate active sites during the functionalisation step, which in turn gives rise to smaller nanoparticles and better dispersion, hence higher catalytic activity.

There are some examples in the literature that reported an inverse relationship between temperature applied to the synthesis process and surface area, for CO-OP SA SBA-15 materials. [3, 10, 11] Fulvio explained this effect as a consequence of the increase in pore size. [10] Shen and Kawi reported a study on the hydrothermal stability of MCM-41, [27] unveiled that a 24 hours treatment with boiling water caused a loss of the material's uniform mesoporous structure. Zhang and co-workers, [3] who reported the effect of high-temperature steam (600 °C) on CO-OP SA SBA-15, stated that the decrease in the surface area stems from the collapse of micropores and mesopores on the silica walls. They attributed this effect to the continuous hydrolysis of Si-O-Si bonds according to **Figure 3.13**:

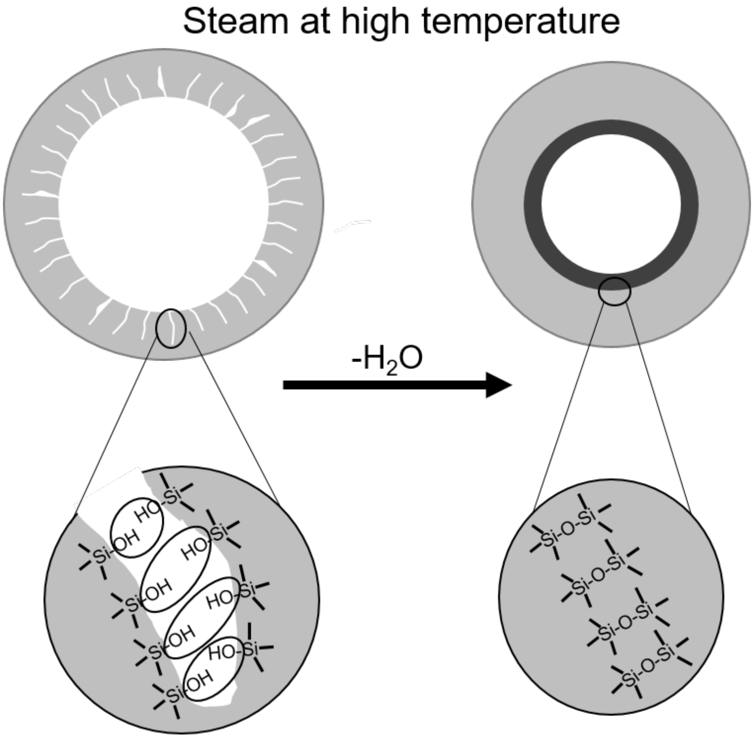

Figure 3.13: Hydrolysis and de-hydrolysis reactions at high temperature can cause recombination of Si-O-Si on CO-OP SA SBA-15 silica walls (adapted from ref. [3]).

In the case of HT-TLCT SBA-15 materials reported in the present thesis, the surface area decrease has been observed only in the case of longer aging times, while for one day the opposite effect could be appreciated. The results related to seven days treatment might be due to a deterioration of the silica framework when the heat is applied for longer times, in accordance with pore diameter distributions getting broader when the treatment is longer, especially at higher temperatures (**Figure 3.11**, right). Therefore, in the case of hydrothermal treatment applied for one week, the mechanism in **Figure 3.13** might be happening, resulting in a decrease in surface area and broader pore size distribution.

All the information regarding pore wall thickness and surface area (**Table 3.2** and **Table 3.3**) lead to the conclusion that a shorter hydrothermal treatment is preferable, as in the former case both pore diameter and surface area increase, while keeping pore wall thickness constant, this being an additional sign that the materials are hydrothermally stable. [28] This signifies that HT-TLCT SBA-15 properties are enhanced when heat is applied for no longer than 24 hours. This behaviour will be highly beneficial at a later stage when the materials are functionalised with active sites and used as catalysts because an improvement in internal diffusion can be achieved due to the successfully applied pore expansion that did not provoke any structural damage.

The extent of the pore expansion described in the current section up to this point was found to be less effective in comparison with the hydrothermally treated CO-OP SA SBA-15. The maximum pore width reported in the scientific literature corresponds to 11.4 nm, for materials heated with a microwave apparatus up to 160 °C for 10 hours. [11] More traditional treatments (not microwave-assisted) were able to swell the mesopores up to 11 nm at 120 °C for 72 hours. [10] The TLCT route did not afford these results as the preparation method, consisting of the use of higher concentration of triblock copolymer P123, led to the formation of a liquid crystal mesophase at the beginning of the synthesis around which the silica condensed. This resulted in the formation of a rigid framework, [6] less prone to micelle expansion when moderately high temperature is applied.

After disclosing the rationale behind the application of hydrothermal treatment to TLCT SBA-15 materials, the reproducibility of this methodology was tested from 80 to 120 ˚C for 24 hours. It was chosen not to raise the temperature to 150 ˚C and to protract the treatment to one week, because pore diameter distribution broadened becoming less uniform and surface area decreased, according to **Figure 3.11** (right) and **Table 3.3**, respectively. Three experiments per each temperature were performed, in order to assess whether a good agreement with the initial attempt (**Figure 3.10** and **Figure 3.11**) could be obtained.

Low-angle XRD showed a good consistency of d_{100} peak for every temperature (**Figure 3.14**): as explained above, the pore spacing shifted towards lower angles as the temperature increased, causing a pore spacing enlargement of 1.1 nm.

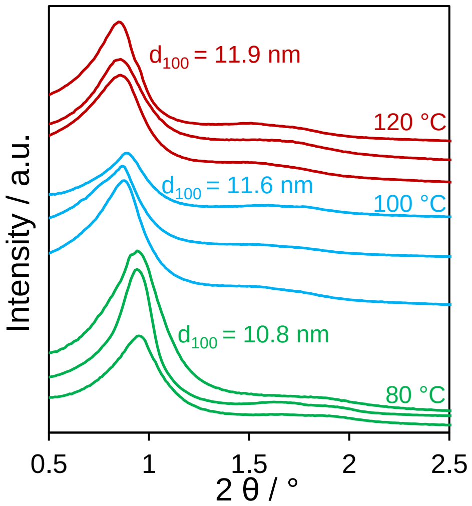

Figure 3.14: Low-angle XRD patterns show good reproducibility of HT-TLCT SBA-15 at 80, 100 and 120 ˚C for 1 d (offset for clarity).

The reproducibility was also tested through nitrogen physisorption porosimetry (**Figure 3.15**).

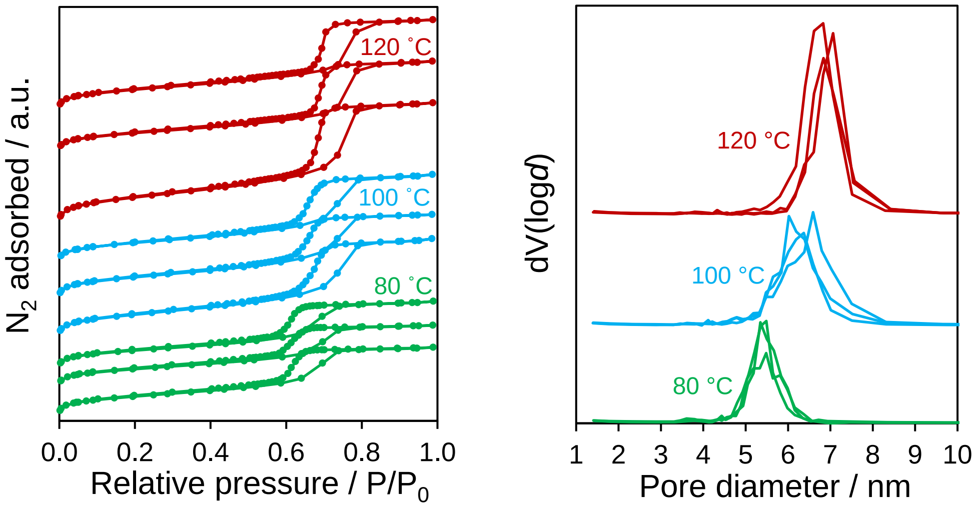

Figure 3.15: N_2 physisorption isotherms and PD show good reproducibility of HT-TLCT SBA-15 at 80, 100 and 120 ˚C for 1 d (offset for clarity).

Every set of isotherms reported in **Figure 3.15** (left) looks alike. The area of the isotherms expanded as the temperature increased, accounting for a surface area expansion. Also, the isotherms shifted towards higher relative pressures reflecting an increase in pore diameter, whose enlargement is mirrored in **Figure 3.15** (right), were shifted towards bigger sizes as the temperature increased.

The properties of these materials were compared to those explained above (**Table 3.2** and **Table 3.3**), and their parameters are shown in **Table 3.4**.

T / °C	*a* / nm	PD / nm	PWT / nm
3 × 80	10.8 ± 0.039 (10.8)	5.4 ± 0.05 (5.5)	5.4 (5.3)
3 × 100	11.6 ± 0.136 (11.6)	6.3 ± 0.3 (6.3)	5.3 (5.3)
3 × 120	11.9 ± 0.000 (11.9)	6.9 ± 0.1 (6.8)	5 (5.1)
T / °C	**SA / m^2 g^{-1}**	**MA / m^2 g^{-1}**	**PV / cm^3 g^{-1}**
3 × 80	805 ± 80 (805 ± 80)	203 ± 20 (203 ± 20)	1.0 (1.0)
3 × 100	876 ± 88 (876 ± 88)	142 ± 14 (142 ± 14)	1.4 (1.2)
3 × 120	895 ± 89 (895 ± 89)	168 ± 17 (168 ± 17)	1.5 (1.4)

Table 3.4: *a*, PD, PWT, SA, MA and PV of triplicates of HT-TLCT SBA-15 at different temperatures. **Table 3.2** and **Table 3.3** in brackets, for comparison. (*a* = pore spacing, PD = pore diameter, PWT = pore wall thickness, SA = BET surface area, MA = micropore area, PV = pore volume).

As shown in **Table 3.4**, all the parameters are in excellent agreement with the initial experiments (**Table 3.2** and **Table 3.3**); therefore it can be concluded that the hydrothermal treatment methodology applied to TLCT SBA-15 is perfectly reproducible.

STEM was performed on HT-TLCT SBA-15 at 120 °C for 24 hours (**Figure 3.16**), and its pore diameter was confirmed by using ImageJ 1.41 software, together with nitrogen physisorption porosimetry (**Table 3.2**).

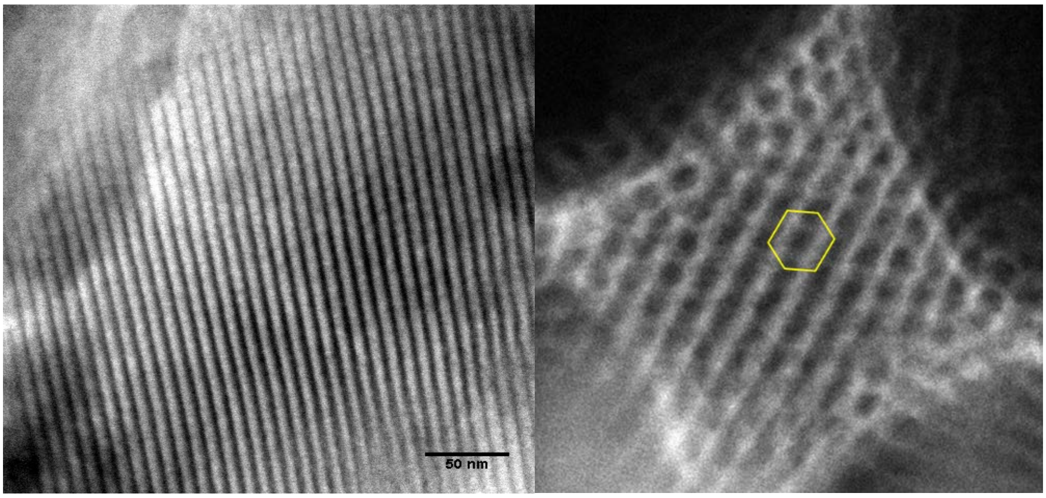

Figure 3.16: STEM images of HT-TLCT SBA-15 (120 °C, 24 h). They show the typical ordered parallel channels (left) and the hexagonal structure (right) of mesoporous silica structures.

As **Figure 3.16** shows, the aging step did not damage the ordered parallel porous channels (left) and the hexagonal structure (right), typical of SBA-15 materials. Overall, it can be concluded that the pore expansion process has had no detrimental effect on silica morphology.

3.1.4. Characterisation of TLCT SBA-15 with swelling agents

Another commonly used methodology to enlarge CO-OP SA SBA-15 mesopores makes use of swelling agents (commonly called porogens). [1, 5, 12-22] An attempt in this regard, employing TLCT SBA-15 support, was also made in this thesis project for the first time.

3.1.4.1. Use of 1,3,5-trimethylbenzene

In literature there are plenty of examples that show that 1,3,5-trimethylbenzene (TMB, **Figure 3.17**), in amounts ranging from 1 to 2 g (from 0.5 to 1 TMB:P123 molar ratio), was able to successfully enlarge CO-OP SA SBA-15 mesopores up to 7.4 or 35 nm, alone [20] or in combination with additives or/and hydrothermal treatment, [1, 5, 18, 19, 21, 29] respectively.

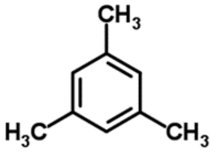

Figure 3.17: 1,3,5-trimethylbenzene (TMB).

The first attempt made in this regard was investigating the effect of TMB alone for the preparation of pore-expanded silica materials with a swelling agent (SA-TLCT SBA-15).

In literature it is claimed that the effect of the porogen, which scales with its amount, is related to its capacity to enter the micelles of Pluronic P123 so that the micellar and the total pore volume are increased. [12] In the present study, amounts of TMB ranging from 0.25 to 2 g were added to the synthesis of TLCT SBA-15, in order to assess the optimal quantity able to expand the pores without ruining the *p6mm* symmetry.

Low-angle XRD diffractograms proved that the addition of up to 1 g of porogen maintained the original framework of the material unaltered, but more than 1 g contributed to its complete collapse (**Figure 3.18**).

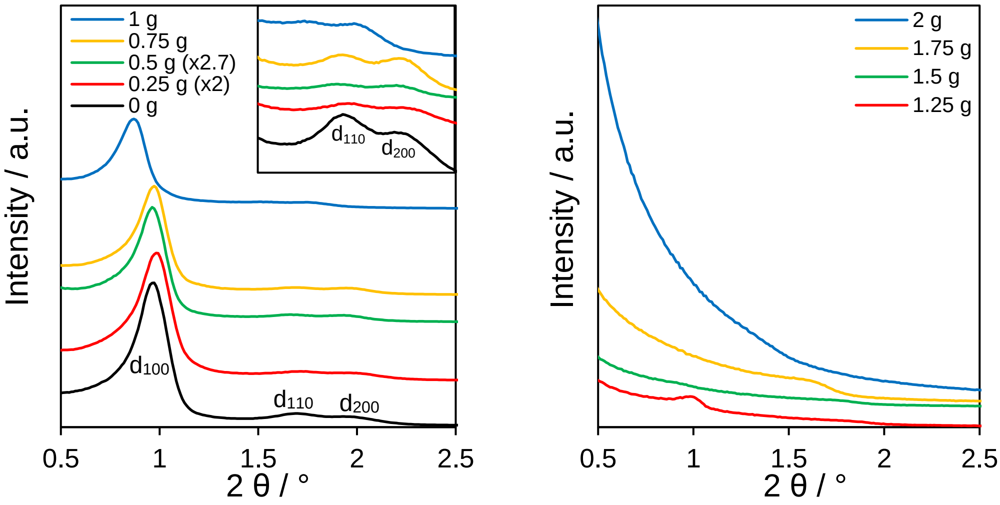

Figure 3.18: Low-angle XRD patterns of SA-TLCT SBA-15 treated with TMB. Amounts between 0.25 and 1 g (left), and above 1 g (right). Inset (left): detail of d_{110} and d_{200} peaks. (Offset for clarity).

When samples were treated with amounts of TMB between 1.25 and 2 g, the diffraction peaks d_{100}, d_{110} and d_{200} gradually disappeared from the diffractograms (**Figure 3.18**, right). Nevertheless, it is still possible to observe the presence of the d_{100} diffraction peak when 1.25 g of TMB is added, which will then disappear in the presence of higher quantities. This is an indication that the structural ordering of the obtained materials decreases as the ratio of TMB/P123 increases. Examining more in-depth **Figure 3.18** (left), together with the confirmation that all the materials possess good long-range order with the characteristic peaks consistent with the *p6mm* hexagonal symmetry, low-angle XRD diffraction shows that by increasing the amount of TMB, d_{100} diffraction peaks shifted towards lower angles. This is associated with an increased *d*-spacing, consistent with the fact that higher amounts of porogen are added to the synthesis of the material, leading to a gradual pore enlargement. The effect of the porogen, which scales with its amount until an optimal value is reached, is related to its capacity to enter the micelles so that the micellar pore volume and total pore volume are increased. [12]

Nitrogen physisorption porosimetry was carried out on the materials treated with 0.25 to 1 g of TMB (**Figure 3.19**, left).

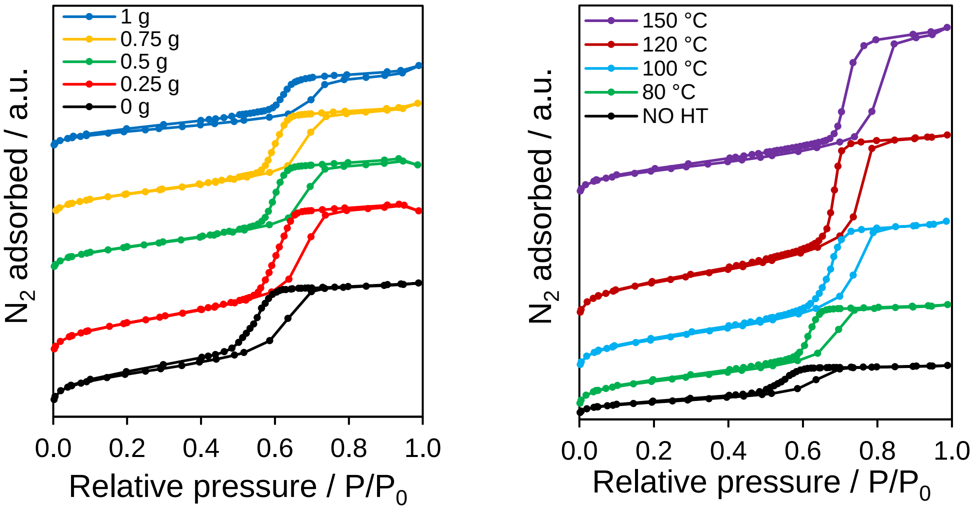

Figure 3.19: N_2 physisorption isotherms of SA-TLCT SBA-15 treated with TMB (left) and of HT-TLCT SBA-15 (24 h, right), (offset for clarity).

A further confirmation that the porogen maintained the mesoporous framework without ruining it, is given by the type IV (H-1 type hysteresis) isotherms in **Figure 3.19** (left). It is noticeable that two changes are occurring at the same time along with the series of isotherms: on one side, relative pressures slightly move towards higher values when an increasing amount of TMB, indicating a certain increase of mesopore size. On the other side, the hysteresis becomes smaller as porogen concentration increases, mirroring a reduction in surface area. This may be due to structural deterioration of the materials, evidently caused by a minimal amount of TMB. The isotherm's shape varies when a change in the surface area occurs. **Figure 3.19** compares the isotherms of SA-TLCT SBA-15 treated with TMB (left) with those relative to materials treated with heat (right, discussed in section 3.1.3, Characterisation of TLCT SBA-15 with hydrothermal treatment). In this way, it is easier to appreciate the effect of two distinct pore expansion treatments on surface area parameter. In the case of hydrothermally treated materials, it is possible to see a strong isotherm expansion in conjunction with a rise in temperature. When TMB is used for pore expansion, it is appreciable an opposite behaviour: compared to the untreated sample, the isotherms progressively shrink with the amount of TMB, indicating a decrease in surface area.

In **Figure 3.20** (left), the change in pore diameter achieved with TMB is monitored and compared to that obtained with hydrothermal treatment (right).

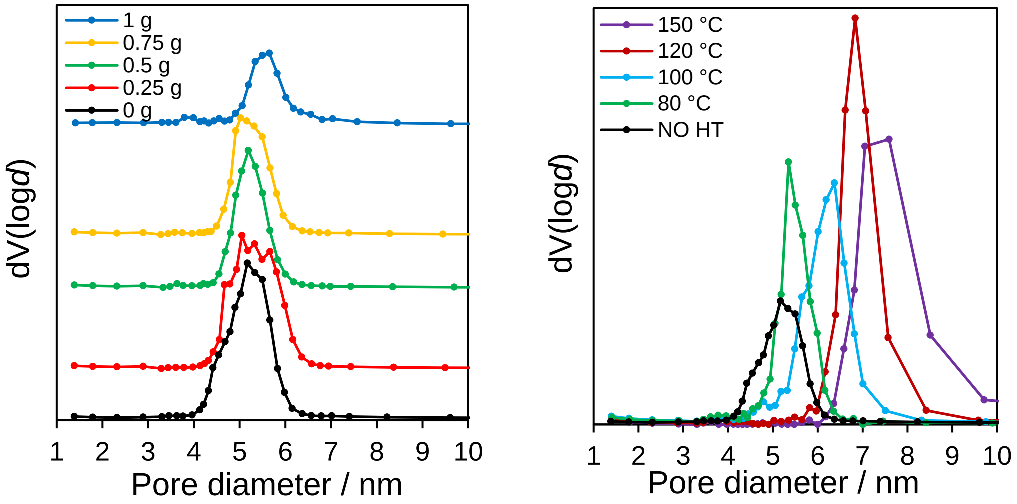

Figure 3.20: PD of SA-TLCT SBA-15 treated with TMB (left). PD of HT-TLCT SBA-15 (24 h, right), (offset for clarity).

When comparing the extent of pore enlargement obtained with TMB and heat, it is clear that the former did not have as much effect as the hydrothermal treatment methodology, in which case the pore size distributions shifted more strongly towards higher pore diameters.

Pore spacing, pore diameter and pore wall thickness obtained for SA-TLCT SBA-15 treated with 0 to 1 g of TMB are summarised in **Table 3.5**.

TMB / g	***a* / nm**	**PD / nm**	**PWT / nm**
0 (Sample **1**)	10.5	5.2	5.3
0.25	10.4	5.0	5.4
0.5	10.6	5.2	5.4
0.75	10.5	5.0	5.5
1	11.7	5.6	6.1

Table 3.5: Comparison of *a*, PD and PWT trends of SA-TLCT SBA-15 treated with 0-1 g of TMB, (*a* = pore spacing, PD = pore diameter, PWT = pore wall thickness).

It is appreciable how the presence of 1 g (TMB: P123 = 0.5) of TMB resulted in a pore spacing enlargement of about 1.2 nm and a pore diameter increase of about 0.4 nm when compared to the untreated sample. These results look negligible when compared to those obtained with the hydrothermal methodology. Compared to the untreated material, a pore spacing expansion up to 3.4 nm and a pore diameter expansion up to 2.4 nm were obtained when 150 ˚C aging for seven days was applied (**Table 3.2**).

Table 3.6 shows the surface area and micropore area trends for materials treated with TMB ranging from 0 to 1 g, and it is possible to appreciate what was explained previously for **Figure 3.19**.

TMB / g	**SA / m^2 g^{-1}**	**MA / m^2 g^{-1}**
0 (Sample **1**)	466 ± 47	0
0.25	408 ± 41	30 ± 3
0.5	299 ± 30	12 ± 1
0.75	295 ± 29	19 ± 2
1	192 ± 19	8 ± 1

Table 3.6: Comparison of SA and MA of SA-TLCT SBA-15 treated with TMB, (SA = BET surface area, MA = micropore area).

The fact that both surface and micropore area decreased proportionally with TMB amount shows that this porogen by itself does not represent a valid methodology for pore diameter expansion. However, it might be of interest to combine TMB with a different pore expansion method, as well as trying a different swelling agent.

3.1.4.2. Combination of TMB and hydrothermal treatment

As anticipated in section 3.1.4.1 (Use of 1,3,5-trimethylbenzene), several literature examples reported the combination of TMB as micelle expander together with a hydrothermal treatment up to 130 ˚C or additives (i.e. $ZrOCl_2 \cdot 8H_2O$), to achieve a more efficient swelling effect. [1, 5, 18, 19, 21, 29]

As observed in the previous section, since the use of TMB did not expand the pore diameter as successfully as hydrothermal treatment did, an attempt to combine both techniques has been made, to see if the porogen produced any additional improvement to the previous methodology. Therefore, 1 g of TMB was added to the synthesis of SA-TLCT SBA-15, as explained in Chapter 2, section 2.2.4. (Synthesis of pore expanded TLCT SBA-15 mesoporous silica with swelling agents), and then the material underwent hydrothermal treatment at 100, 120 and 150 ˚C for 24 hours, to afford hydrothermally treated materials in combination with TMB (HT/SA TLCT SBA-15).

Figure 3.21 shows low-angle X-ray diffraction patterns of the materials prepared with this procedure, and it is clear that, compared to the untreated sample **1**, they have lost the typical long-range order that characterises TLCT SBA-15. In fact, d_{110} and d_{200} peaks are not as well defined as those in the reference sample.

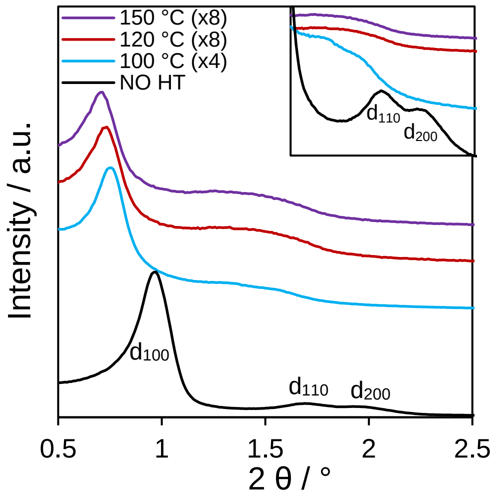

Figure 3.21: Low-angle XRD patterns of HT/SA-TLCT SBA-15 treated with 1 g of TMB and HT at 100, 120 and 150 ˚C for 24 h, compared to sample **1**. Inset: detail of d_{100} and d_{200} peaks. (Offset for clarity).

From **Figure 3.21** it is also possible to notice that the d_{100} peaks of the treated samples has lost intensity, and had to be manually improved by multiplying it by a factor of 4 or 8, to make it comparable to sample **1**'s pattern.

On the other hand, the aid of 1 g of TMB to hydrothermal treatment helped pore spacing and pore diameter to improve even more (**Table 3.7**).

HT	***a* / nm**		**PD / nm**		**PWT / nm**	
NO HT (Sample **1**)	10.5		5.2		5.3	
T / °C	***w/o TMB***	***w/ TMB***	***w/o TMB***	***w/ TMB***	***w/o TMB***	***w/ TMB***
100	11.6	13.5	6.3	6.8	5.3	6.7
120	11.9	13.9	6.8	7.0	5.1	6.9
150	13	14.2	7.1	8.5	5.4	5.7

Table 3.7: Comparison of *a*, PD and PWT of HT-TLCT and HT/SA-TLCT SBA-15 (1 d treatment) with and without 1 g of TMB, (*a* = pore spacing, PD = pore diameter, PWT = pore wall thickness).

Nitrogen physisorption porosimetry highlights how the combination of swelling agent and hydrothermal treatment caused a strong deformation of type IV isotherms and pore size distributions of the mesoporous silica materials (**Figure 3.22**).

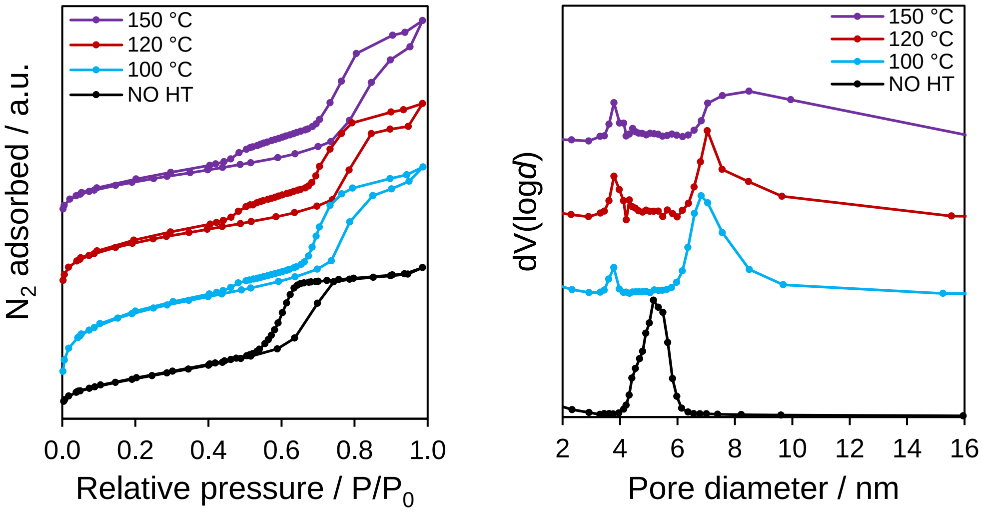

Figure 3.22: Comparison of N_2 physisorption isotherms (left) and PSD (right) of untreated TLCT SBA-15 (sample **1**) and HT/SA-TLCT SBA-15 treated with TMB (offset for clarity).

Compared to sample **1** (untreated), the adsorption-desorption isotherms of the treated materials were strongly affected by the combination of heat and TMB, proportionally with the temperature of the treatment. This effect is visible by the presence of a bulge in the desorption branch at P/P_0 = 0.5-0.7 in the isotherms of each treated sample (**Figure 3.22**, left).

When pores of different sizes are present in the material, pore network effects become involved, and PSD derived from the desorption branch is strongly affected. This results in the appearance of a forced hysteresis loop in the desorption branch around $P/P_0 \approx 0.5$ (for N_2 at 77 K), producing a bulge. This is the consequence of forced closure of the branch, due to a sudden drop in the volume adsorbed along the desorption branch. This phenomenon is referred to as Tensile Strength Effect (TSE), [30, 31], which leads to extra contributions in the adsorption-desorption isotherms, and therefore has an impact in pore size determination. From a thermodynamic point of view, it is more favourable to derive PSD from the desorption branch, because it accounts for the contribution of TSE, and therefore will give a more cautious and precise estimation of the PSD of the material. [30] The hysteresis loop is observed for reasonably large pores as these show capillary condensation and evaporation at different values of P/P_0. However, pores with diameters smaller than 4 nm show no hysteresis and are completely filled and emptied at similar pressures, resulting in a reversible adsorption and desorption isotherm. [32] Consequently, when the nitrogen isotherms show a step-wise desorption branch, presence of bimodal porosity is suggested. [30, 33] On the other hand, the adsorption branch shows only one step representing all the sizes of mesopores with different shapes or diameters. The step-wise desorption isotherm is due to the fact that the encapsulated mesopores empty at a lower pressure than the open pores of similar size. In addition, the isotherms of the treated samples in **Figure 3.22** (left) show that the adsorption and desorption branches do not reach closure at P/P_0 = 0.8-1.0, corresponding to the upper closure point, differently from the untreated sample.

The TSE is mirrored in **Figure 3.22** (right), where pore size distributions clearly lost their uniformity proportionally with temperature, even though an improvement in pore diameter of a portion of mesopores is observed, it indicates that, nonetheless, the hydrothermal treatment has the desired pore enlargement effect. The presence of two peaks in the pore size distribution curves, one of which is located in the pore width range below 4 nm, reflects what has been previously explained in relation to **Figure 3.22** (left). In fact, the peak located below 4 nm indicates the presence of small complementary pores (**Figure 3.23**), while the second one represents the ordered mesopores. [23]

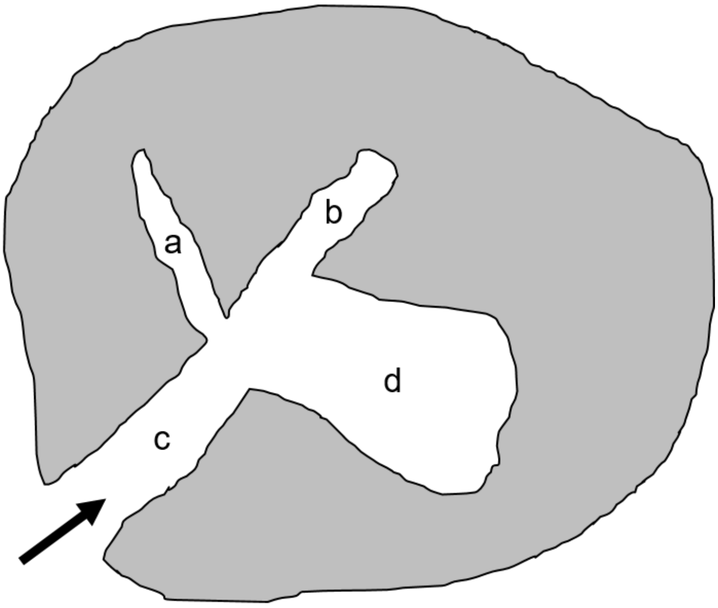

Figure 3.23: Pore network effects in adsorption-desorption measurements by interconnected small (a, b), intermediate (c) and large (d) pores (adapted from ref. [30]).

When the presence of complementary pores is developed during the treatment, it means that a structure shrinkage is occurring and consequently, the material suffers from thermal instability. [11] When this phenomenon occurs, a situation similar to that represented in **Figure 3.23** might be developed in the porous architecture.

As observed in section 3.1.3 (Characterisation of TLCT SBA-15 with hydrothermal treatment, **Figure 3.11**, right), also in this case (**Figure 3.22**, right) at 150 ˚C pore size distribution becomes broader in comparison with lower temperatures: this is further evidence that 150 ˚C is not suitable for a uniform pore enlargement.

Table 3.8 shows a correlation between surface area, micropore area and pore volume of the silica materials treated with heat and with TMB and heat together, compared to those relative to the untreated sample.

TMB / g	**SA / m^2 g^{-1}**		**MA / m^2 g^{-1}**		**PV / cm^3 g^{-1}**	
0 (Sample **1**)	466 ± 47		0		0.7	
T / °C	***w/o TMB***	***w/ TMB***	***w/o TMB***	***w/ TMB***	***w/o TMB***	***w/ TMB***
100	876 ± 88	1194 ± 119	142 ± 14	672 ± 67	1.5	1.1
120	895 ± 89	738 ± 74	168 ± 17	291 ± 29	1.4	1.0
150	1200 ± 120	514 ± 51	165 ± 16	101 ± 10	2.6	1.0

Table 3.8: SA, MA and PV of HT-TLCT and HT/SA-TLCT SBA-15 with 1 g TBM and 1-day HT, compared to those relative to the untreated sample, (SA = BET surface area, MA = micropore area, PV = pore volume).

All trends in **Table 3.8** point out that HT/SA-TLCT SBA-15 materials display an increase in surface area exclusively caused by addition of microporosity. As the total BET surface area calculated with nitrogen porosimetry is a combination of meso- and microporosity, the net surface area (only relative to mesoporosity) is rationalised in **Table 3.9**.

TMB / g	**Net SA / m^2 g^{-1}**	
0 (Sample **1**)	466 ± 47	
T / °C	***w/o TMB***	***w/ TMB***
100	734 ± 73	522 ± 52
120	727 ± 73	447± 45
150	1035 ± 103	413 ± 41

Table 3.9: Net SA of HT/SA-TLCT and HT-TLCT SBA-15 materials treated with heat and with TMB and heat (1 d treatment), compared to the untreated sample, (SA = BET surface area).

All hydrothermally treated samples have gained a good amount of mesoporous surface area with respect to the untreated TLCT SBA-15, whereas those treated with TMB before the hydrothermal step show either very little gain (100 °C) or a drop in mesoporous surface area. This deleterious effect caused by the combination of TMB and heat in terms of surface area, together with loss of long-range order and pore diameter uniformity, clearly shows that this methodology cannot be applied to the TLCT synthetic route, despite it being successful for the conventional CO-OP SA methodology. [1, 5, 18, 29] The different preparation of the two procedures, as anticipated in

Chapter 1 (section 1.2.1. Synthetic routes to SBA-15), reflects in major structural dissimilarities that do not lead to comparable results.

As surface area, pore diameter and structural long-range order are key parameters for supports in heterogeneous catalysis, this procedure has been discarded.

3.1.4.3. Use of Heptane

Over the past two decades, different linear alkanes have been successfully used for the pore expansion of CO-OP SA SBA-15. [12-17, 22] According to Nagarajan, [16] the uptake of linear alkanes by micelles of Pluronic P123 is rather small, and increases as the alkane chain decreases. This behaviour has been supported by Sun [14] and Zhang, [15] who reported a *d*-spacing and pore size increase when the chain length of the hydrocarbon decreased from decane to pentane. The experiments reported for CO-OP SA SBA-15 showed a maximum pore expansion of 24 nm. [23]

Among the alkanes proposed as suitable micelle expanders, it has been decided to employ heptane (**Figure 3.24**, Heptane: P123 = 8.5: 2 g (235 molar ratio) [17]) in the current thesis, to evaluate if its pore swelling effect could be better than that of TMB or hydrothermal treatment.

Figure 3.24: Heptane.

Low-angle XRD diffractogram of SA-TLCT SBA-15 treated with heptane is compared to the untreated material as a benchmark (sample **1**) and is illustrated in **Figure 3.25**.

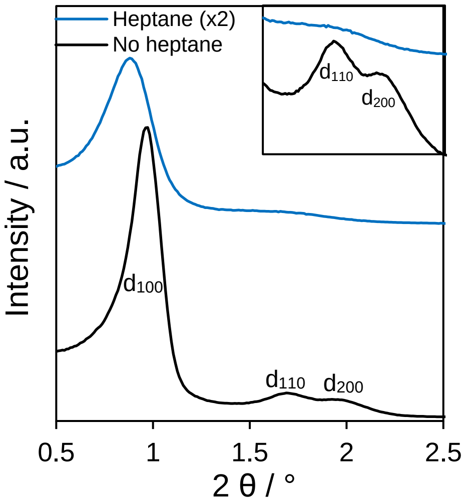

Figure 3.25: Comparison of low-angle XRD patterns of SA-TLCT SBA-15 treated with heptane and untreated sample **1**. Inset: detail of d_{110} and d_{200} peaks. (Offset for clarity).

The comparison of the two diffractograms emphasises the lack of long-range order of the treated material, which lacks the d_{110} and d_{200} reflections, well visible in sample **1** instead. Besides, the heptane-treated SA-TLCT SBA-15 pattern significantly lost intensity if compared to the untreated sample. This is due to the loss of long-range order of the silica structure consequent to the introduction of the alkane. On the other hand, the d_{100} peak of the treated material shifted to a lower angle, reflecting an increase in *d*-spacing.

Although XRD seemed to prove a successful pore expansion in terms of pore spacing, despite showing loss of *p6mm* symmetry, nitrogen physisorption porosimetry (**Figure 3.26**) revealed a pore shrinkage of a portion of mesopores.

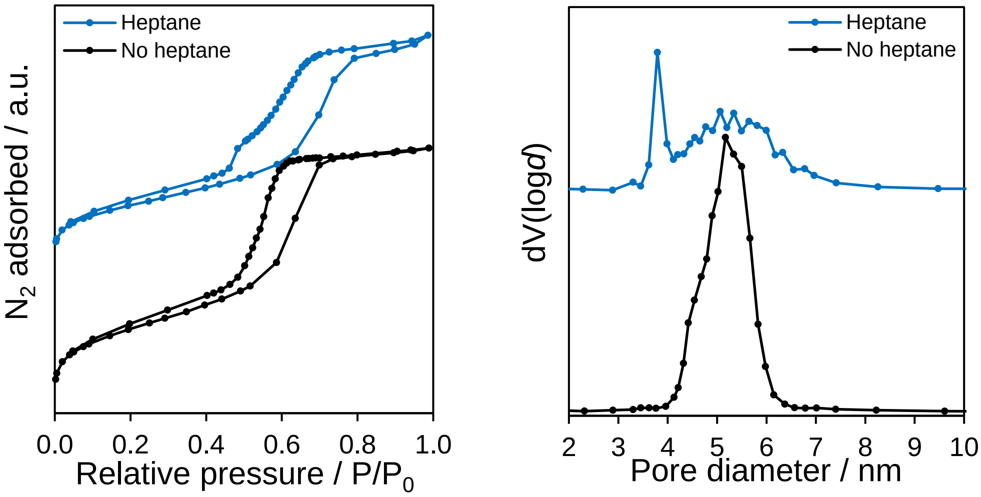

Figure 3.26: Comparison of N_2 physisorption isotherms (left) and PSD (right) of untreated TLCT SBA-15 (sample **1**) and SA-TLCT SBA-15 treated with heptane (offset for clarity).

Adsorption-desorption isotherm (**Figure 3.26**, left) of the treated material reveals that heptane had a significant influence on its shape. This is evidenced by the bulge in the desorption branch at $P/P_0 = 0.5$, that reflects the presence of a percentage of mesopores under 4 nm size, according to the explanation reported in section 3.1.4.2 (Combination of TMB and hydrothermal treatment). [30, 31] The presence of bimodal porosity, which implies interconnected pores of different sizes (3.8 and 5.3 nm – **Figure 3.26**, right), also leads to a loss of surface area.

Table 3.10 summarises the key parameters (pore spacing, pore diameter, surface area) of the mesoporous silica materials prepared in the sections dedicated to pore expansion methodologies (sections 3.1.3, Characterisation of TLCT SBA-15 with hydrothermal treatment and 3.1.4, Characterisation of TLCT SBA-15 with swelling agents).

Pore expansion method	***a* / nm**	**PD / nm**	**SA / m^2 g^{-1}**
No treatment (Sample **1**)	10.5	5.2	466 ± 47
HT-TLCT 80°C (24 h) HT-TLCT 100°C (24 h) HT-TLCT 120°C (24 h) HT-TLCT 150°C (24 h)	10.8 11.6 11.9 13	5.5 6.3 6.8 7.1	805 ± 80 876 ± 88 895 ± 89 1200 ± 120
SA-TLCT TMB (1 g)	11.7	5.6	192 ± 19
SA-TLCT Heptane (8.5 g)	11.6	3.8	286 ± 29

Table 3.10: Comparison of a, PD and SA of pore-expanded TLCT SBA-15 materials obtained with different methodologies, (*a* = pore spacing, PD = pore diameter, SA = BET surface area).

From **Table 3.10** it is possible to appreciate the effect of any pore expansion methodology used on TLCT SBA-15 materials. The hydrothermal treatment has clearly been the most effective methodology when applied for 24 hours as pore spacing, pore diameter and surface area increased at the same time with temperature, preventing the structure from collapse or loss of long-range order. The use of swelling agents (TMB and heptane) caused a strong surface area shrinkage, as a consequence of porogen molecules inserting in the silica framework. Temperature, on the other hand, produced a surface area and pore diameter expansion as it provoked higher hydrophobicity of the whole micelle domain. However, when the hydrothermal treatment was combined with TMB, the ordered mesoporous structure suffered from the insertion of additional porosity, which contributed to a loss of pore size uniformity and surface area. Therefore, in order to prepare a support that lays the foundation for the synthesis of a valuable catalyst, an increase in surface area and maintenance of narrow pore size distribution together with long-range ordered silica framework is critical.

In conclusion, after screening different pore swelling methodologies, it has been decided to adopt only the one that makes use of heat (applied for 24 hours) for the preparation of macro-meso TLCT SBA-15 supports, which will be described further on the course of this chapter.

3.1.5. Characterisation of larger batches of mesoporous silica materials

In addition, larger batches of mesoporous silica materials were synthesised, to be compared to the 2 g of Pluronic P123 batches presented over the previous sections, with the aim of exploring the possibility to scale-up this synthesis methodology to the industry volumes. However, the materials prepared at a certain scale will not always be successfully upsized; therefore, it is important to find the optimal conditions that allow the reproduction of a material on a larger scale without compromising its fundamental properties.

3.1.5.1. Characterisation of larger batches of TLCT SBA-15 materials

Two attempts for increasing the scale of TLCT SBA-15 were made, using 5 and 10 g of Pluronic P123 (the whole synthesis was then adapted to the new amounts).

Figure 3.27 shows the stacked low-angle XRD diffractograms of TLCT SBA-15 for the 5 and 10 g batches, compared to the benchmark material prepared with 2 g of Pluronic P123 (sample **1**).

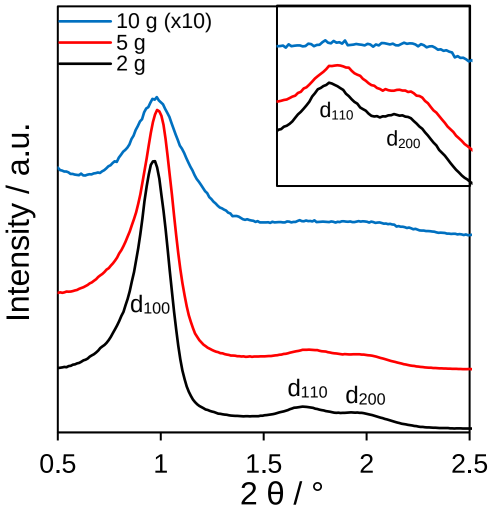

Figure 3.27: Low-angle XRD patterns of 5 and 10 g TLCT SBA-15 batches, compared to the 2 g benchmark material (sample **1**). Inset: detail of d_{100} and d_{200} peaks. (Offset for clarity).

The 5 g TLCT SBA-15 batch shows that the *p6mm* symmetry has been well retained, which is confirmed by the presence of defined (100), (110) and (200) reflections. On the contrary, the 10 g batch is missing the d_{110} and d_{200} peaks, symptomatic of a loss of long-range order. From the d_{100} peaks in the figure above, it is possible to appreciate the retention of the *d*-spacing.

Nitrogen physisorption porosimetry, represented in **Figure 3.28**, depicts an oscillation of the larger-batch materials' pore diameter, compared to the original TLCT SBA-15.

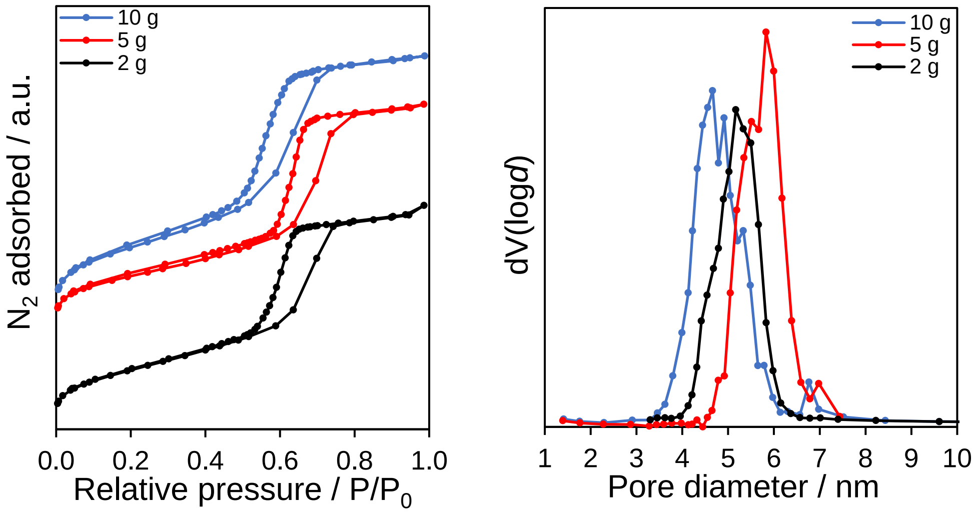

Figure 3.28: N_2 physisorption porosimetry of 5 and 10 g TLCT SBA-15 batches, compared to the 2 g benchmark material (sample **1**). Adsorption-desorption isotherms (left) and PSD (right), (offset for clarity).

In fact, it is noticeable that the adsorption-desorption isotherm (**Figure 3.28**, left) relative to the 10 g batch shifts towards lower relative pressures, indicating a decrease in pore diameter. Although the 5 and 10 g batch materials show a small fluctuation of the pore size, the pore size distributions remained as narrow as that relative to the 2 g material, meaning that the increase of Pluronic P123 amount did not affect the micelles dimension and the silica framework formation around them.

When comparing pore spacing, pore diameter, pore wall thickness and pore volume (**Table 3.11**), the larger batch materials showed a slight fluctuation of pore diameter and, consequently, of pore wall thickness.

Batch size / g	***a* / nm**	**PD / nm**	**PWT / nm**
2 (Sample **1**)	10.5	5.2	5.3
5	10.4	5.8	4.6
10	10.4	4.7	5.6

Table 3.11: Comparison of *a*, PD and PWT of the larger batch samples, compared to the 2 g material (sample **1**), (*a* = pore spacing, PD = pore diameter, PWT = pore wall thickness).

Also, comparing surface and micropore areas (**Table 3.12**), the 10 g batch showed a strong increase in surface area.

Batch size / g	**PV / cm^3 g^{-1}**	**SA / m^2 g^{-1}**	**MA / m^2 g^{-1}**
2 (Sample **1**)	0.7	466 ± 47	0 ± 0
5	0.8	457 ± 46	24 ± 2
10	0.9	641 ± 64	18 ± 2

Table 3.12: Comparison of PV, SA and MA of the larger batch samples, compared to the 2 g material (sample **1**), (PV = pore volume, SA = BET surface area, MA = micropore area).

Increasing the size of the batch led to the formation of a small portion of micropores inside the mesoporous network. Even though the micropore area remained constant for both 5 and 10 g scaled-up materials, the surface area of the latter increased by almost 200 m^2 g^{-1}.

Table 3.11 and **Table 3.12** unveiled how increasing the batch size to 5 g allowed to retain the material's properties, whereas up to 10 g resulted in a complete loss of the *p6mm* symmetry and a variation of surface area and pore diameter.

3.1.5.2. Characterisation of larger batches of hydrothermally treated TLCT SBA-15 materials

Also, hydrothermally treated TLCT SBA-15 materials were produced at a larger scale because among the different methodologies attempted, they have been the only successfully pore-expanded materials prepared. The chosen treatment temperatures were 100 and 120 °C because, as seen in Section 3.1.3 (Characterisation of TLCT SBA-15 with hydrothermal treatment), 80 °C had a small expansion effect on the material when applied for 24 hours.

Shown below are low-angle XRD patterns of the hydrothermally treated materials for to 5 g and 10 g (**Figure 3.29**), compared to their untreated counterparts.

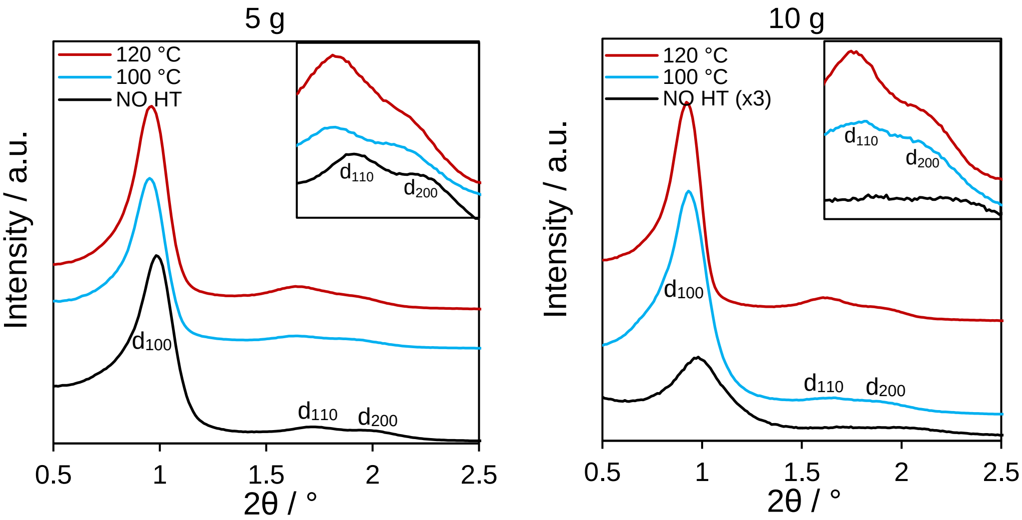

Figure 3.29: Low-angle XRD patterns of 5 g (left) and 10 g (right) HT-TLCT SBA-15 batches, treated at 100 and 120 °C materials compared to the scaled-up untreated samples. Inset: detail of d_{110} and d_{200} peaks. (Offset for clarity).

The patterns shown above confirm that both scaled-up samples were successfully affected by temperature even though not to a great extent, as the *d*-spacing moves towards lower angles, indicating a slight pore spacing increment. At the same time, the ordered periodic mesostructure was retained, as the (110) and (200) reflections in the inset show.

Table 3.13 shows pore spacing, pore diameter (obtained from nitrogen porosimetry) and pore wall thickness of the 5 g batch hydrothermally treated materials, compared to the 5 g batch untreated.

HT / °C	***a* / nm**	**PD / nm**	**PWT / nm**
NO HT	10.4	5.8	4.6
100	10.7	5.3	5.4
120	10.6	5.7	4.9

Table 3.13: Comparison of *a*, PD and PWT of 5 g batch HT-materials, compared to the untreated one, (*a* = pore spacing, PD = pore diameter, PWT = pore wall thickness).

The hydrothermal treatment of the 5 g HT-TLCT SBA-15 batch caused a very small pore spacing increment and no pore diameter enlargement.

Figure 3.30 shows nitrogen physisorption porosimetry of the hydrothermally treated 5 g batch, compared to the untreated 5 g batch sample.

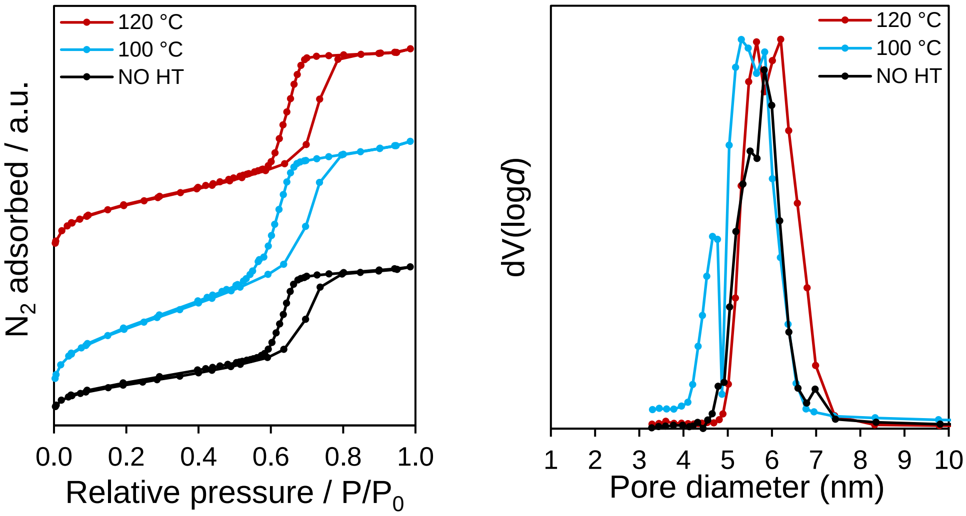

Figure 3.30: N_2 physisorption porosimetry of the 5 g HT-TLCT SBA-15 batch compared to the untreated 5 g batch material (left, adsorption-desorption isotherms; right, PSD), (offset for clarity).

It is possible to appreciate that pore diameters of the hydrothermally treated samples were not successfully enlarged, as anticipated in **Table 3.13**. On the other hand, isotherms in **Figure 3.30** (left) show that by raising temperature the adsorption-desorption isotherms expanded, indicating that, especially the sample treated at 100 °C, underwent an increase in surface area as well as in pore volume, as shown in **Table 3.14**.

HT / °C	PV / cm^3 g^{-1}	SA / m^2 g^{-1}	MA / m^2 g^{-1}
NO HT	0.8	457 ± 46	24 ± 2
100	1.2	1077 ± 108	191 ± 20
120	1.0	838 ± 84	264 ± 26

Table 3.14: Comparison of PV, SA and MA of 5 g batch HT-materials, compared to the 5 g batch untreated one, (PV = pore volume, SA = BET surface area, MA = micropore area).

As for the 10 g hydrothermally treated batch, **Figure 3.29** (right) showed a bigger pore spacing increment, which is mirrored in **Table 3.15**. Compared to the 5 g batch whose pore spacing increment is negligible, with the 10 g samples it is possible to obtain 0.8 nm increase at 120 °C, with a concomitant increase in pore diameter (obtained from nitrogen porosimetry) and retention of pore wall thickness.

HT / °C	*a* / nm	PD / nm	PWT / nm
NO HT	10.3	4.7	5.6
100	10.8	5.2	5.6
120	11.1	5.8	5.3

Table 3.15: Comparison of *a*, PD and PWT of 10 g batch HT-materials, compared to the 10 g batch untreated one, (*a* = pore spacing, PD = pore diameter, PWT = pore wall thickness).

Nitrogen physisorption porosimetry shows adsorption-desorption isotherms and pore diameter distributions of 10 g batch hydrothermally treated samples, compared to the untreated one (**Figure 3.31**).

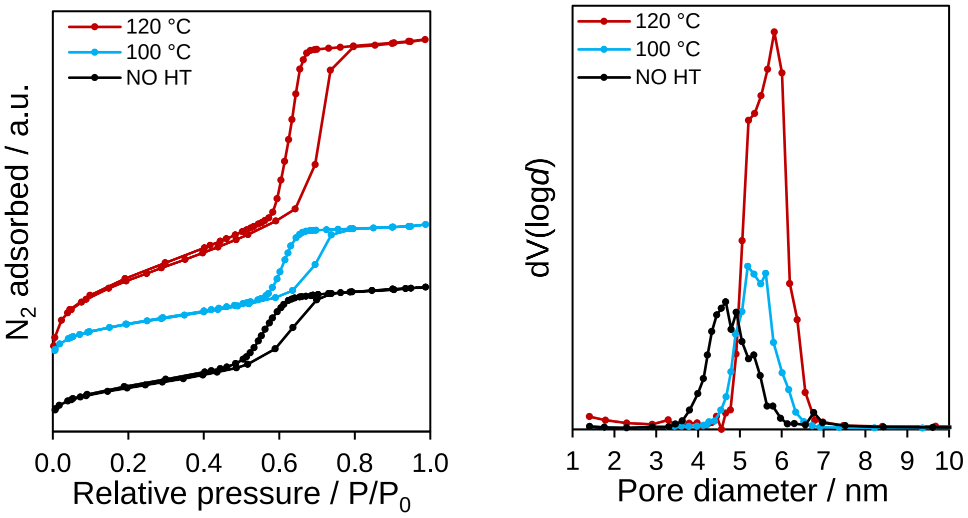

Figure 3.31: N_2 physisorption porosimetry of the 10 g batch HT-TLCT SBA-15 compared to the 10 g batch untreated material (left, adsorption-desorption isotherms; right, PSD), (offset for clarity).

Contrary to 5 g hydrothermally treated batch, the surface area gradually increased with temperature, as well as the micropore area. In this case, in contrast to what has been previously observed for TLCT SBA-15 standard batches (2 g), increasing the temperature did not promote the withdrawal of Pluronic P123's PEO chains towards the hydrophobic domain of the micelle, impeding microporosity reduction (**Table 3.16**).

HT / °C	PV / cm^3 g^{-1}	SA / m^2 g^{-1}	MA / m^2 g^{-1}
NO HT	0.9	641 ± 64	18 ± 2
100	0.8	841 ± 84	290 ± 29
120	2.2	1669 ± 167	401 ± 40

Table 3.16: Comparison of PV, SA and MA of 10 g batch HT-materials, compared to the untreated one, (PV = pore volume, SA = BET surface area, MA = micropore area).

The results shown in the table above are symptomatic of a poorer control over the silica morphology during the synthesis of hydrothermally treated 10 g scaled-up materials.

To sum up, the results obtained after hydrothermally treating the 5 and 10 g batch HT-TLCT SBA-15 materials, it was not possible to achieve a significant improvement in terms of pore diameter, which in the first case was not successfully expanded, whereas in the second case it showed a slight improvement of 1.1 nm. On the other hand, a surface area improvement was promoted with temperature, as it occurred when 2 g batches were aged.

As the results of the current section were not satisfactory in terms of pore enlargement and retention of long-range order compared to those reported for CO-OP SA SBA-15 (for which a successful synthesis was obtained with batch sizes up to 27 g), [23] it was decided not to continue the investigation of material synthesis on a larger scale.

3.2. Characterisation of macro-mesoporous silica supports

Adding macropores (> 50 nm) to a mesoporous network is another strategy for improving the diffusion limitations that large molecules experience in restricted structures. In the following sections, the characterisation of macro-mesoporous TLCT SBA-15 (*MM*-TLCT SBA-15) will be described, together with the implementation of hydrothermal treatment to hierarchical materials, as a further application of this pore enlargement technique. This methodology has never been reported in the scientific literature up to this date.

3.2.1. Characterisation of polystyrene beads

Three different polystyrene (PS) nanosphere sizes were prepared following the procedure illustrated in Chapter 2, section 2.2.5. (Synthesis of polystyrene nanospheres, **Figure 2.1**). As indicated in **Table 3.17**, the nanosphere diameters obtained were 229 ± 26, 354 ± 12 and 426 ± 22 nm with 70, 100 and 100% yield, respectively.

PS size / nm	**Yield / %**
229 ± 26	70
354 ± 12	100
426 ± 22	100

Table 3.17: PS nanosphere dimensions and yields.

The styrene amount needed for the synthesis of polystyrene nanospheres of different sizes increased proportionally with the desired nanosphere diameter, and the agreement between actual and desired size decreased with the volume of monomer required for the synthesis. Three attempts to synthesise polystyrene beads of 600 nm were carried out, and all of them resulted in beads diameter of 400-430 nm. Polystyrene beads of 354 nm exhibited the narrower deviation, indicating that these nanospheres resulted in the most uniform in size if compared to the other two.

The nanospheres size was calculated with Scanning Electron Microscopy (SEM) (**Figure 3.32**), a suitable technique for imaging materials with particles diameter over 50 nm.

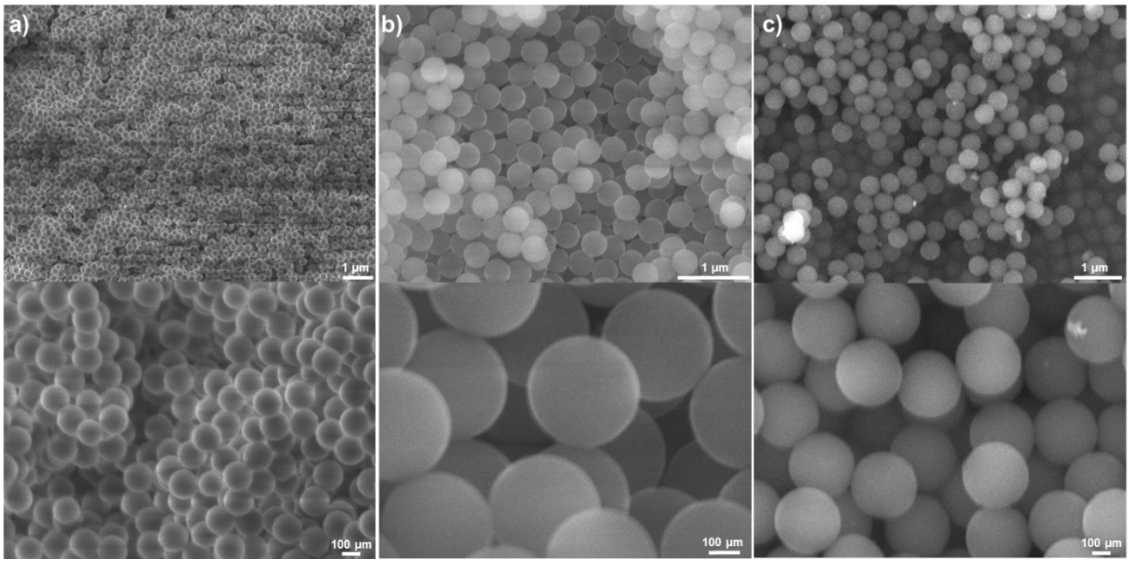

Figure 3.32: SEM images of PS beads with different sizes in two different scales. **a)** 229 ± 26, **b)** 354 ± 12, **c)** 426 ± 22 nm.

The images obtained show spherical particles with a good degree of uniformity.

3.2.2. Characterisation of *MM*-TLCT SBA-15

MM-TLCT SBA-15 materials have been obtained by incorporating polystyrene nanospheres of different diameters (229 ± 26, 354 ± 12, 426 ± 22 nm) in the TLCT SBA-15 mesostructure, affording three hierarchical ordered porous materials.

Figure 3.33 (left) depicts low-angle X-ray diffractograms of the obtained *MM*-TLCT SBA-15, each with a different macropore size.

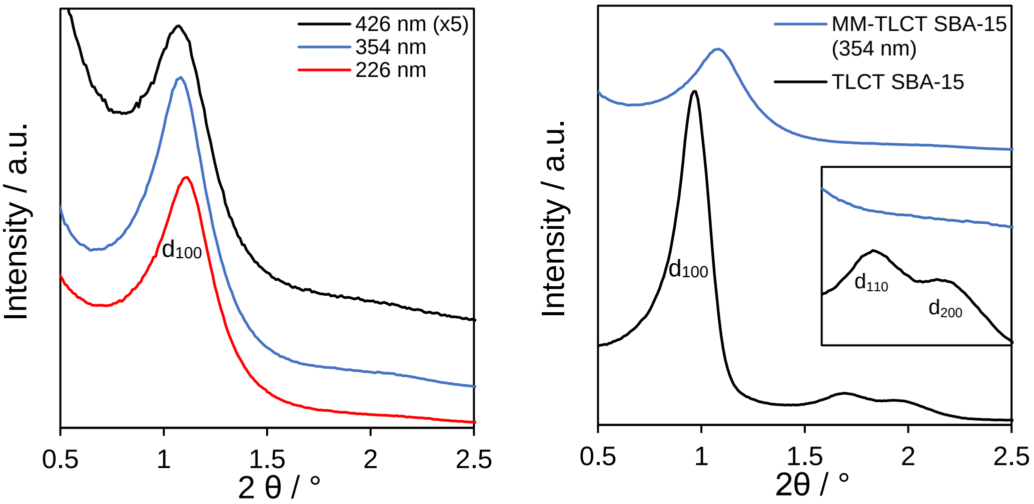

Figure 3.33: Low-angle XRD patterns of *MM*-TLCT SBA-15 materials prepared with different PS nanospheres sizes (226, 354, 426 nm), (left). Comparison of TLCT SBA-15 (sample **1**) and *MM*-TLCT SBA-15 (354 nm) patterns (right). Inset: detail of d_{110} and d_{200} peaks. (Offset for clarity).

Compared to the typical diffractogram representing mesoporous SBA-15 (**Figure 3.33**, right), the hierarchical structures have completely lost the (110) and (200) reflections, indicating that the integrity of the mesoporous structure was affected during the synthesis process, as macropores were incorporated in the silica framework.[34] This is also reflected in their (100) reflection, which presents larger half-width and decreased intensity, compared to their mesoporous counterpart. These elements indicate a lower degree of long-range order, due to the incorporation of macropores, but overall the XRD patterns in **Figure 3.33** (left) indicate the presence of a mesophase, though without any indication of special ordering.

Figure 3.34 shows the effect of the incorporation of polystyrene beads with different sizes into the mesoporous structure of TLCT SBA-15, on adsorption-desorption isotherms and pore size distributions.

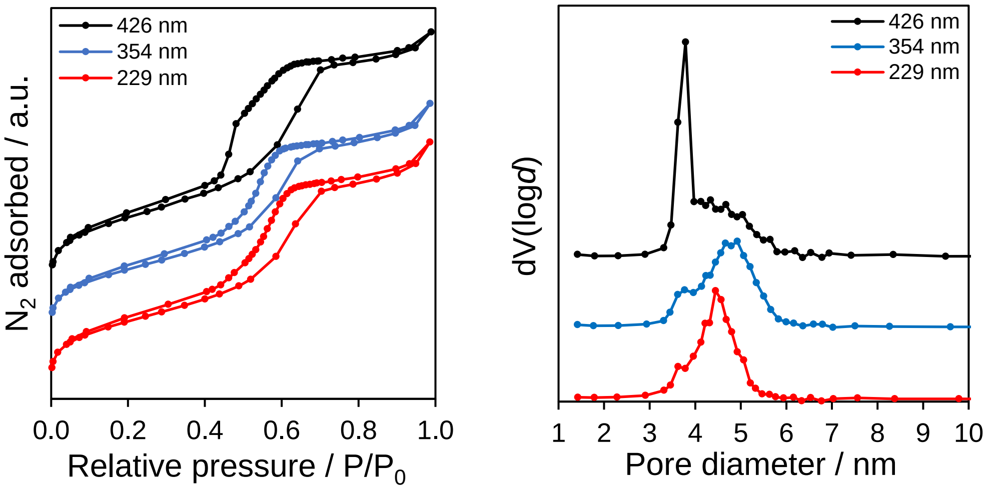

Figure 3.34: N_2 physisorption isotherms (left) and PSD (right) of *MM*-TLCT SBA-15 materials prepared with different PS nanospheres sizes (226, 354, 426 nm), (offset for clarity).

From both isotherms and pore size distributions, it is noticeable that the porous architectures have been affected by the introduction of macropores, more strongly as the polymer nanosphere’s dimension increases. The isotherm related to the biggest macropore size presents a considerable bulge in the desorption branch at $P/P_0 \approx 0.5$, due to the tensile strength effect, [30, 31] as pores of different sizes empty at different pressures and give rise to a step-wise isotherm (section 3.1.4.2, Combination of TMB and hydrothermal treatment). **Figure 3.34** (right) mirrors the bimodal porosity, whereby pore size distributions lost their uniformity proportionally with increasing macropore size. While the materials prepared with 229 and 354 nm polystyrene nanospheres still present the majority of the pores with a diameter of 4-5 nm, the one prepared with 426 nm size results in an almost complete shrinkage of the mesopores to less than 4 nm. The loss of pore size uniformity is reflected in the shape of the isotherms (**Figure 3.34**, left), whose step in the adsorption-desorption branches is not as steep as in the case of the previously presented TLCT SBA-15. These observations lead to the conclusion that including a different porosity to the *MM*-TLCT SBA-15 system entails a loss of mesoporous uniformity, which escalates with macroporosity size. Repetition of *MM*-TLCT SBA-15 with PS = 426 nm confirmed that the largest template nanospheres are not suitable to obtain macro-mesoporous supports with narrow and uniform pore size distribution (**Figure 3.35**).

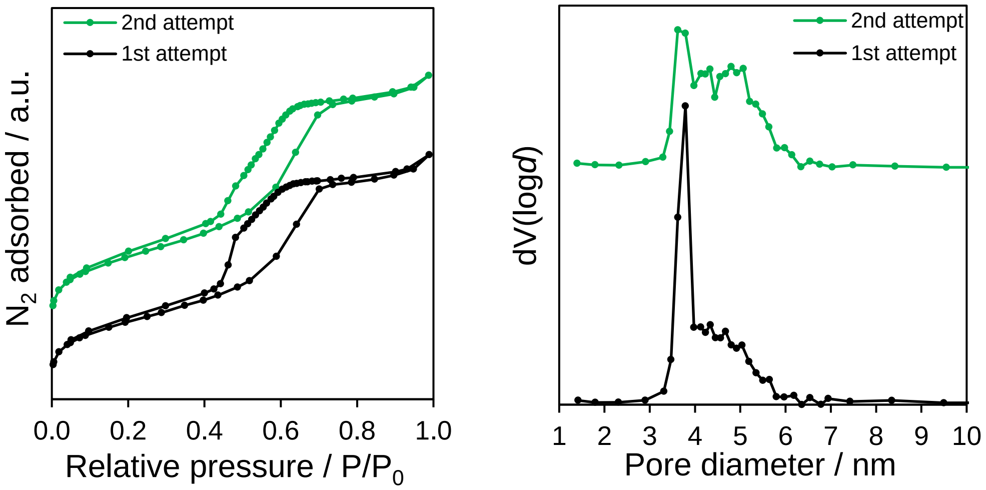

Figure 3.35: N_2 physisorption isotherms (left) and PSD (right) of *MM*-TLCT SBA-15 materials prepared twice with 426 nm PS nanospheres size (offset for clarity).

The retention of the original mesoporosity (≈ 5 nm) in a macro-meso material is an important feature when this will be employed as a catalyst further on. The aim of introducing an additional porosity to mesoporous supports concerns the improvement of the mass-transport of chemicals inside the pores. In order to be able to make a correct comparison between the catalytic performances of a mesoporous and a macro-mesoporous material, it is important that the latter maintains the mesoporosity of the former, from which it has been prepared. In this regard, **Table 3.18** presents more clearly what **Figure 3.34** (right) showed above.

PS size / nm	**Mesoporosity in TLCT SBA-15 / nm**	**Mesoporosity in *MM*-TLCT SBA-15 / nm**
229 ± 26	4.7	4.4
354 ± 12	4.7	4.7
426 ± 22	4.7	3.8

Table 3.18: Evaluation of the mesoporosity in *MM*-TLCT SBA-15 materials, compared to that of the mesoporous materials they have been prepared from.

Apart from the hierarchical material prepared with intermediate PS size, not only the insertion of the template created a complementary porosity with dimension < 4 nm

(**Figure 3.34**), but also caused a shrinkage of the original mesoporosity, which decreased from 4.7 to 3.8 nm, in the case of polystyrene nanospheres of 426 nm diameter. The reason for this phenomenon will be explained in detail further on, in section 3.2.3 (Characterisation of *MM-TLCT* SBA-15 with hydrothermal treatment).

Surface and micropore area of the prepared hierarchical porous materials are shown in **Table 3.19**.

Support	**PS size / nm**	**SA / m^2 g^{-1}**	**MA / m^2 g^{-1}**
TLCT SBA-15 (Sample **1**)	-	466 ± 47	0
MM-TLCT SBA-15	229 ± 26	401 ± 40	0
MM-TLCT SBA-15	354 ± 12	409 ± 41	0
MM-TLCT SBA-15	426 ± 22	473 ± 47	13 ± 1

Table 3.19: SA and MA of *MM*-TLCT SBA-15 materials prepared with different PS nanospheres sizes, compared to TLCT SBA-15 (sample **1**), (SA = BET surface area, MA = micropore area).

While the mesopore diameter has been affected by the introduction of macroporosity in the silica framework, as it brought on some degree of shrinkage, the total BET surface area has not been much affected, compared to the original mesoporous material. The fact that the surface area has been mostly retained is due to the almost total absence of microporosity. This evidence has been observed before by Sen and co-workers, [35] who proposed a theory that supports the poor microporosity in hierarchical porous materials after calcination. They compared the removal of polystyrene template from the materials by calcination and toluene extraction and reported the presence of microporosity only in the second case. This fact can be explained with the heat-generated melting and burning of the template that inhibits the formation of micropores, whereas it is facilitated by extraction of polystyrene template by toluene. In their study, the aforementioned authors proposed a mechanism for the formation of macrospheres, interconnecting windows and mesopores as pictured in **Figure 3.36**.

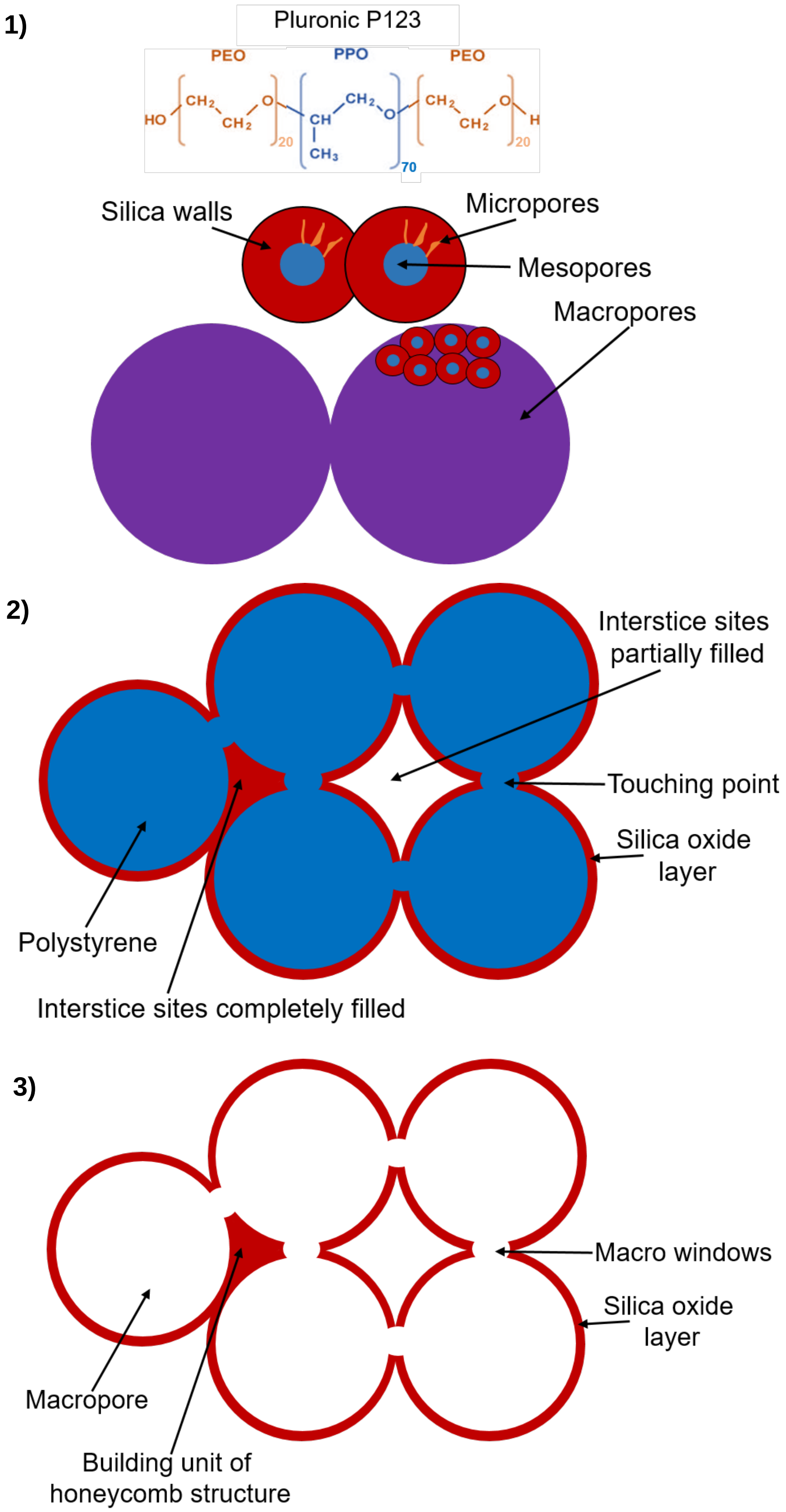

Figure 3.36: Representation of formation of macro- and mesopores in a hierarchical porous material (adapted from ref. [35]).

This visual model describes how mesopores are formed around the macropores during the synthesis of hierarchical porous materials. After the silica precursor has condensed around the P123 Pluronic micelles, it diffuses into the interstitial voids of the polystyrene monoliths (**Figure 3.36**, **1**). This diffusion may be due to the attractive interaction between cationic silicate species (TMOS has previously hydrolysed in acidic medium) with anionic surface charges (SiO^-). The silica-micellar solution then precipitates around the macrospheres of polystyrene (**Figure 3.36**, **2**). Finally, P123 and polystyrene will be removed upon calcination (**Figure 3.36**, **3**).

The macropore diameter of the prepared samples was determined with SEM (**Figure 3.37**), which gave a representation of the long-range order of the macroporous framework.

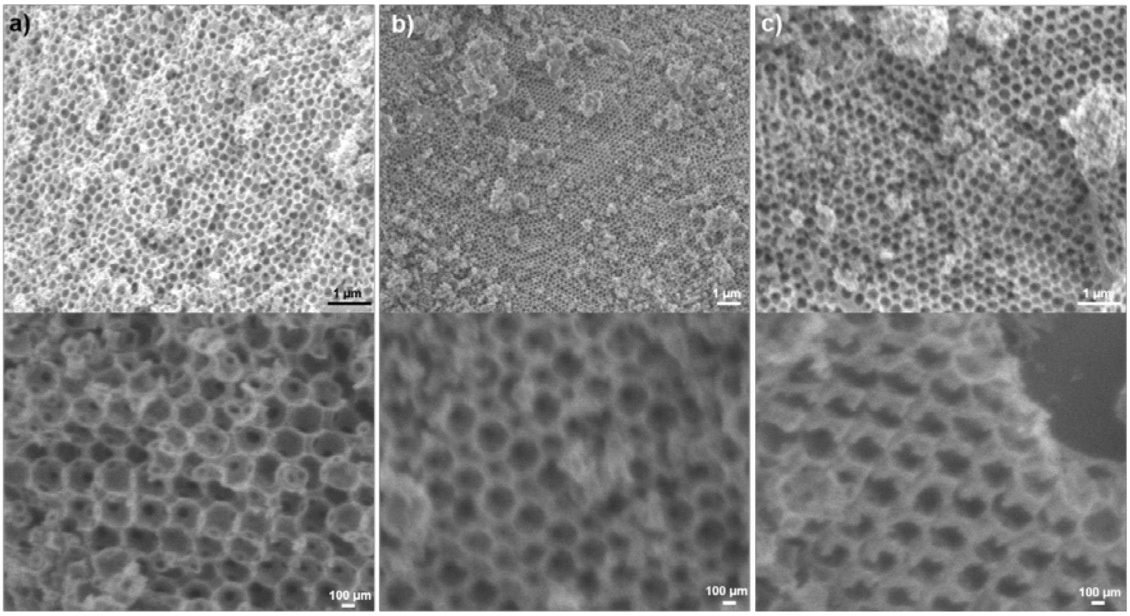

Figure 3.37: SEM images of *MM*-TLCT SBA-15 materials in two different scales, **a)** 229 ± 26, **b)** 354 ± 12, **c)** 426 ± 22 nm.

All samples exhibited a honeycomb structure with a long-range order of porosity. The size of the macrospheres, determined by SEM, is summarised in **Table 3.20**. In all cases, the macropore diameter has shrunk with respect to the polystyrene spheres used as the template. This contraction in macropore size is due to the removal of the polystyrene template by calcination. [35]

PS size / nm	Macropore diameter / nm (SEM)	Macropore shrinkage / nm
229 ± 26	150 ± 10	79
354 ± 12	253 ± 28	101
426 ± 22	290 ± 34	136

Table 3.20: Macropore diameter determined by SEM and assessment of the macropore shrinkage with respect to the original PS size.

From the table above, the fluctuation from the average macropore diameter (± errors) and the macropore shrinkage increase with the diameter of the original template nanospheres. Apparently, the contraction is stronger when the nanosphere template is bigger because more energy is required for its removal from the monolith.

The mesophase and detailed macrostructure of the hierarchical materials were further determined by STEM (**Figure 3.38**).

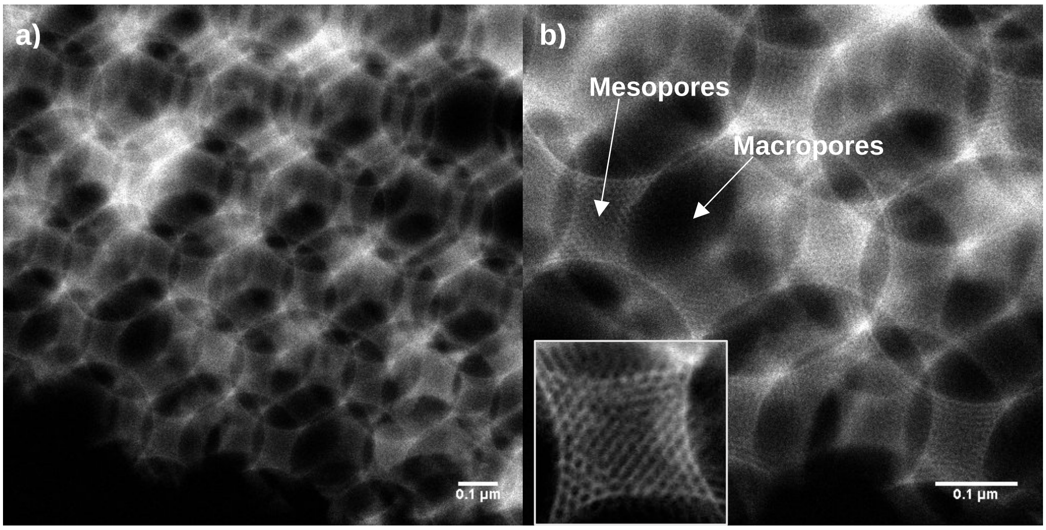

Figure 3.38: Dark field STEM images of *MM*-TLCT SBA-15 (PS size = 354 ± 12 nm). Inset: detail of mesopores.

The STEM images show the presence of both macro- and mesopores arranged in a honeycomb-like structure, both possessing long-range order. Both figures **a)** and **b)** show interconnecting windows related to the two different porosities and are congruent with the pictorial representation proposed by Sen and co-workers in **Figure 3.36**. [35] The inset in picture **b)** shows the mesopores, located in between the macroporous array as for **Figure 3.36**. Their framework has not been ruined by the insertion of macropores.

3.2.3. Characterisation of *MM*-TLCT SBA-15 with hydrothermal treatment

As for TLCT SBA-15, the aim of this project was attempting to expand *MM*-TLCT SBA-15 mesopores, as in literature there is no example of mesopore expanded *MM*-CO-OP SA SBA-15 supports. As it has been extensively explained in sections 3.1.3 (Characterisation of TLCT SBA-15 with hydrothermal treatment) and 3.1.4 (Characterisation of TLCT SBA-15 with swelling agents), the only methodology that allowed a successful pore enlargement in mesoporous TLCT silica materials has been hydrothermal treatment. Therefore, the same procedure has been applied to *MM*-TLCT SBA-15, i.e. 80 to 150 ˚C for 24 hours, affording hydrothermally treated hierarchical structures (HT-*MM*-TLCT SBA-15). The treatment has not been extended to 7 days, as no big difference was observed in longer times for mesoporous HT-TLCT SBA-15.

In Chapter 2, section 2.2.5 (Synthesis of polystyrene nanospheres) and section 3.2.1 (Characterisation of polystyrene beads) it has been reported the synthesis and characterisation of polystyrene beads of different sizes (229 ± 26, 354 ± 12, 426 ± 22 nm), respectively. The previous section reported their incorporation to TLCT SBA-15 to create hierarchical porous materials, while in the current section these materials have undergone hydrothermal treatment (80, 100, 120, 150 ˚C) to attempt mesoporous expansion. The final twelve samples (three macropore diameters per temperature) have been characterised, and the results are explained as follows.

Figure 3.39 depicts low angle X-ray diffraction of the hydrothermally treated (80, 100, 120, 150 ˚C for 24 hours) HT-*MM*-TLCT SBA-15 materials.

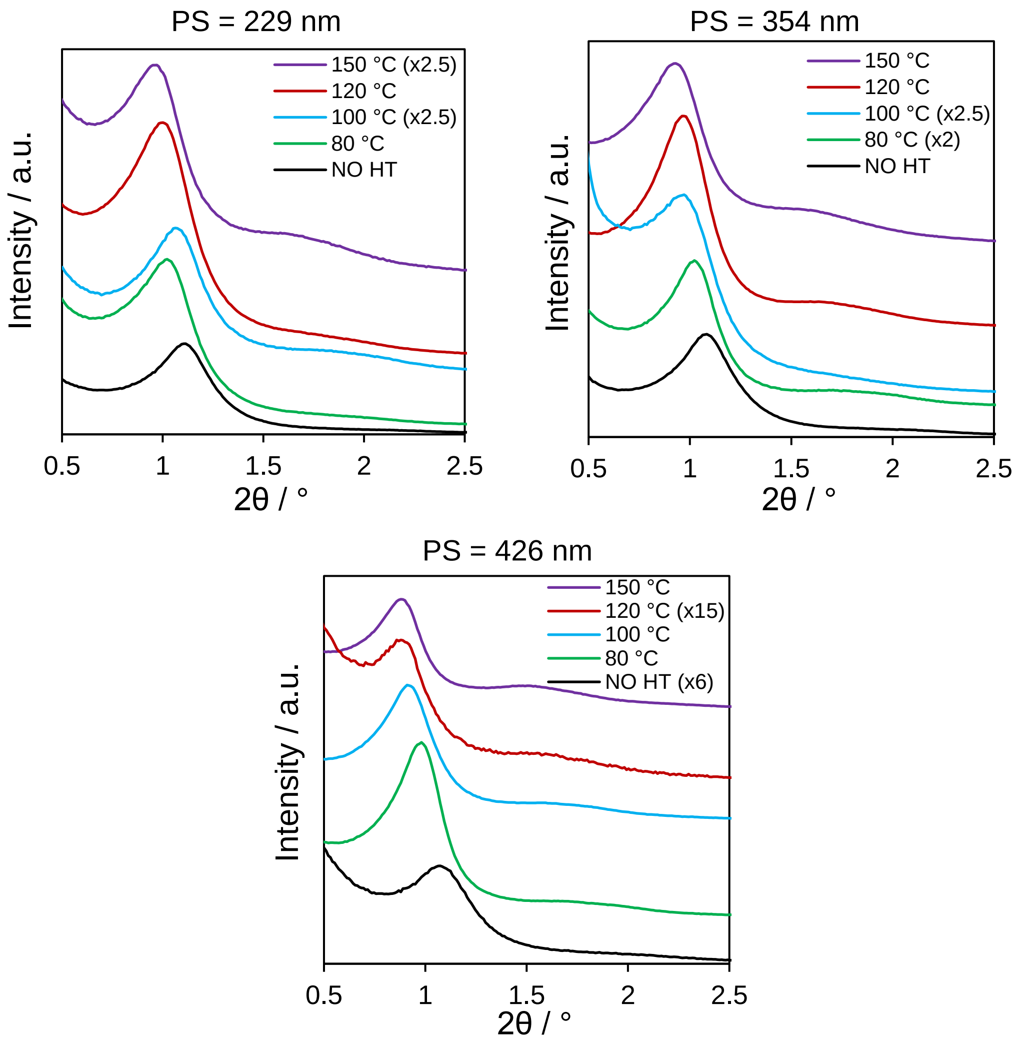

Figure 3.39: Low angle XRD patterns of HT-*MM*-TLCT SBA-15 (80 to 150 ˚C for 24 h), compared to the untreated one (offset for clarity).

As explained in section 3.2.2 (Characterisation of *MM-TLCT* SBA-15), macro-mesoporous silica supports do not present (110) and (200) reflections in their low-angle XRD diffractograms. Besides, the half-width of the d_{100} peak is lower, compared to that relative to mesoporous materials (**Figure 3.33**, right). This indicates that the integrity of the mesoporous structure has been affected by the introduction of macroporosity, and therefore has lost long-range order, typical of silica mesoporous supports. In all graphs in **Figure 3.39**, however, the d_{100} peak shifts towards lower angles, revealing that the hydrothermal treatment is causing the desired enlargement of the mesopores. This methodology is suitable to uniquely swell the mesopores, as macropores have been introduced in the silica framework using the parent polymer (removed later via calcination) and it is bland enough not to alter the macroporosity of the system.

Figure 3.40 shows adsorption-desorption isotherms of the HT-*MM*-TLCT SBA-15 materials.

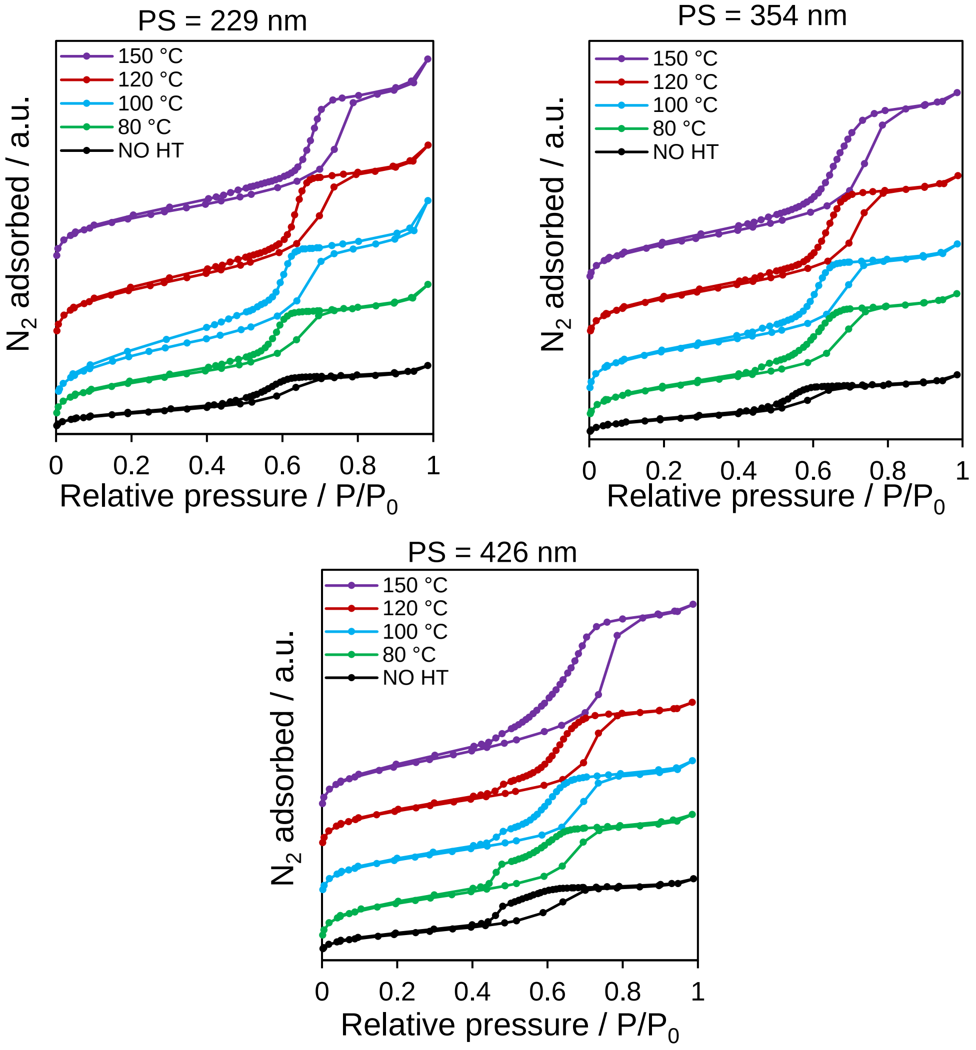

Figure 3.40: N$_2$ physisorption isotherms of HT-*MM*-TLCT SBA-15 (80 to 150 °C for 24 h), compared to the untreated one (offset for clarity).

The isotherms clearly suggest an increase in mesopore size and surface area in all cases, since the hystereses gradually become bigger as the temperature rises from 80 to 150 ˚C. Particularly in the case of PS = 426 nm, it is noticeable the presence of a bulge appearing at $P/P_0 \approx 0.5$ on the desorption branch of each isotherm. This reveals that, as explained in section 3.1.4.2 (Combination of TMB and hydrothermal treatment), the mesoporosity of the materials has lost uniformity and part of the mesopores has shrunk to < 4 nm due to the tensile strength effect (**Figure 3.41**).

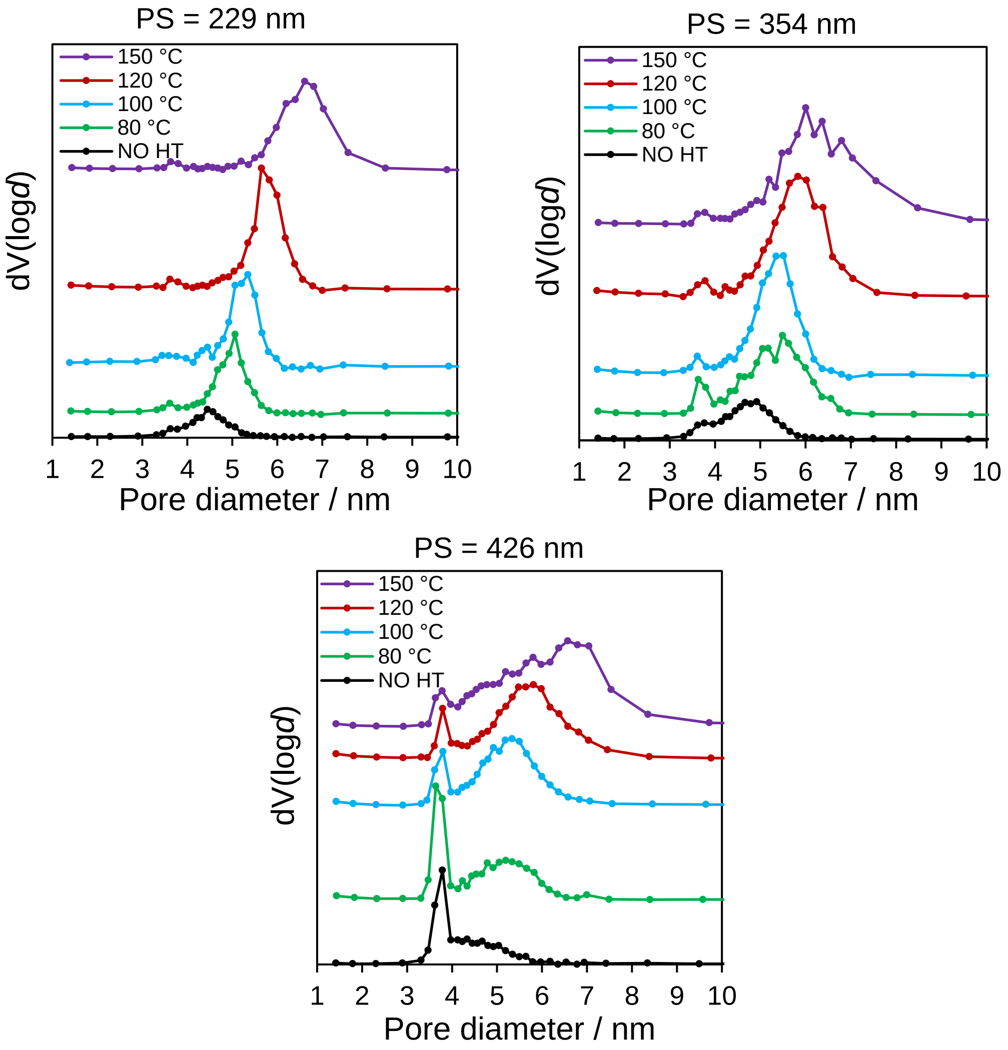

Figure 3.41: PSD of HT-*MM*-TLCT SBA-15 (80 to 150 °C for 24 h), compared to the untreated one (offset for clarity).

From the figure above, it is possible to appreciate that, for each class of polystyrene beads, an expansion in pore diameter has occurred as the temperature rose from 80 to 150 ˚C. This indicates that the hydrothermal treatment has had a successful outcome when applied to hierarchical materials, as in the case of their mesoporous counterparts. On the other hand, as the template nanosphere diameter increases, the pore size curves become wider at any temperature, indicating a broader mesoporous distribution. This is also mirrored in the isotherms depicted in **Figure 3.40**, whose step becomes less steep as the template size increases from 229 to 426 nm. In addition, the bulge present on the nitrogen isotherms is reflected in the secondary peak in each pore size distribution in **Figure 3.41**, which becomes more intense as the template nanosphere size increase.

The preparation of all HT-*MM*-TLCT SBA-15 materials has been carried out twice to verify whether the mesopore shrinkage was a recurring characteristic. Since both syntheses have been reproducible, it can be concluded that the presence of big macropores in the silica framework causes the formation of a complementary porosity with a diameter corresponding to < 4 nm. This phenomenon has been observed earlier in section 3.2.2 (Characterisation of *MM-TLCT* SBA-15); therefore, it is not necessarily associated with the hydrothermal treatment step. Referring to the formation mechanism of hierarchical materials described in **Figure 3.36** the polystyrene template expands (more likely during calcination, during which T = 550 ˚C is applied) provoking a contraction of the red space (mesopores) in between the blue nanospheres (step **2** in **Figure 3.36**). Possibly, while the internal space of the red spots maintains the original pore diameter, the mesopores in direct contact with the nanospheres undergo the pressure from them and accordingly shrink. It is therefore probable that the mesopore shrinkage is a phenomenon that occurs as a consequence of a set of factors, namely macropores insertion, calcination and hydrothermal treatment, or of the first two.

Overall, the hydrothermal treatment applied to hierarchical materials consisted of a maximum enlargement of mesopore diameter up to 6.6 nm with a concomitant loss of uniformity in pore size distribution, together with some degree of mesoporosity shrinkage, both factors becoming more severe as the polystyrene template nanosphere size increased.

The extent of mesopore swelling conducted on hierarchical materials has been compared to that carried out on mesoporous silicas described in section 3.1.3 (Characterisation of TLCT SBA-15 with hydrothermal treatment), to assess whether the presence of an additional porosity represented an obstacle to the successful mesoporous expansion by means of temperature. In **Table 3.21,** surface and micropore area of the hydrothermally treated macro-mesoporous materials are also shown.

Mesopores / nm (w/o PS)	HT / °C (24 h)	PS beads / nm	Mesopores / nm	SA / m^2 g^{-1}	MA / m^2 g^{-1}
5.5	80	229 ± 26	5.1	796	199
		354 ± 12	5.5	788	250
		426 ± 22	5.2	781	265
6.3	100	229 ± 26	5.3	1182	336
		354 ± 12	5.3	984	372
		426 ± 22	5.3	770	272
6.8	120	229 ± 26	5.6	1093	278
		354 ± 12	5.8	906	226
		426 ± 22	6.0	751	239
7.1	150	229 ± 26	6.6	915	212
		354 ± 12	6.0	803	94
		426 ± 22	6.6	798	106

Table 3.21: Comparison of mesopore diameter of HT-TLCT SBA-15 and HT-*MM*-TLCT SBA-15 materials, and SA and MA of the hierarchical materials, (SA = BET surface area, MA = micropore area).

Table 3.21 brings attention to how the mesopore enlargement of HT-*MM*-TLCT SBA-15 materials have been slightly restricted by the presence of macroporosity, which rendered the silica structure more rigid and less prone to hydrothermal modification. Nonetheless, as depicted in **Figure 3.41**, the pore size distributions underwent a certain degree of expansion. Contrary to the non-hydrothermally treated hierarchical porous materials (**Table 3.19**), those described in the table above showed an increase in surface area, partly due to the development of microporosity. However, the growth in surface area when temperature was applied to the synthesis route has been previously observed for the hydrothermally treated mesoporous silicas (**Table 3.3**); hence the current pore enlargement methodology is able to not only expand the pore diameter but also has the capability to increase the surface area of the materials considered. Both these characteristics are of critical importance for the preparation of a functionalised material in the field of catalysis.

To assess the order of the macroporous framework, SEM was conducted on the hydrothermally treated materials (**Figure 3.42**).

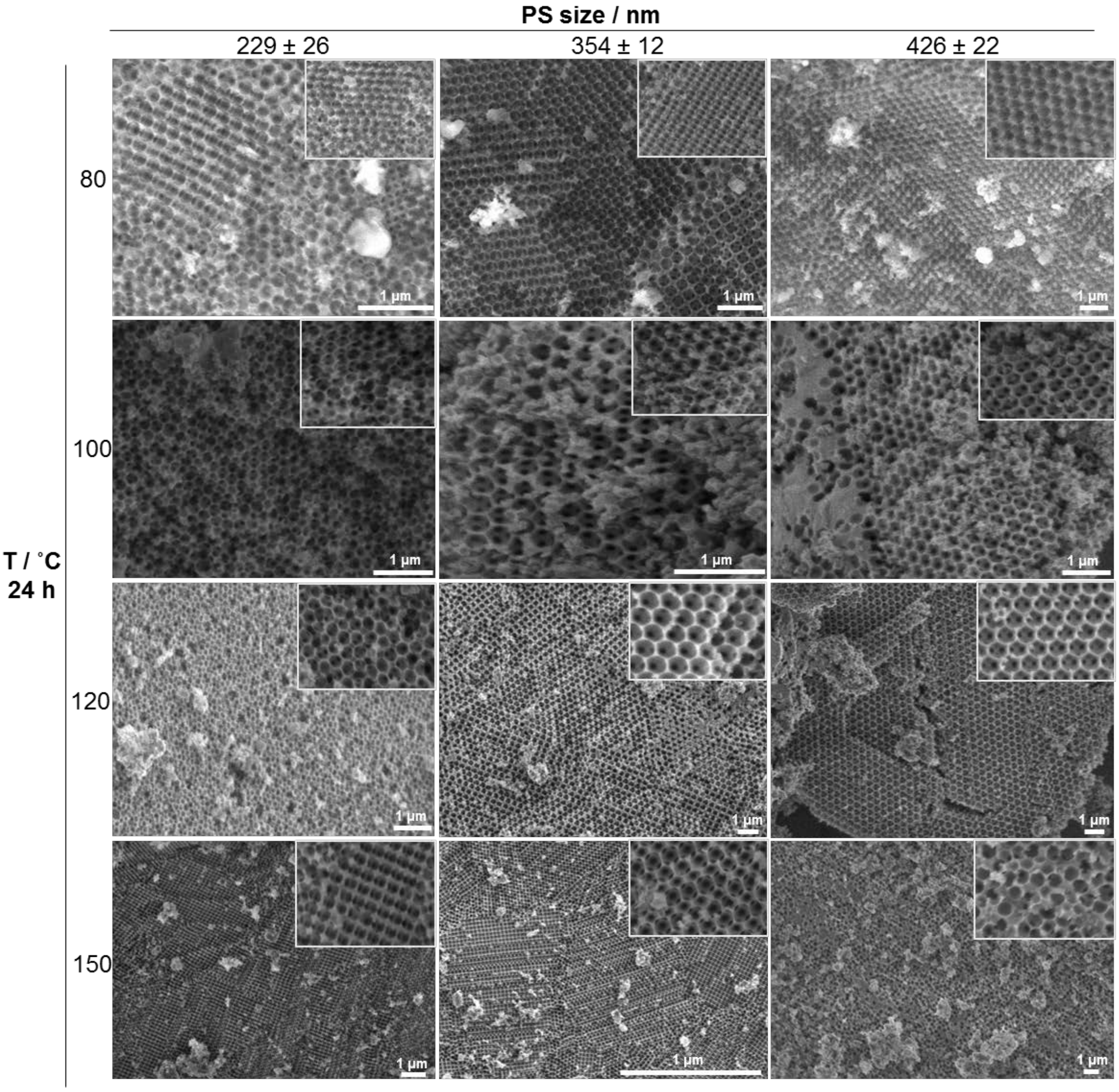

Figure 3.42: SEM images of HT-*MM*-TLCT SBA-15 materials (80 to 150 °C for 24 h), on 1 μm scale.

Despite the treatment, the materials were clearly able to retain their ordered macroporous arrangement, as can be seen from the SEM images above, showing long-range ordered structures. All samples exhibit a honeycomb framework with a long-range order of the macroporous network. The size of the obtained macropores, as in the case of *MM*-TLCT SBA-15 in section 3.2.2 (Characterisation of *MM-TLCT* SBA-15), underwent a contraction due to the removal of polystyrene template upon calcination [35] (**Table 3.22**).

HT / °C (24 h)	PS beads / nm	Macropore diameter / nm (SEM)	Macropore shrinkage / nm
80	229 ± 26	187 ± 21	42
	354 ± 12	274 ± 20	80
	426 ± 22	328 ± 18	98
100	229 ± 26	202 ± 15	27
	354 ± 12	261 ± 12	93
	426 ± 22	262 ± 24	164
120	229 ± 26	197 ± 18	32
	354 ± 12	287 ± 19	67
	426 ± 22	340 ± 24	86
150	229 ± 26	131 ± 11	98
	354 ± 12	251 ± 24	103
	426 ± 22	377 ± 45	49

Table 3.22: Macropore diameter determined by SEM and assessment of the macropore shrinkage with respect to the original PS size.

As in the case of the untreated hierarchical materials, the macropores contraction increased with the original polystyrene beads diameter.

Figure 3.43 shows STEM of the material hydrothermally treated at 120 ˚C (PS size = 354 nm).

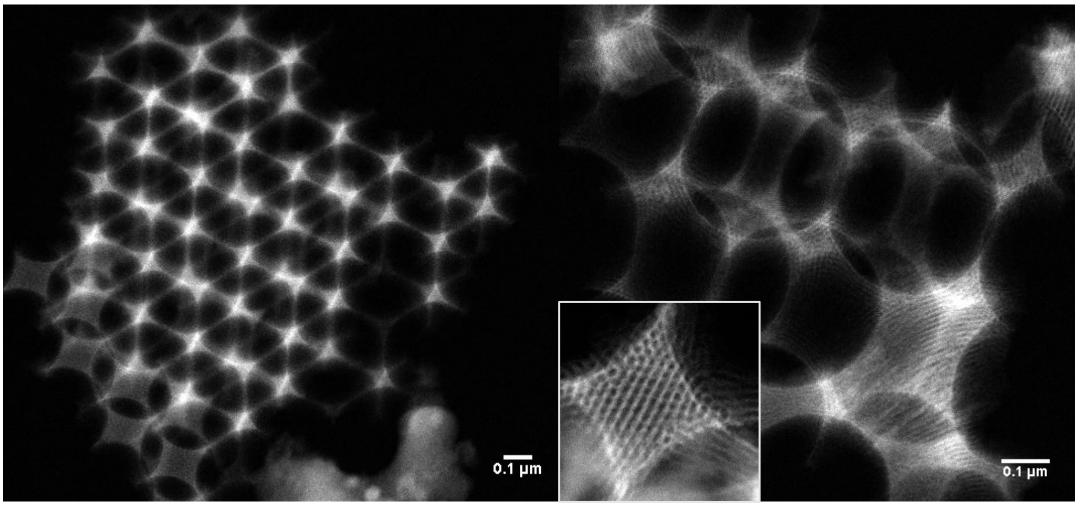

Figure 3.43: Dark field STEM images of HT-*MM*-TLCT SBA-15 (PS size = 354 ± 12 nm). Inset: detail of mesopores.

The images above confirm that the hydrothermal treatment did not ruin the hierarchical porous structure, in fact, it is still possible to appreciate the ordered framework that alternates between the macro- and mesoporosities in an ordered arrangement.

In conclusion, the novelty of this section not only consists of the synthesis of *MM*-TLCT SBA-15 but also of the mesopore expansion in a hierarchical silica support, as pore enlargement in hierarchical CO-OP SA SBA-15 has never been reported in the literature.

3.3. Characterisation of platinum catalysts

Platinum-group metals (particularly platinum and palladium) are active catalysts in the liquid-phase oxidation of alcohols, diols and carbohydrates with molecular oxygen under mild conditions. [36-40] Specifically, platinum nanoparticles supported on mesoporous silicas have attracted significant interest because of their potential application in catalysis. [41-44] Platinum nanoparticles on different silica supports have been prepared for the study presented in the current chapter and will be described in this section.

The meso- and macro-mesoporous supports previously synthesised, which presented the best characteristics in terms of pore diameter and surface area expansion, have been functionalised with platinum, in order to be employed as catalysts in the oxidation of a large aldehyde, with the aim of demonstrating the feasibility of pore-expanded materials in the field of heterogeneous catalysis. Their characterisation is described in detail in the following sections.

3.3.1. Characterisation of Pt-CO-OP SA SBA-15 catalyst

In order to compare the catalytic performance of CO-OP SA and TLCT synthetic routes, the support prepared following the methodology described in section 2.2.1. (Synthesis of CO-OP SA SBA-15 mesoporous silica) was functionalised with ammonium tetrachloroplatinate (II) $(NH_4)_2PtCl_4$ precursor (**Figure 3.44**), to impart 0.5 wt% by weight loading of platinum.

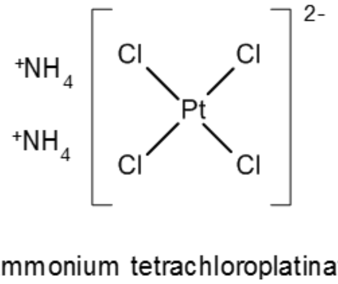

Figure 3.44: Structure of $(NH_4)_2PtCl_4$ precursor.

Inductively-Coupled Plasma-Mass Spectrometry (ICP-MS) provided the exact platinum loading, corresponding to 0.44 wt%. In the present section and in section 3.4.1 (Catalytic results), 0.44 wt%-CO-OP SA SBA-15 catalyst will be named M-0.

Low-angle and wide-angle X-ray diffractograms of the platinum catalyst compared to its support are shown in **Figure 3.45** (left and right, respectively).

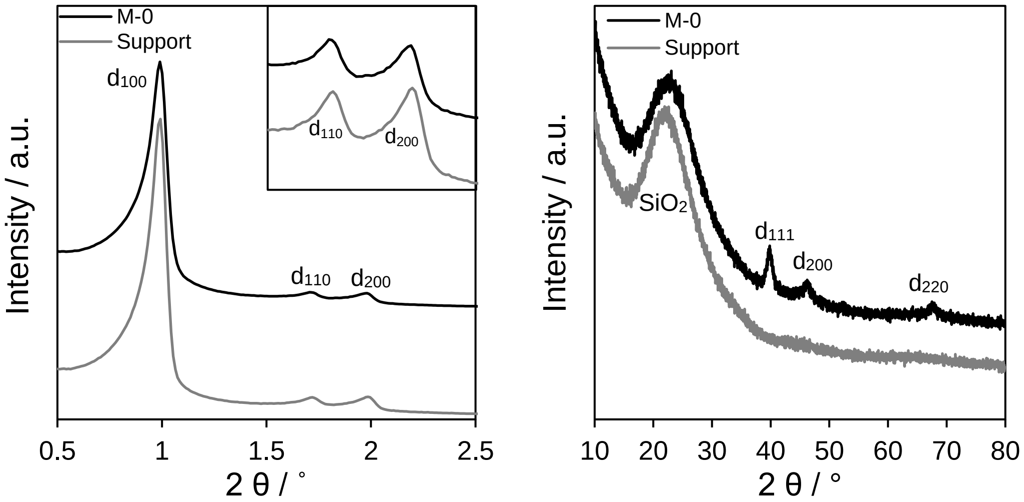

Figure 3.45: Low-angle (left) and wide-angle (right) XRD of M-0 catalyst compared to its parent support (offset for clarity).

Figure 3.45 (left) shows that impregnation with platinum did not cause any damage to the long-range order of the material, as in the catalyst's diffractogram the peaks relative to the hexagonal structure remained unaltered. In addition, the position of pore spacing in both support and catalyst is 10.3 nm, indicating that the unit cell parameter did not undergo any modification. In the wide-angle XRD patterns (**Figure 3.45**, right), three reflections relative to different metal planes are identified, namely (111), (200) and (220). The big peak at ≈ 22° represents the silica, the material of the support. Wide-angle XRD, besides visualising what species is present, as each metal shows reflections at specific 2θ, is also able to provide the particle size of the crystallites. To do this, the first reflection (d_{111}) has been chosen because it is the most visible of the three; therefore, it will be used to evaluate the particle size throughout the entire thesis.

Table 3.23 compares the particle size determined with wide-angle XRD and STEM.

M-0 / wt%	XRD / nm	STEM / nm
0.44	6.4	5.7 ± 1.6

Table 3.23: Pt particle size of M-0 catalyst evaluated with XRD and STEM (particle dimension evaluated over ≈ 250 particles).

As explained in Chapter 2 (section 2.4.1. Powder X-ray Diffraction), the particle size calculated with wide-angle XRD tends to be bigger than that calculated with STEM because the former technique is able to detect particles above 3 nm, and not those below this size. This fact is related to the number of diffraction planes being high enough to lead to a constructive interference when the metal particle is above 3 nm, whereas below this size the peak begins to broaden and lose its shape due to destructive interference. Instead, STEM is able to identify the smallest particles as well as the biggest ones, hence the calculation of the particle size is more reliable on the areas of the material that have been imaged. In fact, it is not possible to rule out the possible existence of particles with different size within the pores that are not imaged by the operator. Throughout the experimental chapters of this thesis (3rd, 4th, 5th), the particle sizes calculated with XRD and STEM has always been reported, to identify the discrepancies due to the limitations of both techniques.

Representations of M-0 catalyst obtained with STEM is illustrated in **Figure 3.46**.

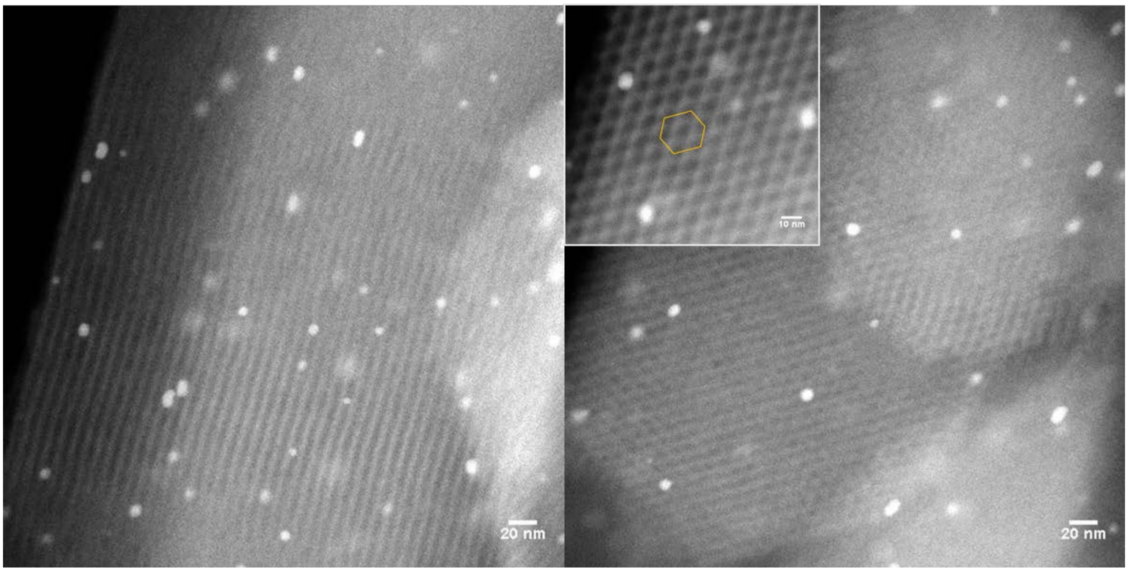

Figure 3.46: Dark field STEM images of M-0 catalyst. Image taken vertical to the parallel pore channels (left) and taken along the parallel pore channels (right). Inset: identification of the hexagonal arrangement of the mesopores.

The functionalisation of the silica support with platinum has not affected the *p6mm* symmetry, characterised by the presence of parallel channels (**Figure 3.46**, left) and hexagonal porous arrangement (**Figure 3.46**, right), typical features of SBA-15 materials. It is also possible to appreciate the presence of metal particles (white dots) uniformly distributed inside the porous architecture, which represents the active sites responsible for the catalytic reaction.

Figure 3.47 shows nitrogen physisorption porosimetry of the platinum catalyst compared to its parent support.

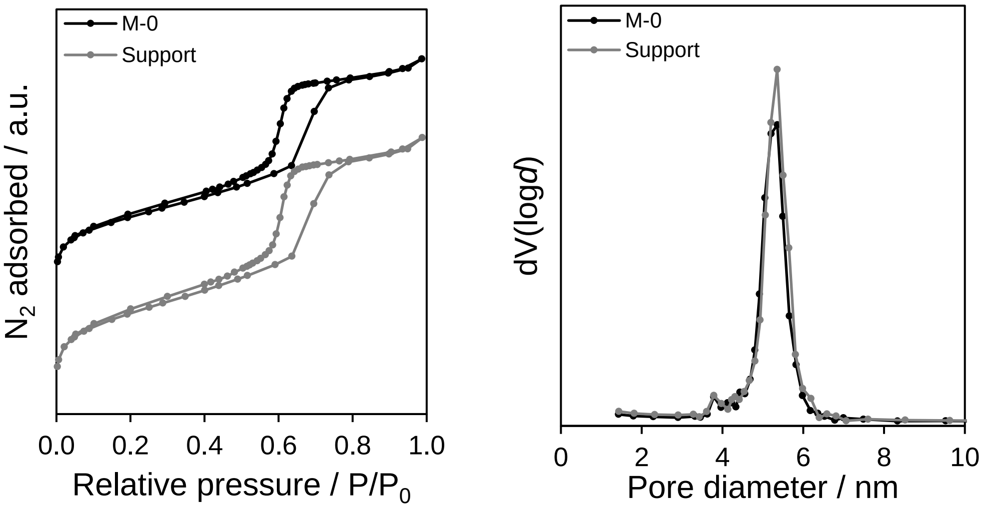

Figure 3.47: N_2 isotherms (left) and PSD (right) of M-0 catalyst compared to its parent support (offset for clarity).

From the figures above it can be appreciated that wet-impregnation of the silica support did not generate any critical modification to the material, in fact, the shape of the isotherms and pore size distributions do not look different. The mesoporous parameters are closely analysed in **Table 3.24**.

	PD / nm	PV / $cm^3\ g^{-1}$	SA / $m^2\ g^{-1}$	MA / $m^2\ g^{-1}$
Parent support	5.4	0.9	805 ± 81	229 ± 23
M-0	5.4	0.8	678 ± 68	167 ± 17

Table 3.24: Comparison of PD, PV, SA and MA of M-0 catalyst compared to its parent support, (PD = pore diameter, PV = pore volume, SA = BET surface area, MA = micropore area).

The surface area was altered during the process of metal functionalisation. This stems from the partial occupation of the available surface area by platinum particles; therefore, less space was free for nitrogen adsorption during porosimetry analysis. Micropore area also decreased due to the same reason, as the smallest particles were able to enter the micropores.

3.3.2. Characterisation of pore-expanded Pt-TLCT SBA-15 catalysts

Sections 3.1.3 (Characterisation of TLCT SBA-15 with hydrothermal treatment) and 3.1.4 (Characterisation of TLCT SBA-15 with swelling agents) have described pore-expanded materials obtained with different procedures. As summarised in **Table 3.10**, the methodology that afforded the best results in terms of pore spacing and pore diameter expansion, as well as surface area and pore volume improvement, is represented by the application of hydrothermal treatment up to 120 ˚C, specifically for

24 hours. Higher temperature or longer treatment resulted in the loss of narrow pore size distribution and decrease in surface area.

Section 3.1.2 (TLCT SBA-15: reproducibility and characterisation), presented the preparation of seven identical supports, prepared with a high degree of reproducibility. Among the prepared materials, the one with 4.8 nm pore diameter (sample **4**) has been chosen to be functionalised with platinum and will be named M-1. In the matter of the pore-expanded supports described in section 3.1.3 (Characterisation of TLCT SBA-15 with hydrothermal treatment, only those with 6 and 6.8 nm pore diameter have been selected for the synthesis of catalysts and will be described as M-2 and M-3, respectively. In this way, it has been possible to prepare three platinum catalyst with different pore sizes, as far away from each other as possible, in order to be able to monitor the improvement in internal mass diffusion inside different pore diameters, as will be described in section 3.4.1 (Catalytic results). The different pore size materials are shown in **Table 3.25**.

Catalyst name	**HT / ˚C (24 h)**	**Mesopore size / nm**
M-1	No HT (sample **4**)	4.7
M-2	100	6.3
M-3	120	6.8

Table 3.25: List of TLCT SBA-15 materials used in this section to prepare pore-expanded Pt-TLCT SBA-15 catalysts.

The materials presented in **Table 3.25** have been functionalised with platinum utilising the wet impregnation method, as described in Chapter 2, section 2.3.1. (Synthesis of platinum catalysts). The metal precursor employed has been ammonium tetrachloroplatinate (II) $(NH_4)_2PtCl_4$ (**Figure 3.44**), to impart 0.5 wt% by weight loading of platinum.

The actual platinum wt% was measured using ICP-MS (**Table 3.26**).

Catalyst name	**Nominal Pt wt%**	**Actual Pt wt%**
M-1	0.5	0.26
M-2	0.5	0.31
M-3	0.5	0.25

Table 3.26: Nominal and actual Pt loading of the three different pore size catalysts.

All catalysts showed an equal decrease in platinum loading during functionalisation, consistent with the preparation method, which might indicate the loss of some amount of metal, probably due to sticking to the walls of the beaker during the overnight agitation of the slurries.

Low-angle XRD diffractograms of the platinum catalysts described in this section are compared to those of their supports (**Figure 3.48**).

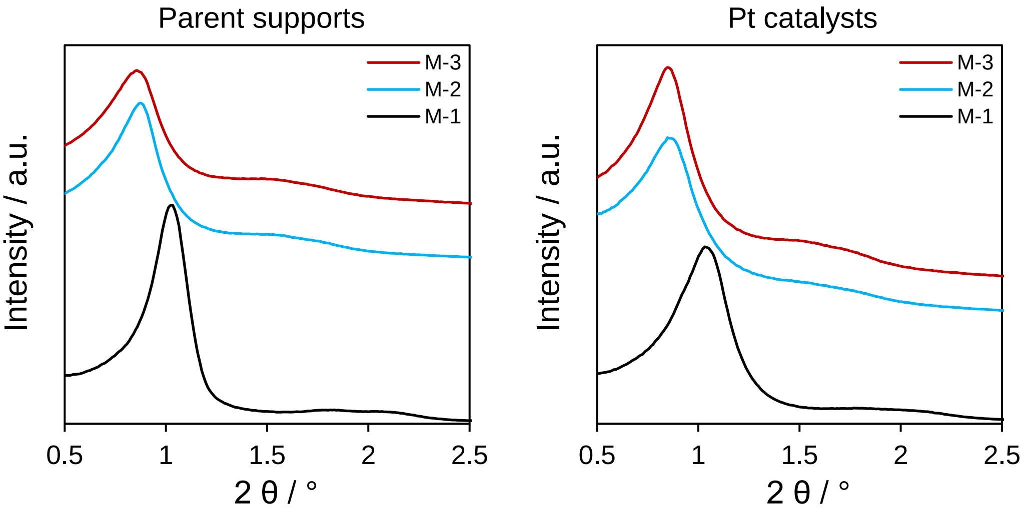

Figure 3.48: Low-angle XRD patterns of pore-expanded Pt-TLCT SBA-15 catalysts (right) with those of the parent supports (left), (offset for clarity).

As it is possible to observe in **Table 3.27**, the diffractograms after metal functionalisation show the same characteristics of those of the supports, as the pore spacing remained unaltered.

	***a* / nm**
Parent support M-1	9.9 9.9
Parent support M-2	11.6 11.7
Parent support M-3	11.9 12

Table 3.27: Comparison of *a* of the pore-expanded Pt-TLCT SBA-15 catalysts, (*a* = pore spacing).

Figure 3.49 illustrates wide-angle X-ray diffraction of the catalysts described in **Table 3.26**, compared to the diffractogram of pure support.

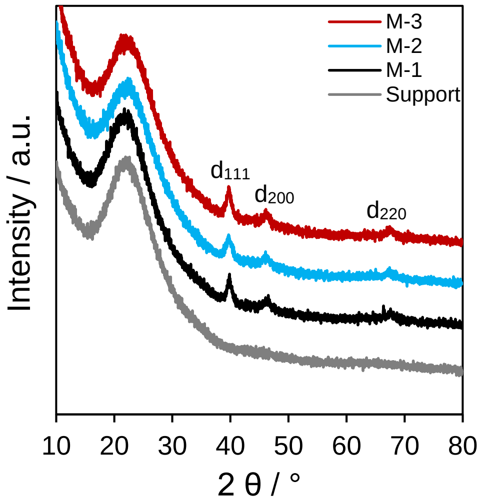

Figure 3.49: Wide-angle XRD patterns of pore-expanded Pt-TLCT SBA-15 catalysts.

The platinum catalysts in **Figure 3.49** show the three reflections relative to different platinum planes, while the parent support does not show any of these reflections, consistent with the fact that it has not been functionalised. The particle size of platinum on each catalyst has been determined with wide-angle XRD and STEM (**Table 3.28**).

Catalyst name	Mesopore size / nm	XRD / nm	STEM / nm
M-1	4.7	7.2	1.5 ± 0.9
M-2	6.3	5.7	1.7 ± 1.2
M-3	6.8	6.3	3.0 ± 1.7

Table 3.28: Metal particle size of the pore-expanded Pt-TLCT SBA-15 catalysts determined by XRD and STEM (particle dimension evaluated over ≈ 250 particles).

As explained in the last section, the particle size calculated with wide-angle XRD appears to be bigger than that calculated by STEM, as the former technique is only able to detect particles above 3 nm, and therefore can overestimate the real average particle size. On the other hand, STEM can identify also smaller particles; therefore, the calculation of the particle size is more reliable for the areas of the material that this technique has imaged. The particle size measure with STEM increases with the support pore diameter, as does the error associated with it. There are a few literature examples that report an increasing metal nanoparticle size with the pore diameter of the mesoporous silica support. [45, 46]

Figure 3.50 shows STEM images of the platinum catalysts described in **Table 3.28**.

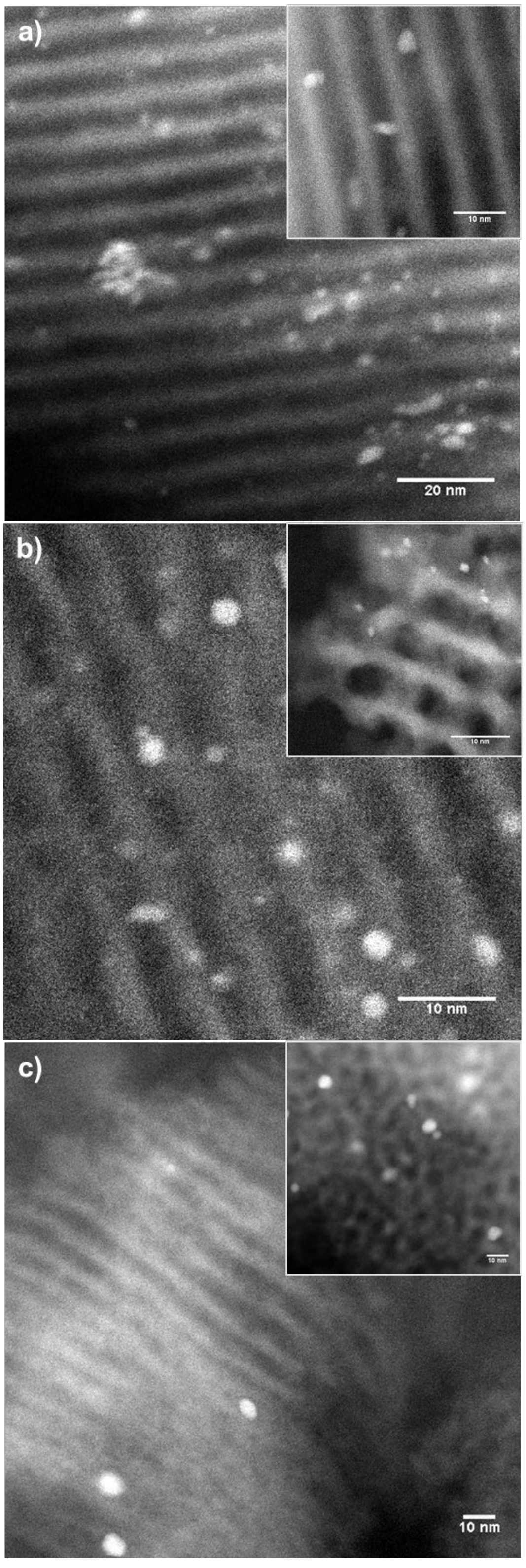

Figure 3.50: Dark field STEM images of **a)** M-1, **b)** M-2), **c)** M-3.

The functionalisation of the silica supports with platinum has not affected the *p6mm* symmetry characterised by the presence of parallel channels and hexagonal porous arrangement, typical of SBA-15 materials. The metal particles are represented by white dots, which reveal their spherical shape, uniformly distributed inside the porous framework.

Nitrogen physisorption porosimetry was carried out on the three catalysts. Their adsorption-desorption isotherms were compared to those of the corresponding parent supports (**Figure 3.51**), to evaluate if the metal functionalisation provoked any structural change.

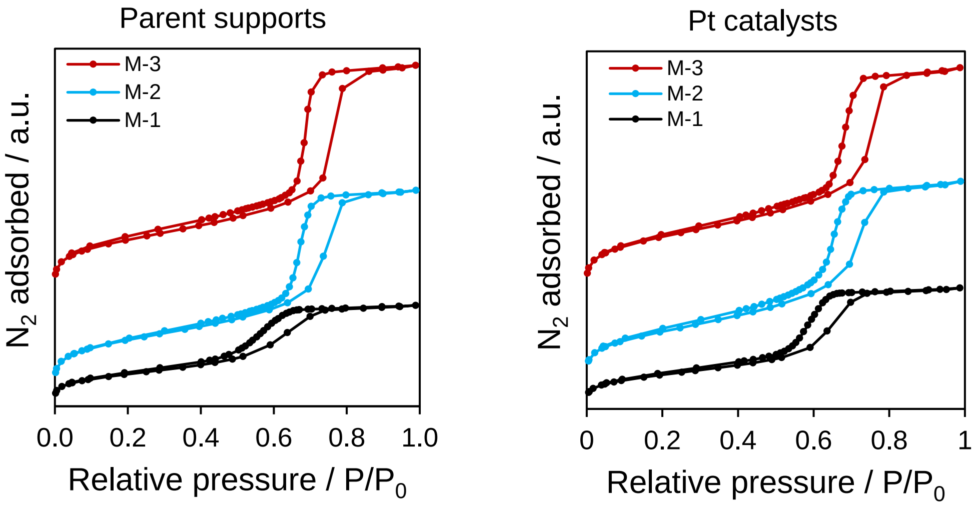

Figure 3.51: Comparison of N_2 isotherms of pore-expanded Pt-TLCT SBA-15 catalysts (right) with those of the parent supports (left), (offset for clarity).

Analysing the isotherms' shape, it is possible to infer a change in surface area during the functionalisation process. The hysteresis of all catalysts has slightly shrunk with respect to their corresponding parent supports, indicating a loss of surface area. However, the steep step and narrow hysteresis loops in the adsorption-desorption branches are still evidencing retention of the parent SBA-15 cylindrical and parallel pore channels. Compared to their parent supports, the functionalised materials show slightly broader pore size distributions, since the step on the adsorption branches is less sharply sloped. This is reflected in **Figure 3.52**, from which it is possible to appreciate the pore size distributions of the catalysts in relation to their supports.

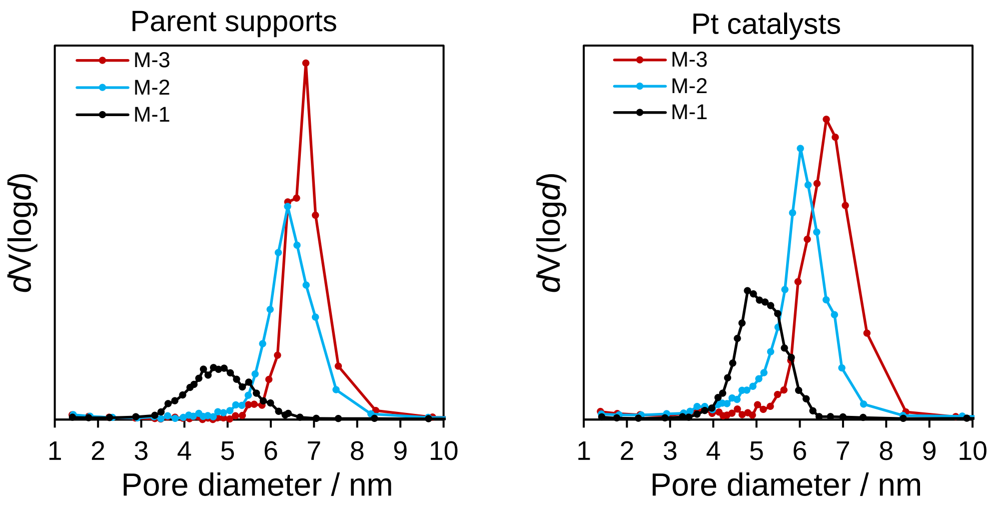

Figure 3.52: Comparison of PSD of pore-expanded Pt-TLCT SBA-15 catalysts (right) with those of the parent supports (left), (offset for clarity).

As suggested above, the distribution curves relative to the catalysts (**Figure 3.52**, right) are slightly broader than those of their supports, indicating that the insertion of the metal inside the silica framework has caused a small loss of porous uniformity. Nitrogen porosimetry is a useful tool to monitor pore diameter, pore volume and surface area change during the process of platinum functionalisation of TLCT SBA-15 materials (**Table 3.29**).

	PD / nm	**PV / cm^3 g^{-1}**	**SA / m^2 g^{-1}**	**MA / m^2 g^{-1}**
Parent support	4.7	0.7	456 ± 46	40 ± 4
M-1	4.7	0.6	416 ± 42	26 ± 3
Parent support	6.3	1.2	876 ± 88	142 ± 14
M-2	6.0	1.1	687 ± 69	57 ± 5
Parent support	6.8	1.4	895 ± 90	168 ± 17
M-3	6.6	1.2	753 ± 75	138 ± 14

Table 3.29: Comparison of PD, PV, SA and MA of pore-expanded Pt-TLCT SBA-15 catalysts with those of the parent supports, (PD = pore diameter, PV = pore volume, SA = BET surface area, MA = micropore area).

While pore diameter and pore volume have mostly been retained during the process of functionalisation via wet-impregnation with platinum, surface area is the parameter that has been most affected, as anticipated in **Figure 3.51** from the isotherms' shapes. As **Table 3.29** confirms, a loss of BET surface area and pore volume is attributed to partial pore blockage, a consequence of the partial occlusion of available free surface area from platinum nanoparticles. However, it is possible to state that overall, the materials, once functionalised, have retained the properties of the parent supports. It is acceptable that the presence of platinum particles has created a slight alteration of pore diameter and surface area.

X-ray Photoelectron Spectroscopy (XPS) was carried out on M-0 catalyst described in section 3.3.1 (Characterisation of Pt-CO-OP SA SBA-15 catalyst) and on the three pore-expanded Pt-TLCT SBA-15 catalysts (M-1, M-2, M-3) described in the current section. The XPS data have been gathered together in the current section, in order to compare the information obtained from the study of these four catalysts' surface region. This technique allows the X-rays to enter the sample with < 10 nm depth, therefore is extremely useful to obtain information about the surface region (XPS has been explained in detail in Chapter 2, section 2.4.6. X-ray Photoelectron Spectroscopy).

Table 3.30 lists the wt% composition of platinum on the surface of the catalysts, in relation to the metal content previously determined with ICP-MS.

Catalyst (support)	**Particle size / nm (STEM)**	**ICP-MS Pt / wt%**	**Pt Surface / wt%**	**Oxide content / %**
M-0 (CO-OP SA)	5.7 ± 1.6	0.44	0.25	27
M-1 (TLCT)	1.5 ± 0.9	0.26	0.82	20
M-2 (HT-TLCT 100 ˚C)	1.7 ± 1.2	0.31	0.36	23
M-3 (HT-TLCT 120 ˚C)	3.0 ± 1.7	0.25	0.31	22

Table 3.30: Surface composition properties obtained from XPS fitting.

The platinum content determined by ICP-MS corresponds to the metal present in the bulk and on the surface of the catalysts, as this technique does not discriminate between the two regions. As the metal nanoparticles of M-0 catalyst have the biggest size, they present the lowest amount of platinum on their surface, as illustrated in **Figure 3.53** (**a**). This is reflected in the lowest surface to total platinum ratio, indicating that more platinum is exposed per gram of catalyst, but less of it is present on the surface. The low loading catalysts present the majority of the content of metal on their surface, while the high loading catalysts display the metal partly on the surface (determined by XPS) and partly in the bulk, as illustrated in **Figure 3.53**.

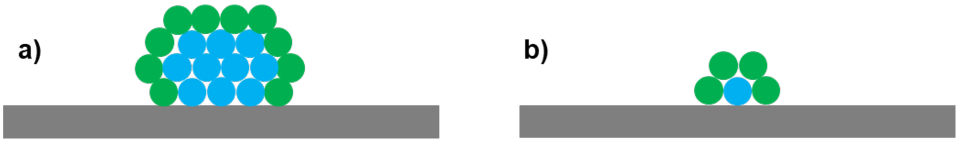

Figure 3.53: Representation of Pt distribution over the bulk (blue pellets) and the surface (green pellets) of the catalyst. The grey bar represents the support.

Smaller particles prefer to be distributed on the surface of the catalyst in the form of PtO_2, as smaller particles are more liable to stabilise the oxide rather than the metal due to energy requirements, [47] and due to the fact that when platinum is exposed to the environment, it is more sensitive to oxidative processes. The TLCT catalysts, having smaller nanoparticles with respect to the CO-OP SA catalyst, present more metal on the surface of the nanoparticles (**Figure 3.53**, **b**). Specifically, M-1 catalyst presents the majority of metal on the surface; therefore, it has the highest PtO_2 content. This is mirrored in **Figure 3.54** (left), which shows the detection of platinum on the mesoporous SBA-15 catalysts. **Figure 3.54** (right) presents the detection of silicon.

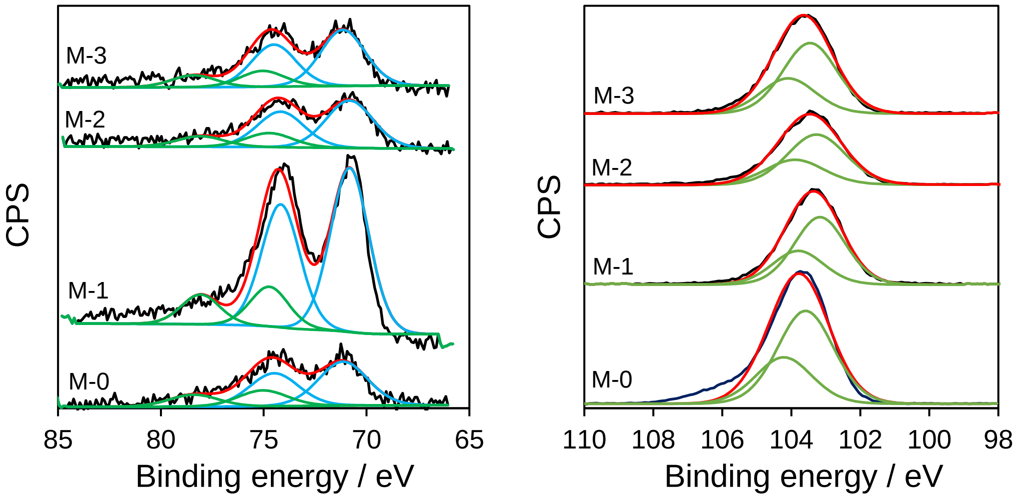

Figure 3.54: Pt 4f (left) and Si 2p (right) spectra of M-0 (CO-OP SA SBA-15) and M-1, M-2, M-3 (TLCT SBA-15) catalysts (offset for clarity).

In **Figure 3.54** (left), the black lines and the red lines indicate the raw data and the full envelope fitting of the region, respectively. Contributions due to $Pt^{(0)}$ (blue lines) and PtO_2 (green lines) fitted components are shown, revealing the emergence of the oxide feature, confirming that the formation of PtO_2 species is favoured on the surface of the catalysts. Platinum content on the surface of the catalysts reflects the data shown in **Table 3.30**: the most intense 4f peaks are, in fact, associated with M-1 catalyst, whose surface metal content corresponds to 0.82 wt%.

Figure 3.54 (right), instead, shows the fitting for silicon 2p species. No silicon on its elemental state ($Si^{(0)}$) has been detected, reflecting the composition of the silica support. The green lines represent the contributions due to SiO_2, whereas the black lines and the red lines indicate the raw data and the full envelope fitting of the region, respectively. Since all the catalysts used in the present thesis consist of platinum supported on silica, the XPS analysis of the support is only depicted in **Figure 3.54** (right) and will not be presented again, as the surface information related to SiO_2 does not vary.

3.3.3. Characterisation of pore-expanded Pt-*MM*-TLCT SBA-15 catalysts

As described in section 3.2 (Characterisation of macro-mesoporous silica supports) ordered hierarchical porous materials have been prepared including polystyrene template nanospheres of different diameter (229 ± 26, 354 ± 12, 426 ± 22 nm) to the synthesis of TLCT SBA-15 prior to mesopore expansion, consisting of a 24 hours hydrothermal treatment. The prepared *MM*-TLCT SBA-15 supports amounted to fifteen samples: three materials that did not undergo the pore enlargement protocol and twelve pore-expanded materials.

Regarding the untreated *MM*-TLCT SBA-15 materials, the sample prepared from a template dimension of 354 ± 12 nm was selected as reference catalyst and will be identified as MM-1. Out of the twelve hydrothermally treated materials HT-*MM*-TLCT SBA-15, it has been chosen to functionalise only those treated at 120 ˚C, because they reached a pore size enlargement corresponding to 5.6, 5.8, 6 nm (for 229, 354, 426 nm template diameter), without suffering from strong structure damage (**Table 3.21**). These materials will be named MM-2, MM-3 and MM-4, respectively. The aim of preparing three representative pore-expanded *MM*-TLCT SBA-15 catalysts relied on the necessity to validate the enhancement in the internal mass transfer of the reactant inside a pore-expanded macro-mesoporous system, to be compared with a uniquely mesoporous architecture. The hierarchical porous materials employed as catalysts are itemised in **Table 3.31**.

Catalyst name	HT / ˚C (24 h)	Mesopore size / nm	Macropore size / nm
MM-1	No HT	4.7	253 ± 28
MM-2	120	5.6	197 ± 18
MM-3	120	5.8	287 ± 19
MM-4	120	6.0	340 ± 24

Table 3.31: List of *MM*-TLCT SBA-15 materials used in this section to prepare pore-expanded Pt-*MM*-TLCT SBA-15 catalysts.

These silica supports have been functionalised with platinum utilising the wet impregnation method, as described in section 2.3.1. (Synthesis of platinum catalysts). The metal precursor employed has been ammonium tetrachloroplatinate (II) $(NH_4)_2PtCl_4$ (**Figure 3.44**), to impart 0.5 wt% by weight loading of platinum.

ICP-MS has provided the exact platinum loading of the three catalysts (**Table 3.32**), to which a label has been assigned for convenience. From this point onwards, these platinum catalysts will be defined by these labels.

Catalyst name	Nominal Pt wt%	Actual Pt wt%
MM-1	0.5	0.31
MM-2	0.5	0.30
MM-3	0.5	0.44
MM-4	0.5	0.34

Table 3.32: Nominal and actual Pt loading of the pore-expanded Pt-*MM*-TLCT SBA-15 catalysts.

All catalysts showed a small decrease in platinum content after functionalisation, consistent with the preparation method, which might imply a slight loss of metal, probably due to material sticking to the walls of the beaker during overnight agitation of the slurries.

Wide-angle X-ray diffractometry was conducted on the catalysts in **Table 3.32** (**Figure 3.55**).

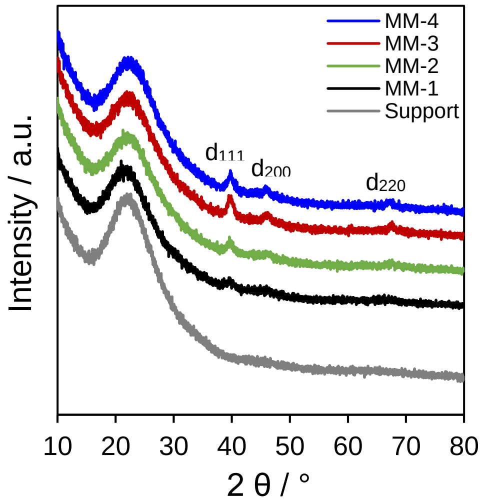

Figure 3.55: Wide-angle XRD of the pore-expanded Pt-*MM*-TLCT SBA-15 catalysts.

The patterns show the reflections related to platinum metal, and the particle size of the active site was determined with both wide-angle XRD and STEM (**Table 3.33**).

Catalyst name	Mesopore size / nm	XRD / nm	STEM / nm
MM-1	4.7	5.0	1.9 ± 0.98
MM-2	5.6	5.6	3.3 ± 2.45
MM-3	5.8	5.2	3.0 ± 1.85
MM-4	6.0	5.4	2.8 ± 1.74

Table 3.33: Metal particle size of the three pore-expanded Pt-*MM*-TLCT SBA-15 catalysts determined with XRD and STEM.

As explained for pore-expanded Pt-TLCT SBA-15 catalysts in section 3.3.2 (Characterisation of pore-expanded Pt-TLCT SBA-15 catalysts), these two characterisation techniques are based on different principles; therefore the size of the particles does not match. In contrast to the particle size trend observed across the pore-expanded mesoporous catalysts series (**Table 3.28**), the size of platinum nanoparticles determined with STEM does not follow a proportional increase with the mesopore diameter. This phenomenon might be due to the insertion of macropores in the support framework that lead to a slight difference in metal particle size distribution within the silica skeleton. Moreover, Song and co-workers did not observe a dependence of platinum nanoparticle size with pore expansion of a mesoporous silica support. [48]

STEM images of the hierarchical porous catalysts are shown below (**Figure 3.56**).

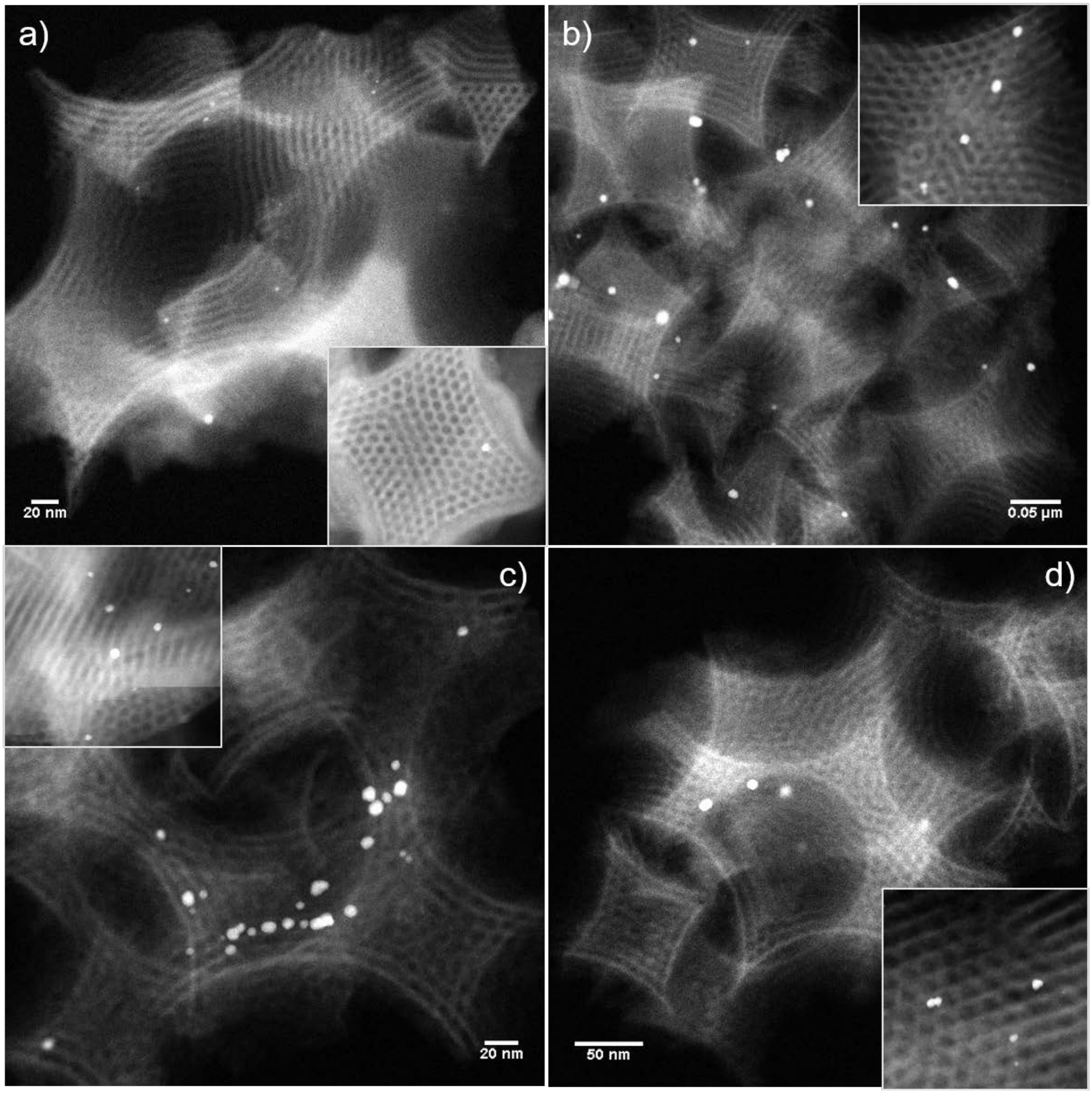

Figure 3.56: Dark field STEM images of **a)** MM-1, **b)** MM-2), **c)** MM-3, **d)** MM-4. Insets: details of mesoporous regions.

All images depict a representative portion of the materials, which appear to consist of a repeating alternation of windows of macropores and mesoporous plots, based on the principle described in **Figure 3.36**, which illustrates the precipitation of the silica-micellar solution around the macrospheres of polystyrene, giving rise to the hierarchical framework above represented. The mesoporous network appears well ordered, and it presents the parallel channels and the hexagonal structure belonging to the space group *p6mm*. The white dots that stand for the platinum particles are dispersed through the macropores as well as the mesopores, and represent the active site that will be responsible for the catalysis, as described later on.

Nitrogen physisorption porosimetry was performed on the four platinum catalysts. Their adsorption-desorption isotherms were compared to those of the corresponding parent supports to evaluate if the insertion of the metal caused any structural change (**Figure 3.57**).

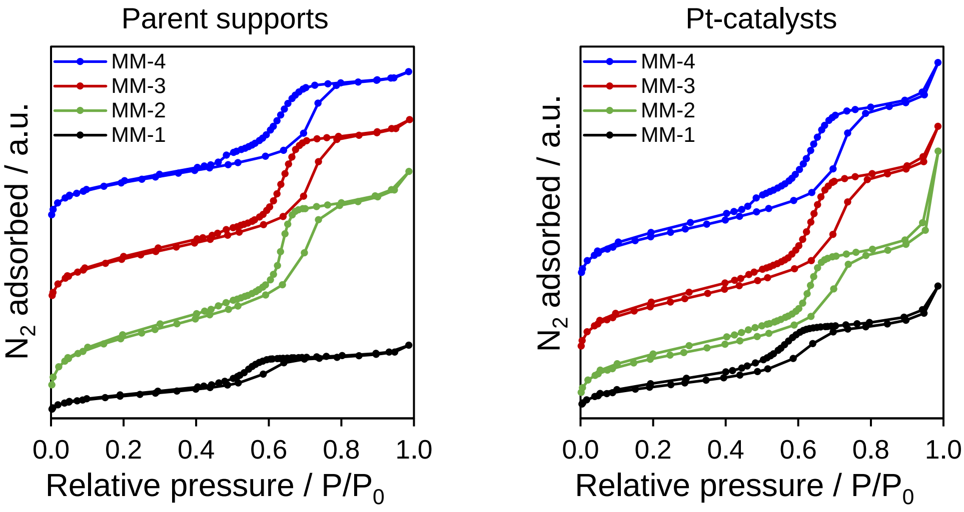

Figure 3.57: Comparison of N_2 isotherms of pore-expanded Pt-*MM*-TLCT SBA-15 catalysts (right) with those of the parent supports (left), (offset for clarity).

From the figures above, it is noticeable that the shape of the isotherms underwent some changes over functionalisation: elongation of the upper closure point at $P/P_0 \approx 0.95$ and an accentuation of the bulge on the desorption branch at $P/P_0 \approx 0.5$. The upper closure point corresponds to the moment when the nitrogen desorbs from the pores. The presence of platinum particles in a hierarchical system may render this process more difficult, and the nitrogen does not desorb uniformly as if the pores were free. On the other side, the bulge on the desorption branch is due, as extensively explained in previous sections, to complementary porosity formed as a result of mesopore shrinkage from the original size to < 4 nm. This phenomenon is reflected in **Figure 3.58**, which shows the pore size distribution curves of the pore-expanded platinum macro-mesoporous catalysts compared to their parent supports.

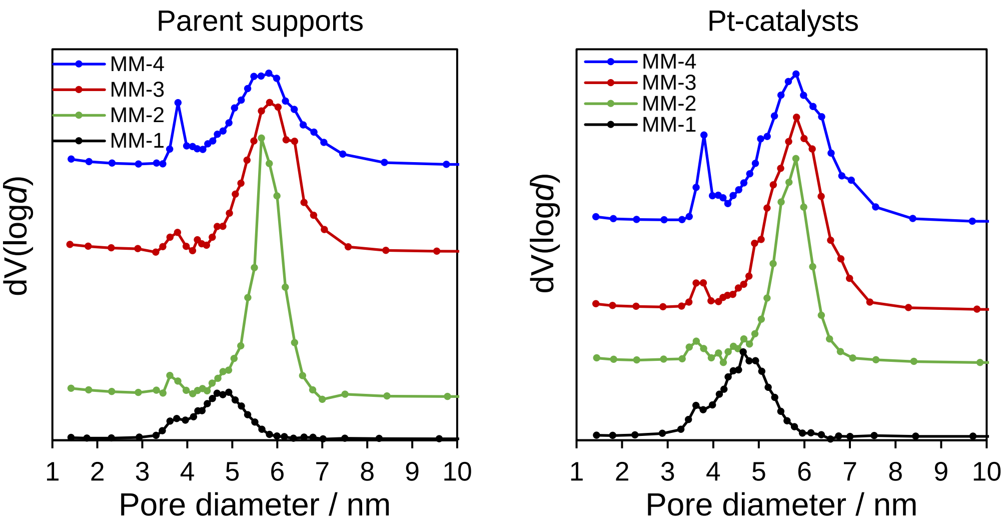

Figure 3.58: Comparison of PSD of pore-expanded Pt-*MM*-TLCT SBA-15 catalysts (right) with those of the parent supports (left), (offset for clarity).

As observed in sections 3.2.2 (Characterisation of *MM-TLCT* SBA-15) and 3.2.3 (Characterisation of *MM-TLCT* SBA-15 with hydrothermal treatment), the insertion of macropores in the TLCT SBA-15 system entails the development of a portion of smaller mesopores (< 4 nm) that cause the appearance of the bulge on the desorption branch of the isotherms at P/P0 ≈ 0.5 that has been observed in **Figure 3.57**. The mesopores contraction to a smaller size may be due to the pressure applied by the polystyrene template nanospheres on the mesopores in between them as explained in section 3.2.3 (Characterisation of *MM-TLCT* SBA-15 with hydrothermal treatment). The presence of this complementary porosity is the reason why the shape of the nitrogen isotherms is distorted by the bulge at P/P0 ≈ 0.5, which is due to the tensile strength effect, as previously elucidated.

Table 3.34 summarises pore diameter, volume, surface area and micropore area of the hierarchical porous materials before and after the process of functionalisation.

	PD / nm	**PV / cm^3 g^{-1}**	**SA / m^2 g^{-1}**	**MA / m^2 g^{-1}**
Parent support	4.7	0.4	409 ± 41	0 ± 0
MM-1	4.7	0.5	308 ± 31	0 ± 0
Parent support	5.6	1.3	1093 ± 109	278 ± 28
MM-2	5.8	0.8	579 ± 58	122 ± 12
Parent support	5.8	1.1	906 ± 91	226 ± 23
MM-3	5.8	0.9	657 ± 66	132 ± 13
Parent support	6.0	1.9	751 ± 75	239 ± 24
MM-4	5.8	0.8	648 ± 65	138 ± 14

Table 3.34: Comparison of PD, PV, SA and MA of pore-expanded Pt-*MM*-TLCT SBA-15 catalysts with those of the parent supports, (PD = pore diameter, PV = pore volume, SA = BET surface area, MA = micropore area).

Platinum insertion did not cause any strong modification to mesopore diameter but implicated a loss of pore volume, surface area and micropore area. This is consistent with the fact that metal nanoparticles occupy some of the space that was free in the bare parent support; therefore, it is no longer detectable by nitrogen during physisorption analysis.

XPS was carried out on the four pore-expanded Pt-*MM*-TLCT SBA-15 catalysts, in order to obtain information about their surface region. The obtained data have been processed based on the principles explained in section 3.3.2 (Characterisation of pore-expanded Pt-TLCT SBA-15 catalysts).

In **Table 3.35** is listed the wt% composition of platinum on the surface of the catalysts, in relation to the metal content previously determined with ICP-MS.

Catalyst	Particle size / nm (STEM)	ICP-MS Pt / wt%	Pt Surface / wt%	Oxide content / %
MM-1 (*MM*-TLCT 354 nm PS)	1.9 ± 0.98	0.31	0.30	33
MM-2 (HT-*MM*-TLCT 120 ˚C 229 nm PS)	3.3 ± 2.45	0.30	0.18	20
MM-3 (HT-*MM*-TLCT 120 ˚C 354 nm PS)	3.0 ± 1.85	0.44	0.23	24
MM-4 (HT-*MM*-TLCT 120 ˚C 426 nm PS)	2.8 ± 1.74	0.34	0.28	26

Table 3.35: Surface composition properties obtained from XPS fitting.

The platinum content determined by ICP-MS corresponds to the metal present in the bulk and on the surface of the catalysts, as this technique does not discriminate between the two regions. As the size of metal nanoparticles increases (in the order MM-1 < MM-4 < MM-3 < MM2), the metal content on the surface of the catalysts decreases accordingly, due to the arrangement of platinum atoms on the bulk and surface of the catalyst, as previously illustrated in **Figure 3.53** (section 3.3.2 Characterisation of pore-expanded Pt-TLCT SBA-15 catalysts). Smaller particles prefer to be distributed on the surface of the catalyst in the form of PtO_2, as they are more capable of stabilising the oxide rather than the metal due to energy requirements, [47] and due to the fact that when platinum is exposed to the environment, it is more sensitive to oxidative processes. For this reason, the oxide content in **Table 3.35** decreases in inverse proportion to the particle size.

Figure 3.59 shows the detection of platinum on the macro-mesoporous TLCT SBA-15 catalysts.

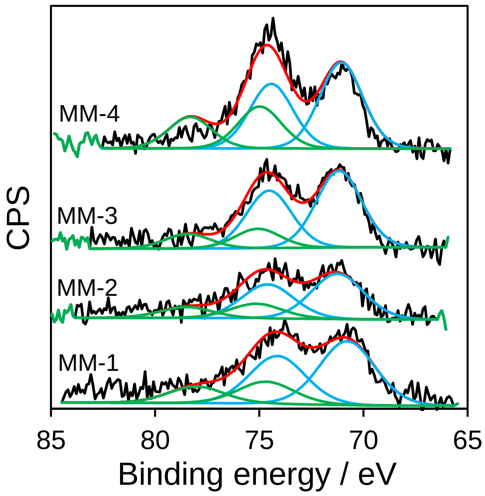

Figure 3.59: Pt 4f spectrum of MM-1, 2, 3, 4 catalysts (offset for clarity).

The black lines and the red lines indicate the raw data and the full envelope fitting of the region, respectively. Contributions due to $Pt^{(0)}$ (blue lines) and PtO_2 (green lines) fitted components are shown, revealing the emergence of the oxide feature, confirming that the formation of PtO_2 species is favoured on the surface of the catalysts.

The importance of the last two sections, (3.3.2 Characterisation of pore-expanded Pt-TLCT SBA-15 catalysts and 3.3.3 Characterisation of pore-expanded Pt-*MM*-TLCT SBA-15 catalysts), resides in the concept that diffusion of the molecules during a catalytic reaction occurs in a porous system, accordingly the shape and size of the pores are crucial for a productive catalyst. Therefore, optimised catalyst design requires larger pores to improve the accessibility of the catalyst for the reactants in addition to smaller pores providing high surface area and activity. The general idea is that larger pores inside a catalyst provide a bypass for diffusive transport of reactants inside the catalyst and thus improve the effective mass transport. [49] The advantages generated by the utilisation of the pore-expanded catalysts described in the previous paragraphs will be explicated in detail in the following section.

3.4. Platinum catalysed dodecyl aldehyde aerobic oxidation

The catalysts described in section 3.3 (Characterisation of platinum catalysts) have been designed with the final aim to improve diffusion, transportation and adsorption of large molecules throughout the porous network. In fact, reactant's internal diffusion is the main concern when applying SBA-15 materials in the catalysis of bulky molecules. Both meso- and macro-mesoporous architectures have been applied to the same catalytic reaction, namely the aerobic oxidation of dodecyl aldehyde (**Scheme 3.1**), to compare the internal mass transfer of the reactant inside a two-dimensional and a hierarchical system. Up to this date, there are no heterogeneous catalysed examples of this reaction reported in the literature.

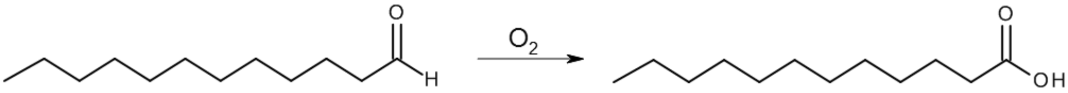

Scheme 3.1: Aerobic oxidation of dodecyl aldehyde to dodecanoic acid.

The aerobic oxidation of dodecyl aldehyde represents a clean and sustainable transformation for the production of a compound that finds applications in the antibiotic therapy of acne vulgaris, as dodecanoic acid possesses antimicrobial properties against skin bacterium *Propionibacterium acnes*, which promotes follicular inflammation (inflammatory acne); therefore it can be used as an alternative treatment for antibiotic therapy of acne vulgaris. Besides, it has stronger antimicrobial properties than that of benzoyl peroxide, one of the most frequently used topical medications for acne treatment. [50]

Dodecyl aldehyde's molecular diameter measures 1.6 nm (calculated with Materials Studio - Accelrys - software) if it is assumed that the molecule is always perfectly linear. Hence, its transportation inside small mesopores should be restricted, while it should be facilitated in bigger mesopores or upon introduction of macropores. The aim of utilising hierarchical supports for comparison with the mesoporous is demonstrating that the insertion of an additional porosity represents a way to overcome mass diffusion limitations often related to SBA-15 materials, whose restricted mesoporous network hinders the free movement of large molecules.

3.4.1. Catalytic results

In sections 3.3.1 (Characterisation of Pt-CO-OP SA SBA-15 catalyst), 3.3.2 (Characterisation of pore-expanded Pt-TLCT SBA-15 catalysts) and 3.3.3. (Characterisation of pore-expanded Pt-*MM*-TLCT SBA-15 catalysts) the characterisation of the platinum catalysts that will be screened in the present section has been presented in detail. The aim of carrying out the oxidation reaction with these materials consists of evaluating the catalytic performance of different synthetic routes (CO-OP SA *versus* TLCT) of SBA-15, and the feasibility of pore-expansion applied to TLCT silica supports in the aerobic oxidation of a large molecule. All the catalysts employed for this purpose, to which has been assigned a label, are listed in **Table 3.36**.

Catalyst name	**Pt wt%**	**SBA-15 type**	**Mesopores / nm**	**Macropores / nm**	**Particle size / nm (STEM)**
M-0	0.44	CO-OP SA	5.4	-	5.7 ± 1.6
M-1	0.26	TLCT	4.7	-	1.5 ± 0.9
M-2	0.31	HT-TLCT	6.0	-	1.7 ± 1.2
M-3	0.25		6.8	-	3.0 ± 1.7
MM-1	0.31	*MM*-TLCT	4.7	253 ± 28	1.9 ± 0.98
MM-2	0.30	HT-*MM*-TLCT	5.6	197 ± 18	3.3 ± 2.45
MM-3	0.44		5.8	287 ± 19	3.0 ± 1.85
MM-4	0.34		6.0	340 ± 24	2.8 ± 1.74

Table 3.36: Pt catalysts screened in the aerobic oxidation of dodecyl aldehyde.

As explained in Chapter 2, section 2.5.1. (Dodecyl aldehyde aerobic oxidation), the only product identified with Gas-Chromatography coupled with Mass-Spectrometry (GC-MS) has been dodecanoic acid, hence **Figure 3.60** (right) shows the obtained yield, while **Figure 3.60** (left) shows the conversion of the reactant at 24 hours, for all the catalysts listed in **Table 3.36**. Other minor side-products have not been identified; hence they remained unknown.

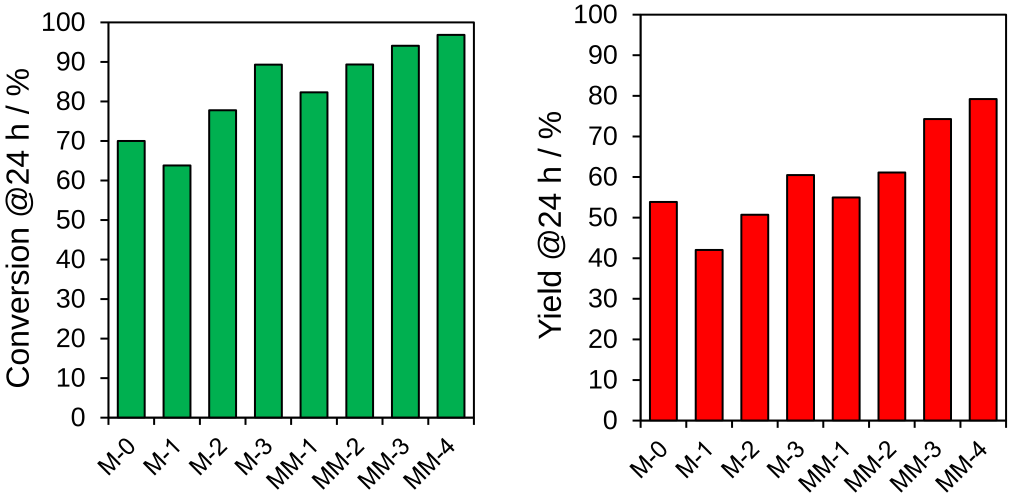

Figure 3.60: Dodecyl aldehyde conversion (left) and dodecanoic acid yield (right) at 24 h obtained with the catalysts in **Table 3.36**.

Comparing catalysts M-0 and M-1, whose pore diameters are 5.4 and 4.7 nm, respectively, after 24 hours, conversion and yield are slightly higher with the former, as larger pores promote better internal mass diffusion of the reactant inside the support architecture.

As expected, a substantial enhancement of reactant conversion, as well as acid yield, has been observed across the series of porous materials employed. Analysing the catalytic behaviour of the mesoporous Pt-TLCT and macro-mesoporous Pt-*MM*-TLCT SBA-15 materials, there is a gradual improvement in conversion and yield. This behaviour is due to increasing mesoporous diameter (M-1 to M-3 catalysts), which further on is combined with insertion of macropores, whose diameter increases from MM-2 to MM-4 catalysts. The internal mass diffusion of a bulky molecule has been clearly restricted in the silica network with a porous dimension of 4.7 nm (M-1). This material afforded ≈ 60% of dodecyl aldehyde conversion associated with ≈ 40% yield of dodecanoic acid. Both conversion and yield have improved with the pore diameter of the support. In fact, the biggest mesopore size (6.8 nm, M-3) afforded almost 90% conversion and 60% acid yield. These results are in agreement with the reactant internal diffusion facilitation in a more spacious porous architecture, as it occurs with the same probability in any direction of the reactant. When the mesopores and macropores measured 6 and 340 nm, respectively (MM-4), almost complete conversion has been achieved in 24 hours reaction.

The reason why M-3 catalyst showed a superior performance to MM-1, a hierarchical support, is due to the fact that even if M-3 does not include any macroporosity in its architecture, its mesopores are larger than those in MM-1, contributing to a better internal mass diffusion of the reactant. This demonstrates that mesopores represent the primary factor that promotes the transformation of the aldehyde, indicating that pores in the range of 5-10 nm allow the reactant (molecular diameter = 1.6 nm) to reach all the active sites distributed inside them, whereas pores in the range of 200-300 nm are extremely large and there is the possibility that the molecule passes through them without encountering a single metal nanoparticle, anchored to the pore walls. For the same reason, there is a catalytic improvement between MM-1 and MM-2 catalysts, due to a mesopore enlargement that overcomes the macropore shrinkage.

The mass balance of dodecyl aldehyde aerobic oxidation at 24 hours is presented in **Figure 3.61** for all catalysts:

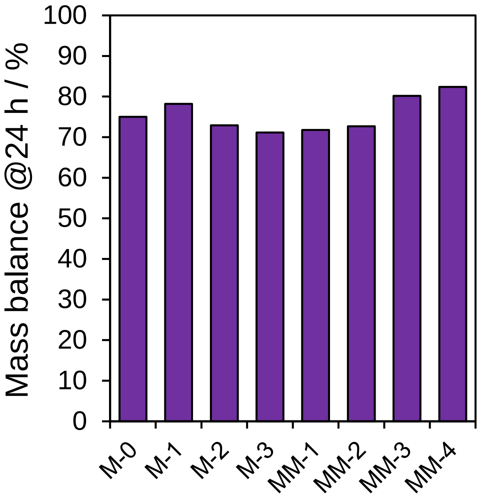

Figure 3.61: Mass balance at 24 h obtained with the catalysts in **Table 3.36**.

The total mass balance of the reaction, over all catalysts, varied between 71 and 82%. This parameter is related to the loss of carbon during the reaction, associated not only with some by-products that have not been identified with GC-MS, but also to the production of combustion products not detectable by gas-chromatography (CO and/or CO_2, typically formed during the oxidation of aldehydes), [51, 52] or to the sticking of by-products to the catalyst surface, or both events occurring at the same time. [52] Considering M-0 and M-1 catalysts, their mass balance profiles are very similar, although the balance related to the former appeared to be slightly lower due to a 7% conversion difference, which probably has produced a bigger percentage of side-products during the reaction.

A decrease in mass balance at 24 hours has been observed across the series of M-1, M-2 and M-3 catalysts (4.7, 6, 6.8 nm of mesopore diameter, respectively). The reason why this phenomenon occurs depends on the correlation between conversion and formation of products. In the case of highest conversion, both acid yield and formation of side-products are improved. This is due to the enhanced catalytic activity occurring in the case of the biggest pore-expanded catalyst, as pore diameter and surface area induce improved metal dispersion, which in turn helps to achieve better catalytic performance. When the pores are bigger, the reactant reaches more easily every single active site located inside the porous architecture. This situation is represented in **Figure 3.62**, which shows the chromatograms of the reactions with the three catalysts at 24 hours.

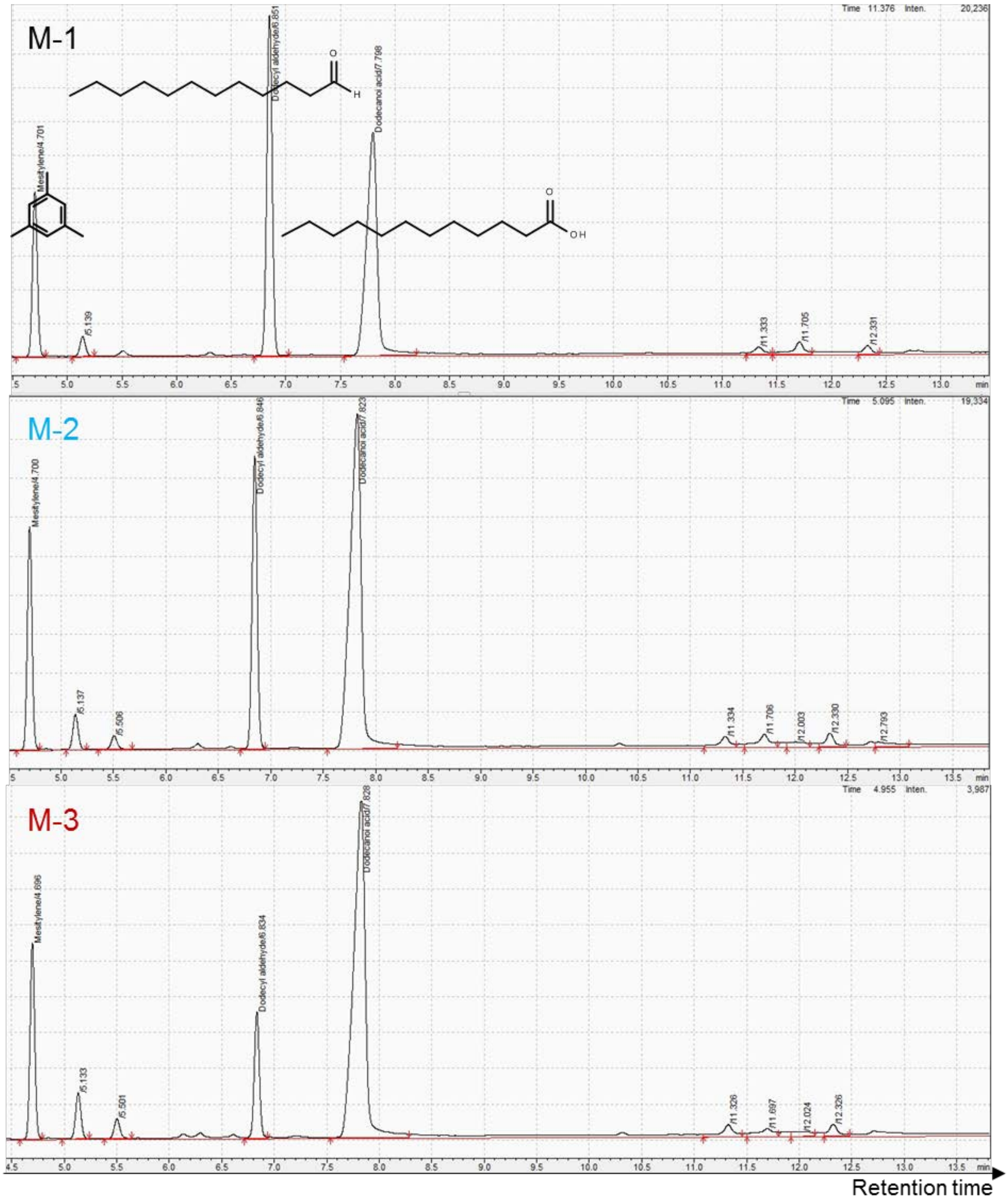

Figure 3.62: Chromatograms of dodecyl aldehyde aerobic oxidation at 24 h, with pore-expanded Pt-TLCT SBA-15 catalysts. The spectra show the presence of mesitylene (internal standard, 4.7 min), dodecyl aldehyde (6.8 min) and dodecanoic acid (7.8 min). The unidentified peaks represent the side-products of reaction. (GC Shimadzu-2010 Plus with AOC-20i autosampler fitted with a Zebron ZB-50 column: 30 m x 0.32 mm x 0.25 µm).

The chromatograms above show how the formation of by-products (not identified) slightly increased with aldehyde conversion, which in turn is related to its internal mass transportation inside the porous architecture of the materials. From the spectra, the change of aldehyde to acid peaks ratio from the 4.7 nm (M-1) to the 6.8 nm (M-3) catalysts is also evident, that highlights the importance of a larger porous network for the facile transportation of the reactant.

The total mass balances related to hierarchical materials (**Figure 3.61**) do not follow the same trend observed for pore-expanded mesoporous catalysts. In this instance, in fact, the opposite trend has been observed: the catalyst that promoted the lowest conversion due to smaller mesopores (MM-1), presented the lowest total mass balance as well, while for MM-4 catalyst almost total conversion and highest mass balance are reported. This indicates that the former catalyst promoted the loss of the highest content of carbon during the reaction. The chromatograms in **Figure 3.63** show aldehyde to acid ratios obtained with the pore-expanded hierarchical catalysts, as well as the presence of dodecyl aldehyde aerobic oxidation’s unidentified side-products, at 24 hours.

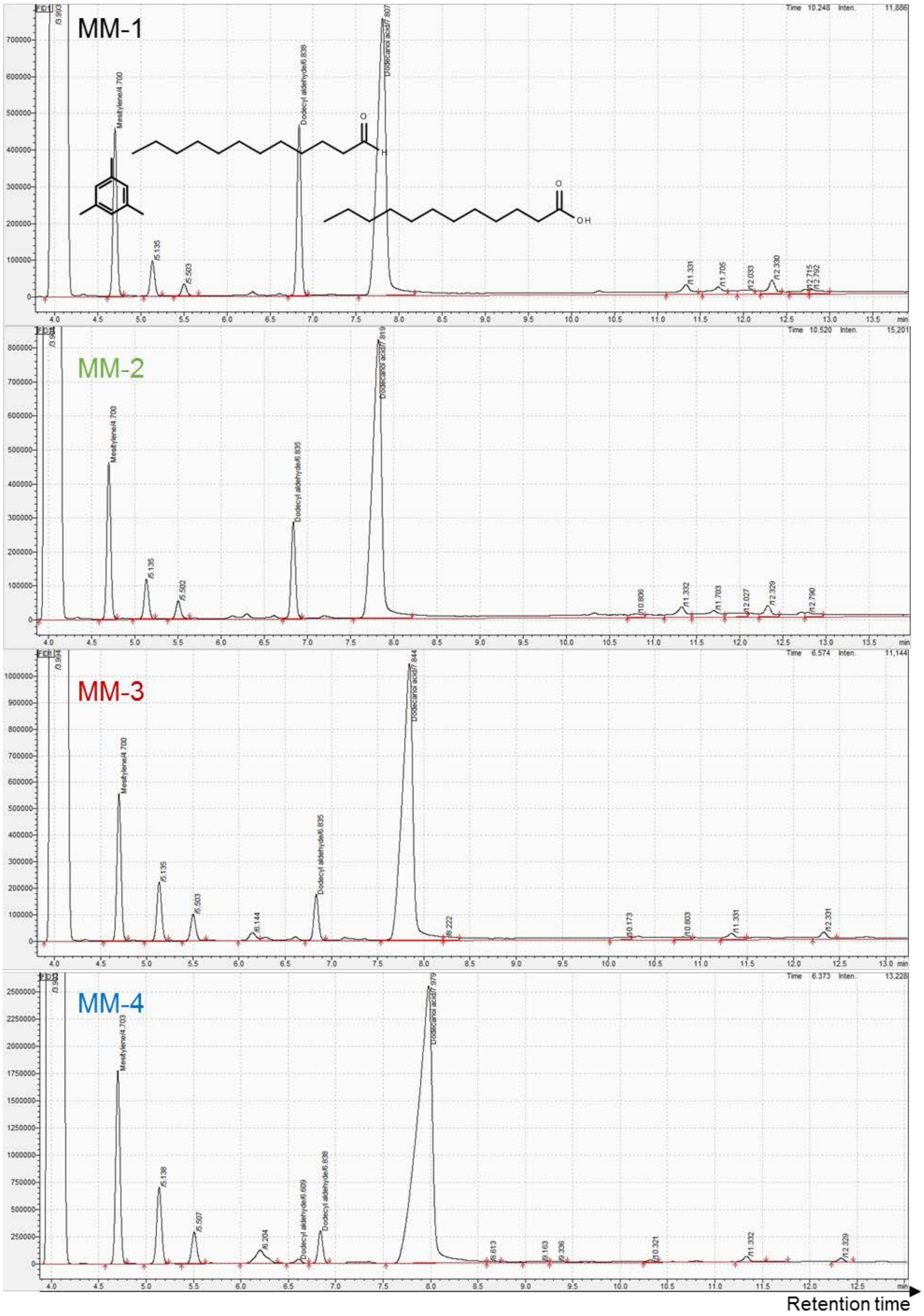

Figure 3.63: Chromatograms of dodecyl aldehyde aerobic oxidation at 24 h, with pore-expanded Pt-*MM*-TLCT SBA-15 catalysts. The spectra show the presence of mesitylene (internal standard, 4.7 min), dodecyl aldehyde (6.8 min) and dodecanoic acid (7.8 min). The unidentified peaks represent the side-products of reaction. (GC Shimadzu-2010 Plus with AOC-20i autosampler fitted with a Zebron ZB-50 column: 30 m x 0.32 mm x 0.25 µm).

The chromatograms above appear to show, as in the case of pore-expanded mesoporous catalysts (**Figure 3.62**), that the formation of unidentified by-products is promoted when aldehyde conversion is higher, which in turn is related to the pore diameter of the supports. This seems to be in contrast with what has been observed in the mass balance profiles; however, it can be explained by analysing the ratio of acid to by-products peaks. In the case of MM-4 catalysed reaction, even if the peaks related to the side-products have a bigger area than those in the MM-1 spectrum, their ratio to the acid peak is smaller. This indicates that, since the conversion with MM-4 catalyst is higher, the overall product formation is improved, but is shifted towards dodecanoic acid, that makes up for the majority of the total mass balance. Conversely, the MM-1 catalyst promotes lower conversion, which is shifted towards unidentified by-products formation, leading to lower carbon balance as those are not part of the mass balance calculation. **Figure 3.63** shows that the retention time of the peak associated with dodecanoic acid shifts towards higher values from MM-1 to MM-4 catalysts. This anomaly is due to a phenomenon called "fronting peak", which consists of a moderate to severe asymmetry towards the front or left side of the peak, which occurs when the GC column is overloaded as a result of injection volume and split ratio. [53] In the present case, this phenomenon might be caused by samples containing dodecanoic acid being injected in the GC. If their concentration is excessive for the column, it affects its performance. During the current research project, this circumstance has been observed when using carboxylic acids in progressively higher concentrations (i.e. during their calibration and during the course of aldehyde oxidation reactions, when the amount of the product increases over time), even with different chromatographic columns. As a consequence of fronting peaks, their position shifts towards higher retention times. **Figure 3.63** shows that this phenomenon is more pronounced than in **Figure 3.62**. This is due to the fact that the former presents data concerning hierarchical catalysts, which are able to produce a higher yield of dodecanoic acid than their mesoporous counterparts, thanks to the presence of macroporosity.

Analysing the conversion of dodecyl aldehyde in-depth over the different catalysts examined in this chapter, it is possible to infer their catalytic activity over the first 30 minutes of reaction. **Figure 3.64** shows platinum normalised initial rates (IR) of the reaction with all the catalysts, calculated from **equation 2.11** (Chapter 2, section 2.5.1. Dodecyl aldehyde aerobic oxidation).

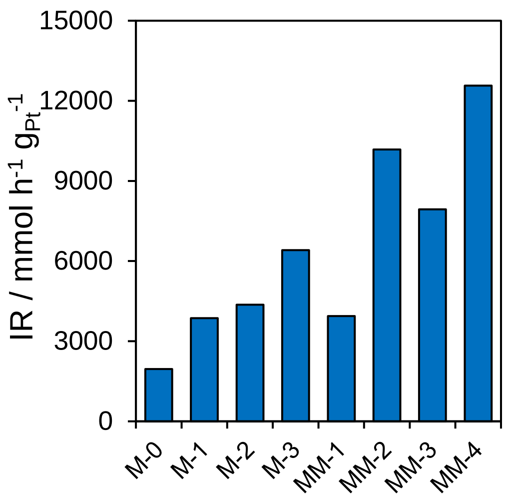

Figure 3.64: Pt normalised IR related to the catalysts in **Table 3.36**.

Despite M-0 catalyst producing a superior conversion over the whole reaction time (**Figure 3.60**, left), the rate at which aldehyde mmol have been converted during the first 30 minutes was lower than that obtained with TLCT support (M-1). When comparing these two catalysts, the higher initial rate of M-1 is mainly due to the fact that its metal loading is lower than that of M-0 catalyst (0.26 and 0.44wt%, respectively); therefore the parameter that influences the reaction rate is the dispersion of platinum, as lower content of metal corresponds to higher dispersion and smaller nanoparticles (1.5 ± 0.9 nm for M-1, 5.7 ± 1.6 nm for M-0). On the other hand, the support pore diameter has less influence in this regard as does not present a massive difference between the two catalysts (4.7 nm for M-1 and 5.4 nm for M-0). However, the rate of conversion of dodecyl aldehyde's mmol increased as the supports' pores expanded from 4.7 to 6.8 nm (M-1, M-2, M-3 catalysts). This confirms that the mass transfer of a bulky molecule takes advantage from a larger porous architecture, where it can more easily reach the active sites located inside the pores, and it is consistent with the higher conversions reached at 24 hours in **Figure 3.60** (left).

Metal dispersion is a key parameter that determines the activity of a catalyst because it describes how well the metal nanoparticles are distributed over the surface, and how many of them are the effective active sites for the catalytic transformation of the substrate. Dispersion is not only related to loading and particle size but also to support architecture. It has been previously demonstrated that platinum dispersion over non-porous support (i.e. fumed silica) is inferior to that of a porous support (SBA-15), which in turn is inferior to that of hierarchical support (*MM*-SBA-15). [54] This is due to the fact that a porous framework allows the nanoparticles to be distributed not only on the surface, as happens for fumed silica, but also inside the pores. When the architecture further improves the accessibility thanks to the insertion of an additional porosity, this feature is enhanced even more. During the course of this research project, it has not been possible to evaluate the dispersion of the materials utilised for catalysis with CO chemisorption analysis; however, the results presented in this chapter are in excellent agreement with what has been previously explained regarding the correlation between metal dispersion and catalytic activity. In fact, the improvement in conversion observed when using pore-expanded Pt-TLCT SBA-15 catalysts, which has been even more emphasised in the case of pore expanded Pt-*MM*-TLCT SBA-15 catalysts, depended upon the capability of the porous architectures to accommodate the metal nanoparticles with an improved degree of dispersion (smaller platinum particles for TLCT supports). This phenomenon is accompanied by the internal mass diffusion of dodecyl aldehyde inside pores of different size.

3.5. Conclusions

In the first instance, the present study has investigated the applicability of pore expansion methodologies to a different synthetic route for the production of one of the most used mesoporous materials in catalysis, namely SBA-15. Due to its inherent disadvantages to being used as support in the catalysis of large molecules, TLCT SBA-15's porous architecture has been successfully enlarged accordingly to its nature, less deformable than its conventional counterpart. At a later stage, the pore expansion methodology that afforded the best results has been extended to hierarchical *MM*-TLCT SBA-15 supports, which have never undergone such an expansion treatment (for both macro- and mesopores), up to this date.

As the study concerning the TLCT materials brought encouraging results, these have then been applied to the catalysis of a bulky molecule that can find applications in the medical field, for the antibiotic therapy of acne vulgaris. It has been demonstrated how the attentive choice of the type of support architecture is able to confer significant advantages in terms of internal diffusion and catalytic activity. The examination of conversion and product yield profiles has revealed the huge impact upon mesopore expansion or macropore introduction, evidencing the elimination of mass-transport barriers inherent in SBA-15 materials and thus vastly improved accessibility to mesopores wherein the majority of active site nanoparticles reside.

3.6. References

1. Zhao D., Feng J., Huo Q., Melosh N., Fredrickson G., Stucky G.D., Triblock copolymer syntheses of mesoporous silica with periodic 50 to 300 angstrom pores. Science, 1998. **279**(5350): p. 548-552.
2. Zhao D., Huo Q., Feng J., Chmelka B., Stucky G.D., Nonionic triblock and star diblock copolymer and oligomeric surfactant syntheses of highly ordered, hydrothermally stable, mesoporous silica structures. Journal of the American Chemical Society, 1998. **120**(24): p. 6024-6036.
3. Zhang F., Yan Y., Yang H., Meng Y., Yu C., Tu B., Zhao D., Understanding effect of wall structure on the hydrothermal stability of mesostructured silica SBA-15. The Journal of Physical Chemistry B, 2005. **109**(18): p. 8723-8732.
4. Dhainaut J., Dacquin J.P., Lee A.F., Wilson K., Hierarchical macroporous-mesoporous SBA-15 sulfonic acid catalysts for biodiesel synthesis. Green Chemistry, 2010. **12**(2): p. 296-303.
5. Dacquin J.P., Lee A.F., Pirez C., Wilson K., Pore-expanded SBA-15 sulfonic acid silicas for biodiesel synthesis. Chemical Communications, 2012. **48**(2): p. 212-214.
6. Wan Y., Zhao D., On the controllable soft-templating approach to mesoporous silicates. Chemical Reviews, 2007. **107**(7): p. 2821-2860.
7. Wainwright S.G., Parlett C.M.A., Blackley R., Zhou W., Lee A.F., Wilson K., True liquid crystal templating of SBA-15 with reduced microporosity. Microporous and Mesoporous Materials, 2013. **172**: p. 112-117.
8. Attard G.S., Glyde J.C., Goltner C.G., Liquid-crystalline phases as templates for the synthesis of mesoporous silica. Nature, 1995. **378**(6555): p. 366-368.
9. Kruk M., Jaroniec M., Ko C., Ryoo R., Characterization of the porous structure of SBA-15. Chemistry of Materials, 2000. **12**(7): p. 1961-1968.
10. Fulvio P.F., Pikus S., Jaroniec M., Tailoring properties of SBA-15 materials by controlling conditions of hydrothermal synthesis. Journal of Materials Chemistry, 2005. **15**(47): p. 5049-5053.
11. Celer E.B., Jaroniec M., Temperature-programmed microwave-assisted synthesis of sba-15 ordered mesoporous Silica. Journal of the American Chemical Society, 2006. **128**(44): p. 14408-14414.
12. Cao L., Man T., Kruk M., Synthesis of ultra-large-pore SBA-15 silica with two-dimensional hexagonal structure using triisopropylbenzene as micelle expander. Chemistry of Materials, 2009. **21**(6): p. 1144-1153.
13. Shan W., Wang W., Ru H., Siliceous mesocellular foams modified via a partitioned cooperative self-assembly process using hexane as pore swelling agent. Journal of Non-Crystalline Solids, 2015. **425**: p. 183-189.
14. Sun J., Zhang H., Ma D., Chen Y., Bao X., Klein-Hoffman A., Pfaender N., Su D., Alkanes-assisted low temperature formation of highly ordered SBA-15 with large cylindrical mesopores. Chemical Communications, 2005(42): p. 5343-5345.
15. Zhang H., Sun J., Ma D., Weinberg G., Su D., Bao X., Engineered complex emulsion system: toward modulating the pore length and morphological architecture of mesoporous silicas. The Journal of Physical Chemistry B, 2006. **110**(51): p. 25908-25915.

16. Nagarajan R., Solubilization of hydrocarbons and resulting aggregate shape transitions in aqueous solutions of Pluronic (PEO-PPO-PEO) block copolymers. Colloids and Surfaces B: Biointerfaces, 1999. **16**(1): p. 55-72.
17. Johansson E.M., Córdoba J.M., Odén M., The effects on pore size and particle morphology of heptane additions to the synthesis of mesoporous silica SBA-15. Microporous and Mesoporous Materials, 2010. **133**(1): p. 66-74.
18. Calin N., Galarneau A., Cacciaguerra T., Denoyel R., Fajula F., Epoxy-functionalized large-pore SBA-15 and KIT-6 as affinity chromatography supports. Comptes Rendus Chimie, 2010. **13**(1): p. 199-206.
19. Qiao W.J., Zhai S., Zhang F., Xiao Z., An Q., Song X., Correlation between pore-expanding and dye adsorption of platelet C/SBA-15 prepared by carbonization and oxidation of P123-TMB/SBA-15 composites. Journal of Sol-Gel Science and Technology, 2014. **70**(3): p. 451-463.
20. Ma J., Liu Q., Chen D., Wen S., Wang T., Synthesis and characterisation of pore-expanded mesoporous silica materials. Micro & Nano Letters, 2015. **10**(2): p. 140-144.
21. Chen S.Y., Chen Y., Lee J., Cheng S., Tuning pore diameter of platelet SBA-15 materials with short mesochannels for enzyme adsorption. Journal of Materials Chemistry, 2011. **21**(15): p. 5693-5703.
22. Kruk M., Cao L., Pore size tailoring in large-pore SBA-15 silica synthesized in the presence of hexane. Langmuir, 2007. **23**(13): p. 7247-7254.
23. Thielemann J., Girgsdies F., Schloegl R., Hess C., Pore structure and surface area of silica SBA-15: influence of washing and scale-up. Beilstein journal of nanotechnology, 2011. **2**: p. 110-8.
24. Owens G.J., Singh R.K., Foroutan F., Alqaysi M., Han C.M., Mahapatra C., Kim H.W., Knowles J.C., Sol-gel based materials for biomedical applications. Progress in Materials Science, 2016. **77**: p. 1-79.
25. Boissière C., Larbot A., Bourgaux C., Prouzet E., Bunton C.A., A study of the assembly mechanism of the mesoporous MSU-X silica two-step synthesis. Chemistry of Materials, 2001. **13**(10): p. 3580-3586.
26. Zana R., Micellization of amphiphiles: selected aspects. Colloids and Surfaces A: Physicochemical and Engineering Aspects, 1997. **123-124**: p. 27-35.
27. Shen S.C., Kawi S., Understanding of the effect of al substitution on the hydrothermal stability of MCM-41. The Journal of Physical Chemistry B, 1999. **103**(42): p. 8870-8876.
28. Wang J., Ge H., Bao W., Synthesis and characteristics of SBA-15 with thick pore wall and high hydrothermal stability. Materials Letters, 2015. **145**: p. 312-315.
29. Fan J., Yu C., Tu B., Zhao D., Sakamoto Y., Teresaki O., Mesotunnels on the silica wall of ordered SBA-15 to generate three-dimensional large-pore mesoporous networks. Journal of the American Chemical Society, 2001. **123**(48): p. 12113-12114.
30. Groen J.C., Peffer L.A.A., Pérez-Ramírez J., Pore size determination in modified micro- and mesoporous materials. Pitfalls and limitations in gas adsorption data analysis. Microporous and Mesoporous Materials, 2003. **60**(1): p. 1-17.
31. Burgess C.G.V., Everett D.H., The lower closure point in adsorption hysteresis of the capillary condensation type. Journal of Colloid and Interface Science, 1970. **33**(4): p. 611-614.

32. Cychosz K.A., Guillet-Nicolas R., García-Martínez J., Thommes M., Recent advances in the textural characterization of hierarchically structured nanoporous materials. Chemical Society Reviews, 2017. **46**(2): p. 389-414.
33. Qiu Y., Chen S., Wang C., Lyu R., Zhang D., Liu C., Zhang Y., Li J., Preparation of SBA-15 with penetrating pores and their performance in Fischer-Tropsch synthesis. New Journal of Chemistry, 2017. **41**(23): p. 14109-14115.
34. Qu F., Lin H., Wu X., Li X., Qui S., Zhu G., Bio-templated synthesis of highly ordered macro-mesoporous silica material for sustained drug delivery. Solid State Sciences, 2010. **12**(5): p. 851-856.
35. Sen T., Tiddy G., Casci J., Anderson M., Synthesis and characterization of hierarchically ordered porous silica materials. Chemistry of Materials, 2004. **16**(11): p. 2044-2054.
36. Vinke P., de Wit D., de Goede A., van Bekkum H., Noble metal catalyzed oxidation of carbohydrates and carbohydrate derivatives. Studies in Surface Science and Catalysis, P. Ruiz and B. Delmon, Editors. 1992, Elsevier. p. 1-20.
37. Mallat T., Baiker A., Oxidation of alcohols with molecular oxygen on platinum metal catalysts in aqueous solutions. Catalysis Today, 1994. **19**(2): p. 247-283.
38. Gallezot P., Selective oxidation with air on metal catalysts. Catalysis Today, 1997. **37**(4): p. 405-418.
39. Besson M., Gallezot P., Selective oxidation of alcohols and aldehydes on metal catalysts. Catalysis Today, 2000. **57**(1): p. 127-141.
40. Kluytmans J.H.J., Markusse J., Kuster B., Marin G., Schoten J., Engineering aspects of the aqueous noble metal catalysed alcohol oxidation. Catalysis Today, 2000. **57**(1): p. 143-155.
41. Song H., Rioux R., Hoefelmeyer J., Komor R., Niesz K., Somoriaj G.A., Hydrothermal growth of mesoporous SBA-15 silica in the presence of PVP-stabilized Pt nanoparticles: synthesis, characterization, and catalytic properties. Journal of the American Chemical Society, 2006. **128**(9): p. 3027-3037.
42. Giovanetti L.J., Ramallo-Lopez J., Foxe M., Jones L., Koebel M., Requejo F., Shape changes of Pt nanoparticles induced by deposition on mesoporous silica. Small, 2012. **8**(3): p. 468-473.
43. Zhu J., Kailasam K., Xie X., Shomaeker R., Arne T., High-surface-area SBA-15 with enhanced mesopore connectivity by the addition of poly(vinyl alcohol). Chemistry of Materials, 2011. **23**(8): p. 2062-2067.
44. Pushkarev V.V., Musselwhite N., An K., Alayoglu S., Somorjai G.A., High structure sensitivity of vapor-phase furfural decarbonylation/hydrogenation reaction network as a function of size and shape of Pt nanoparticles. Nano Letters, 2012. **12**(10): p. 5196-5201.
45. Ghampson I.T., Newman C., Kong L., Pier E., Hurley K., Frederick B., Austin R., Effects of pore diameter on particle size, phase, and turnover frequency in mesoporous silica supported cobalt Fischer-Tropsch catalysts. Applied Catalysis A: General, 2010. **388**(1): p. 57-67.
46. Saib A.M., Claeys M., van Steen E., Silica supported cobalt Fischer-Tropsch catalysts: effect of pore diameter of support. Catalysis Today, 2002. **71**(3): p. 395-402.
47. Durndell L.J., Parlett C.M.A., Hondow N., Wilson K., Lee A.F., Tunable Pt nanocatalysts for the aerobic selox of cinnamyl alcohol. Nanoscale, 2013. **5**(12): p. 5412-5419.

48. Song S., Wang K., Liu Y., He C., Wang Y., Highly ordered mesoporous carbons as the support for Pt catalysts towards alcohol electrooxidation: the combined effect of pore size and electrical conductivity. International Journal of Hydrogen Energy, 2013. **38**(3): p. 1405-1412.
49. Becker H., Güttel R., Turek T., Enhancing internal mass transport in Fischer-Tropsch catalyst layers utilizing transport pores. Catalysis Science & Technology, 2016. **6**(1): p. 275-287.
50. Nakatsuji T., Kao M., Fang J., Zouboulis C., Zhang L., Gallo R., Huang C., Antimicrobial property of lauric acid against propionibacterium acnes: its therapeutic potential for inflammatory acne vulgaris. Journal of Investigative Dermatology, 2009. **129**(10): p. 2480-2488.
51. Rucinska E., Miedziak P., Pattisson S., Brett G., Iqbal S., Morgan D., Hutchings G.J., Cinnamyl alcohol oxidation using supported bimetallic Au-Pd nanoparticles: an investigation of autoxidation and catalysis. Catalysis Science & Technology, 2018. **8**(11): p. 2987-2997.
52. Ide M.S., Falcone D.D., Davis R.J., On the deactivation of supported platinum catalysts for selective oxidation of alcohols. Journal of Catalysis, 2014. **311**: p. 295-305.
53. Phenomenex, GC troubleshooting guide. 2014: p. 1-43.
54. Durndell L.J., Cucuzzella C., Parlett C.M.A., Isaacs M.A., Wilson K., Lee A.F., Platinum catalysed aerobic selective oxidation of cinnamaldehyde to cinnamic acid. Catalysis Today, 2018. **333**: p.161-168.

CHAPTER 4:

Cinnamaldehyde aerobic oxidation

The aerobic oxidation of cinnamaldehyde, a lignin-derived chemical [1, 2] and the main component of cassia oil [3] and cinnamon bark oil, [3, 4] represents a sustainable and environmentally friendly molecular transformation for the production of cinnamic acid and benzaldehyde. The latter is an important intermediate for perfumes, organic synthesis and pharmaceuticals, [5] and its synthesis via oxidative cleavage of cinnamaldehyde has been widely investigated over the past decades. Cinnamic acid is an organic acid with low toxicity present naturally in all green plants [6] and, together with its derivatives, is a promising compound to be developed in the medical field. The formation of both benzaldehyde and cinnamic acid has been proven to occur spontaneously when starting from cinnamaldehyde with heat and atmospheric oxygen, as some examples in literature confirm. [7-10]

Traditionally, the oxidation of cinnamaldehyde to cinnamic acid is carried out by using stoichiometric amounts of toxic and hazardous inorganic agents, such as chromates, [11] permanganates [12] and hydrogen peroxide, [13] which lead to the production of contaminated waste and consequently represent a danger for the environment. On the other hand, the use of heterogeneous catalysis based on supported transition metal nanoparticles in catalytic amounts offers a sustainable and green alternative, as it uses air as the oxidant, which is inexpensive and non-toxic. However, contrary to benzaldehyde, heterogeneously catalytic methods for the synthesis of cinnamic acid have not been developed to date. Platinum group metals have been successfully employed as heterogeneous catalysts for the selective aerobic oxidation of various alcohols and aldehydes [14-18] but, specifically, the selective oxidation of cinnamaldehyde to cinnamic acid remains mostly unexplored. However, initial attempts have been recently made in this regard. [19] The first part of the current chapter is based on the study of the reaction mechanism, by considering only oxygen pressure and concentration in the synthesis of the desired product, cinnamic acid. Once the role of oxygen has been rationalised, the reaction has been examined catalytically in order to study the effect of platinum nanoparticles on fumed silica. Contrary to the previous chapter, a non-porous material has been employed as a support due to the need to lay the foundations on a reaction that is still unknown from a heterogeneous catalysis perspective.

4.1. Results and discussion

Cinnamaldehyde aerobic transformation leads to the fast and spontaneous formation of cinnamic acid and benzaldehyde (and other minor products), however, it is possible to control the formation of the former, by cautiously tailoring the conditions under which the reaction is carried out. The role of oxygen and the role of platinum have been proven to be critical in this regard. Both contributions will be examined separately in the two following sections, in order to analyse their effect independently and convey the results in the clearest possible way.

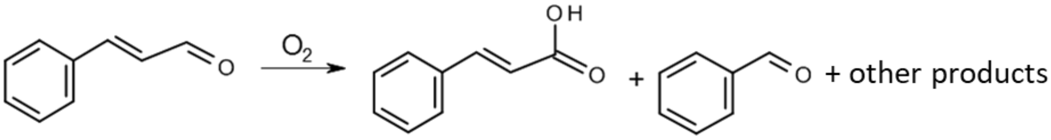

Scheme 4.1: Aerobic oxidation of cinnamaldehyde to cinnamic acid and benzaldehyde.

4.1.1. Role of oxygen concentration and pressure

The overall reaction is driven by a radical mechanism, as previously demonstrated by several research groups, among which Hutchings, [10] Costa [20] and Harden, [7] and confirmed in the present study with the use of an oxygen radical scavenger, hydroquinone (HQ). It was observed that hydroquinone inhibited cinnamaldehyde conversion in inverse proportion to the oxygen pressure applied to the system (**Figure 4.1**).

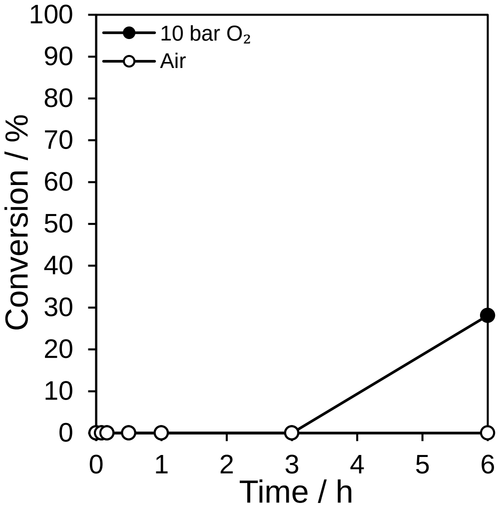

Figure 4.1: Cinnamaldehyde conversion in presence of HQ (0.02 mmol in 8.4 mmol of cinnamaldehyde), under air and 10 bar O_2 (without catalyst).

As shown in **Figure 4.1**, a small amount of hydroquinone is able to completely inhibit conversion when the generation of oxygen radical is limited by the use of air.

Conversely, when high-pressure oxygen is used, the generation of radicals is so high that the scavenger effect of hydroquinone is partially eclipsed.

This result is related to the amount of oxygen radicals generated in the reaction mixture: the higher the oxygen partial pressure, the more radicals are available to promote the conversion of cinnamaldehyde, partially overcoming the effect of the scavenger, in the presence of which 30% of the reactant is converted after 6 hours.

To assess cinnamaldehyde sensitivity to oxygen partial pressure, four experiments under different conditions were performed (in the absence of radical scavenger): under nitrogen, air (21% O_2), 1 bar and 10 bar O_2. Conversions and product selectivities were compared over 24 hours (**Figure 4.2**).

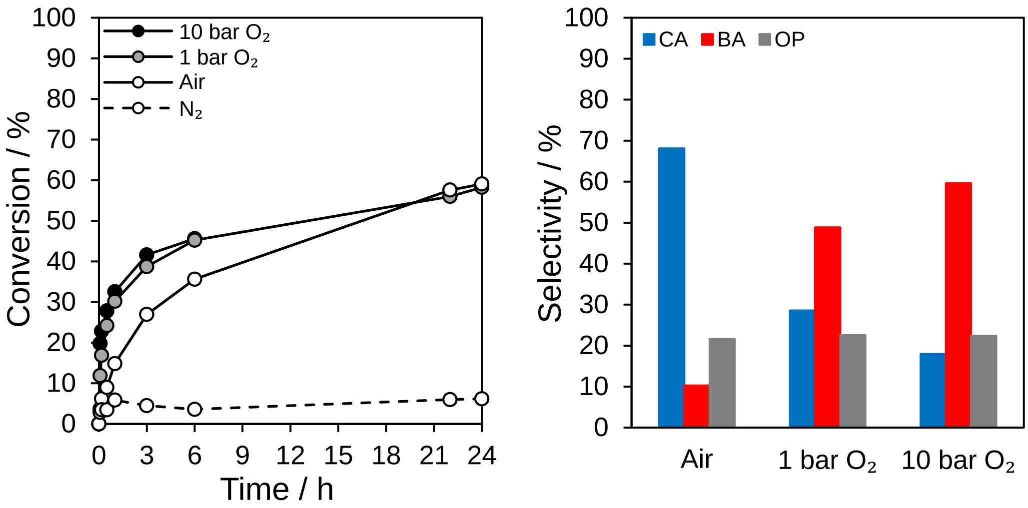

Figure 4.2: Effect of O_2 pressure on cinnamaldehyde conversion (left) and on product selectivities at 25% conversion (right), at different O_2 pressures (without catalyst), (CA = cinnamic acid, BA = benzaldehyde, OP = other products).

Having previously clarified that cinnamaldehyde conversion is an overall radical process, **Figure 4.2** (left) shows that it is also oxygen dependent. When running the reaction under pure nitrogen, negligible conversion was obtained (6%). On the other hand, it is noticeable how conversion is susceptible to oxygen: during the first 6 hours of reaction, applying a low amount of oxygen (air) strongly improves the conversion, when compared to pure nitrogen. At even higher pressures, when oxygen quickly saturates the environment, more reactant is converted during the first 6 hours, but no significant difference is observed between 1 and 10 bar. However, over a longer period of time, the amount of oxygen is no longer critical for conversion, which does not exceed 60% regardless of the pressure applied. The explanation of this behaviour is that lower oxygen pressure saturates cinnamaldehyde more slowly if compared to 1 bar pressure. Also, is not possible to reach complete conversion of the reactant, as after three days a stable equilibrium (≈ 80%) is obtained, under different oxygen pressures (**Figure 4.3**).

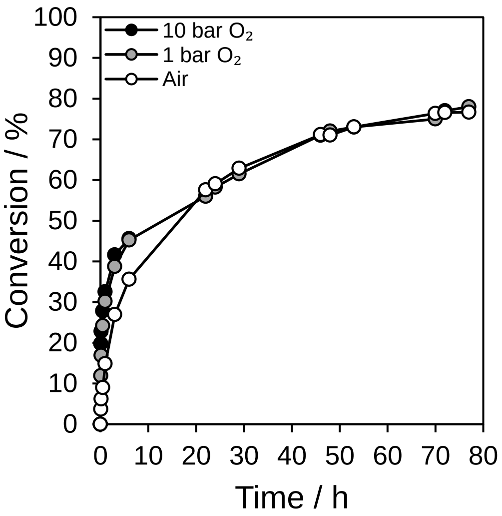

Figure 4.3: The equilibrium for cinnamaldehyde aerobic oxidation conversion is obtained after 3 days (without catalyst).

In the presence of oxygen, both benzaldehyde and cinnamic acid are formed spontaneously – without the need of a catalyst – and their selectivities depend on the oxygen pressure applied to the system (**Figure 4.2**, right). As their formation does not require the use of a catalyst, it can be stated that both are autoxidation products. Autoxidation is a very common process that takes place in almost every oxidation process, and it is generally known for having a radical nature. [21] The fact that both products are formed radically finds further proof in **Figure 4.1**, as the only effect the radical scavenger has on the reaction is an initial inhibition on cinnamaldehyde conversion. The extent of the scavenger's inhibition depends on the oxygen pressure applied to the system. The inhibition stops once all the available radical trap sites have interacted with the oxygen radicals so that these are free in the gas stream and able to initiate conversion. In other words, as soon as the scavenger is consumed and not able to neutralise the radicals anymore, these can again interact with cinnamaldehyde, which is now able to evolve.

Figure 4.4 shows the impact of hydroquinone on conversion and selectivities patterns under 10 bar O_2 pressure, compared to the reaction carried out without radical scavenger.

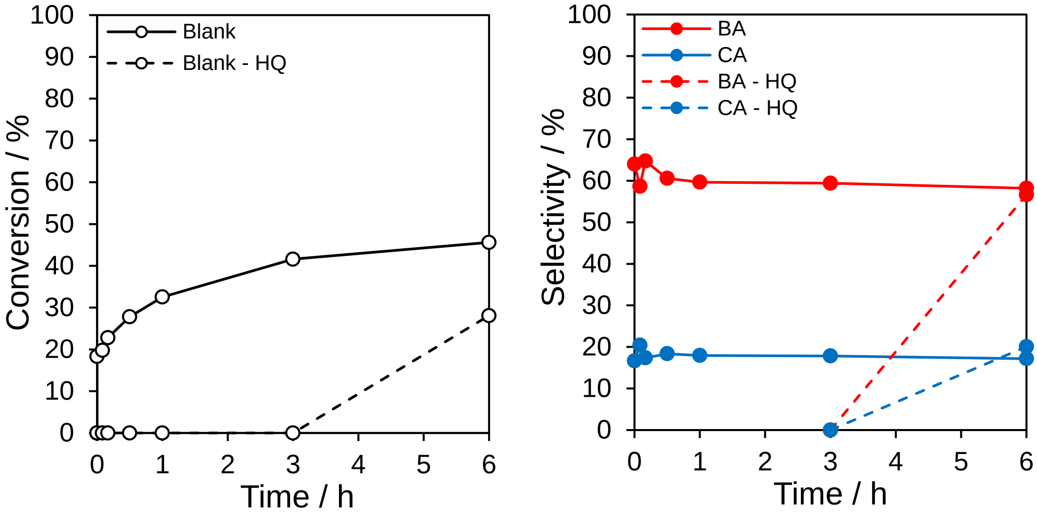

Figure 4.4: Comparison of conversion (left) and selectivity patterns (right) in absence and in presence of HQ (0.02 mmol in 8.4 mmol of cinnamaldehyde) at 10 bar O_2 (without catalyst), (CA = cinnamic acid, BA = benzaldehyde).

In **Figure 4.4** (left) is clearly shown the difference that the scavenger causes to the conversion profile. In the first 3 hours of reaction, the conversion is inhibited by the interaction of the hydroquinone with oxygen radicals. Later on, the amount of radicals very high, the effect of hydroquinone is partially overcome, and the free radicals allow cinnamaldehyde to be converted, even though not as much as it does when hydroquinone does not participate. The outcome of the conversion is then shown in **Figure 4.4** (right). In the presence of radical scavenger, the products are formed from 3 hours onwards, but the final selectivities are equal to those obtained in the absence of a scavenger, indicating that the only effect hydroquinone has is inhibition of conversion, without favouring one or the other product. Hence, the radical nature of cinnamic acid and benzaldehyde is confirmed by the fact that both are formed with the same selectivity in the presence and absence of a radical trap, once the radical trap has been consumed and oxygen radicals are free to react with cinnamaldehyde.

Examining in-depth the behaviour of cinnamaldehyde aerobic oxidation in the absence of a radical trap, it is noteworthy that during the first 6 hours of reaction, cinnamaldehyde conversion seemed to benefit when a higher amount of oxygen was present in the gas stream (**Figure 4.2**, left). Nevertheless, the selectivity ratio of cinnamic acid to benzaldehyde seemed to benefit from the opposite situation, that is, with a lower oxygen pressure in the reaction environment (**Figure 4.2**, right).

Even though both products are formed via radical pathways, benzaldehyde (red bar, **Figure 4.2**, right) is favoured when higher oxygen pressure is applied, and it seems to be the result of cinnamaldehyde oxidative cleavage. [4, 7] On the other hand, cinnamic acid (blue bar), the desired product, is generated in higher selectivity at lower oxygen partial pressure. As a result, the oxygen pressure applied to the system was crucial in terms of product selectivities, as the amount of oxygen radicals present in the gas stream controls the product distribution. Also, even though using air as the oxidative agent does not allow cinnamaldehyde to be converted as fast as with higher oxygen pressure (**Figure 4.2**, left), this operating condition is more convenient in terms of selectivity. Hence it can be stated that cinnamic acid formation benefits from the use of air.

In literature the reaction mechanism of hydroquinone as an antioxidant has been extensively explained. [22, 23] It consists of hydrogen atom abstraction by a peroxy radical species (ROO•) to generate a semiquinone radical that in turn reacts with oxygen or another peroxy radical, to afford 1,4-benzoquinone. However, when hydroquinone is used as a radical scavenger in the present study to assess whether the mechanism follows a free radical pathway, it is assumed that no peroxy radical is present in the reaction environment, or pre-formed, as cinnamaldehyde conversion is suppressed in the presence of hydroquinone (or at least at the beginning of the reaction, **Figure 4.1**). Therefore it is assumed that the mechanism proposed by Valgimigli [22] or Bendary [23] does not apply to the present case, and a different mechanism of interaction between hydroquinone and oxygen, a diradical species, [21] has been proposed (**Scheme 4.2**), taking into account that the starting aldehyde is not interacting with the scavenger (**1**) to form ROO• species.

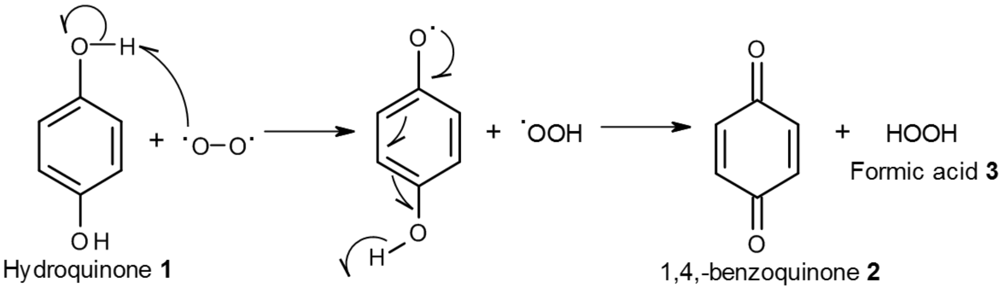

Scheme 4.2: Proposed mechanism of HQ interacting with O_2 radicals.

This proposed mechanism explains the reason why cinnamaldehyde, in the presence of hydroquinone **1**, does not evolve to any product for the whole reaction under air and, when oxygen pressure is higher, its conversion is initially suppressed (**Figure 4.1**). Hydroquinone is transformed into its corresponding diketone (1,4-benzoquinone **2**) by the oxygen radicals present in the reaction environment, preventing these from interacting with cinnamaldehyde. When a higher amount of oxygen radicals is participating in the reaction (10 bar O_2), only part of them are consumed by the scavenger. Once the latter is consumed, oxygen radicals are again free in the gas stream and able to convert cinnamaldehyde (**Figure 4.4**, left). When more hydroquinone participates in the reaction, even at high pressure, the conversion is fully suppressed because the amount of scavenger is enough to prevent all oxygen radicals from reacting with cinnamaldehyde (**Figure 4.5**).

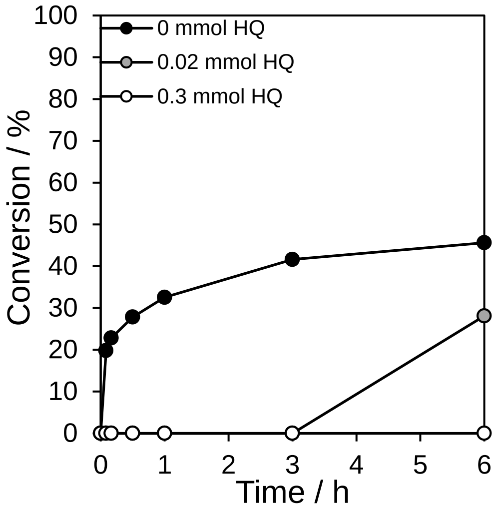

Figure 4.5: Effect of HQ on cinnamaldehyde conversion (10 bar O_2, without catalyst).

As further evidence for the validity of **Scheme 4.2**, traces of 1,4-benzoquinone **2** and formic acid **3** were detected with Gas-Chromatography coupled with Mass-Spectrometry (GC-MS) when hydroquinone participated in the reaction.

After elucidating the rationale behind the mechanism occurring when hydroquinone and oxygen come in contact with each other, it has been found the most favourable condition to control the formation of benzaldehyde, the undesired by-product that prevents the selective formation of cinnamic acid. Due to the intrinsic nature of the aerobic oxidation of cinnamaldehyde, benzaldehyde formation is not entirely avoidable, but it was found to be controllable to a certain extent, i.e. controlling the oxygen pressure applied to the reaction.

Ever since it has been discovered that aldehydes convert into their corresponding acids in air, [24] the general reaction mechanism has been widely investigated. It has been established that it follows a radical pathway, where the aldehyde is oxidised to the corresponding peracid, which further reacts with the original aldehyde to form the carboxylic acid through a non-radical mechanism. It is well known that free radical chain processes involve a series of steps, i.e. initiation, propagation and termination. [25-28] As molecular oxygen in its ground state is a diradical species existing in a triplet spin state ($^3\Sigma_g^-$), it can react with organic substrates via autoxidation pathways, typically not driven by a catalyst. [21] **Scheme 4.3** illustrates these reaction steps, specifically for cinnamaldehyde:

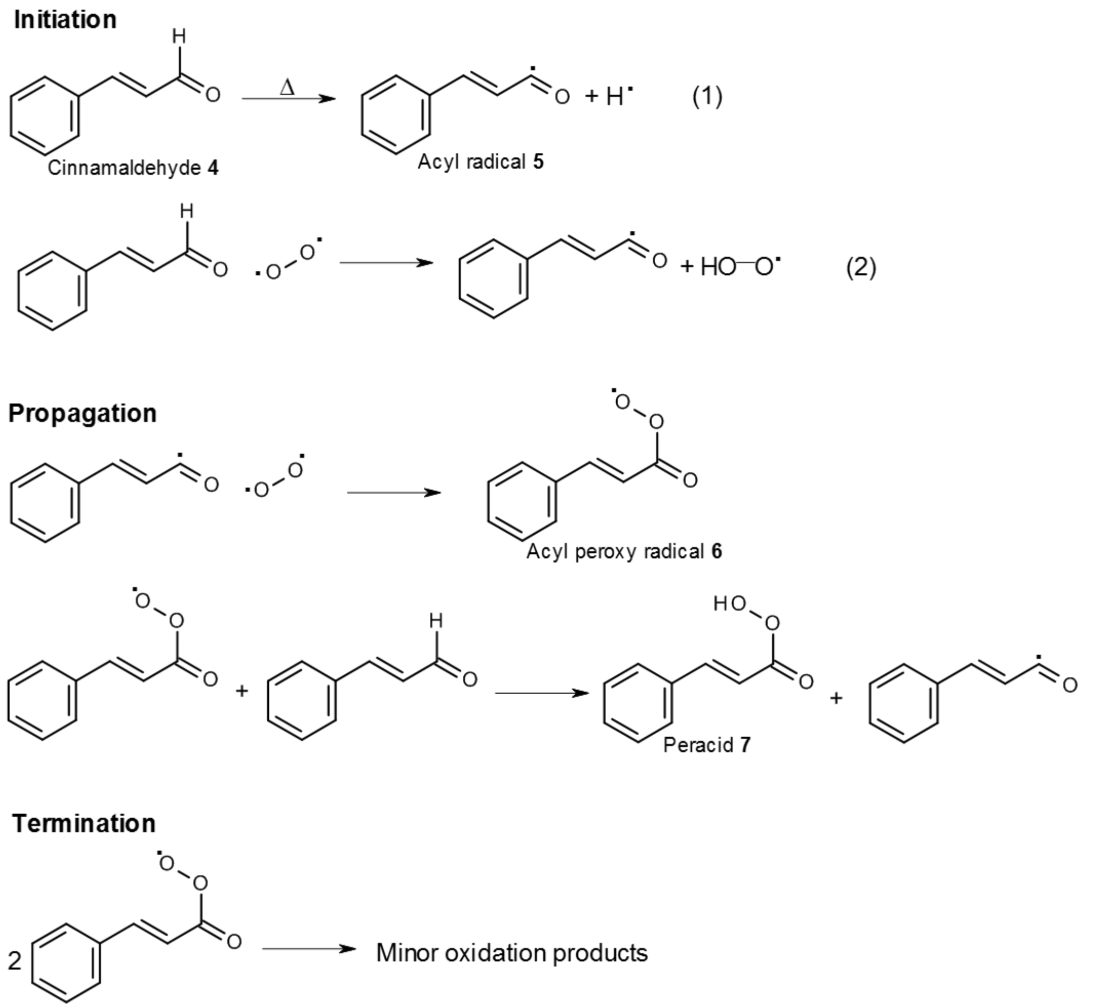

Scheme 4.3: Initiation, propagation and termination steps of the free radical process that involves cinnamaldehyde and O_2 (adapted from ref. [25-28]), (Δ = temperature).

Examining the initiation step occurring in the scheme reported above, cinnamaldehyde **4** seems to be more temperature than light sensitive, as the experiments carried out to test its activation showed (**Figure 4.6**).

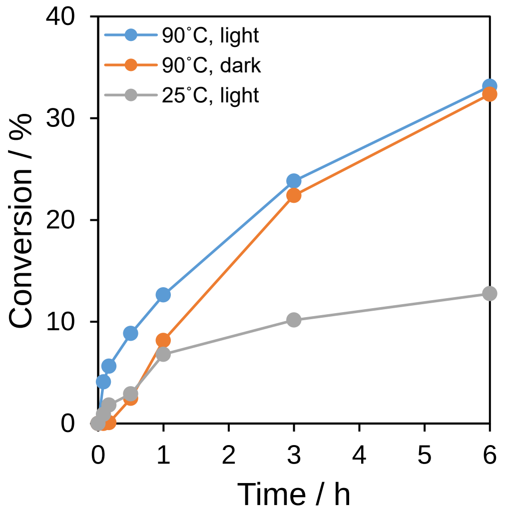

Figure 4.6: Study on cinnamaldehyde activation effect, with heat and light.

Studying the evolution of cinnamaldehyde under different conditions (25 and 90 ˚C, dark and light), it has been concluded that at the standard reaction temperature (90 ˚C) the overall conversion is similar in a dark and a lit environment, despite under the dark condition the initial conversion is slowed down. At room temperature, on the other hand, the reactant has been converted three times less.

Therefore, the initiation step in **Scheme 4.3** can occur either following equation (1) [28] (thermal homolytic cleavage) or (2), [27] however in both cases cinnamaldehyde decomposes to its corresponding acyl radical **5**, essential for the continuation of the chain process. During the first step of propagation, diradical oxygen reacts with the acyl radical to afford the acyl peroxy radical species **6**, which in turn abstracts the aldehydic hydrogen to another aldehyde molecule to give the peracid **7** and another acyl radical. This step occurs with a relatively high rate constant, [27] because the bond dissociation energy (BDE) of the formyl C-H bond is weaker than that of a typical bond between hydrogen and a sp^2-hybridised carbon. This is the reason why aldehydes are prone to undergo hydrogen abstraction in the presence of free radicals (in this case the acyl peroxy radical), a fact that accounts for the ease with which aldehydes undergo autoxidation. [26] In the termination step, the acyl peroxy radical **6** recombines, leading to minor oxidation products, such as alcohols, aldehydes or ketones. [27]

However, according to Marteau and co-workers, [27] the formation of cinnamic acid itself is a non-radical process, because it stems from the addition of the peracid **7** (formed during the propagation step in **Scheme 4.3**) on the starting aldehyde through the Baeyer-Villiger rearrangement (**Scheme 4.4**, right).

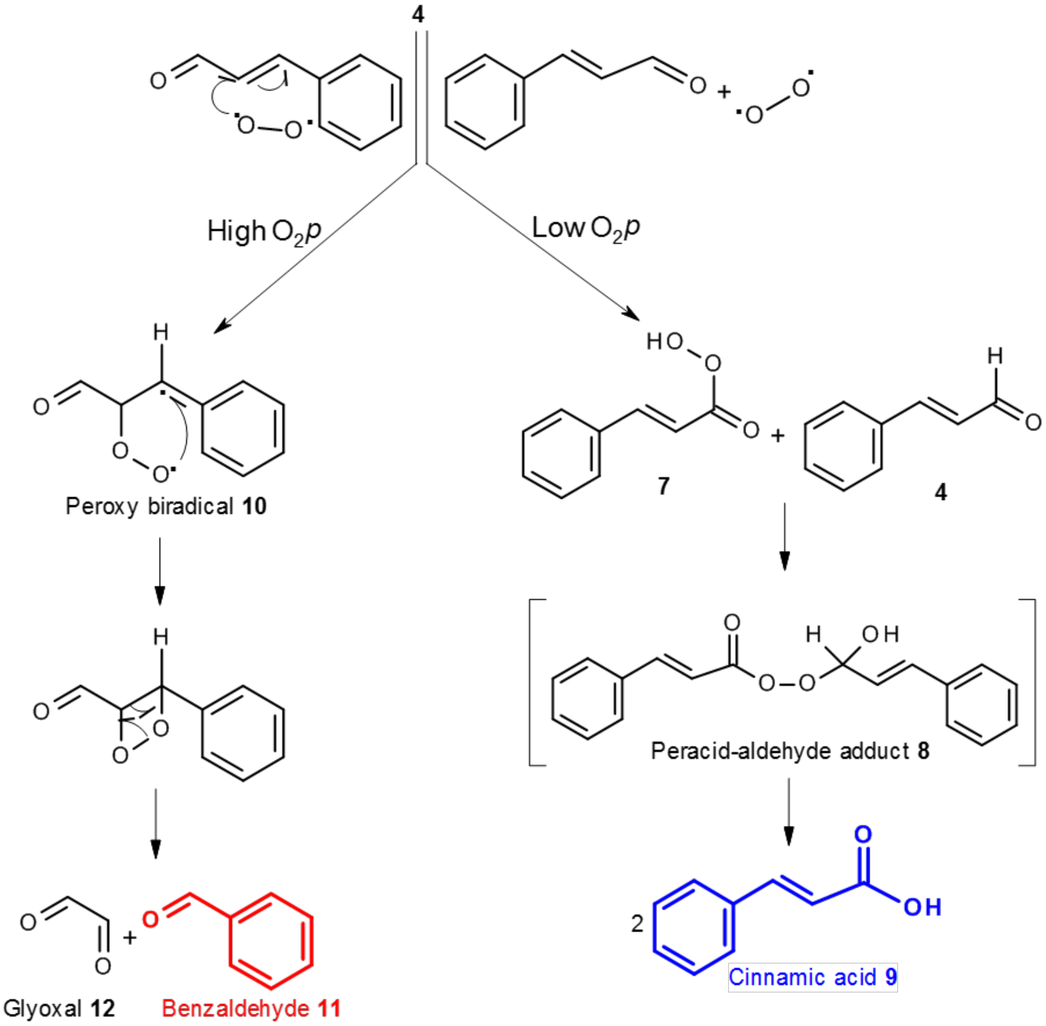

Scheme 4.4: Postulated radical mechanism of formation of benzaldehyde (adapted from ref. [7]) and cinnamic acid under different oxygen partial pressures (adapted from ref. [25-28]).

As it is possible to appreciate from **Scheme 4.4** (right), the Baeyer-Villiger mechanism consists of the addition of the peracid **7** on to the carbonyl group of cinnamaldehyde **4**, forming a peracid-aldehyde adduct **8**. After migration of the aldehydic hydrogen onto the oxygen atom on the *ipso*-carbon, two molecules of the final cinnamic acid **9** are obtained.

On the other hand, the most plausible mechanism for benzaldehyde formation, among many proposed in the literature, seems to be the one suggested by Harden and co-workers [7] (**Scheme 4.4**, left). They only consider the presence of oxygen that, in contact with cinnamaldehyde, first generates a peroxy biradical **10** that undergoes a heat-induced elimination (carbon-carbon bond cleavage) to benzaldehyde **11** and glyoxal **12**. They did not observe the presence of the latter, and neither was identified in the present study. This might be because glyoxal has low molecular weight and boiling point, therefore either is not detectable by gas-chromatography, or its peak is superimposed with others (e.g. the solvent of reaction). In addition, contrary to what the authors mentioned above suggested, the present work has demonstrated that the carbon-carbon bond cleavage to benzaldehyde is not heat-induced, as benzaldehyde selectivity is favoured at lower temperatures. In contrast, cinnamic acid follows the opposite trend (**Figure 4.7**).

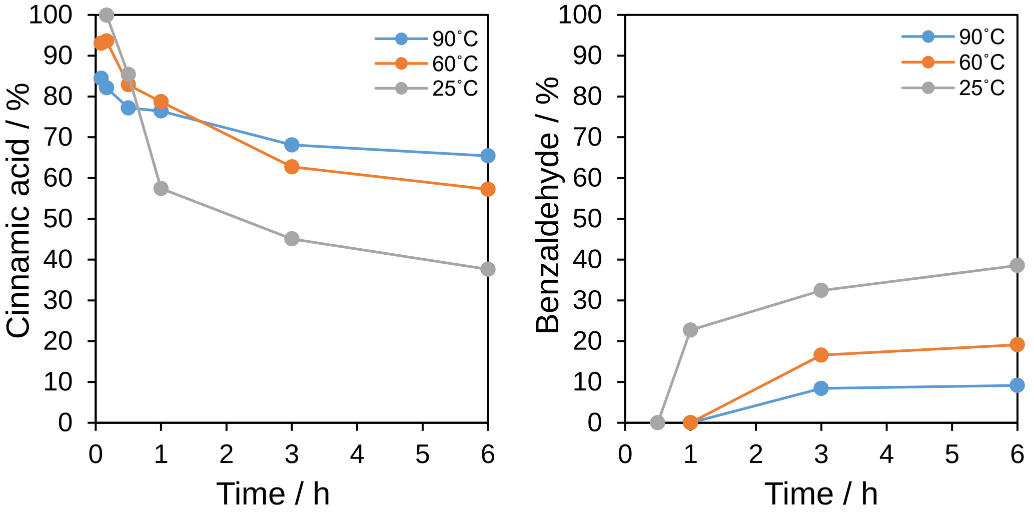

Figure 4.7: Investigation of cinnamic acid and benzaldehyde formation under different temperatures (without catalyst).

However, despite this divergence, the mechanism showed in **Scheme 4.4** (left) is the only one found in literature that accounts for the radical formation of benzaldehyde in the absence of a catalyst, which is the case presented in this chapter thus far.

As previously explained, while ≥ 1 bar O_2 favours the formation of benzaldehyde, atmospheric air represents the best condition that allows this process to be minimised. This might be due to the mechanisms that regulate the formation of the two products, described in **Scheme 4.4**. When the reaction environment contains an $O_2:N_2 \approx 2:8$ ratio as in the case of atmospheric air, cinnamaldehyde is allowed to evolve to its acyl radical via a heat-induced process or using oxygen, effectively starting the radical chain pathway (initiation step, **Scheme 4.3**). On the other hand, when the applied partial pressure is higher, and the solution is saturated with oxygen radicals ($O_2:N_2 = 10:0$ ratio), these attack cinnamaldehyde with a fast uptake rate, partly preventing the substrate from being converted to its corresponding acyl radical, and the radical process described in **Scheme 4.3**. As an approximation, it is possible to affirm that in this case, oxygen radicals have a “nucleophile-like nature”, since they attack the electron-deficient carbon in α-position to the aldehyde moiety (**Scheme 4.4**, left). Therefore, in the first case (atmospheric air) the free-radical chain process described in **Scheme 4.3** dominates, favouring the formation of cinnamic acid via the non-radical Baeyer-Villiger rearrangement. Instead, a higher amount of oxygen in the reaction environment saturates the solution and quickly reacts with the starting aldehyde with a high rate constant, hindering its evolution in the chain step process, allowing a lower amount of peracid to be formed and consequently minimising the cinnamic acid obtained. This explanation is summarised in **Figure 4.8**.

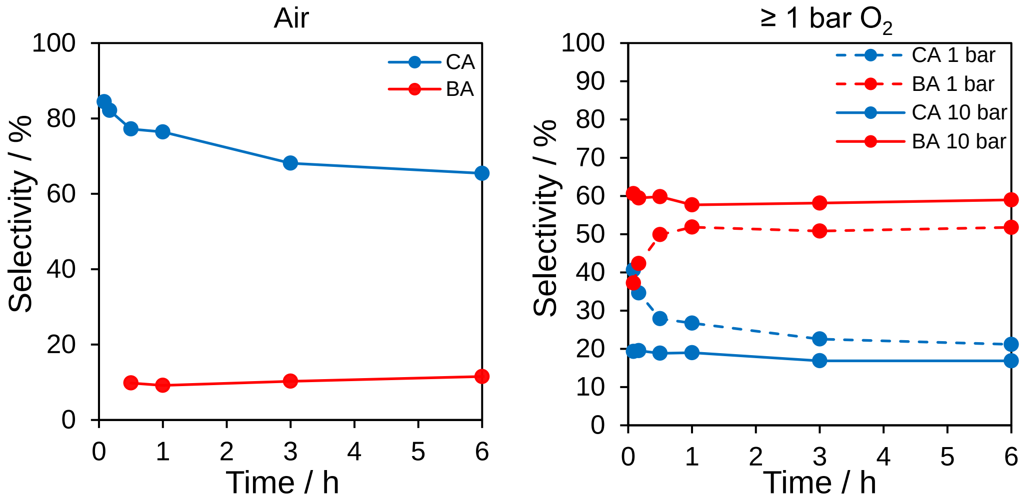

Figure 4.8: Cinnamic acid (CA) and benzaldehyde (BA) selectivities at different O_2 pressures (without catalyst).

When air is applied to the system, the free radical pathway is highly favoured, so that cinnamaldehyde undergoes the process in **Scheme 4.3** and cinnamic acid is produced with the highest selectivity (**Figure 4.8**, left). When 1 bar O_2 is applied, benzaldehyde formation is favoured, however, at the beginning of the reaction, both mechanisms occur with almost the same probability (41% selectivity to cinnamic acid, 37% selectivity to benzaldehyde). Soon after, the equilibrium is shifted towards benzaldehyde formation, because oxygen has saturated the solution. Rising oxygen partial pressure up to 10 bar, as the amount of oxygen radicals is even higher, makes cinnamaldehyde less able to transform to an acyl radical, because oxygen radicals are attacking the α-C to the aldehyde moiety as described **Scheme 4.4** (left).

Considering all the parameters rationalised up to this point, it can be stated that cinnamaldehyde aerobic oxidation (in the absence of catalyst) follows two main pathways, in competition with each other and strongly dependent on the reaction conditions employed.

4.1.2. Role of platinum catalyst

4.1.2.1. Characterisation of platinum catalysts

Two classes of $Pt-SiO_2$ catalysts have been prepared following the wet-impregnation method, as described in Chapter 2, section 2.3.2. (Synthesis of platinum catalysts – cinnamaldehyde aerobic oxidation). Fumed silica (SiO_2) has been functionalised with two different metal precursors, namely tetraammineplatinum (II) nitrate [$Pt(NH_3)_4(NO_3)_2$] and chloroplatinic acid (IV) hexahydrate [$H_2PtCl_6·6H_2O$] (**Figure 4.9**), to impart a specific wt% (0.05 and 2 wt%) by weight loading of platinum upon the support.

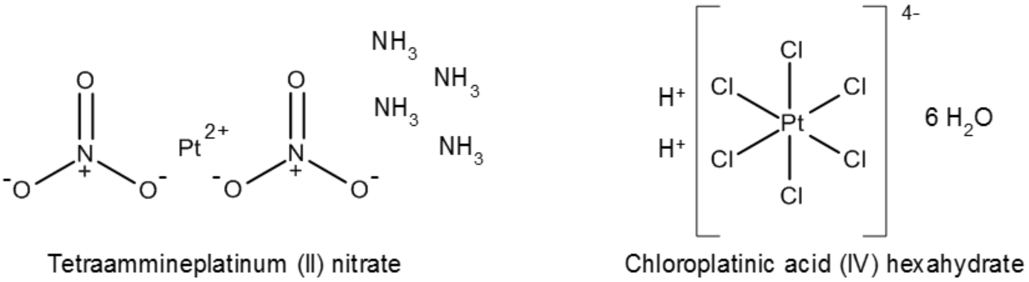

Figure 4.9: Pt precursors used to prepare the catalysts described in this section.

The actual metal wt% has been measured using Inductively-Coupled Plasma-Mass Spectrometry (ICP-MS). These four catalysts, to which has been assigned a name, are summarised in **Table 4.1**.

Catalyst name	Pt precursor	Nominal Pt wt%	Actual Pt wt%
0.057 wt%-PNN	$Pt(NH_3)_4(NO_3)_2$	0.05	0.057
1.54 wt%-PNN	$Pt(NH_3)_4(NO_3)_2$	2	1.54
0.052 wt%-CPA	$H_2PtCl_6·6H_2O$	0.05	0.052
1.50 wt%-CPA	$H_2PtCl_6·6H_2O$	2	1.50

Table 4.1: Pt wt% of the catalyst determined with ICP-MS.

The actual wt% of the catalysts prepared with both precursors was slightly less than the nominal wt%. This decrease in platinum loading is a consequence of the preparation method, which might implicate a slight loss of metal, probably due to sticking to the walls of the beaker during the overnight agitation of the slurries.

Figure 4.10 illustrates wide-angle X-ray diffractograms (XRD) of the catalysts described in **Table 4.1**, together with the pattern of the unfunctionalised support, for comparison.

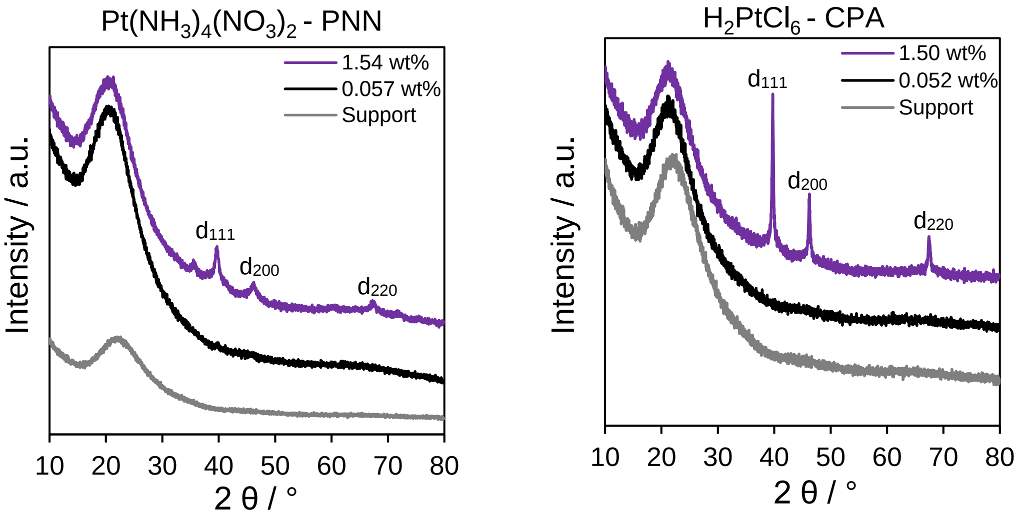

Figure 4.10: Wide-angle XRD of the catalysts in **Table 4.1** (offset for clarity).

Both the highest loading catalysts show well-defined reflections relative to different platinum planes, while the lowest loading catalysts and the parent support do not show any of these reflections. This phenomenon occurs due to the reasons explained throughout the previous chapters (Chapter 2, section 2.4.1. Powder X-ray Diffraction and section 2.4.4. Scanning Transmission Electron Microscopy; Chapter 3, section 3.3 Characterisation of platinum catalysts).

Scanning Transmission Electron Microscopy (STEM) was also employed to obtain the particle sizes of the catalysts. **Table 4.2** shows platinum particle size of each catalyst, calculated with both techniques.

	Pt particle size / nm	
Catalyst	**XRD**	**STEM**
0.057 wt%-PNN	n.d.	1.38 ± 0.69
1.54 wt%-PNN	5.5	2.18 ± 0.80
0.052 wt%-CPA	n.d.	1.88 ± 0.89
1.50 wt%-CPA	13.9	1.89 ± 0.73

Table 4.2: Particle size of the four catalysts used in this chapter calculated with XRD and STEM (particle dimension evaluated over ≈ 250 particles).

The STEM measurement in the table above reveals that the particle size of PNN precursor's catalysts increased with metal loading, indicating a greater assembly of nanoparticles (NPs) as the loading increases. Regarding CPA precursor's catalysts, despite the wide-angle XRD diffractograms in **Figure 4.10** suggested a substantial difference in particle size between low and high platinum loading, the size measured with STEM did not match XRD data. Instead, STEM has identified such discrepancy in the error rather than in the average value of the particle size (± 0.89 for 0.052 wt% and ± 0.73 for 1.50 wt%). This might be a consequence of the fact that since equal amounts of nanoparticle clusters (for this specific case intended as particle assemblies) have been identified in both CPA catalysts (**Figure 4.12**), a more significant variation from the average value (for 0.052 wt%) is due to the presence of smaller metal particles and clusters. On the other hand, a smaller error for 1.50 wt% stems from the simultaneous existence of bigger nanoparticles (due to a higher loading) and clusters. Since 0.052 wt%-CPA diffractogram does not present any metal reflection, it is possible to imply that wide-angle XRD does not identify assemblies of nanoparticles but only single particles. During the estimation of STEM nanoparticle size with ImageJ software, it was avoided the measurement of single particles belonging to clusters because their shape was not defined and clear. Therefore, the determination of CPA catalysts' nanoparticle size is deceptive and may not entirely correspond to their real dimension.

STEM images of all catalysts are displayed in **Figure 4.11** (PNN precursor), and **Figure 4.12** (CPA precursor).

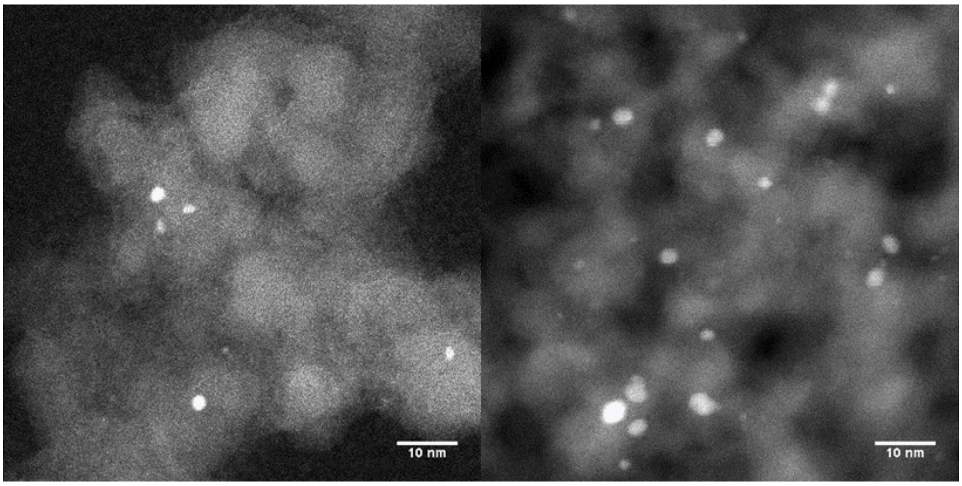

Figure 4.11: Dark field STEM images of 0.057 wt% (left) and 1.54 wt% (right) Pt-SiO$_2$-PNN catalysts.

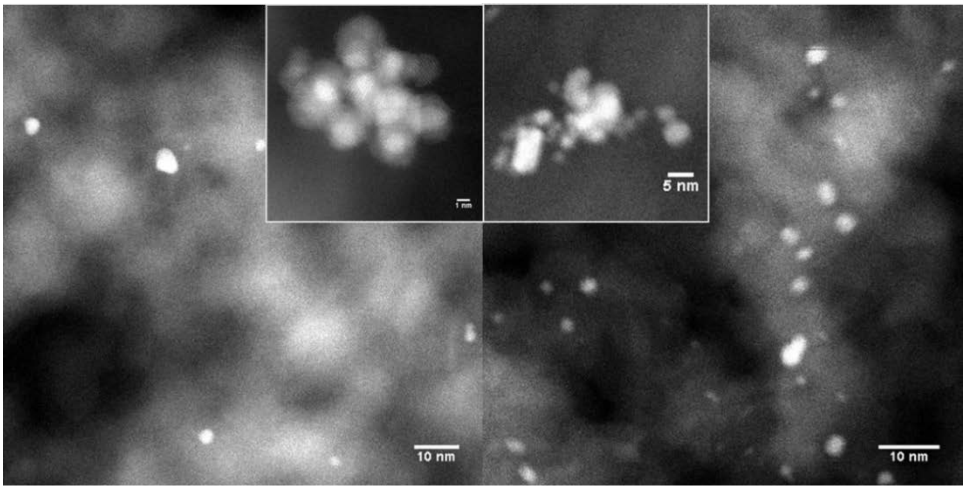

Figure 4.12: Dark field STEM images of 0.052 wt% (left) and 1.50 wt% (right) Pt-SiO$_2$-CPA catalysts. Insets: clusters of Pt NPs.

STEM images show the amorphous silica in the background on which the metal particles have been supported, represented by the circular white spots. **Figure 4.12** highlights the tendency of CPA precursor to form aggregates of nanoparticles that might be confused for bigger particles during the measurement of their size.

The architecture of the support has been identified through nitrogen physisorption porosimetry, which exhibited pseudo-type II isotherms [29] (**Figure 4.13**).

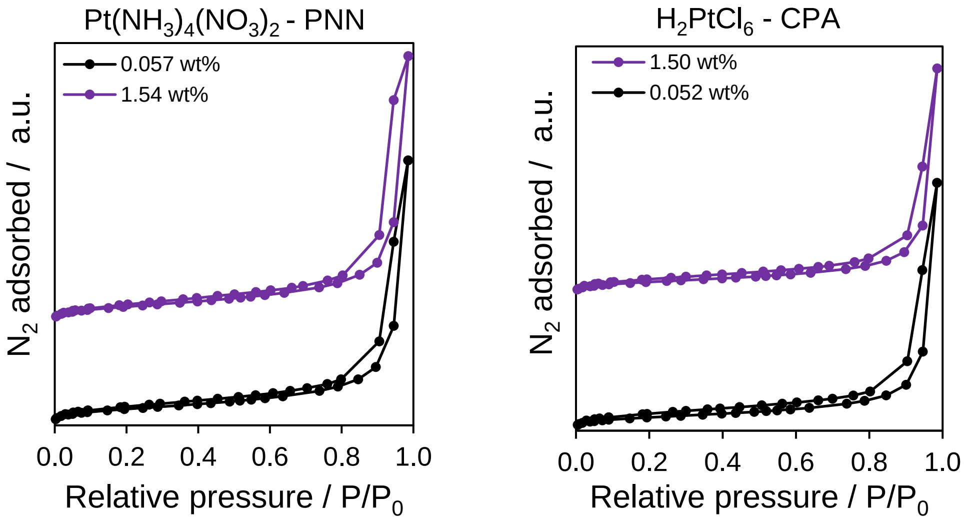

Figure 4.13: Adsorption-desorption N_2 isotherms of the catalysts used in this section (offset for clarity).

BET surface areas of all catalysts measured between 212 and 234 $m^2\ g^{-1}$ and followed an inversely proportional trend with platinum loading (**Table 4.3**). The observed decrease upon platinum impregnation is due to small nanoparticles dispersed on the silica surface that generate ridges and extra roughness and is consistent with nanoparticle deposition on the external surface of the support which, in case of bigger particles, is stronger as there is less free surface to be measured with nitrogen porosimetry (**Table 4.3**).

Catalyst	**Particle size / nm (STEM)**	**Surface area / $m^2\ g^{-1}$**
0.057 wt%-PNN	1.38 ± 0.69	234 ± 23
1.54 wt%-PNN	2.18 ± 0.80	219 ± 22
0.052 wt%-CPA	1.88 ± 0.89	214 ± 21
1.50 wt%-CPA	1.89 ± 0.73	212 ± 21

Table 4.3: Surface area of the Pt-catalysts associated to their particle size.

From the table above it is noteworthy that the two CPA catalysts present very similar STEM particle size and, accordingly, similar surface area of the support.

X-ray Photoelectron Spectroscopy (XPS) has been conducted on the catalysts described in this section, in order to obtain information about the surface region as this technique allows the X-rays to enter the sample with < 10 nm depth (this technique has been explained in detail in Chapter 2, section 2.4.6. X-ray Photoelectron Spectroscopy).

In **Table 4.4** is listed the wt% composition of platinum on the surface of the catalysts, in relation to the metal content previously determined with ICP-MS.

Catalyst	Particle size / nm (STEM)	Pt Bulk / wt%	Pt Surface / wt%	Oxide content / %
0.057 wt%-PNN	1.38 ± 0.69	0.057	0.066	34
1.54 wt%-PNN	2.18 ± 0.80	1.54	0.56	24
0.052 wt%-CPA	1.88 ± 0.89	0.052	0.09	45
1.50 wt%-CPA	1.89 ± 0.73	1.50	0.76	21

Table 4.4: Surface composition properties obtained from XPS fitting.

The results in **Table 4.4** indicate a metal core-oxide shell structure, [30] where PtO_2 formation is favoured on the surface of the catalysts, as previously observed in Chapter 3 (sections 3.3.2. Characterisation of pore-expanded Pt-TLCT SBA-15 catalysts and 3.3.3. Characterisation of pore-expanded Pt-*MM*-TLCT SBA-15 catalysts). The higher loading catalysts indicate that there is higher platinum content exposed per gram of catalyst, but less percentage of it is present on the surface, as the nanoparticles are bigger (Chapter 3, section 3.3.2. Characterisation of pore-expanded Pt-TLCT SBA-15 catalysts, **Figure 3.53**, **a**). When the loading is lower, the particle size is smaller. Therefore, the atoms are more exposed to the surface (**Figure 3.53**, **b**). Smaller particles prefer to be distributed on the surface in the form of PtO_2, as smaller particles are more capable of stabilising the oxide rather than the metal due to energy requirements, [30] and because when platinum is exposed to the environment, it is more sensitive to oxidative processes. From **Table 4.4** it is clear that, for both precursors, the oxide content on the surface decreases as metal loading increases, because lower loadings allow the nanoparticles to be better distributed and have smaller size, and to be located more on the surface of the catalyst.

Figure 4.14 shows the detection of platinum on the surface of the catalysts:

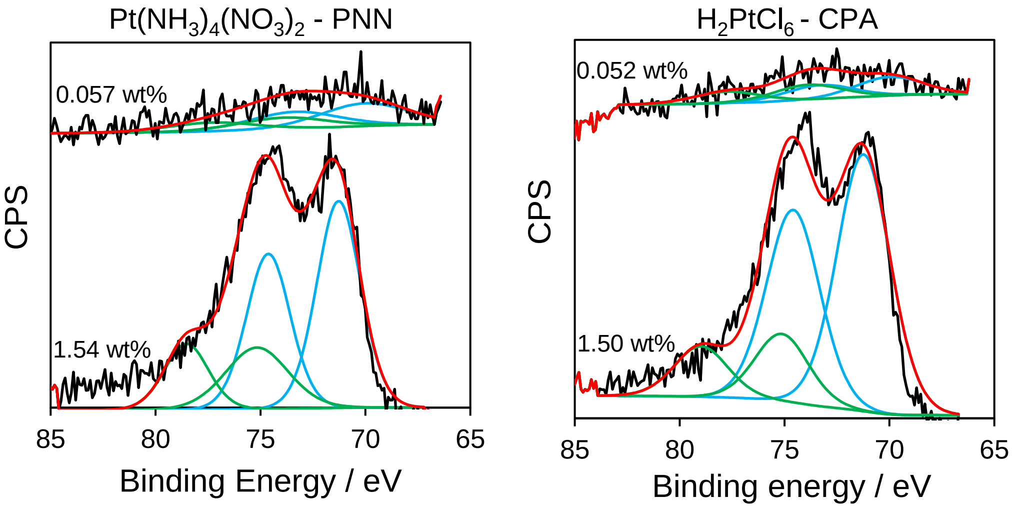

Figure 4.14: Pt 4f spectra of low and high loading catalysts prepared with PNN precursor (left) and CPA precursor (right), (offset for clarity).

The black lines indicate the raw data and the red lines indicate the full envelope fitting of the region. Contributions due to $Pt^{(0)}$ (blue lines) and PtO_2 (green lines) fitted components are shown, revealing the emergence of stronger oxide features at low loadings. This confirms that the formation of PtO_2 species is favoured at lower metal loadings.

4.1.2.2. Catalytic results

Once demonstrated that the optimum oxygen pressure for favouring the selective oxidation of cinnamaldehyde to cinnamic acid was atmospheric air (section 4.1.1, Role of oxygen concentration and pressure), the role of $Pt-SiO_2$ catalysts had been investigated. The catalysts used in this paragraph refer to section 4.1.2.1 (Characterisation of platinum catalysts) and are listed in **Table 4.1**.

The platinum catalysts have been first screened at low and high oxygen pressure, to assess their contribution to the formation of cinnamic acid from cinnamaldehyde. Only in the first case, a difference in initial rate between catalysts and blank (uncatalysed reaction) could be observed (**Figure 4.15**).

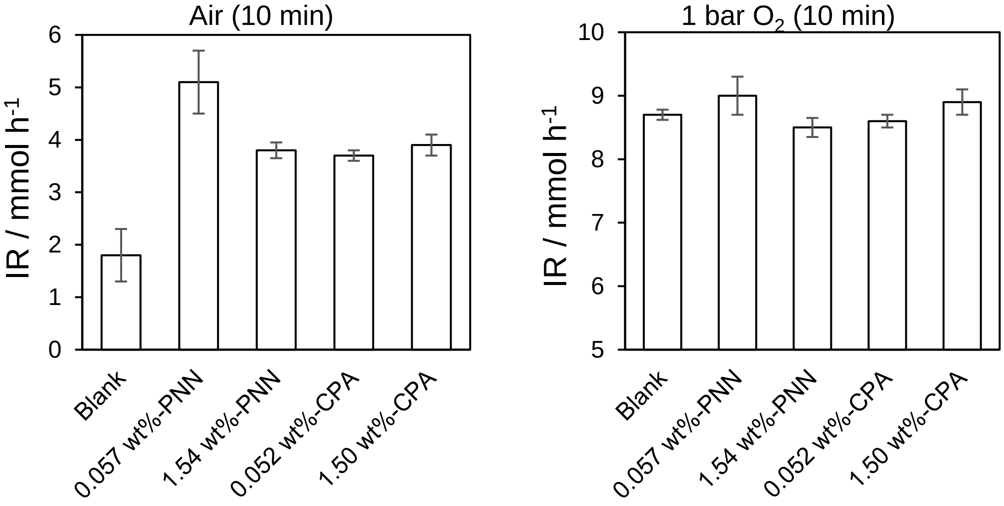

Figure 4.15: "Primary catalytic effect" of Pt-SiO$_2$ catalysts has only been observed under atmospheric air.

The results shown in **Figure 4.15** are consistent with what has been previously explained. Higher oxygen pressure contributes to faster conversion of the reactant; in fact, the initial rate of the blank under air is lower than that obtained under 1 bar pressure. A difference in initial rate was observed only under low oxygen pressure and when platinum catalysts participated in the reaction (**Figure 4.15**, left). This can be addressed as the "primary catalytic effect". Conversely, the same promotion was not observed at higher pressure, probably since higher amount of oxygen radicals contributes to a saturation of the catalyst surface, nullifying the effect of platinum (**Figure 4.15**, right). This saturation must happen extremely quickly, as no catalytic effect is observed since the very beginning of the reaction. Hence, in the latter case oxygen represents the only source for conversion that, as already explained in the previous section (**Figure 4.2**, left), benefits from higher oxygen pressure at an initial stage.

Since it has not been possible to calculate the metal dispersion of the catalysts in **Table 4.1** using CO chemisorption, the turnover frequencies for the reaction have not been determined, as their calculation is derived by dividing the initial rate of reaction by the mmol of platinum on the catalyst surface. The mmol of surface Pt$^{(0)}$ is calculated with CO chemisorption analysis, and correspond to the platinum metal sites present on the catalyst surface that contribute to the catalytic conversion of cinnamaldehyde.

However, the initial rates obtained for the catalytic reactions (displayed in **Figure 4.15**, left) have been first adjusted to the blank reaction, in order to obtain the real catalytic contribution, and then have been normalised to the mass of platinum utilised in the reaction, and are shown in **Figure 4.16**.

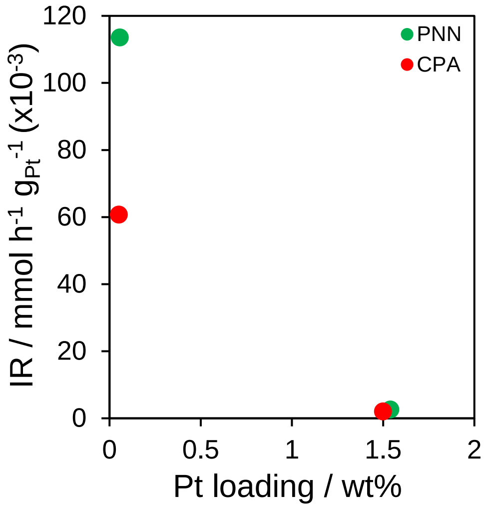

Figure 4.16: Pt normalised IR derived from **Figure 4.15** (left). Experiments carried out under air.

Generally, the lower loading catalysts exhibit superior platinum normalised initial rates compared to higher loading, as the mass of platinum incorporates the metal wt% (see **equation 2.11**, Chapter 2). However, when comparing the low loading catalysts of the two classes in **Figure 4.16**, 0.057 wt%-PNN showed higher initial rate compared to 0.052 wt%-CPA. This might be because the functionalisation with CPA precursor led to the formation of a high amount of nanoparticle clusters, not present instead of in the materials prepared with PNN precursor, as reported in section 4.1.2.1 (Role of platinum catalyst

Characterisation of platinum catalysts - **Figure 4.12**). As the STEM pictures highlight, these clusters seem to have less available surface area to serve as active substrates for the conversion of the reactant, having in turn lower catalytic effect with respect to independent nanoparticles distributed over the material's surface. Accordingly, the nanoparticle dispersion is expected to be lower in the case of CPA precursor; in fact, the metal normalised initial rate is minor in this case. This precursor favours the formation of nanoparticle clusters on a fumed silica support, not enabling the catalyst to work efficiently. On the other hand, the nanoparticles of 0.057 wt%-PNN catalyst are well distributed and separated on the surface (**Figure 4.11**), its platinum normalised initial rate is higher. Nanoparticle dispersion is a key parameter that defines how active is a catalyst.

The reason why one precursor allowed for the preparation of catalysts with a good degree of dispersion may be ascribed to the charge distribution on the elements, appreciable in **Figure 4.9**. PNN possesses a Pt^{2+}, while CPA shows a Pt^{4-}. The support in question displays a certain amount of silanols (SiOH) on its surface, which have more affinity to the former platinum; therefore these particles can anchor more effectively to the support.

As initial rate (mmol h^{-1}) of 0.057 wt%-PNN is superior to the other catalysts (**Figure 4.15**, left), it can be concluded that the aerobic oxidation of cinnamaldehyde is favoured over smaller particle size (0.057 wt%-PNN = 1.38 ± 0.69 nm, while the other three catalysts range from 1.88 to 2.18 ± 0.89 nm, **Table 4.2**) and consequently is dependent on metal dispersion. The literature on Pt-SiO_2 catalysts has well established that metal dispersion is inversely proportional to loading, indicating that lower wt% catalysts possess more active sites on their surface. [19, 30] The explanation to this is that lower metal loadings favour the formation of smaller nanoparticles, which in turn account for a higher number of available active sites for CO chemisorption (which determines metal dispersion).

Since 0.057 wt%-PNN possessed the highest catalytic activity, from this point onwards the data reported will concern only this catalyst.

When oxygen pressure was raised to 10 bar, no difference was observed between blank and catalysed reaction (**Figure 4.17** left, straight lines). However, in the presence of the radical scavenger hydroquinone, it was possible to appreciate a difference in conversion (**Figure 4.17** left, dotted lines).

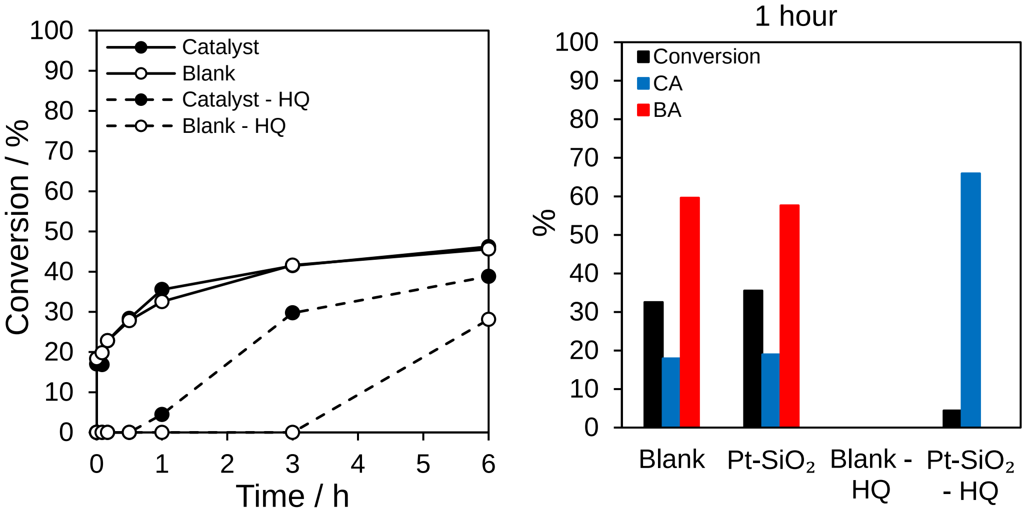

Figure 4.17: Cinnamaldehyde conversion for blank and catalysed reactions, in presence and the absence of HQ (0.02 mmol in 8.4 mmol of cinnamaldehyde), (left). Conversion and product selectivities with HQ and catalyst (right). 10 bar O_2, Pt-SiO_2 catalyst: 0.057 wt%-PNN (CA = cinnamic acid, BA = benzaldehyde).

As explained before, the effect of platinum on the conversion is cancelled when the amount of oxygen radicals is high, due to surface saturation. However, a promoting effect on both conversion and product selectivities has been observed when the catalyst and the radical trap worked simultaneously (**Figure 4.17**). At 1 hour, when some oxygen radicals are free in the gas stream as hydroquinone has been consumed, cinnamic acid is the primary product, as the number of radicals is very low, and the free radical chain reaction described in **Scheme 4.3** is favoured (**Figure 4.17**, right – Pt-SiO_2- HQ). Later on the amount of oxygen radicals increases, and consequently benzaldehyde becomes the favoured product, for the reason explained in **Figure 4.8**. By the end of the reaction, the final selectivities will correspond to those obtained in the absence of the catalyst (**Figure 4.4**, right), as at high pressure, regardless the presence of hydroquinone, the oxidative cleavage to benzaldehyde takes over.

After demonstrating that platinum catalyst plays a catalytic role in the aerobic oxidation of cinnamaldehyde only under low oxygen pressure, conversion and product selectivities were analysed in depth under this condition.

Over 24 hours reaction, there was no appreciable difference in conversion when blank and catalysed reactions were compared under air (**Figure 4.18**, left). However, the effect of platinum previously referred to as "primary catalytic effect" is noticeable over the first hour (**Figure 4.18**, right).

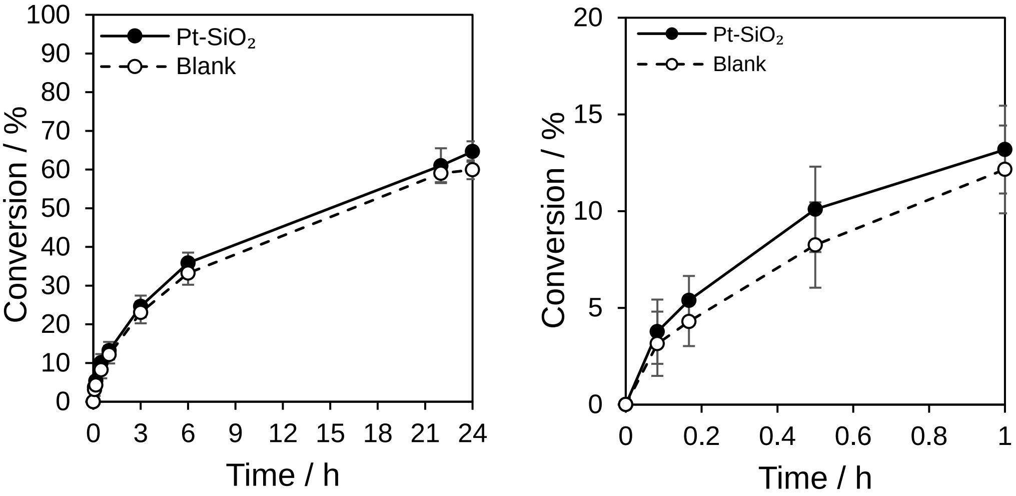

Figure 4.18: Comparison of conversion over 24 h (left) and over the first h (right) of reaction under air. Pt-SiO_2 catalyst: 0.057wt%-PNN.

At 10 minutes (second point in **Figure 4.18**, right), for example, initial rate for the blank reaction is 1.8 ± 0.5 mmol h^{-1} whereas for the catalysed reaction is 5.1 ± 0.6 mmol h^{-1}.

Low amount of oxygen in the gas stream initially activates platinum atoms on the surface, allowing a faster, although not by much, conversion compared to the blank reaction. However, at a later stage, the catalyst surface is saturated with oxygen radicals and its effect is hampered, leading to the results shown in **Figure 4.18** (left). If under air, this saturation effect is delayed, when the reaction is conducted at higher oxygen pressure, this phenomenon becomes uncontrolled, and the catalyst does not play any role from the very beginning.

Besides the conversion of cinnamaldehyde ("primary catalytic effect"), the impact of platinum has been observed when comparing product selectivities with the blank reaction. It was found that the catalyst favours the selective formation of cinnamic acid while minimising benzaldehyde (**Figure 4.19**). We addressed this result as "secondary catalytic effect".

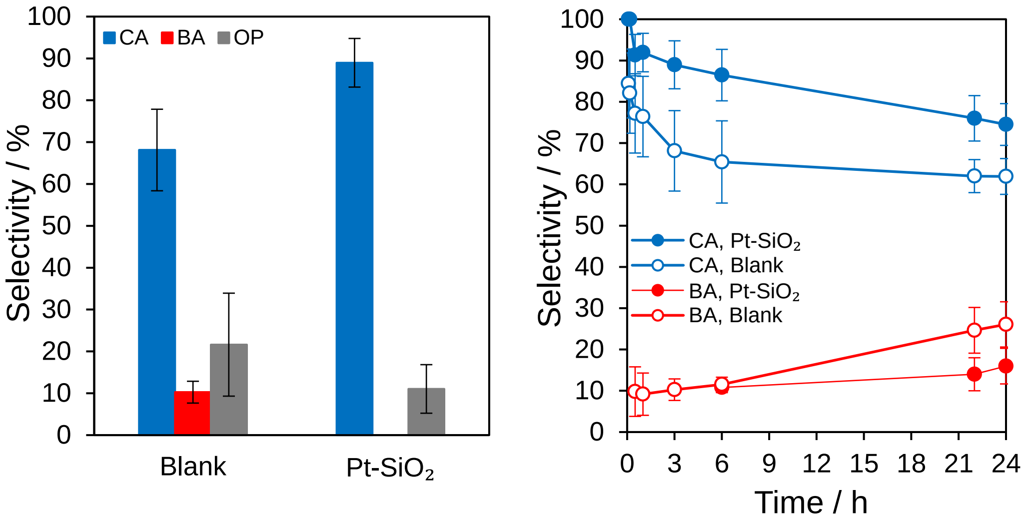

Figure 4.19: "Secondary catalytic effect" played by Pt-SiO$_2$ at 25% conversion (3 h), under air (left). Comparison of 24 h selectivity patterns for blank and catalysed reactions, under air (right). Pt-SiO$_2$ catalyst: 0.057wt%-PNN (CA = cinnamic acid, BA = benzaldehyde, OP = other products).

When Pt-SiO$_2$ catalyst participates in the reaction, the product selectivities change as represented in **Figure 4.19**. This is due to platinum favouring cinnamic acid formation over benzaldehyde. Even though the appearance of the latter is not completely inhibited, it is delayed, and its formation is observed at 6 hours. XPS studies on the Pt-SiO$_2$ catalyst highlighted the presence of PtO$_2$ species on the surface, indicating that the metal is oxidised by oxygen in the atmosphere, while metal in the bulk of the catalyst is mainly present as Pt$^{(0)}$ (**Figure 4.14**). There are two possible explanations for the formation of platinum oxide: either platinum on the catalyst surface passes from 0 to +4 oxidation state because it is oxidised by the oxygen in the atmosphere, or its formation can be seen as a consequence of the homolytic activation of oxygen from the metal, according to investigations performed by Conte and co-workers. They explained that platinum (paramagnetic metal, which possesses an unpaired electron) could activate the paramagnetic ground state oxygen.

Regardless of the way the PtO$_2$ species forms, it has been identified as the active species that promotes both cinnamyl alcohol and cinnamaldehyde aerobic oxidations in previous studies. [19, 30, 31]

Examining the mechanism by which the oxidised platinum favours one product over the other, in this work it has been inferred that it might operate by the so-called Mars-van Krevelen mechanism, [32] which consists of two stages. Firstly, the C-H bond activation of the reactant occurs via electron and proton transfer to the catalyst and oxygen transfer from the catalyst to the reactant. The result of this reaction is the oxygenation of the reactant and formation of a reduced metal oxide with an oxygen vacancy. Then, a re-oxidation of the catalyst by molecular oxygen present in the reaction atmosphere occurs, that re-inserts oxygen to the metal oxide lattice and is often coupled with the formation of water. [21, 33] This mechanism has originally been devised for gas-phase hydrocarbon oxidations catalysed by metal oxides. However, this theory has been previously supported by other research groups that studied the liquid-phase aerobic oxidations of alcohols and aldehydes catalysed by transition metals on SiO_2, [31, 34] Al_2O_3 [35] and TiO_2. [35] A mechanism for the platinum catalysed formation of cinnamic acid from cinnamaldehyde has been proposed, following the pathway above explained (**Figure 4.20**).

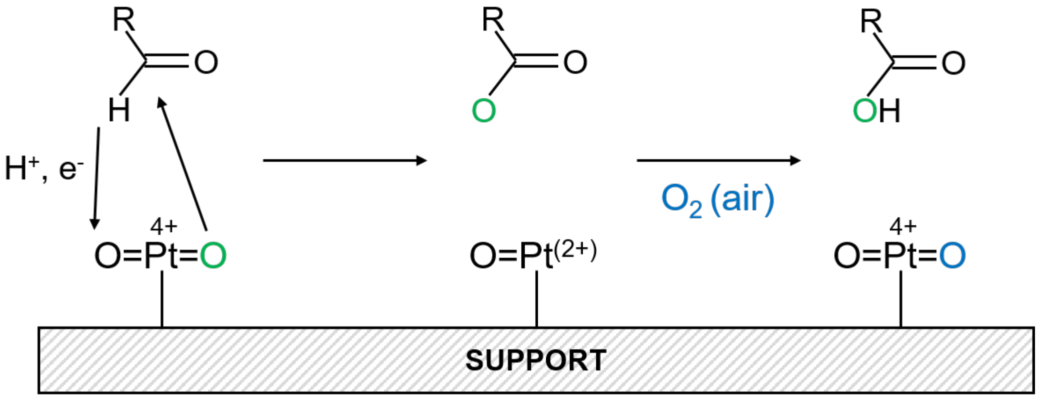

Figure 4.20: Proposed mechanism of formation of cinnamic acid, based on the Mars-van Krevelen mechanism.

Hence, the formation of cinnamic acid when Pt/SiO_2 catalyst participates in the reaction (carried out under air) occurs via the Mars-van Krevelen mechanism and is no longer related with the free radical chain pathway described in **Scheme 4.3**. It has been already explained that, to the best of our knowledge, benzaldehyde formation stems from the attack of molecular oxygen to cinnamaldehyde, which in turn undergoes a carbon-carbon cleavage, according to the mechanism displayed in **Scheme 4.4** (left). The fact that benzaldehyde is formed in 0% selectivity at 25% conversion in the presence of the catalyst (**Figure 4.19**, left) is related to the oxygen present in the atmosphere (in lower amount compared to 1 bar O_2 partial pressure), being initially exclusively involved in the oxidation of surface platinum. This hampers the radical attack to cinnamaldehyde. Later on, when the catalyst surface has been saturated, oxygen is again free in the reaction environment and can form benzaldehyde (**Figure 4.19**, right – formation of benzaldehyde in the presence of catalyst starts at 6 hours reaction).

It is then possible to state that, in the catalysed aerobic oxidation of cinnamaldehyde, while cinnamic acid formation follows a catalytic pathway, benzaldehyde formation is not platinum mediated. The aerobic oxidation of cinnamaldehyde is intrinsically unselective as it is driven by autoxidation pathways consisting of free radical processes that can initiate uncontrollable chain reactions. However, the use of a platinum catalyst helped to control these processes, as it behaved like an "oxygen trap", preventing – until a certain extent – molecular oxygen to attack the reactant to form benzaldehyde. A soon as the catalyst surface is saturated with oxygen, the formation of the main undesired by-product and possibly the free-radical chain processes (**Scheme 4.3**) occur, causing the reaction to lose catalytic control, also because benzaldehyde is responsible for the formation of further by-products (**Scheme 4.5**, see next section).

4.1.3. Further mechanistic considerations

The total mass balance of cinnamaldehyde aerobic oxidation decreased by about 10% over 24 hours, for both uncatalysed and catalysed (with any catalyst) reactions (**Figure 4.21**).

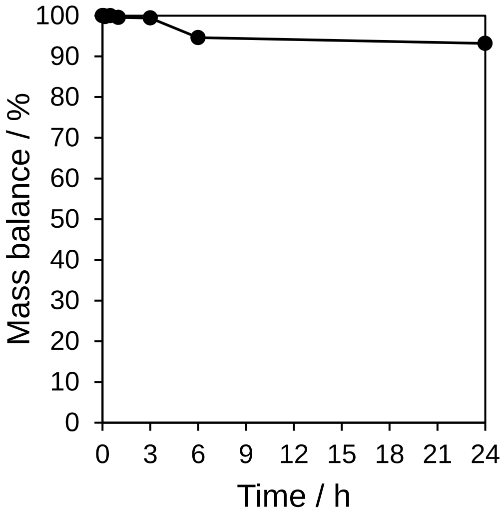

Figure 4.21: Mass balance trend of the aerobic oxidation of cinnamaldehyde.

This is due to further by-products present in negligible selectivity, not identified by GC-MS, together with the formation of combustion products (e.g. CO, CO_2). [10, 36] Thermogravimetric Analysis-Mass Spectrometry (TGA-MS) analysis of cinnamaldehyde oxidation led to a weight loss of 44 g mol^{-1}, which might correspond to CO_2 (**Figure 4.22**).

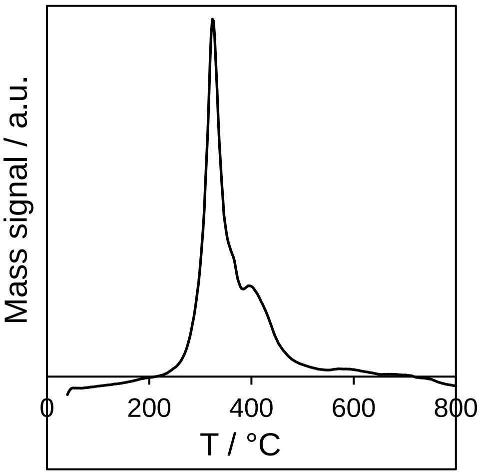

Figure 4.22: TGA-MS analysis of cinnamaldehyde oxidation led to a weight loss of 44 g mol^{-1}.

Alongside with cinnamic acid and benzaldehyde, different minor side-products have been identified (indicated in section 4.1.1, Role of oxygen concentration and pressure, with the acronym “OP”). The complete reaction mechanism is here proposed (**Scheme 4.5**). All the products have been identified with GC-MS and their presence confirmed by retention time in Gas-Chromatography with Flame Ionisation Detector (GC-FID).

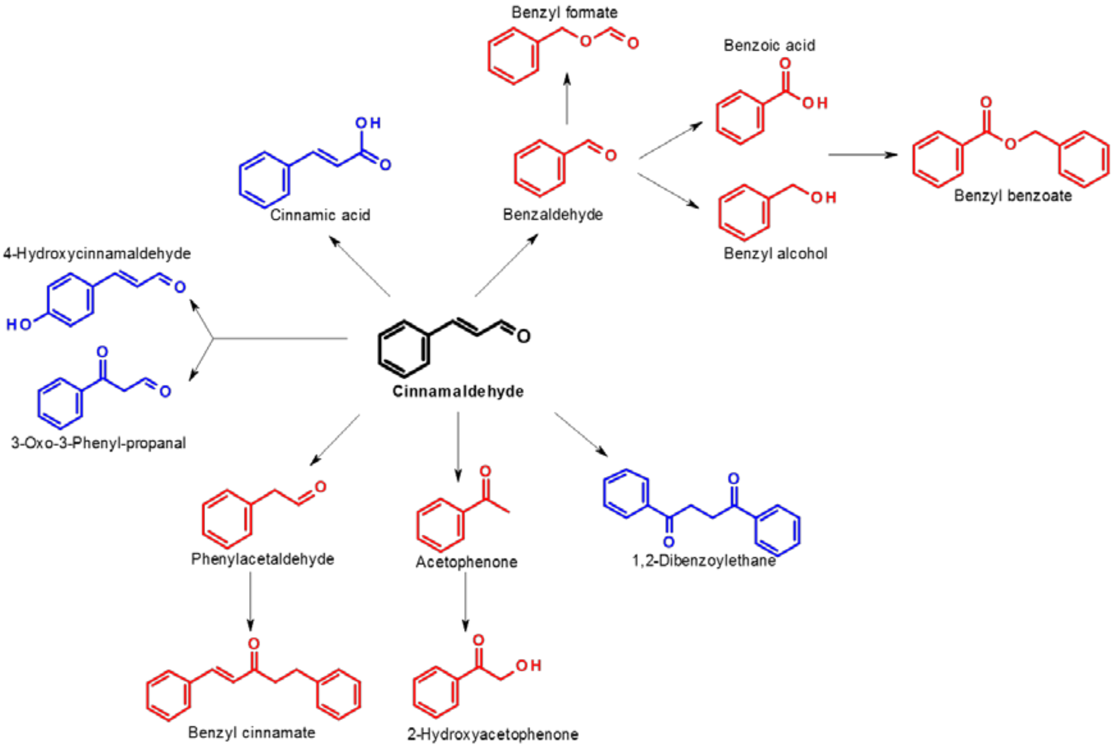

Scheme 4.5: Proposed mechanism for cinnamaldehyde aerobic oxidation at 90 °C.
(Blue products: most abundantly formed under air.
Red products: most abundantly formed under ≥ 1 bar O_2).

Not only low oxygen pressure favours the formation of the desired product cinnamic acid but also hampers the formation of many side-products that contribute to decreasing the degree of selectivity of the whole reaction. This is mostly due to the unselective nature of the aerobic oxidation of cinnamaldehyde which, in the absence of catalyst, proceeds via an autoxidation pathway that initiates unselective chain reactions. In addition, some by-products are formed from benzaldehyde, and others are the result of cinnamaldehyde decomposition under the influence of heat and oxygen radicals. Under air and in the presence of a catalyst, on the other hand, together with cinnamic acid being the product formed with the highest selectivity, two isomers coming from cinnamaldehyde decomposition and 1,2-dibenzoylethane are formed in 16% selectivity in 3 hours reaction (25% conversion). However, at longer reaction times the red side-products in **Scheme 4.5** are formed even in the presence of air and Pt-SiO_2 catalyst, hence to obtain cinnamic acid in high selectivity it is necessary to stop the reaction at 3 hours in the case presented in this study.

4.1.4. From cinnamyl alcohol to cinnamic acid

Literature concerning the aerobic oxidation of cinnamyl alcohol to cinnamaldehyde is vast. [10, 14-16, 20, 30, 31, 34, 35, 37-45] Yet, the reason why it is not possible to obtain the complete transformation to the corresponding acid in a one-pot reaction has never been reported. In this work, the aerobic oxidation of cinnamyl alcohol was also examined with a Pt-SiO_2 catalyst, to find an explanation to the fact that, when starting from the alcohol, the formation of cinnamic acid is never observed. A mechanism of this reaction was also proposed (**Scheme 4.6**).

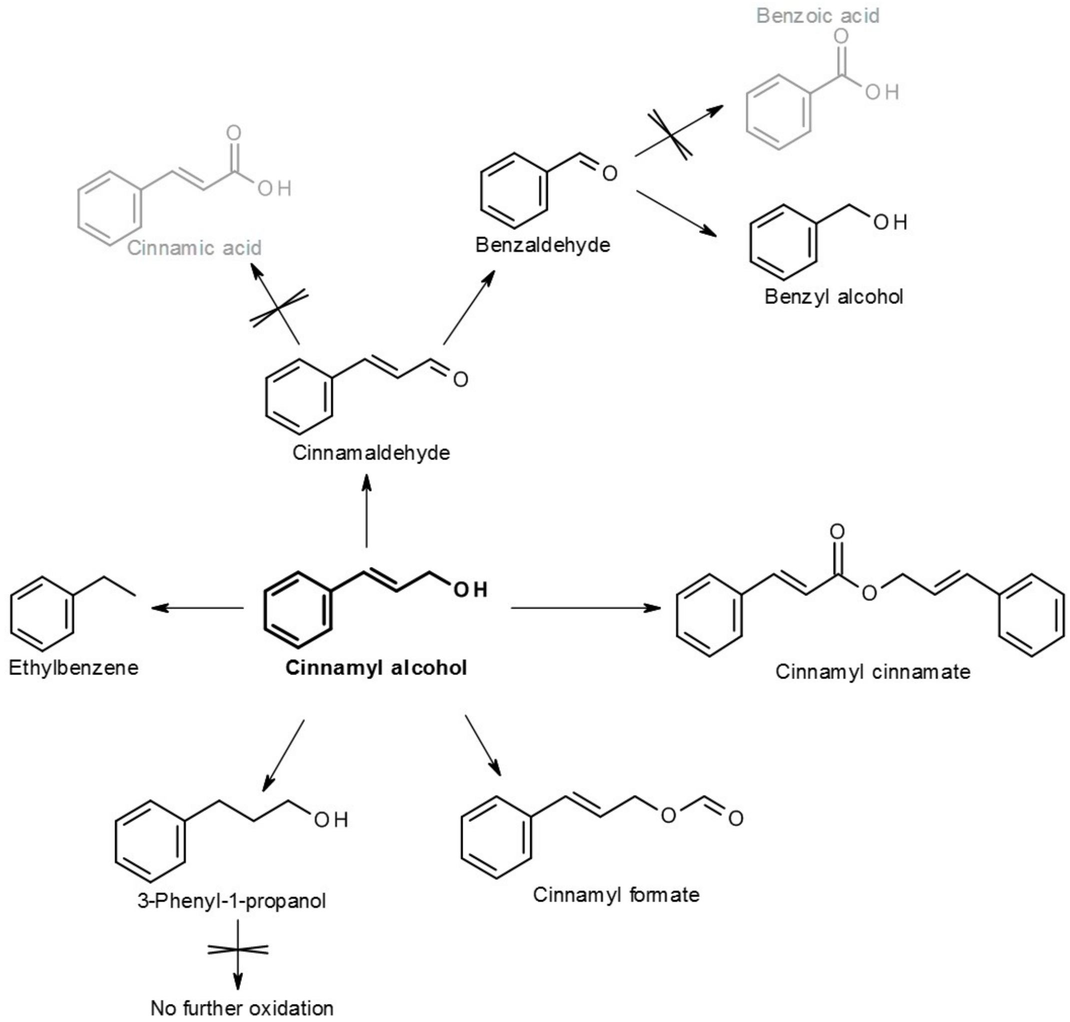

Scheme 4.6: Proposed mechanism of cinnamyl alcohol aerobic oxidation, under 1 bar O_2 (90 °C, 24 h, Pt-SiO_2 catalyst: 0.057wt%-PNN).

As several research groups reported, one of the main by-products of cinnamyl alcohol oxidation is benzaldehyde, [4, 7, 8, 10, 20, 46] proven to be the autoxidation product of cinnamaldehyde (section 4.1.1, Role of oxygen concentration and pressure, **Scheme 4.4**). However, in literature cinnamyl cinnamate is never mentioned as one of cinnamyl alcohol aerobic oxidation by-products (**Scheme 4.6**). In the present study, its presence was identified with GC-MS, and it might represent one of the reasons why cinnamaldehyde, cinnamyl alcohol oxidation product, does not evolve to its corresponding acid. Thus, in this study, the presence of cinnamyl cinnamate has been related to cinnamaldehyde. Once the latter has been formed from the alcohol, not only undergoes autoxidation to benzaldehyde but also reacts with the starting alcohol to afford cinnamyl cinnamate, as represented in the proposed retrosynthesis in **Scheme 4.7**.

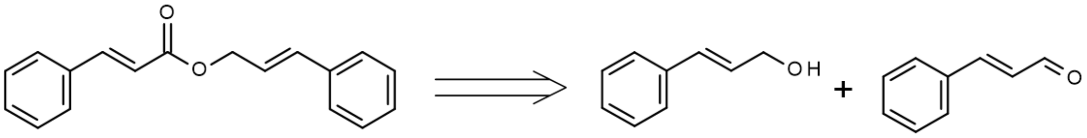

Scheme 4.7: Proposed cinnamyl cinnamate retrosynthesis to cinnamyl alcohol and cinnamaldehyde.

This theory is confirmed by the fact that, when cinnamaldehyde is the starting material of the aerobic oxidation, cinnamyl cinnamate is never observed as a by-product due to the absence of cinnamyl alcohol in the reaction mixture.

In addition, as explained in detail in the previous sections, for cinnamaldehyde to be converted to cinnamic acid with the highest selectivity possible, the reaction environment needs low pressure of oxygen (atmospheric air) to minimise the oxidative cleavage to benzaldehyde. Conversely, cinnamyl alcohol needs higher oxygen pressure (≤ 1 bar) [10, 30, 42, 43, 45] in order to be oxidised to cinnamaldehyde with good selectivity.

As these two conditions are in contrast to each other, it is highly unlikely that cinnamic acid is formed in one-pot reaction starting from its alcohol. In fact, in the present study cinnamic acid was observed in negligible amount when cinnamyl alcohol was oxidised for a minimum of three days, and its presence has been only reported by Niklasson and co-workers, [47] who exposed cinnamyl alcohol to the atmosphere for eight days.

4.2. Conclusions

After the examination of the most appropriate oxygen pressure to be applied to cinnamaldehyde oxidation in order to favour the formation of the desired product cinnamic acid, platinum was found to play a key role in establishing a catalytic control in the reaction, being able to overcome its intrinsic radical nature. In fact, at ≥ 1 bar O_2 and in the absence of a catalyst, the radical nature of the reaction takes full control, making benzaldehyde the primary product whereas at lower oxygen pressure (atmospheric air) and in the presence of platinum the reaction is governed by catalytic control, which favours cinnamic acid. Therefore, in order to observe the effect of platinum, oxygen pressure must be kept low, to ensure cinnamaldehyde evolution to the corresponding carboxylic acid via the Mars-van Krevelen mechanism, and minimise the direct attack of oxygen to cinnamaldehyde that leads to its oxidative cleavage. This is the most favourable condition able to, at least, control the radical reaction. Due to the inherent nature of the aerobic oxidation of cinnamaldehyde, the radical pathway is not completely avoidable, but it was found to be controllable to a certain extent. In order not to lose control over product selectivities, it is necessary that platinum assert its role, i.e. establishing a catalytic control that assures the oxidation to cinnamic acid to follow the Mars-van Krevelen mechanism, hampering the oxidative cleavage to benzaldehyde.

The utilisation of two different platinum precursors allowed an extensive investigation of the nature of the metal nanoparticles formed upon functionalisation on the silica support. After examination of the characteristics of the Pt-SiO_2 materials concerning their catalytic performance, it has been identified 0.057wt% Pt-SiO_2 catalyst, prepared with tetraammineplatinum (II) nitrate precursor, as the most efficient one for cinnamaldehyde conversion under low oxygen pressure. This precursor allowed the formation of active sites with the smallest size, leading to a high initial rate.

Further fundamental research around this subject is required, primarily for the importance of designing a more suitable catalyst, in order for cinnamaldehyde aerobic oxidation to become more selective. As a first brick on the wall in the exploration of a mostly unknown reaction, the current chapter has focused on the catalysis of cinnamaldehyde with non-porous support. Thanks to the recent striking developments in the field of heterogeneous catalysis, [48-55] this reaction can be further tested with different porous supports and transition metals, in order to accurately find the most appropriate materials that can assess a sheer catalytic control on the reaction and avoid the side-mechanisms promoted by autoxidation pathways.

4.3. References

1. Garrote G., Cruz J., Moure A., Dominguez H., Parajo J., Antioxidant activity of byproducts from the hydrolytic processing of selected lignocellulosic materials. Trends in Food Science & Technology, 2004. **15**(3): p. 191-200.
2. Isikgor F.H., Becer C.R., Lignocellulosic biomass: a sustainable platform for the production of bio-based chemicals and polymers. Polymer Chemistry, 2015. **6**(25): p. 4497-4559.
3. Gholivand M.B., Ahmadi F., Simultaneous determination of *trans*-cinnamaldehyde and benzaldehyde in different real samples by differential pulse polarography and study of heat stability of *trans*-cinnamaldehyde. Analytical Letters, 2008. **41**(18): p. 3324-3341.
4. Chen H., Ji H., Zhou X., Xu J., Wang L., Aerobic oxidative cleavage of cinnamaldehyde to benzaldehyde catalyzed by metalloporphyrins under mild conditions. Catalysis Communications, 2009. **10**(6): p. 828-832.
5. Murray W.D., Williams R.E., Katz I., Microbiological and enzymatic production of flavor and fragrance chemicals. Critical Reviews in Biotechnology, 1989. **9**(2): p. 105-169.
6. Lichtenthaler H.K., Schweiger J., Cell wall bound ferulic acid, the major substance of the blue-green fluorescence emission of plants. Journal of Plant Physiology, 1998. **152**(2): p. 272-282.
7. Friedman M., Kozukue N., Harden L.A., Cinnamaldehyde content in foods determined by Gas Chromatography-Mass Spectrometry. Journal of Agricultural and Food Chemistry, 2000. **48**(11): p. 5702-5709.
8. Pound A.W., Pound J.R., Note on the oxidation of cinnamaldehyde. The Journal of Physical Chemistry, 1933. **38**(8): p. 1045-1049.
9. Cinnamaldehyde, MAK Value Documentation, the MAK-Collection for occupational health and safety, 2003.
10. Rucinska E., Miedziak P., Pattisson P., Brett G., Iqbal S., Hutchings G.J., Cinnamyl alcohol oxidation using supported bimetallic Au-Pd nanoparticles: an investigation of autoxidation and catalysis. Catalysis Science & Technology, 2018. **8**(11): p. 2987-2997.
11. Lee D.G., Spitzer U.A., Aqueous dichromate oxidation of primary alcohols. The Journal of Organic Chemistry, 1970. **35**(10): p. 3589-3590.
12. Prabhakaran P.V., Venkatachalam S., Ninan K.N., Permanganate ion supported over crosslinked polyvinylamine as an oxidising agent for alcohols. European Polymer Journal, 1999. **35**(9): p. 1743-1746.
13. Sato K., Hyodo M., Takagi J., Noyori R., Hydrogen peroxide oxidation of aldehydes to carboxylic acids: an organic solvent-, halide- and metal-free procedure. Tetrahedron Letters, 2000. **41**(9): p. 1439-1442.
14. Mallat T., Baiker A., Oxidation of alcohols with molecular oxygen on solid catalysts. Chemical Reviews, 2004. **104**(6): p. 3037-3058.
15. Besson,M., Gallezot P., Selective oxidation of alcohols and aldehydes on metal catalysts. Catalysis Today, 2000. **57**(1): p. 127-141.
16. Muzart J., Palladium-catalysed oxidation of primary and secondary alcohols. Tetrahedron, 2003. **59**(31): p. 5789-5816.

17. Anderson R., Griffin K., Johnston P., Alsters P., Selective oxidation of alcohols to carbonyl compounds and carboxylic acids with platinum group metal catalysts. Advanced Synthesis & Catalysis, 2003. **345**(4): p. 517-523.
18. Ali M.E., Rahman M., Sarkar S., Hamid S., Heterogeneous metal catalysts for oxidation reactions. Journal of Nanomaterials, 2014. **2014**: p. 23.
19. Durndell L.J., Cucuzzella C., Parlett C.M.A., Isaacs M.A., Wilson K., Lee A.F., Platinum catalysed aerobic selective oxidation of cinnamaldehyde to cinnamic acid. Catalysis Today, 2018. **333**: p.161-168.
20. Costa J.C.S., Corio P., Rossi L.M., Catalytic oxidation of cinnamyl alcohol using Au-Ag nanotubes investigated by surface-enhanced Raman spectroscopy. Nanoscale, 2015. **7**(18): p. 8536-8543.
21. Liu X., Ryabenkova Y., Conte M., Catalytic oxygen activation versus autoxidation for industrial applications: a physicochemical approach. Physical Chemistry Chemical Physics, 2015. **17**(2): p. 715-731.
22. Valgimigli L., Amorati R., Fumo M.G., DiLabio G., Pedulli G., Pratt D., The unusual reaction of semiquinone radicals with molecular oxygen. The Journal of Organic Chemistry, 2008. **73**(5): p. 1830-1841.
23. Bendary E., Francis R., Ali H., Sarwat M., El Hady S., Antioxidant and structure-activity relationships (SARs) of some phenolic and anilines compounds. Annals of Agricultural Sciences, 2013. **58**(2): p. 173-181.
24. von Liebig J., Justus Liebig's Annalen der Chemie. Annalen der Chemie, 1832.
25. McNesby J.R., Heller C.A., Oxidation of liquid aldehydes by molecular oxygen. Chemical Reviews, 1954. **54**(2): p. 325-346.
26. Hammond G.B., Oxidation and antioxidants in organic chemistry and biology by Evgeny T. Denisov (Russian Academy of Sciences, Chernogolovka, Russia) and Igor B. Afanas'ev (Vitamin Research Institute, Moscow, Russia). CRC Press (an imprint of Taylor & Francis Group): Boca Raton, FL. 2005. p. xxxviii + 982. Journal of the American Chemical Society, 2006. **128**(13): p. 4495-4496.
27. Marteau C., Ruyffelaere F., Aubry J., Penverne C., Favier D., Nardello-Rataj V., Oxidative degradation of fragrant aldehydes. Autoxidation by molecular oxygen. Tetrahedron, 2013. **69**(10): p. 2268-2275.
28. Ingold K.U., Inhibition of the autoxidation of organic substances in the liquid phase. Chemical Reviews, 1961. **61**(6): p. 563-589.
29. Goeppert A., Meth S., Surya Prakash G.K., Olah G.A., Nanostructured silica as a support for regenerable high-capacity organoamine-based CO_2 sorbents. Energy & Environmental Science, 2010. **3**(12): p. 1949-1960.
30. Durndell L.J., Parlett C.M.A., Hondow N., Wilson K., Lee A.F., Tunable Pt nanocatalysts for the aerobic selox of cinnamyl alcohol. Nanoscale, 2013. **5**(12): p. 5412-5419.
31. Durndell L.J., Isaacs M.A., Li C., Parlett C.M.A., Wilson K., Lee A.F., Cascade aerobic selective oxidation over contiguous dual-catalyst beds in continuous flow. ACS Catalysis, 2019. **9**(6): p. 5345-5352.
32. Mars P., van Krevelen D.W., Oxidations carried out by means of vanadium oxide catalysts. Chemical Engineering Science, 1954. **3**: p. 41-59.
33. Neumann R., Khenkin A.M., Molecular oxygen and oxidation catalysis by phosphovanadomolybdates. Chemical Communications, 2006(24): p. 2529-2538.

34. Guo Z., Liu B., Zhang Q., Deng W., Yang Y., Recent advances in heterogeneous selective oxidation catalysis for sustainable chemistry. Chemical Society Reviews, 2014. **43**(10): p. 3480-3524.
35. Vinod C.P., Wilson K., Lee A.F., Recent advances in the heterogeneously catalysed aerobic selective oxidation of alcohols. Journal of Chemical Technology and Biotechnology, 2011. **86**(2): p. 161-171.
36. Ide M.S., Falcone D.D., Davis R.J., On the deactivation of supported platinum catalysts for selective oxidation of alcohols. Journal of Catalysis, 2014. **311**: p. 295-305.
37. Mori K., Hara T., Mizugaki T., Ebitani K., Kaneda K., Hydroxyapatite-supported palladium nanoclusters: a highly active heterogeneous catalyst for selective oxidation of alcohols by use of molecular oxygen. Journal of the American Chemical Society, 2004. **126**(34): p. 10657-10666.
38. Nishimura T., Onoue T., Ohe K., Uemura S., Palladium(II)-catalyzed oxidation of alcohols to aldehydes and ketones by molecular oxygen. The Journal of Organic Chemistry, 1999. **64**(18): p. 6750-6755.
39. Davis S.E., Ide M.S., Davis R.J., Selective oxidation of alcohols and aldehydes over supported metal nanoparticles. Green Chemistry, 2013. **15**(1): p. 17-45.
40. Hackett S.F.J., Brydson R., Gass M., Harvey I., Newman A., Wilson K., Lee A.F., High-activity, single-site mesoporous Pd/Al_2O_3 catalysts for selective aerobic oxidation of allylic alcohols. Angewandte Chemie, 2007. **119**(45): p. 8747-8750.
41. Lee A.F., Hackett S., Hargreaves J., Wilson K., On the active site in heterogeneous palladium selox catalysts. Green Chemistry, 2006. **8**(6): p. 549-555.
42. Parlett C.M.A., Bruce D., Hondow N., Lee A.F., Wilson K., Support-enhanced selective aerobic alcohol oxidation over Pd/mesoporous silicas. ACS Catalysis, 2011. **1**(6): p. 636-640.
43. Parlett C.M.A., Bruce D., Hondow N., Lee A.F.,Wilson K., Mesoporous silicas as versatile supports to tune the palladium-catalyzed selective aerobic oxidation of allylic alcohols. ChemCatChem, 2013. **5**(4): p. 939-950.
44. Parlett C.M.A., Isaacs M.A., Beaumont S., Bingham L., Hondow N., Lee A.F.,Wilson K., Spatially orthogonal chemical functionalization of a hierarchical pore network for catalytic cascade reactions. Nat Mater, 2016. **15**(2): p. 178-182.
45. Parlett C.M.A., Keshwalla P., Wainwright S., Bruce D., Hondow N., Lee A.F.,Wilson K., Hierarchically ordered nanoporous Pd/SBA-15 catalyst for the aerobic selective oxidation of sterically challenging allylic alcohols. ACS Catalysis, 2013. **3**(9): p. 2122-2129.
46. Yang Z., Zeng H., Zhou X., Ji H., Mechanism into selective oxidation of cinnamaldehyde using β-cyclodextrin polymer as phase-transfer catalyst. Tetrahedron, 2012. **68**(29): p. 5912-5919.
47. Niklasson I.B., Delaine T., Islam M., Karllson R., Luthman K., Karlberg A., Cinnamyl alcohol oxidizes rapidly upon air exposure. Contact Dermatitis, 2013. **68**(3): p. 129-138.
48. Gupta K., Rai R.K., Singh S.K., Metal catalysts for the efficient transformation of biomass-derived HMF and furfural to value added chemicals. ChemCatChem, 2018. **10**(11): p. 2326-2349.
49. Song H., Rioux R.M., Hoefelmeyer J.D., Komor R., Niesz K., Grass M., Yang P., Somorjai G.A., Hydrothermal growth of mesoporous SBA-15 silica in the

presence of PVP-stabilized Pt nanoparticles: synthesis, characterization, and catalytic properties. Journal of the American Chemical Society, 2006. **128**(9): p. 3027-3037.

50. Giovanetti L.J., Ramallo-López J.M., Foxe M., Jones L.C., Koebel M.M., Somorjai G.A., Craievich A.F., Salmeron M.B., Requejo F.G., Shape Changes of Pt Nanoparticles Induced by Deposition on Mesoporous Silica. Small, 2012. **8**(3): p. 468-473.
51. Zhu J., Kailasam K., Xie X., Schomaecker R., Thomas A., High-surface-area SBA-15 with enhanced mesopore connectivity by the addition of poly(vinyl alcohol). Chemistry of Materials, 2011. **23**(8): p. 2062-2067.
52. Pushkarev V.V., Musselwhite N., An K., Alayoglu S., Somorjai G.A., High structure sensitivity of vapor-phase furfural decarbonylation/hydrogenation reaction network as a function of size and shape of Pt nanoparticles. Nano Letters, 2012. **12**(10): p. 5196-5201.
53. Gómez Millán G., Hellsten S., Llorca J., Luque R., Sixta H., Balu A.M., Recent advances in the catalytic production of platform chemicals from holocellulosic biomass. ChemCatChem, 2019. **11**(8): p. 2022-2042.
54. Wilson K., Lee A.F., Catalyst design for biorefining. Philosophical Transactions of the Royal Society A: Mathematical, Physical and Engineering Sciences, 2016. **374**(2061).
55. Polshettiwar V., Varma R.S., Green chemistry by nano-catalysis. Green Chemistry, 2010. **12**(5): p. 743-754.

CHAPTER 5:

Hydroxymethylfurfural aerobic oxidation

The selective oxidation of 5-hydroxymethylfurfural (hydroxymethylfurfural or HMF) represents a green and sustainable transformation of lignocellulosic biomass into different valuable chemicals that find large application in the pharmaceutical and polymer industries, as well as for the production of fuel components. [1-5]

The oxidation of HMF has been extensively studied in liquid water as the solvent of reaction. Water represents a low-cost and non-toxic solvent for oxygenated molecules derived from biomass such as HMF, and catalytic oxidation in water provides a sustainable and environmentally friendly route for the conversion of biomass-derived feedstocks. However, a high pH is often required for the reaction to proceed. [6]

Among the vast array of transition metals that can be employed in heterogeneous catalysed reactions, the performance of supported platinum and gold nanoparticles has been proven to be excellent for the production of 2,5-dicarboxylic acid (FDCA), one of the most important oxidised products of this reaction as it is considered to be a promising building block for the production of sustainable polymeric materials. [5] However, recently, it has been demonstrated that gold is more active for HMF oxidation in terms of conversion, but is less selective than platinum for the desired product FDCA. [6, 7]

In the course of the present chapter, the HMF oxidation reaction is investigated with platinum nanoparticles dispersed over fumed silica, an acidic support that has not been exhaustively reported in previous examples in the scientific literature regarding this reaction, which has instead been widely investigated with supports with a different nature. Contrary to Chapter 3 (TLCT SBA-15 and *MM*-TLCT SBA-15 materials and catalysis), a non-porous support has been utilised in order to assess the importance of an acidic solid material in HMF aerobic oxidation.

5.1. Reaction mechanism

As the aerobic oxidation of HMF has been widely investigated over the past decade from different research groups in the heterogeneous catalysis field, its reaction mechanism has been initially explained in detail in the current section, in order to allow a clear understanding of the results that will be reported later on in the course of this chapter.

The metals and supports that have led to the most successful results for the catalysed oxidation of HMF have been gold, [6, 8-13] platinum [6, 7, 10, 11, 14-19] and palladium [10, 11] supported on TiO_2, CeO_2, C, γ-Al_2O_3, ZrO_2 and hydrotalcite. The mechanism that has been generally observed, regardless of the catalyst used, is reported in **Figure 5.1.**

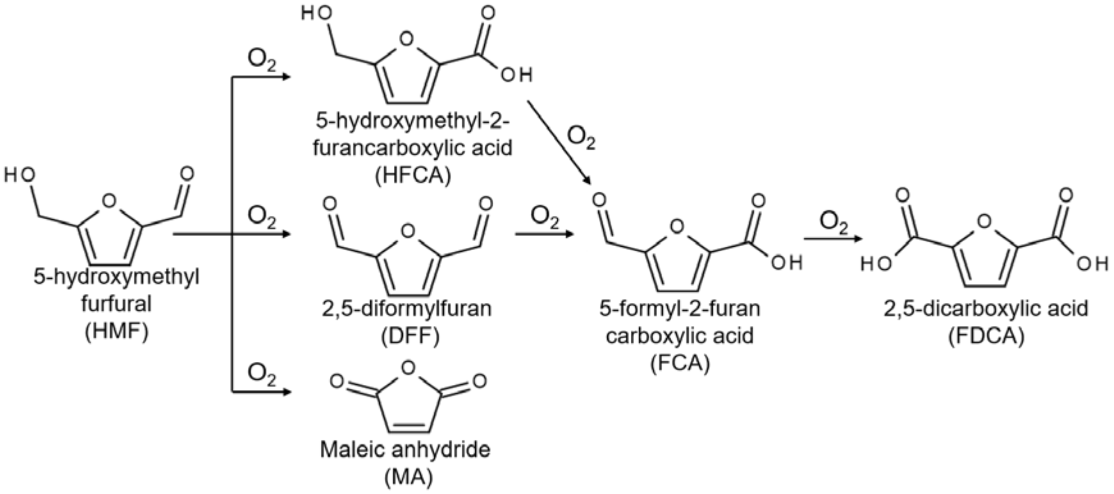

Figure 5.1: Mechanism of heterogeneously catalysed HMF aerobic oxidation (adapted from ref. [1]).

As far as platinum catalysed reactions are concerned, excellent results have been reported in the scientific literature, with HMF conversions up to 90-100% and FDCA as the main oxidation product in excellent selectivities (up to 90%). The supports mentioned above have in common a basic or neutral nature, as a basic environment favours the oxidation of the reactant to FDCA. To favour the oxidation process in presence of noble catalyst systems, the presence of excess base is required, to accelerate the reaction and to maintain the oxidation intermediates formed in the aqueous solution as their salts, so that the catalyst surface is not deactivated. [15, 18]

Even though the nature and the amount of the base to be used in order to obtain optimal conversion and selectivities have not found unanimous consensus in the scientific community, the most employed bases for heterogeneously catalysed reactions have been NaOH [6, 7, 10, 13, 15, 16] or Na_2CO_3. [7, 14, 15, 19] However, it has been generally agreed that a high pH is necessary for the oxidation of HMF to FDCA in water.

The previous experimental chapters (3. TLCT SBA-15 and *MM*-TLCT SBA-15 materials and catalysis and 4. Cinnamaldehyde aerobic oxidation) described the aerobic oxidation of model compounds catalysed by platinum nanoparticles supported on silica supports, which are slightly acidic as they contain silanol groups on the surface. [20, 21] Therefore, it has been decided to investigate if the same material could be successfully employed in the reaction described in the current chapter, to evaluate whether the nature of the support played a key role for the successful oxidation of HMF, or if this depended more strongly on the reaction conditions (temperature, oxygen pressure and base) and the support metal used.

A fundamental understanding of the role of molecular oxygen, base and water is important to developing an environmentally friendly method for FDCA production from HMF. Davis [6] and Gorbanev [13] (and co-workers) demonstrated that, in the absence of oxygen, HMF undergoes Cannizzaro rearrangement and is oxidised to 5-hydroxymethyl-2-furancarboxylic acid (HFCA) and 2,5-bishydroxymethylfuran (BHMF) in a 6:4 ratio, respectively. The Cannizzaro disproportionation reaction involves the base-induced disproportionation of two molecules of a non-enolisable aldehyde to give a primary alcohol and a carboxylic acid, [22] as represented in **Figure 5.2** for the case of HMF.

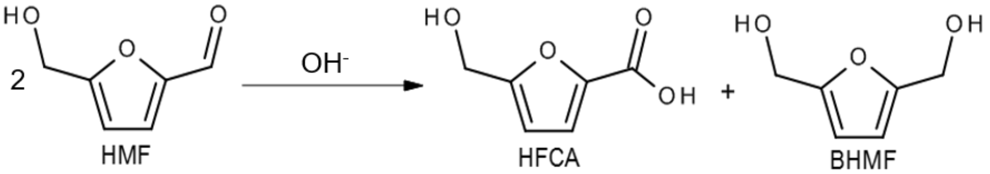

Figure 5.2: Cannizzaro disproportionation reaction occurring when HMF reaction is carried out in absence of O_2. [22]

On the other hand, when oxygen is present, the rate of oxidation of the aldehyde moiety of HMF is significantly greater than the Cannizzaro reaction, and the selectivity to BHMF is annulled or minimised. [6]

Davis and co-workers proposed a mechanism for the oxidation of HMF in aqueous solution catalysed by either platinum or gold in the presence of an excess base (OH^-) at 22 °C. [6] This mechanism is reported in **Figure 5.3**.

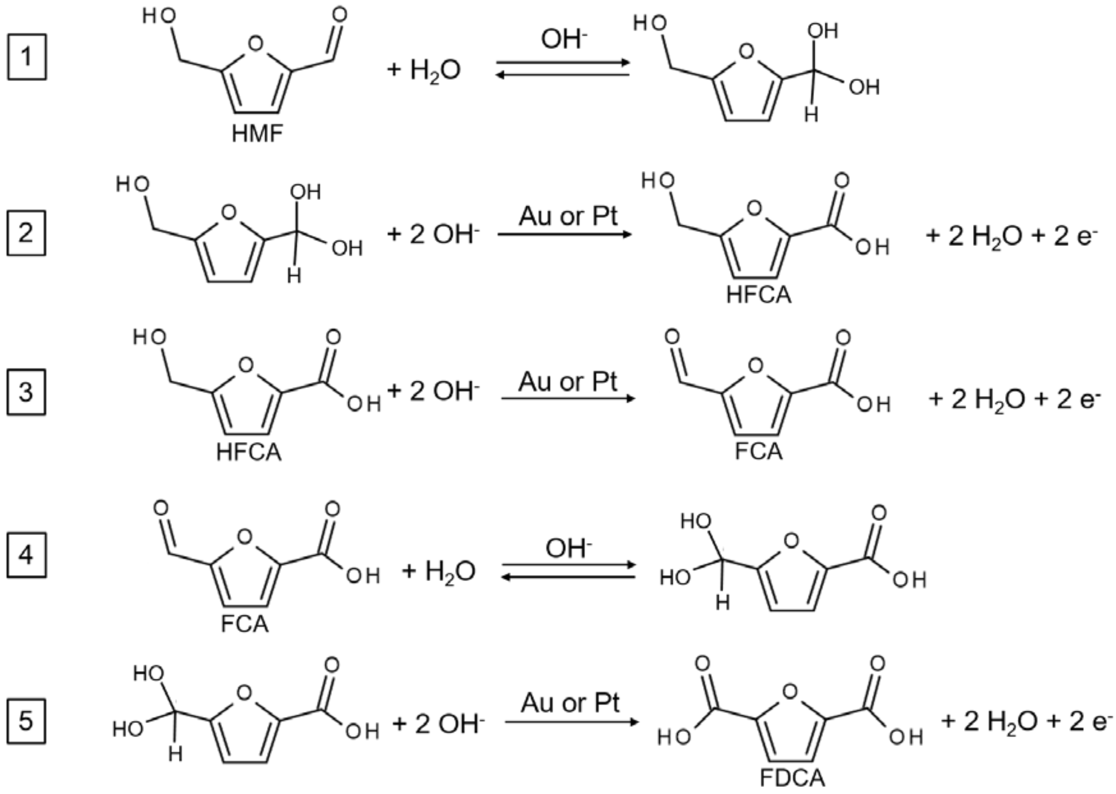

Figure 5.3: Proposed mechanism of HMF oxidation in presence of an excess base and either Pt or Au catalyst (adapted from ref. [6]).

The authors mentioned above conducted studies in labelled water ($H_2{}^{18}O$), in order to acquire a better comprehension of the role of water, base and oxygen. The appearance of ^{18}O in the oxidation products suggested that the aqueous-phase oxidation proceeds through a geminal diol formed by the reaction of the aldehyde with the solvent (step 1 in **Figure 5.3**). The oxidation of HMF proceeding through a geminal diol intermediate has been supported by different studies. [6, 15, 18] The geminal diol is formed based on the reversible hydration of aldehydes in water in the presence of a base (OH^-), which consists of two steps. Firstly, the nucleophilic addition of a hydroxide ion to the carbonyl group, followed by proton transfer from water to the alkoxide ion intermediate. [23]

The second step of **Figure 5.3** consists of the dehydrogenation of the geminal diol intermediate, facilitated by the hydroxide ions adsorbed on the metal surface, to produce the carboxylic acid. The product of this step is 5-hydroxymethyl-2-furancarboxylic acid (HFCA). These steps account for the incorporation of two ^{18}O atoms in HFCA when the reaction is performed in $H_2{}^{18}O$.

In the third step, the base is believed to deprotonate the alcohol side-chain to form an alkoxy intermediate, a step that may occur primarily in the solution. [24] Hydroxide ions on the catalyst surface then facilitate the activation of the C-H bond in the alcohol side-chain to form the aldehyde intermediate, 5-formyl-2-furancarboxylic acid (FCA).

In steps 4 and 5, finally, the aldehyde moiety of FCA is oxidised to 2,5-dicarboxylic acid (FDCA). These two steps are expected to proceed analogously to steps 1 and 2 for the oxidation of HMF to HFCA. The reversible hydration of the aldehyde group in step 4 to a geminal diol accounts for two more ^{18}O atoms incorporated in FDCA when the oxidation is performed in $H_2{}^{18}O$.

Hence, the sequence in **Figure 5.3** explains that four oxygen atoms have been incorporated in FDCA from H_2O solvent. These results demonstrated how crucial the role of water in this reaction is.

Differently from water and base, the role of oxygen has been long debated in literature as its precise contribution to the reaction has not been completely clarified up to date. Davis and co-workers suggested that its role consists of completing the catalytic redox cycle. [6] They reported the presence of H_2O_2 in the reaction mixture catalysed by Au/TiO_2, a fact that suggested that oxygen undergoes reduction with H_2O by removing the electrons deposited into the metal particles during the adsorption and reaction of hydroxide ions. As there are no other extensive investigations in this regard and the mentioned study concerned a reaction catalysed by different metal and support than presented in this chapter, this represents one of the possible explanations to the exact role that oxygen plays in the reaction. [24]

A challenge observed in the past by different scientists regards HMF self-degradation, which entails a decrease of the desired oxidation products' yield. Degradation is generally defined as the change of reactant into lower-value products, as opposed to conversion, which is the change of reactant into high-value products. [11] A scheme for the degradation of HMF has been proposed by Ait Rass and co-workers and is reported in **Figure 5.4**.

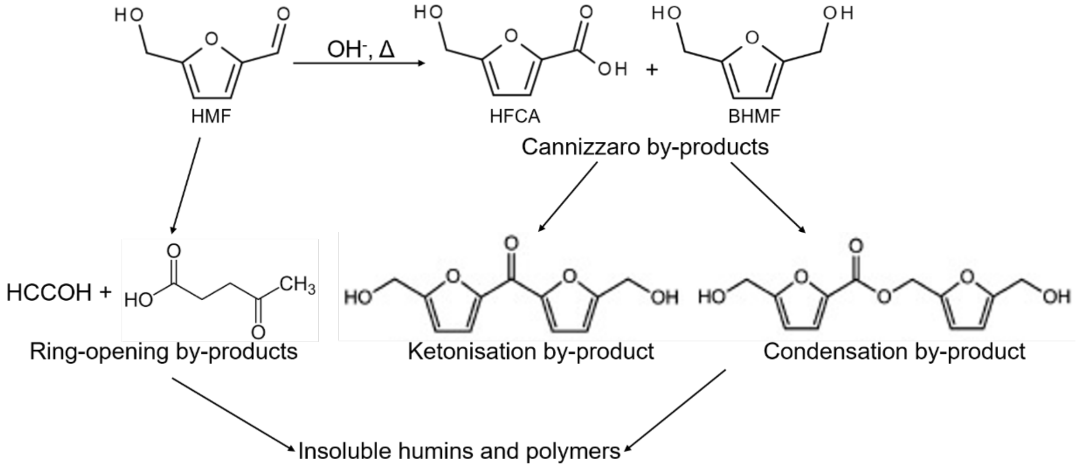

Figure 5.4: Possible pathways of HMF degradation products (adapted from ref. [18]).

5.2. Characterisation of platinum catalysts

Two classes of platinum catalysts have been prepared following the wet-impregnation method, as described in Chapter 2, section 2.3.3. (Synthesis of platinum catalysts – hydroxymethylfurfural aerobic oxidation). Fumed silica (SiO_2) has been functionalised with two different metal precursors, namely ammonium tetrachloroplatinate (II) [$(NH_4)_2PtCl_4$] and hydrogen hexachloroplatinate (IV) hexahydrate [$H_2PtCl_6 \cdot 6H_2O$] (**Figure 5.5**), to impart a specific wt% (0.1 and 2 wt%) by weight loading of platinum upon the support.

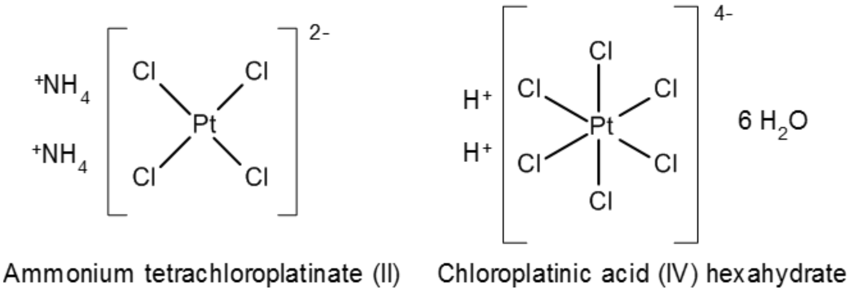

Figure 5.5: Pt precursors used to prepare the catalysts described in this section.

The actual wt% has been measured using Inductively-Coupled Plasma-Mass Spectrometry (ICP-MS). These four catalysts, each with a name assigned, are summarised in **Table 5.1**.

Catalyst name	Pt precursor	Nominal Pt wt%	Actual Pt wt%
0.12 wt%-ATP	$(NH_4)_2PtCl_4$	0.1	0.12
1.98 wt%-ATP	$(NH_4)_2PtCl_4$	2	1.98
0.08 wt%-CPA	$H_2PtCl_6 \cdot 6H_2O$	0.1	0.08
1.50 wt%-CPA	$H_2PtCl_6 \cdot 6H_2O$	2	1.50

Table 5.1: Pt wt% of each catalyst determined with ICP-MS, and corresponding catalyst name.

The catalysts prepared with ammonium tetrachloroplatinate (II) precursor maintained the nominal loading more than those prepared with hydrogen hexachloroplatinate (IV) hexahydrate precursor. This might be because each class of materials has been prepared at different times. The decrease in platinum loading that is observed for the second metal precursor might be the consequence of a slight loss of metal, probably due to sticking to the walls of the beaker during the overnight agitation of the slurries.

Figure 5.6 illustrates wide-angle X-ray diffraction of the catalysts described in **Table 5.1**, together with the diffractogram of the unfunctionalised support for comparison.

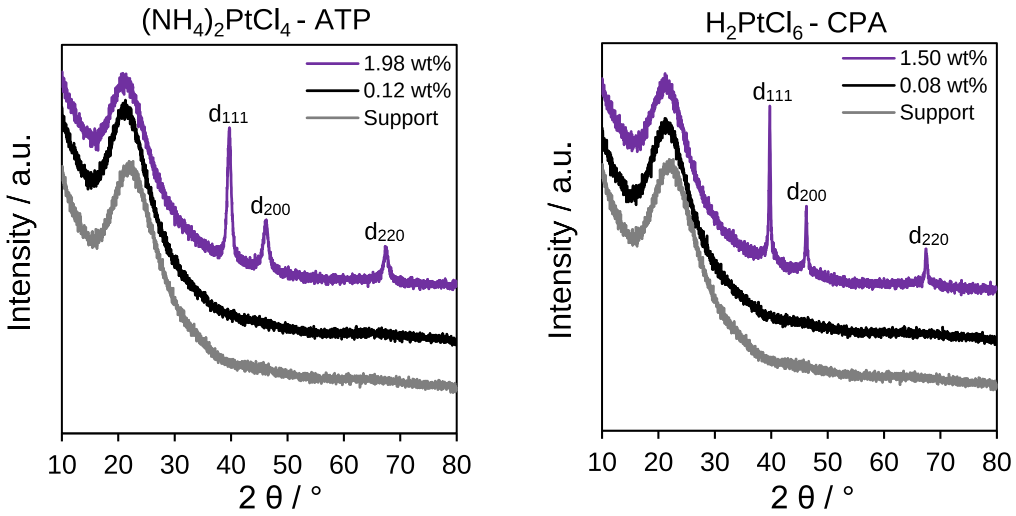

Figure 5.6: Wide-angle XRD of 0.12 and 1.98 wt% (ATP precursor, left) and 0.08 and 1.50 wt% (CPA precursor, right) Pt-SiO_2 catalysts (offset for clarity).

The highest loading platinum catalysts in **Figure 5.6** show very well defined reflections relative to different platinum planes, while the lowest loading catalysts and the parent support do not show any of these reflections. The metal planes of 0.08 and 0.12 wt% catalysts are not detected, as this technique is not able to identify particles sizes below 3 nm; therefore it is expected that the particle size determined for the other catalysts it is overestimated. **Table 5.2** shows the platinum particle size of each catalyst, calculated with wide-angle XRD and Scanning Transmission Electron Microscopy (STEM).

	Pt particle size / nm	
Catalyst	**XRD**	**STEM**
0.12 wt%-ATP	n.d.	1.48 ± 0.66
1.98 wt%-ATP	8.2	3.6 ± 2.4
0.08 wt%-CPA	n.d.	1.72 ± 0.81
1.50 wt%-CPA	13.9	1.89 ± 0.73

Table 5.2: Particle size determined by XRD and STEM of the four Pt catalysts in **Table 5.1** (STEM particle dimension evaluated over ≈ 250 particles).

The error associated with STEM calculations increases with size for ATP precursor, while it decreases in the case of CPA precursor. STEM can detect particles below the detection limit of XRD; in fact, 0.12 wt%-ATP and 0.08 wt%-CPA particle size values are located below 3 nm. The two catalysts prepared with hydrogen hexachloroplatinate (IV) hexahydrate precursor showed the presence of many clusters (identified with STEM), consisting of agglomerates of more particles that adhere to one another. Due to a higher number of clusters in 1.50 wt%-CPA compared to 0.08 wt%-CPA, XRD overestimated the particle size as it has mistaken the clusters for single particles, leading to a misinterpretation of the real value. However, STEM identified the particles below 3 nm for all the catalysts, as it is possible to appreciate in **Figure 5.7** and **Figure 5.8**.

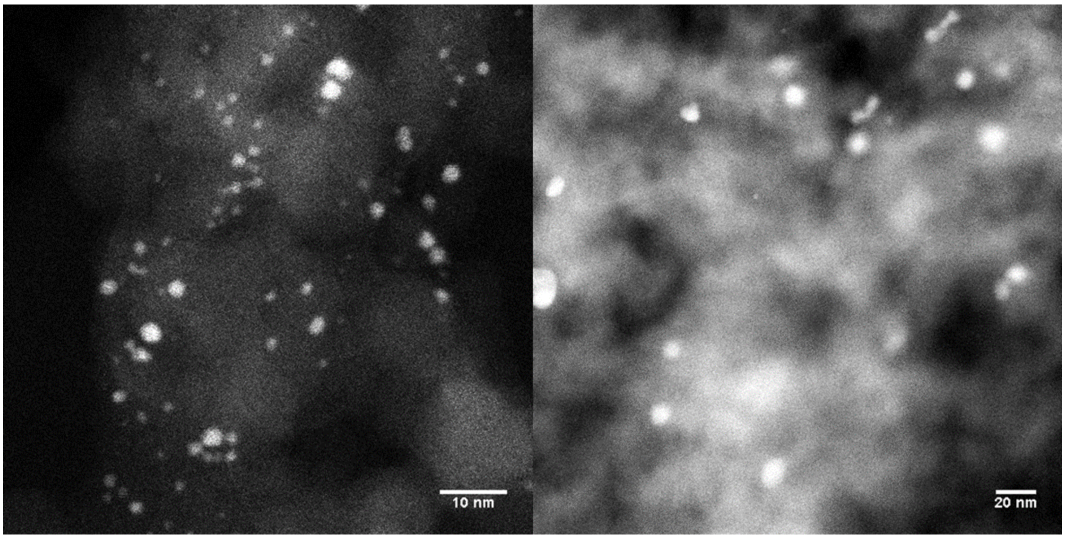

Figure 5.7: Dark field STEM images of 0.12 wt% (left) and 1.98 wt% (right) Pt-SiO_2 catalysts prepared from ATP precursor.

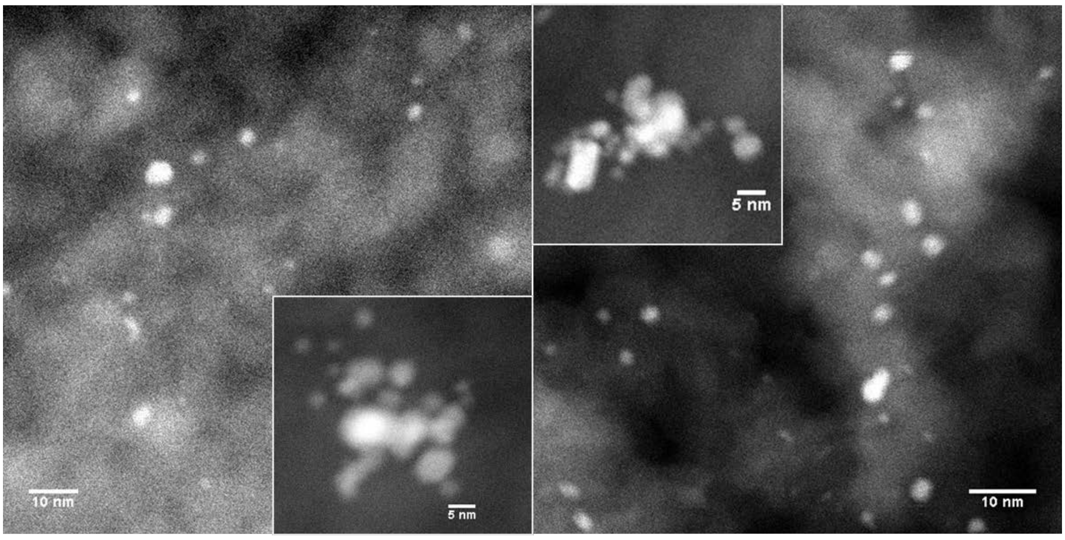

Figure 5.8: Dark field STEM images of 0.08 wt% (left) and 1.50 wt% (right) Pt-SiO_2 catalysts prepared from CPA precursor. Insets: clusters of particles.

The architecture of the catalysts in **Table 5.1** was identified through nitrogen physisorption porosimetry, and it is shown in **Figure 5.9**.

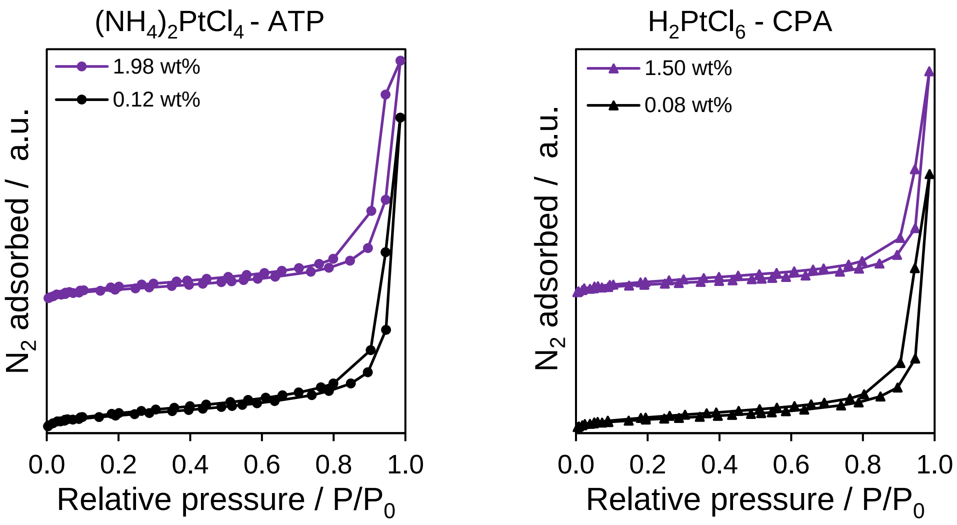

Figure 5.9: Adsorption-desorption N_2 isotherms of 0.12 and 1.98 wt% (ATP precursor, left) and 0.08 and 1.50 wt% (CPA precursor, right) Pt-SiO_2 catalysts (offset for clarity).

The architecture of the support has been identified through nitrogen physisorption porosimetry, which exhibited pseudo-type II isotherms, [25] typical of non-porous materials. BET surface areas of all catalysts measured between 212 and 253 $m^2\ g^{-1}$, compared to 210 $m^2\ g^{-1}$ of the unfunctionalised support and followed an inversely proportional trend with metal loading (**Table 5.3**).

Catalyst	**Particle size / nm (STEM)**	**Surface area / $m^2\ g^{-1}$**
0.12 wt%-ATP	1.48 ± 0.66	253 ± 25
1.98 wt%-ATP	3.6 ± 2.4	225 ± 22
0.08 wt%-CPA	1.72 ± 0.81	221 ± 22
1.50 wt%-CPA	1.89 ± 0.73	212 ± 21

Table 5.3: Surface area of the four Pt catalysts characterised in the present chapter.

This phenomenon is attributed to the fact that at low loadings the surface area of the catalyst increases, as a consequence of the dispersion of platinum on the support, which generates ridges and extra roughness on the surface, and of the deposition of the active sites on the external surface of the support. When the platinum amount increases, bigger nanoparticles are formed, leading to poorer dispersion that affects the surface area negatively. The catalysts that belong to CPA class display the lowest surface area as nanoparticle clusters tend to occupy more space on the support than single and better-dispersed nanoparticles.

X-ray Photoelectron Spectroscopy (XPS) was carried out on the four Pt-SiO_2 catalysts. As this technique allows the X-rays to enter the sample with < 10 nm depth, it is extremely useful to obtain information about the surface region (this technique has been explained in detail in Chapter 2, section 2.4.6. X-ray Photoelectron Spectroscopy).

In **Table 5.4** is listed the wt% composition of platinum on the surface of the catalysts, in relation to the total metal content previously determined with ICP-MS.

Catalyst	**Particle size / nm (STEM)**	**ICP-MS Pt / wt%**	**Pt Surface / wt%**	**Oxide content / %**
0.12 wt%-ATP	1.48 ± 0.66	0.12	0.08	31
1.98 wt%-ATP	3.6 ± 2.4	1.98	0.52	21
0.08 wt%-CPA	1.72 ± 0.81	0.08	0.08	39
1.50 wt%-CPA	1.89 ± 0.73	1.50	0.76	21

Table 5.4: Surface composition properties obtained from XPS fitting.

The platinum content determined with ICP-MS is the metal present both in the bulk and on the surface of the catalysts. The low loading catalysts present the total content of metal on their surface, while the high loading catalysts display the metal partly on the surface (determined by XPS) and partly in the bulk, as illustrated in Chapter 3, section 3.3.2. (Characterisation of pore-expanded Pt-TLCT SBA-15 catalysts, **Figure 3.53**). The higher loading indicates that there is higher platinum content exposed per gram of catalyst, but a lower percentage of it is present on the surface, due to bigger metal nanoparticles (**Figure 3.53**, **a**). When the loading is lower, the particles are smaller, therefore, the atoms are more exposed to the surface (**Figure 3.53**, **b**). Smaller particles prefer to be distributed on the surface in the form of PtO_2, as they are more capable of stabilising the oxide rather than the metal due to energy requirements, [26] and because when platinum is exposed to the environment, it is more sensitive to oxidative processes. From **Table 5.4** is clear that, for both precursors, the oxide content on the surface decreases as metal loading increases, as lower loadings allow the nanoparticles to be better distributed and have smaller size, and to be located more on the surface of the catalyst, as explained above.

Figure 5.10 shows the detection of platinum on the surface of the catalysts:

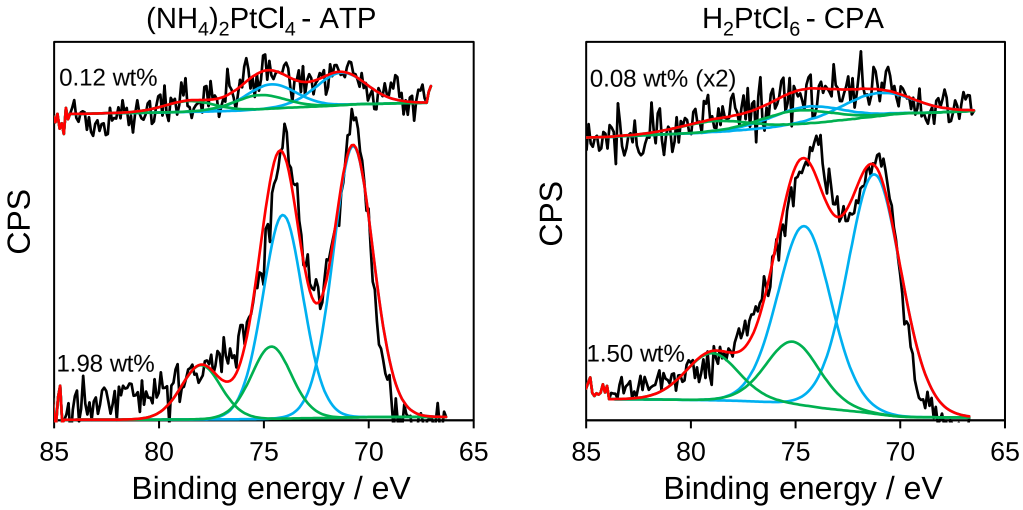

Figure 5.10: Pt 4f spectra of low and high loading catalysts prepared with ATP precursor (left) and CPA precursor (right), (offset for clarity).

The black lines indicate the raw data and the red lines indicate the full envelope fitting of the region. Contributions due to $Pt^{(0)}$ (blue lines) and PtO_2 (green lines) fitted components are shown, revealing the emergence of oxide features at low loadings. This confirms that the formation of PtO_2 species is favoured at lower metal loadings.

5.3. Results and discussion

5.3.1. Effect of silica support

Before starting the investigation of aerobic oxidation of HMF in the presence of Pt-SiO_2 catalysts, the role of the support has been attentively studied, as it has not been generally employed as typical support for this type of reaction. In the vast literature concerning heterogeneously catalysed HMF oxidation, there is only one study reporting the use of a Pt-SiO_2 catalyst, [14] but the authors did not carry out a process optimisation. Hence the support's impact on the uncatalysed reaction has not been reported. Another paper reports the performance of Ni-Pd nanoparticles over different supports, revealing that the basicity of the support is advantageous for the efficient oxidation of HMF. [27]

As the effective role of silica remains unclear up to date, one of the aims of this chapter consists of examining the effect that this support has on HMF aerobic oxidation, in order to make some clarification and better understand how critical the role of the support for the successful oxidation of HMF is.

Firstly, the oxidation of HMF has been carried out in the absence of a catalyst, with and without SiO_2 at 80 and 130 ˚C, under 1 bar of oxygen pressure and with 1 equivalent of Na_2CO_3 as the base (**Figure 5.11**).

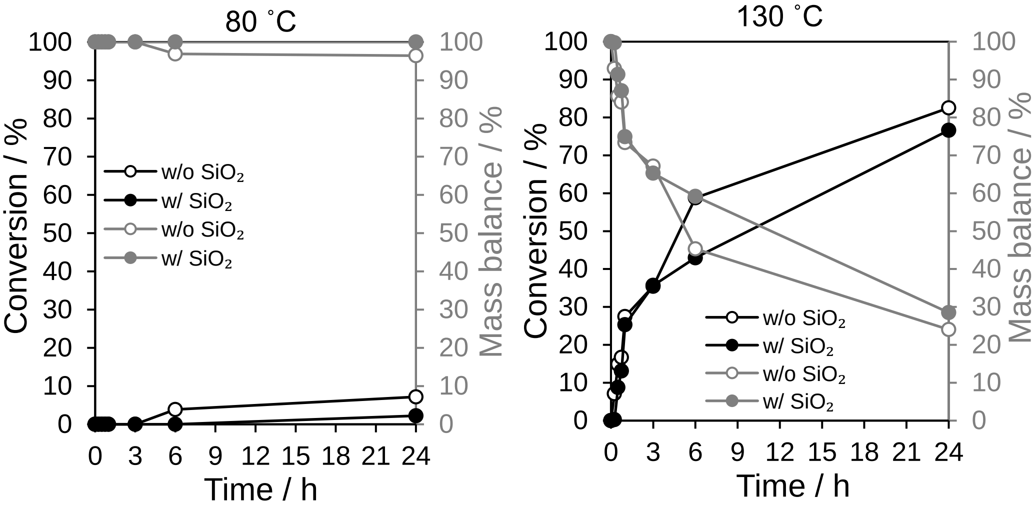

Figure 5.11: Effect of SiO_2 in HMF aerobic oxidation carried out at 80 (left) and 130 ˚C (right), in presence of 1 eq. of Na_2CO_3 under 1 bar O_2 (black lines = conversion, grey lines = mass balance).

In both cases, even if at 130 ˚C the conversion is higher due to temperature effects (discussed later in this chapter), the profiles are slightly affected by the presence of silica support, which tends to inhibit conversion by approximately 5% between 6 and 24 hours. This is an indication that at some point during the reaction, the support interacts with the reactant or the base, hampering HMF transformation. Instead, the support does not affect product selectivities, which remain the same regardless of its presence in the reaction mixture. For this reason, they have not been reported in this paragraph, but will be discussed in the next sections when compared to the catalysed reaction.

The hypothesis of an interaction between the support and one of the species present in the solution finds certainty when analysing the High-Pressure Liquid Chromatography (HPLC) spectra of the reaction. **Figure 5.12** is a generic representation of the refractive index detector (RID) of two chromatograms obtained for the aerobic oxidation of HMF conducted under any temperature and pressure condition, in presence and absence of the support.

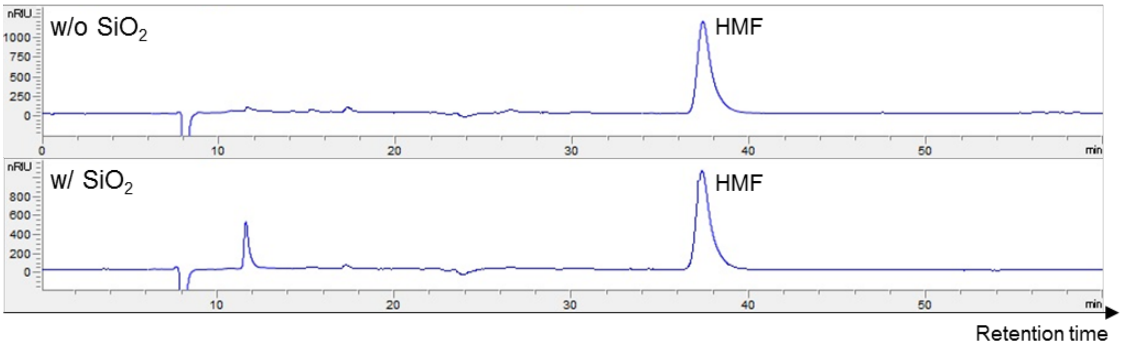

Figure 5.12: Chromatograms of RID detector relatives to the uncatalysed HMF aerobic oxidation carried out at any temperature in presence of Na_2CO_3 at any pressure, in presence and absence of SiO_2 support.

The picture above clearly supports what has been presumed for **Figure 5.11**. The fact that any reaction (catalysed and uncatalysed) carried out in the presence of the support showed the presence of the peak at a retention time of 11.6 minutes (at any time of reaction), led to the certain conclusion that silica is playing a role during the reaction. Besides partly inhibiting HMF conversion, it contributes to the formation of a compound that has not been possible to identify, which stems from the interaction of silica with HMF, Na_2CO_3, or both. More probably, silica only interacts with Na_2CO_3, as the mass balance in **Figure 5.11** is higher when the support is present in the reaction solution. Therefore the unidentified peak should not participate in the total carbon balance calculation. Thus, the reason why the mass balance decreases over the course of the reaction lies with the formation of unidentified products as a result of HMF degradation, but not due to the peak at 11.6 minutes in **Figure 5.12**, as this is not related to the reactant.

The fact that the presence of silica in the uncatalysed reaction leads to the appearance of an unidentified side-product is confirmed by a change in colour of the solutions soon after the reaction has started. **Figure 5.13** is a representation of reaction solutions containing HMF in water and 1 equivalent of base, under bubbling oxygen at 1 bar pressure. Flask **A** corresponds to the reaction carried out in the absence of SiO_2, whereas flask **B** corresponds to the reaction carried out in the presence of SiO_2.

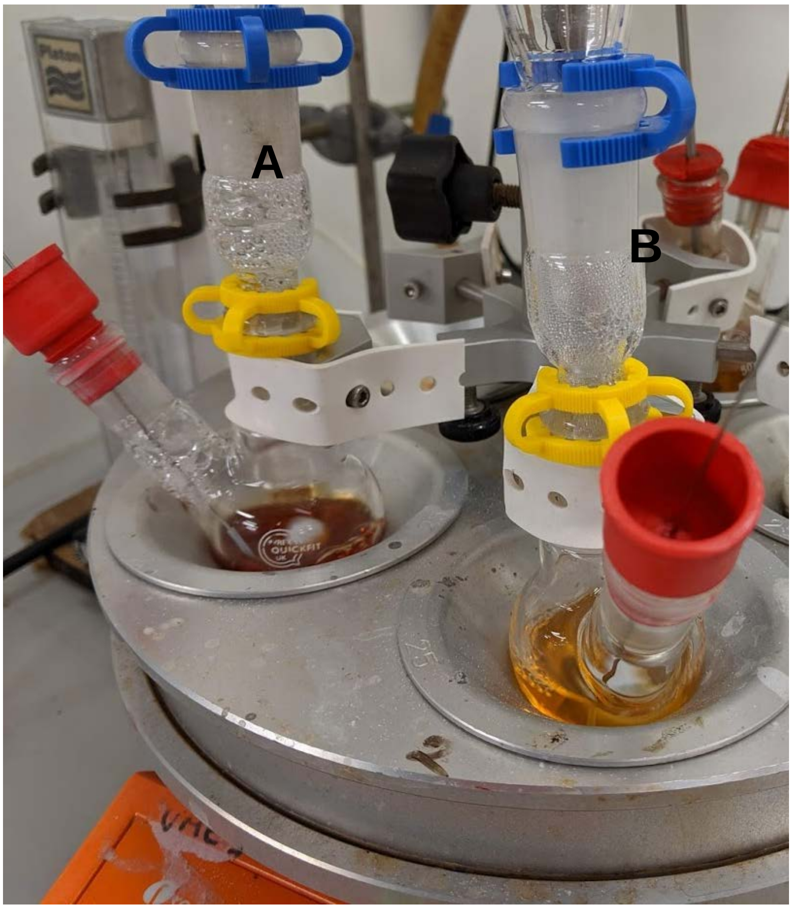

Figure 5.13: Uncatalysed HMF aerobic oxidation carried out at 80 ˚C in presence of 1 eq. of Na_2CO_3 at 1 bar O_2. Flask **A**: without SiO_2, flask **B**: with SiO_2. Picture taken after 1 h the reaction started.

The picture above clearly shows that when the support has been added to the reaction mixture, the solution changed colour due to the interaction with the reaction environment. This evidence is consistent with the presence of an additional peak observed in the RID detector of the HPLC chromatograms (**Figure 5.12**), and with an inhibition of HMF conversion, caused by the presence of a product of the interaction of silica with the base.

In the following sections, in order to make a correct comparison between blank (uncatalysed) and catalysed reactions and a proper assessment of the catalytic activity, the blank reactions are carried out in the presence of silica.

5.3.2. Effect of base at 80 ˚C

The aerobic oxidation of HMF was first investigated at 80 ˚C in the presence of a weak base, in order to observe the impact of different oxygen pressures at the chosen temperature. Most literature examples concerning platinum catalysed HMF oxidation report experiments carried out between room temperature and 100 ˚C under atmospheric pressure and 10 bar oxygen, [1] with an example reported by Sahu and Dhepe, where the temperature is raised up to 140 ˚C at a second stage of the reaction, in order to suppress HMF thermal degradation. [7] Platinum catalysed reactions have been reported to employ either NaOH or Na_2CO_3 as bases, and in the present project it has been decided to utilise the latter, as Sahu and Dhepe have demonstrated its superiority in terms of oxidative performance. [7] The reference catalyst used throughout the current section is 1.98 wt%Pt-SiO_2 (prepared with ATP precursor).

5.3.2.1. Effect of base at 1 bar O_2 pressure

Figure 5.14 shows the effect of different amounts of base on the conversion of HMF and on the total mass balance during 24 hours reaction at 80 ˚C. The effect of 1.98 wt%Pt-SiO_2 catalyst has been compared to the uncatalysed reaction.

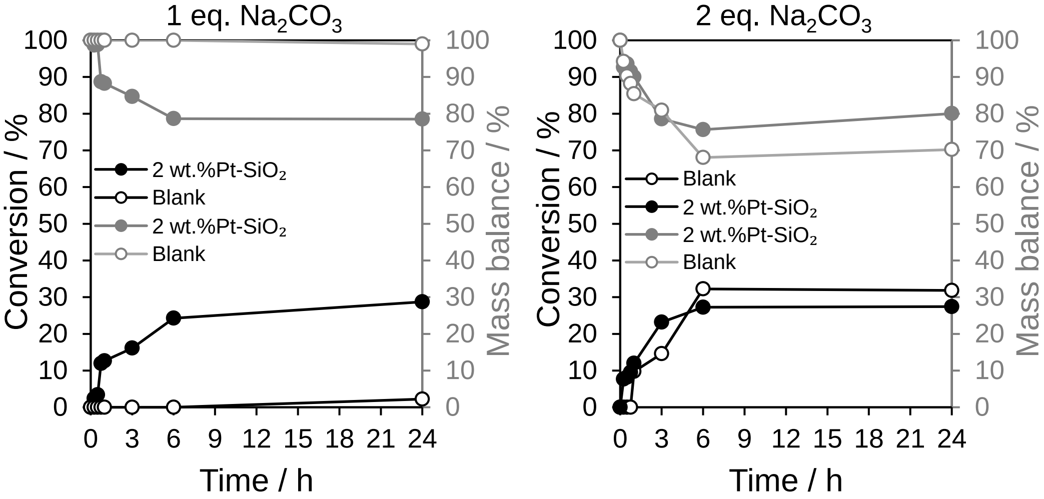

Figure 5.14: HMF aerobic oxidation carried out at 80 ˚C in presence of 1 eq. (left) and 2 eq. (right) of Na_2CO_3 under 1 bar O_2 (black lines = conversion, grey lines = mass balance).

In the presence of 1 equivalent of base (**Figure 5.14**, left), the use of the catalyst afforded 30% higher conversion with a corresponding loss of 20% mass balance in 24 hours, whereas the uncatalysed reaction promoted almost zero conversion. On the other hand, a higher amount of base (**Figure 5.14**, right) affected mainly the uncatalysed reaction, whose conversion increased by 30% over the entire reaction. In the presence of the catalyst, instead, 2 equivalents of base promoted higher conversion only over the first 3 hours, but no significant improvement was achieved overall. The platinum normalised initial rates (IR) of the reactions in **Figure 5.14** have been compared over the first 30 minutes (**Figure 5.15**), in order to assess how much the rate of conversion has been affected by different amounts of base.

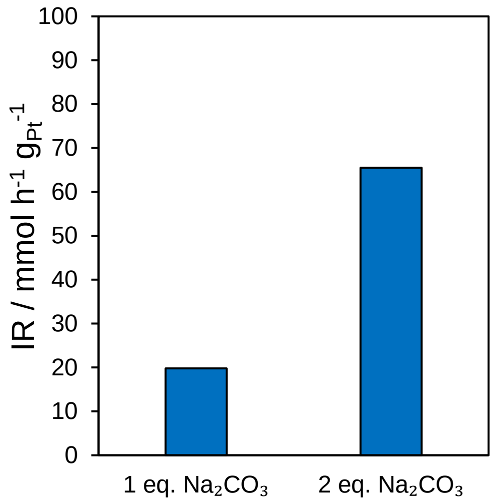

Figure 5.15: Pt normalised IR of HMF aerobic oxidation in presence of 1 and 2 eq. of Na_2CO_3. Catalyst: 1.98 wt%Pt-SiO_2-ATP.

As expected, when the reaction was carried out in the presence of 2 equivalents of base the initial rate was higher, since HMF conversion is promoted by the simultaneous effect of OH^- and water, as explained in section 5.1 (Reaction mechanism).

Figure 5.14, besides showing the conversion profiles obtained with different amounts of base, illustrates the carbon balances associated with them. The fact that mass balance proportionally decreases with HMF conversion indicates that the majority of the peaks observed in the HPLC chromatograms have not been identified. This happens because they do not correspond to the expected oxidation products; hence the majority of conversion is due to reactant degradation (**Figure 5.4**). Looking at the graphs in **Figure 5.14** it is possible to infer that, in the presence of 2 equivalents of base and in the absence of catalyst, the reactant is almost completely degraded, since there is a 30% loss of mass balance (32% of HMF has been converted). On the other hand, when the catalyst participates to the reaction, the mass balance is retained by 10% with 1 and 2 equivalents of base. These results indicate that the catalyst helps to preserve the mass balance, reducing the process of degradation. Even though this effect is not too prominent, it suggests that Pt-SiO_2 has a beneficial effect on the oxidation of HMF. This result is in agreement with reports published in the scientific literature over the last decade.

Figure 5.16 reports the selectivity patterns of blank (left) and catalysed (right) reactions only in the presence of 1 equivalent of base, since higher amount promoted a stronger degradation of the reactant.

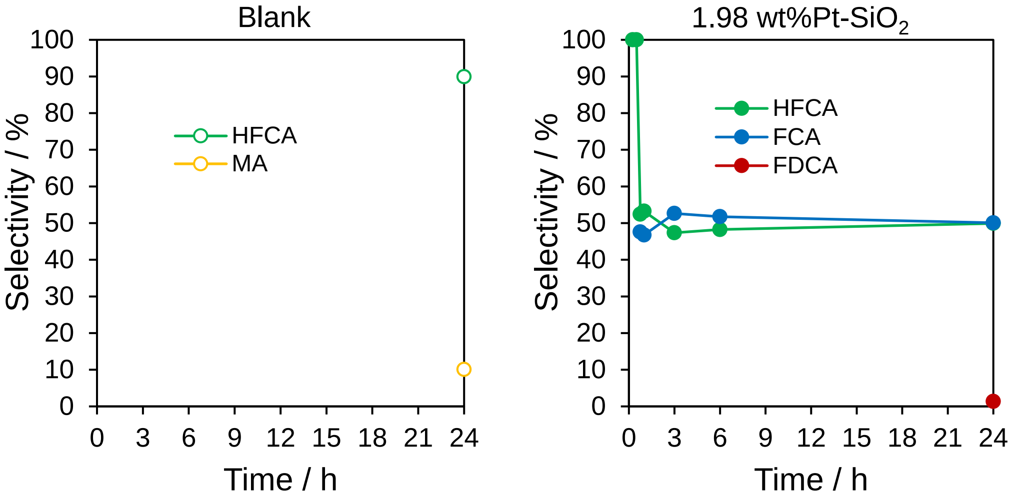

Figure 5.16: Product selectivities obtained for blank (left) and catalysed (right) HMF aerobic oxidation carried out at 80 ˚C in presence of 1 eq. Na_2CO_3 at 1 bar O_2.

In the absence of a catalyst, HMF conversion was negligible, however, the only products obtained were 5-hydroxymethyl-2-furancarboxylic acid (HFCA) and maleic anhydride (MA). On the other hand, the catalyst favoured HMF conversion to HFCA that in turn oxidised to 5-formyl-2-furancarboxylic acid (FCA) and, marginally, to the final oxidation product 2,5-dicarboxylic acid (FDCA), without promoting the formation to MA. This indicates that Pt-SiO_2 catalyst contributes to the oxidation of the reactant, despite 20% out of the 30% of the converted HMF resulted in degradation products (**Figure 5.14**, left).

In the presence of 2 equivalents of base, selectivity patterns did not show any great improvement with respect to **Figure 5.16**; therefore they have not been reported. This indicates that a higher amount of base only caused higher degradation of HMF but did not have any effect on the oxidation of the reactant.

After examination of conversion and product selectivity profiles of HMF oxidation conducted in a basic environment at 80 °C, it is possible to conclude that the addition of 2 equivalents of base did not bring any advantage to the overall reaction and that the platinum catalyst has mostly promoted the oxidation of HMF to HFCA and FCA, two intermediates.

The selectivity patterns observed in **Figure 5.16** are summarised in **Scheme 5.1**, together with the product yields (y%) obtained at 24 hours.

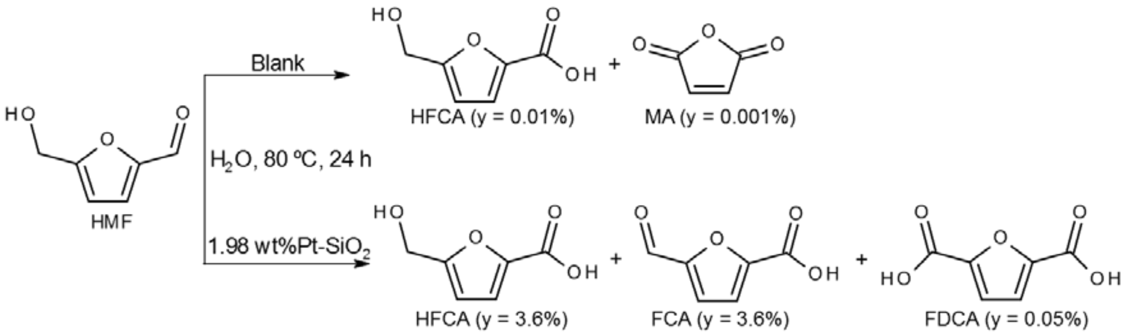

Scheme 5.1: Scheme of blank (top) and catalysed (bottom) HMF aerobic oxidation carried out at 80 ˚C in presence of 1 eq. Na_2CO_3 under 1 bar O_2 (y = yield).

The scheme above represents how the uncatalysed aerobic oxidation of HMF afforded HFCA as the only oxidation product, while the catalyst promoted the further oxidation of HFCA to FCA and a negligible amount of FDCA, regardless of the amount of base. Therefore, the catalytic activity of platinum towards HMF oxidation is evident from the formation of oxidation products in higher yields compared to the blank reaction.

5.3.2.2. Effect of base at 10 bar O_2 pressure

HMF aerobic oxidation at 80 °C was also investigated at higher oxygen pressure, in order to study whether it could have a promoting effect towards the formation of the products. Firstly, the uncatalysed reaction in the presence of different amounts of base was examined, in order to compare the results obtained in this instance to those obtained at lower oxygen pressure examined in section 5.3.2.1 (Effect of base at 1 bar O_2 pressure). **Figure 5.17** correlates conversion, mass balance and product selectivities with 1 and 2 equivalents of base, and the reactions at 10 bar oxygen were carried out for 6 instead of 24 hours (as it happened for 1 bar O_2 pressure) due to safety reasons, as the high-pressure reactor could not be kept running overnight.

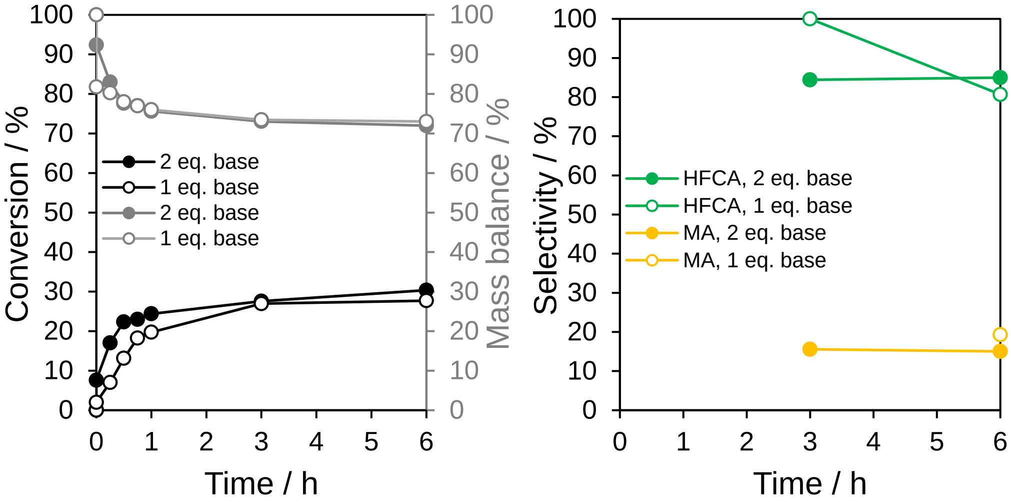

Figure 5.17: Conversion and mass balance (left) and product selectivities (right) profiles obtained for the uncatalysed aerobic oxidation of HMF carried out at 80 ˚C in presence of 1 and 2 eq. of Na_2CO_3, under 10 bar O_2 (black lines = conversion, grey lines = mass balance).

Contrary to what has previously been observed, 10 bar oxygen pressure contributed to a faster transformation of the reactant even in the absence of a catalyst, and no strong difference was observed when the reaction was carried out with more base. However, higher pressure exclusively promoted HMF degradation, and the negligible amount of HMF that has been oxidised was converted to HFCA and MA, which are the products observed for the uncatalysed oxidation of HMF under 1 bar oxygen (**Figure 5.16**, left). Product selectivities, which were not affected by the quantity of base in the reaction mixture, followed the same pattern described in **Scheme 5.1** (top). This highlights the incapability of HMF to be further oxidised to FCA or FDCA in the absence of a catalyst, therefore, oxygen pressure did not play a critical role in this regard.

Since a higher amount of base did not produce any improvement, the same reaction was carried out in the presence of the platinum catalyst utilising only 1 equivalent of base. Conversion, mass balance and product selectivity profiles are displayed in **Figure 5.18.**

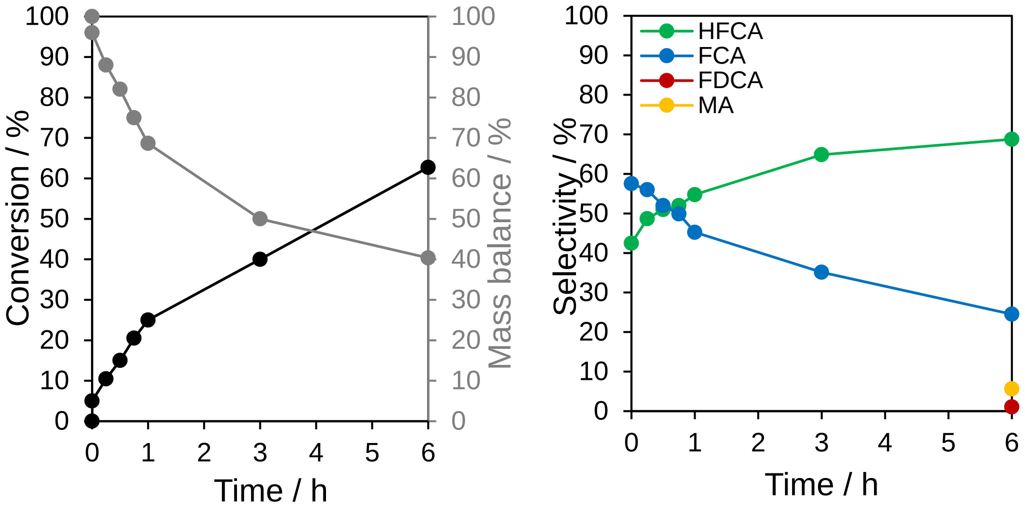

Figure 5.18: Conversion and mass balance (left) and product selectivities (right) profiles obtained for the catalysed aerobic oxidation of HMF carried out at 80 ˚C with 1 eq. Na_2CO_3 under 10 bar O_2. Catalyst: 1.98 wt%Pt-SiO_2-ATP (black lines = conversion, grey lines = mass balance).

Compared to the blank reaction (1 eq. base, **Figure 5.17**, left), the catalyst promoted higher conversion with a concomitant dramatic loss of mass balance, due to HMF degradation promoted at higher oxygen pressure. Therefore, the product selectivities displayed in **Figure 5.18** (right) refer to the very scant portion of HMF that was identified with HPLC, and are similar to those obtained at lower oxygen pressure (**Figure 5.16**). The only difference observed, in this case, was the minor tendency of HFCA to be oxidised to FCA, despite the higher amount of oxygen. While under 1 bar oxygen HFCA : FCA selectivities were obtained in a 48 : 52 ratio, at higher pressure it dropped to 69 : 25 at 6 hours.

The platinum initial rates of HMF aerobic oxidations carried out at 80 ˚C in the presence of 1 equivalent of base at different oxygen pressures are displayed in **Figure 5.19**.

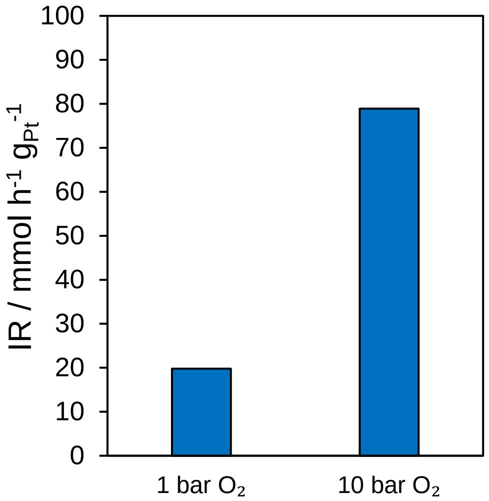

Figure 5.19: Pt normalised IR of HMF aerobic oxidation in presence of 1 and 2 eq. of base. Catalyst: 1.98 wt%Pt-SiO_2-ATP.

As mentioned above, higher oxygen pressure promotes a faster reactant transformation, but to degradation products and not to those of interest. Therefore, despite the initial rate being superior at 10 bar, lower pressure promotes HMF to undergo degradation, helping its oxidation.

To fully understand the impact that oxygen pressure had on the behaviour of the reaction at 80 ˚C, **Figure 5.20** compares conversion and mass balance profiles obtained under 1 and 10 bar oxygen. The graphs reported below refer to reactions carried out in the presence of 1 equivalent of base, as it has been previously observed that adding higher amount of base did not generate any advantage in terms of oxidative effect.

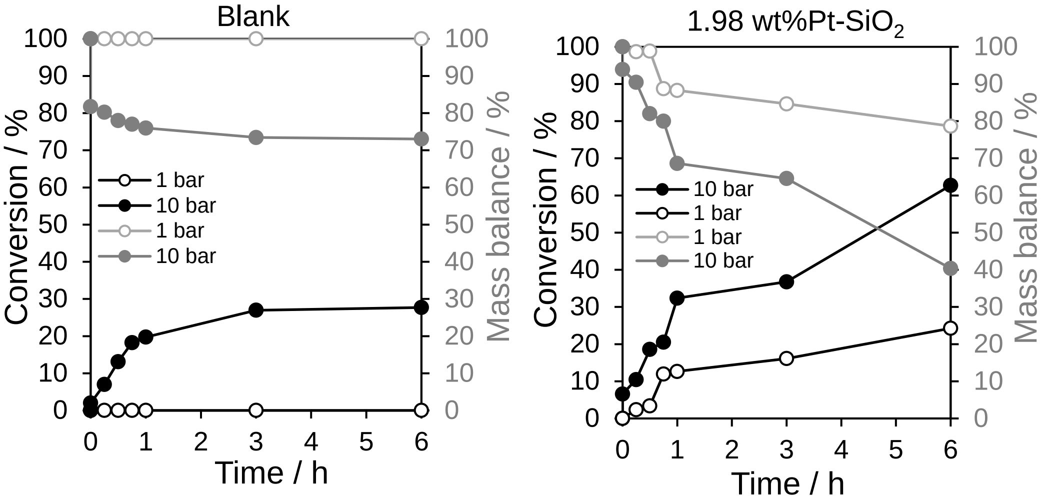

Figure 5.20: Comparison of conversion and mass balance profiles for blank (left) and catalysed (right) aerobic oxidation of HMF, at 80 ˚C in presence of 1 eq. Na_2CO_3 under 1 and 10 bar O_2 (black lines = conversion, grey lines = mass balance).

As explained for **Figure 5.19**, in both cases higher pressure favoured conversion, but at the same time it had a negative effect on the total mass balance, indicating that HMF converted to undesired degradation products that could not be identified with HPLC. **Figure 5.20** (right) shows that at both pressures mass balance decreased to the same extent as conversion increased, even in the presence of a catalyst, indicating that Pt-SiO_2 had a negative effect on the oxidation conducted under 10 bar oxygen pressure.

Examining the product selectivities at 1 and 10 bar oxygen pressure, it has been demonstrated that at both pressures the uncatalysed reaction leads to HFCA as the only oxidation product, while the catalyst can promote an oxidation step further producing FCA. Therefore, higher pressure follows the same pattern depicted in **Scheme 5.1** as well.

These results indicated that 10 bar oxygen is deleterious for the reaction conducted at 80 ˚C even in the presence of a Pt-SiO_2 catalyst because it does not promote the desired oxidation pathway, as most of the converted HMF is transformed to degradation products rather than HFCA, FCA or FDCA.

5.3.3. Base and pressure effect at 130 ˚C

The aerobic oxidation of HMF was also investigated at 130 ˚C, in order to examine the effect of temperature on the possible reaction pathways in the presence and absence of Pt-SiO_2 catalyst. In the first instance, the role of the base was examined: blank and catalysed reactions were carried out with 0 to 4 equivalents of Na_2CO_3 under 1 bar oxygen pressure, and conversion and mass balance profiles are reported in **Figure 5.21**:

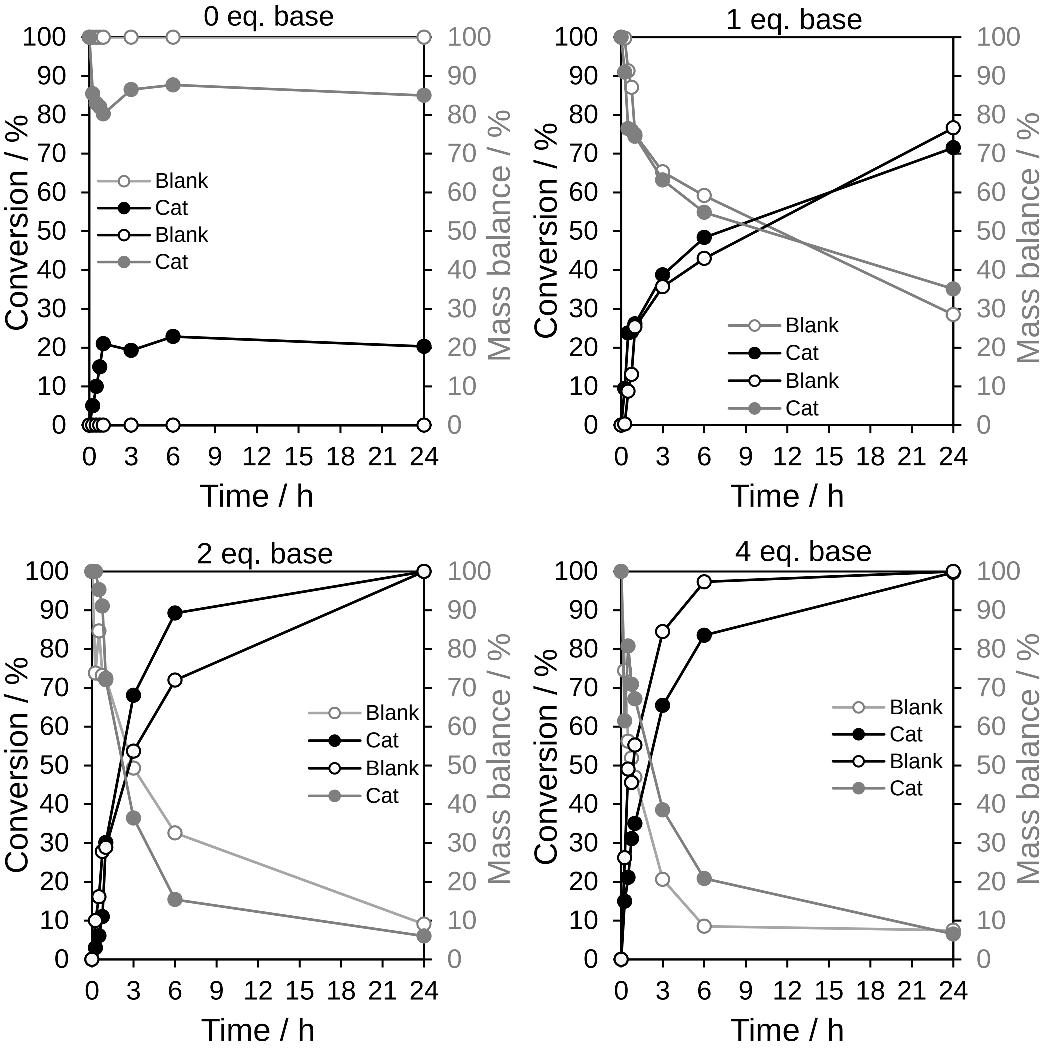

Figure 5.21: Conversion and mass balance profiles of HMF aerobic oxidation in presence of 0, 1, 2, 4 eq. of Na_2CO_3 at 1 bar O_2 (black lines = conversion, grey lines = mass balance).

The top-left graph in **Figure 5.21** highlights that the base is necessary to convert the reactant, which is transformed when the catalyst is added, however almost all conversion is transformed to undesired side-products. Adding only 1 equivalent of base drastically improved conversion to the detriment of mass balance, which was utterly lost, indicating that only traces of HMF are transformed to desired oxidation products. As the amount of base increased, conversion and mass balance profiles highlighted the occurrence of thermal decomposition in a more pronounced way. These results indicate that, even if a basic environment is necessary for the oxidation of HMF, an excessively high pH leads to its gradual degradation. The reactant degradation is visible from the solutions becoming heavily coloured since the beginning of the reaction, with the appearance of dark-brown insoluble solid compounds (humins as in **Figure 5.4**). This factor has already been observed in the literature at pH ≈ 13. [11, 15, 18]

However, similarly to the experiments carried out at 80 ˚C, it has been observed a reproducible mechanism of oxidation: the uncatalysed reaction led to HFCA and MA, whereas the catalysed reaction afforded HFCA, FCA and FDCA. In addition, the catalyst at a higher temperature also favoured the formation of 2,5-diformylfuran (DFF), another oxidation product, whose selectivity decreased over time in favour of FDCA, and was higher in the absence of a base (**Scheme 5.2**).

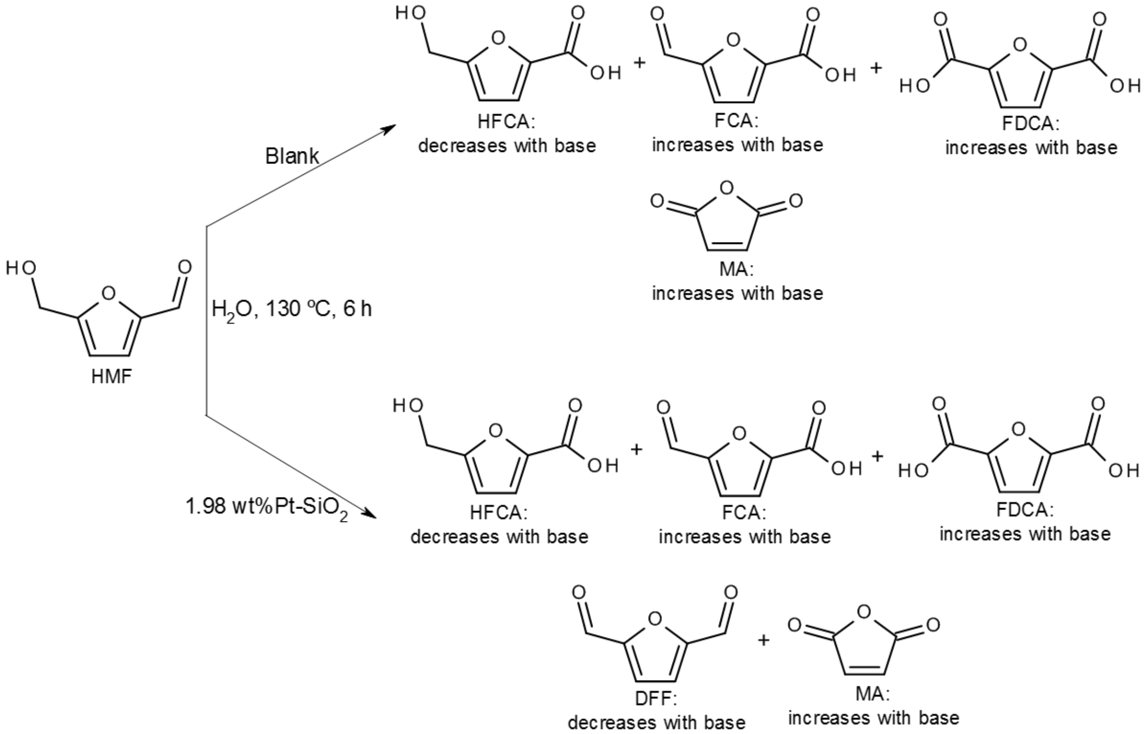

Scheme 5.2: Scheme of blank (top) and catalysed (bottom) HMF aerobic oxidation carried out at 80 ˚C in presence of 0-4 eq. of Na_2CO_3 under 1 bar O_2.

The selectivity profiles have not been reported as the observed oxidation pathway cannot be considered trustworthy, due to a small percentage of HMF converted to oxidation products; product yield never exceeded 5%.

From **Figure 5.21** it is evident how high temperature is detrimental because it promotes the formation of degradation products that it has not been possible to detect, and neither the catalyst nor the base has been able to reduce this effect. Moreover, as previously anticipated, Pt-SiO_2 does not represent a suitable catalyst to achieve satisfactory oxidation to dicarboxylic acid because of its slight acidity that conflicts with the need for a basic environment for this purpose.

Comparing the results obtained at 130 ˚C under 1 and 10 bar oxygen pressure, it is noticeable that increasing pressure has an even more detrimental effect as this affects mass balance, especially during the first hour of reaction, as noticed when the reaction has been conducted at 80 ˚C (**Figure 5.22**).

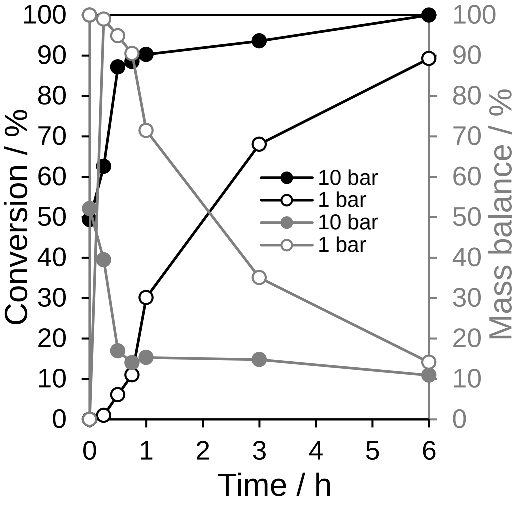

Figure 5.22: Conversion and mass balance profiles of HMF aerobic oxidation with 2 eq. of Na_2CO_3 at 130 ˚C, under 1 and 10 bar O_2 (black lines = conversion, grey lines = mass balance).

In terms of product selectivities, under 10 bar O_2, formation of HFCA has not been observed, presumably because high pressure rapidly transformed HMF alcohol and aldehyde moieties to their corresponding oxidation products, resulting in FCA only. In addition, while at 1 bar O_2, traces of FDCA had been observed not before 24 hours, raising pressure boosted its formation to occur earlier, even though in less of 10% selectivity. Also, MA formation is promoted at 10 bar O_2 (**Figure 5.23**).

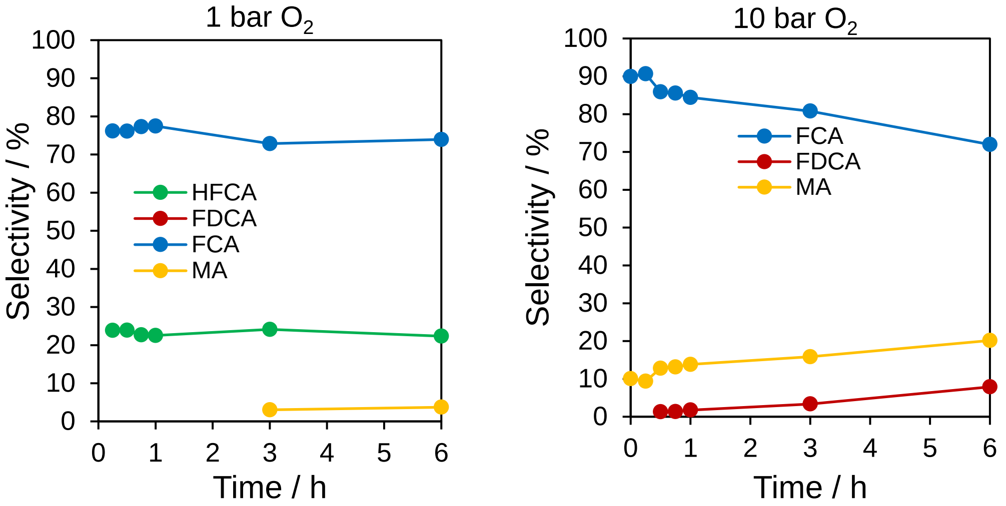

Figure 5.23: Product selectivities profiles of HMF aerobic oxidation with 2 eq. of Na_2CO_3 at 130 ˚C, under 1 and 10 bar O_2.

In conclusion of this section, it has been demonstrated how HMF decomposition occurs at high temperature and pressure, and platinum nanoparticles supported on an acidic material are not able to control this effect.

5.3.4. Catalytic results

After testing different temperature, pressure and base conditions in order to find the most suitable to promote HMF conversion, minimising its deterioration at the same time, in the presence and absence of a Pt-SiO_2 catalyst, it has been concluded that the experiments conducted at 80 ˚C under 1 bar oxygen pressure were those that benefited the most compared to harsher conditions. In addition, it has been decided to restrict the presence of the base to 1 equivalent, as it has previously been observed the importance of limiting the pH in the reaction environment, in order to control the degradation reactions.

Therefore, the catalysts described in section 5.2 (Characterisation of platinum catalysts) have been screened in HMF aerobic oxidation under the conditions above cited. **Figure 5.24** shows conversion (left) and mass balance (right) profiles of HMF aerobic oxidation screened with the catalysts listed in **Table 5.1**.

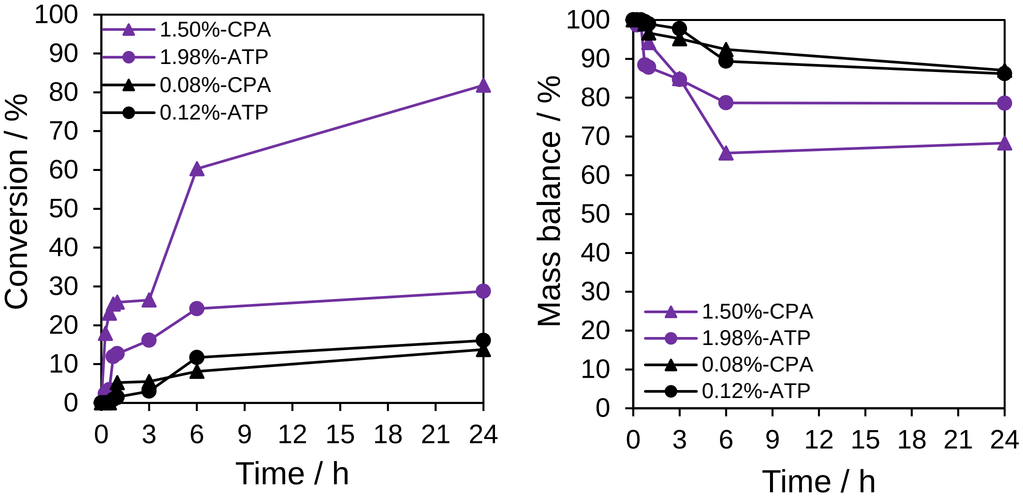

Figure 5.24: Conversion (left) and mass balance (right) profiles of HMF aerobic oxidation with 1 eq. of Na_2CO_3 at 80 ˚C, under 1 bar O_2.

Both high loading catalysts (1.98 wt%-ATP and 1.50 wt%-CPA, purple lines) promoted the conversion of the reactant at all times, compared to low loading catalysts (**Figure 5.24**, left). Apart from 1.50 wt%-CPA catalyst, which afforded the highest conversion (82%), the others fostered strong HMF degradation, as shown in **Figure 5.24** (right). In the case of the other three catalysts, the majority of HMF converted has been lost, and the total carbon balance decreased almost as much as the conversion increased. On the other hand, 1.50 wt%-CPA catalyst caused the loss of "only" 32% of the reactant converted; this represented the only case of 50% conversion retained and transformed into oxidation products. This indicates that 1.50 wt%-CPA catalyst was able to protect HMF from degradation reactions.

The product selectivity profiles of the four catalysts are shown in **Figure 5.25**.

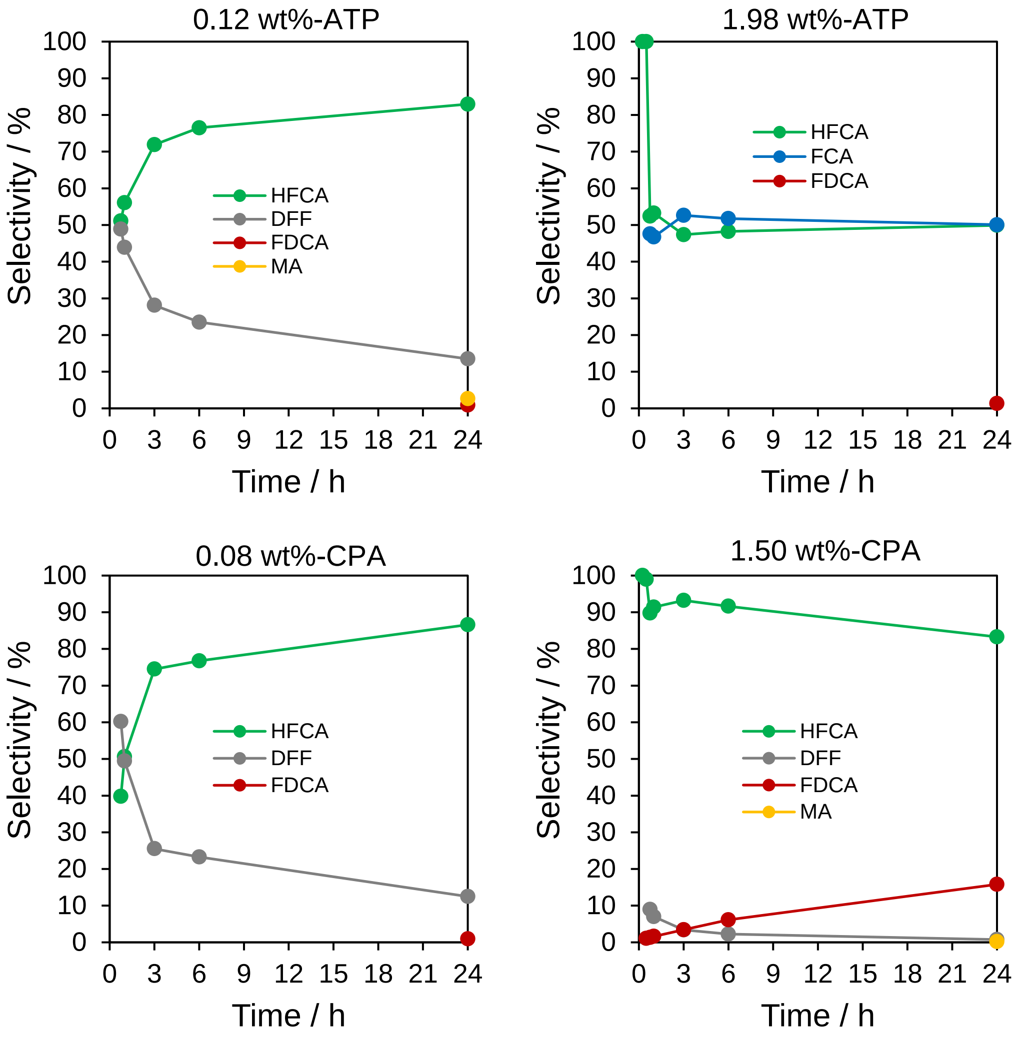

Figure 5.25: Product selectivities profiles of HMF aerobic oxidation with 1 eq. of Na_2CO_3 at 80 ˚C, under 1 bar O_2.

The selectivity profiles highlight that the main oxidation product obtained with Pt-SiO_2 catalysts under these reaction conditions is HFCA, indicating that only the aldehyde side of HMF has been oxidised to carboxylic acid. Similarly to the experiments previously reported, carried out at different temperatures and pressures, traces of FDCA have been formed at the end of the reaction. In the presence of low loading catalysts, another oxidation product is formed, DFF, which stems from the oxidation of the alcohol side of the reactant. 1.50 wt%-CPA catalyst is the only one that promoted not only high conversion with better retention of total carbon balance but also improved oxidation to FDCA, the desired product. As **Figure 5.24** previously showed, the selectivity patterns of 0.12 wt%-ATP, 1.98 wt%-ATP and 0.08 wt%-CPA catalysts are not reliable, as the loss of mass balance almost entirely corresponds to the amount of HMF converted, indicating that the majority of reactant has been transformed to waste products. The only catalyst that allowed a real assessment of the transformation of HMF is 1.50 wt%-CPA. Yields of the products obtained at 24 hours with this catalyst (calculated from **equation 2.9** in Chapter 2) are pictured in **Figure 5.26**.

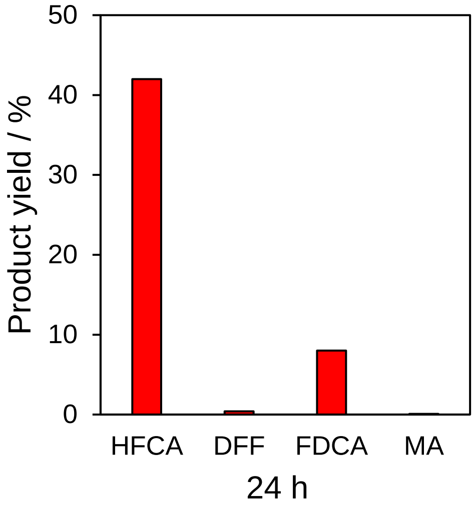

Figure 5.26: Yields of HMF oxidation products obtained with 1.50 wt%-CPA catalyst.

In terms of conversion, the high loading catalysts have afforded a better performance, as over the first 30 minutes of reaction they promoted some transformation of the reactant, while the low loading catalysts have promoted zero conversion. For this reason, platinum normalised initial rates of 1.98 wt%-ATP, and 1.50 wt%-CPA catalysts have been calculated over the first 30 minutes of reaction, based on the straight line *mmol vs time* equation and calculated from **equation 2.11** (Chapter 2), (**Figure 5.27**).

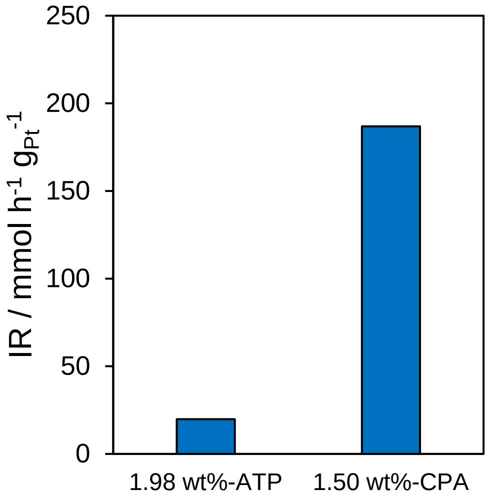

Figure 5.27: Pt normalised IR of 1.98 wt%-ATP and 1.50 wt%-CPA catalysts.

As observed in **Figure 5.24** (left), HMF conversion has been faster for the entire duration of reaction with 1.50 wt%-CPA catalyst. **Figure 5.27** indicates that this catalyst promotes approximately ten times faster initial conversion than 1.98 wt%-ATP. This demonstrates that the type of platinum precursor utilised for the materials synthesis had a strong impact on its catalytic performance, which in the case of hydrogen hexachloroplatinate (IV) hexahydrate (CPA) was superior in terms of initial rate of reaction, conversion and product selectivities, despite the silica not being a suitable support for HMF oxidation.

In section 5.2 (Characterisation of platinum catalysts), **Table 5.4** showed data relative to the surface composition of the catalysts. 1.98 wt%-ATP and 1.50 wt%-CPA have 0.52 wt% and 0.76 wt% of the total amount of platinum on their surface, respectively. Out of this percentage, 21% correspond to PtO_2 in both cases. Since the oxide content is the same, but the catalytic performance of 1.50 wt%-CPA has been remarkably superior with respect to the other catalyst, it can be concluded that HMF oxidation depends on the amount of $Pt^{(0)}$ on the surface of the catalyst, which in the case of 1.50 wt%-CPA is higher. This phenomenon is due to the metal nanoparticles dimension of 1.98 wt%-ATP and 1.50 wt%-CPA: the former's measured 3.6 ± 2.4 nm, the latter's 1.89 ± 0.73 nm (calculated with STEM). As **Figure 3.53** in Chapter 3 showed, bigger nanoparticles expose lower amount of platinum on the surface in relation to the total amount, whereas smaller nanoparticles exhibit higher amount of platinum atoms on their surface.

The comparison of the particle size obtained when the catalysts have been prepared with ammonium tetrachloroplatinate (II) (ATP), and hydrogen hexachloroplatinate (IV) hexahydrate (CPA) led to the conclusion that the latter contributed to the formation of smaller platinum nanoparticles on an amorphous and non-porous silica support, resulting in superior catalytic performance for the oxidation of HMF.

5.4. Conclusions

The first step achieved in the course of this chapter has been the demonstration of the unsuitability of an acidic support, namely silica, for the successful transformation of HMF into the desirable oxidation product FDCA.

Being aware of this issue, a comprehensive study has been carried out to investigate the catalytic abilities of Pt-SiO_2 catalysts in the aerobic oxidation of HMF, explore the effect of different temperatures, pressures and amount of sodium carbonate as the base. The catalysts employed have been prepared with two platinum precursors, in order to examine if diverse precursors had a remarkable impact on the catalysis.

The catalytic results led to the conclusion that, between the two precursors used, hydrogen hexachloroplatinate (IV) hexahydrate is the most suitable for HMF aerobic oxidation, since it allowed the smallest metal nanoparticle size, which in turn allowed higher platinum content to be located on the surface of the catalyst, where the reaction occurred.

5.5. References

1. Gupta K., Rai R.K., Singh S.K., Metal catalysts for the efficient transformation of biomass-derived hmf and furfural to value added chemicals. ChemCatChem, 2018. **10**(11): p. 2326-2349.
2. Besson M., Gallezot P., Pinel C., Conversion of biomass into chemicals over metal catalysts. Chemical Reviews, 2014. **114**(3): p. 1827-1870.
3. Serrano-Ruiz J.C., Luque R., Sepúlveda-Escribano A., Transformations of biomass-derived platform molecules: from high added-value chemicals to fuels via aqueous-phase processing. Chemical Society Reviews, 2011. **40**(11): p. 5266-5281.
4. Sankar M., Dimitratos N., Miedziak P., Wells P., Kiely C., Hutchings G.J., Designing bimetallic catalysts for a green and sustainable future. Chemical Society Reviews, 2012. **41**(24): p. 8099-8139.
5. Li H., Yang S., Riisager A., Pandey A., Luque R., Zeolite and zeotype-catalysed transformations of biofuranic compounds. Green Chemistry, 2016. **18**(21): p. 5701-5735.
6. Davis S.E., Zope B.N., Davis R.J., On the mechanism of selective oxidation of 5-hydroxymethylfurfural to 2,5-furandicarboxylic acid over supported Pt and Au catalysts. Green Chemistry, 2012. **14**(1): p. 143-147.
7. Sahu R. Dhepe P.L., Synthesis of 2,5-furandicarboxylic acid by the aerobic oxidation of 5-hydroxymethyl furfural over supported metal catalysts. Reaction Kinetics, Mechanisms and Catalysis, 2014. **112**(1): p. 173-187.
8. Taarning E., Nielsen I., Edeblad K., Madsen R., Christensen C., Chemicals from renewables: aerobic oxidation of furfural and hydroxymethylfurfural over gold catalysts. ChemSusChem, 2008. **1**(1-2): p. 75-78.
9. Casanova O., Iborra S., Corma A., Biomass into chemicals: one pot-base free oxidative esterification of 5-hydroxymethyl-2-furfural into 2,5-dimethylfuroate with gold on nanoparticulated ceria. Journal of Catalysis, 2009. **265**(1): p. 109-116.
10. Davis S.E., Houk L., Tamargo E., Datye A., Davis R., Oxidation of 5-hydroxymethylfurfural over supported Pt, Pd and Au catalysts. Catalysis Today, 2011. **160**(1): p. 55-60.
11. Vuyyuru K.R., Strasser P., Oxidation of biomass derived 5-hydroxymethylfurfural using heterogeneous and electrochemical catalysis. Catalysis Today, 2012. **195**(1): p. 144-154.
12. Ardemani L., Cibin G., Dent A., Isaacs M.A., Kyriakou G., Lee A.F., Parlett C.M.A., Wilson K., Solid base catalysed 5-HMF oxidation to 2,5-FDCA over Au/hydrotalcites: fact or fiction? Chemical Science, 2015. **6**(8): p. 4940-4945.
13. Gorbanev Y.Y., Klitggard S., Woodley J., Christensen C., Riisager A., Gold-catalyzed aerobic oxidation of 5-hydroxymethylfurfural in water at ambient temperature. ChemSusChem, 2009. **2**(7): p. 672-675.
14. Lilga M.A., Hallen R.T., Gray M., Production of oxidized derivatives of 5-hydroxymethylfurfural (HMF). Topics in Catalysis, 2010. **53**(15): p. 1264-1269.
15. Ait Rass H., Essayem N., Besson M., Selective aqueous phase oxidation of 5-hydroxymethylfurfural to 2,5-furandicarboxylic acid over Pt/C catalysts: influence

of the base and effect of bismuth promotion. Green Chemistry, 2013. **15**(8): p. 2240-2251.

16. Niu W., Wang D., Sun J., Wu M., Tsubaki N., Pt nanoparticles loaded on reduced graphene oxide as an effective catalyst for the direct oxidation of 5-hydroxymethylfurfural (HMF) to produce 2,5-furandicarboxylic acid (FDCA) under mild conditions. Bulletin of the Chemical Society of Japan, 2014. **87**(10): p. 1124-1129.
17. Siankevich S., Savoglidis G., Fei Z., Laurenczy G., Dyson P., A novel platinum nanocatalyst for the oxidation of 5-hydroxymethylfurfural into 2,5-furandicarboxylic acid under mild conditions. Journal of Catalysis, 2014. **315**: p. 67-74.
18. Ait Rass H., Essayem N., Besson M., Selective aerobic oxidation of 5-HMF into 2,5-furandicarboxylic acid with Pt catalysts supported on TiO_2- and ZrO_2-based supports. ChemSusChem, 2015. **8**(7): p. 1206-1217.
19. Zhang Y., Xue Z., Wang J., Zhao X., Deng Y., Mu T., Controlled deposition of Pt nanoparticles on Fe_3O_4@carbon microspheres for efficient oxidation of 5-hydroxymethylfurfural. RSC Advances, 2016. **6**(56): p. 51229-51237.
20. Zhang F., Yan Y., Yang H., Meng Y., Yu C., Tu B., Zhao D., Understanding effect of wall structure on the hydrothermal stability of mesostructured silica SBA-15. The Journal of Physical Chemistry B, 2005. **109**(18): p. 8723-8732.
21. Shylesh S., Hanna D., Gomes J., Canlas C.G., Head-Gordon M., A.T. Bell, The role of hydroxyl group acidity on the activity of silica-supported secondary amines for the self-condensation of *n*-butanal. ChemSusChem, 2015. **8**(3): p. 466-472.
22. Cannizzaro S., Üeber den der benzoësäure entsprechenden alkohol. Justus Liebigs Annalen der Chemie, 1853. **88**(1): p. 129-130.
23. Buschmann H.J., Dutkiewicz E., Knoche W., The reversible hydration of carbonyl compounds in aqueous solution part II: the kinetics of the keto/gem-diol transition. Berichte der Bunsengesellschaft für physikalische Chemie, 1982. **86**(2): p. 129-134.
24. Zope B.N., Hibbitts D., Neurock M., Davis R., Reactivity of the gold/water interface during selective oxidation catalysis. Science, 2010. **330**(6000): p. 74-78.
25. Goeppert A., Meth S., Surya Prakash G.K., G.A. Olah, Nanostructured silica as a support for regenerable high-capacity organoamine-based CO_2 sorbents. Energy & Environmental Science, 2010. **3**(12): p. 1949-1960.
26. Durndell L.J., Parlett C.M.A., Hondow N., Wilson K., Lee A.F., Tunable Pt nanocatalysts for the aerobic selox of cinnamyl alcohol. Nanoscale, 2013. **5**(12): p. 5412-5419.
27. Gupta K., Rai R.K., Singh S.K., Catalytic aerial oxidation of 5-hydroxymethyl-2-furfural to furan-2,5-dicarboxylic acid over Ni-Pd nanoparticles supported on $Mg(OH)_2$ nanoflakes for the synthesis of furan diesters. Inorganic Chemistry Frontiers, 2017. **4**(5): p. 871-880.

CHAPTER 6:

Conclusions and future work

6.1. Dodecyl aldehyde aerobic oxidation

In the first instance, the present study has demonstrated the applicability of pore expansion methodologies to a different synthesis route for the production of one of the most commonly used mesoporous materials in catalysis, namely SBA-15. Due to its inherent disadvantages to being used as support in the catalysis of large molecules, TLCT SBA-15's porous architectures have been successfully enlarged, accordingly to their nature, less deformable than its conventional counterpart. At a later stage, the pore expansion methodology that afforded the best results has been extended to hierarchical TLCT SBA-15 supports, which have never undergone such an expansion treatment (for both macro- and mesopores), up to date.

As the study concerning the TLCT materials brought encouraging results, these have then been applied to the catalysis of a bulky molecule that can find applications in the medical field, specifically for the antibiotic therapy of acne vulgaris. It has been demonstrated how the attentive choice of the type of support architecture can confer significant advantages in terms of internal diffusion and catalytic activity. The examination of conversion and product yield profiles has revealed the huge impact upon mesopore expansion or macropore introduction, evidencing the elimination of mass-transport barriers inherent in SBA-15 materials and thus vastly improved accessibility to mesopores wherein the majority of active site nanoparticles reside.

Besides the effect of pore expansion and introduction of additional porosity for the improvement of internal mass diffusion, to continue the study on pore-expanded TLCT SBA-15 structures the effect of temperature can be investigated as well, in order to observe to what extent the oxidation of dodecyl aldehyde depends on large porous architectures only, or if temperature plays another critical role in this regard. This further examination would be beneficial for the assessment of the parameter that affects more strongly the diffusivity of large molecules in two or three-dimensional porous silica frameworks.

6.2. Cinnamaldehyde aerobic oxidation

After the examination of the most appropriate oxygen pressure to be applied to the system, in order to favour the formation of the desired product cinnamic acid, platinum was found to play a key role in establishing catalytic control in the reaction, being able to overcome its intrinsic radical nature. In fact, at ≥ 1 bar O_2 and in the absence of a catalyst, the radical nature of the reaction takes full control, making benzaldehyde the primary product whereas at lower oxygen pressure (atmospheric air) and in the presence of platinum the reaction is governed by catalytic control which favours cinnamic acid. Therefore, in order to observe the effect of platinum, oxygen pressure must be kept low, to ensure cinnamaldehyde evolution to the corresponding peracid via the free radical chain process, and minimise the direct attack of oxygen to cinnamaldehyde that lead to its oxidative cleavage. This is the most favourable condition able to, at least, control the radical reaction. Due to the inherent nature of the aerobic oxidation of cinnamaldehyde, the radical pathway is not entirely avoidable, but it was found to be controllable to a certain extent. In order not to lose control over product selectivities, platinum must assert its role, i.e. establishing a catalytic control that assures the oxidation to cinnamic acid to follow the Mars-van Krevelen mechanism, hampering the oxidative cleavage to benzaldehyde.

The utilisation of two different platinum precursors allowed an extensive investigation of the nature of the metal nanoparticles formed upon functionalisation of the silica support. After examination of the characteristics of the Pt-SiO_2 materials concerning their catalytic performance, it has been identified 0.057wt% Pt-SiO_2 catalyst, prepared with tetraammineplatinum (II) nitrate precursor, as the most efficient one for cinnamaldehyde conversion under low oxygen pressure. This precursor allowed the formation of active sites with the smallest size, leading to a high initial rate.

Further fundamental research around this subject is required, primarily for the importance of designing a more suitable catalyst, in order for cinnamaldehyde aerobic oxidation to become more selective. Thanks to the recent striking developments in heterogeneous catalysts, this reaction can be tested with different substrates and transition metals, in order to accurately find the most appropriate materials that can assess a sheer catalytic control on the reaction.

6.3. Hydroxymethylfurfural aerobic oxidation

The first step achieved during the study on the aerobic oxidation of HMF has been the demonstration of the unsuitability of silica, an acidic support, for the successful transformation of HMF into the desirable oxidation product FDCA.

Being aware of this issue, a comprehensive study has been carried out to investigate the catalytic abilities of Pt-SiO_2 catalysts in the aerobic oxidation of HMF, explore the effect of different temperatures, pressures and amount of sodium carbonate as the base. The catalysts employed have been prepared with two platinum precursors, in order to examine if diverse precursors had a remarkable impact on the catalysis.

The catalytic results led to the conclusion that, between the two precursors used, hydrogen hexachloroplatinate (IV) hexahydrate is the most suitable for HMF aerobic oxidation, since it allowed the smallest metal nanoparticle size, which in turn allowed higher platinum content to be located on the surface of the catalyst, where the reaction occurred.

In order to further explore the reaction in question with a silica support, it is suggested to perform the experiments discussed in section 5.3.4. (Catalytic results), which have been carried out under the most favourable conditions investigated throughout the chapter, at room temperature. Lowering the temperature would allow evaluation of the thermal decomposition of the reactant can be minimised or, at least, inhibited, and assess whether the formation of FDCA is favoured.